PhD THESIS

Superhydrophobic bio-inspired microarchitectured stainless steel surfaces

Submitted to and defended at

UNIVERSITY OF LILLE
Ecole doctorale de la Science de la Matière, du Rayonnement et de l'Environnement,
Doctoral School n°104
Unité Matériaux et Transformations, CNRS UMR 8207

To obtain the degree of
Doctor of philosophy

In condensed Matter and Molecules
Specialty: Materials Chemistry

Publicly presented by
Kevin DOURGAPARSAD

Supervised by
Prof. Maude JIMENEZ and Prof. David BALLOY

Defended on the 29th of March 2024 before the following PhD committee:

DR HDR Laurence FOURNAISON	INRAe, Paris-Saclay	President
Prof. Frederic GUITTARD	Université de Nice	Reviewer
Dr. HDR Philippe JACQUET	ENSAM, Campus de Cluny	Reviewer
Dr. Ion-Cosmin GRUESCU	Université de Lille, UMET	Co-supervisor
Prof. David BALLOY	Université de Lille, UMET	Co-supervisor
Prof. Maude JIMENEZ	Université de Lille, UMET	Supervisor

Thèse de doctorat

Conception de surfaces superhydrophobes bio-inspirées et microarchitecturées en acier inoxydable

Présentée et soutenue publiquement à

UNIVERSITÉ DE LILLE
Ecole doctorale de la Science de la Matière, du Rayonnement et de l'Environnement,
Ecole doctorale n°104
Unité Matériaux et Transformations, CNRS UMR 8207

Pour obtenir le grade de
Docteur

Molécule et Matière Condensée
Spécialité : Chimie des Matériaux

Présentée publiquement par
Kevin DOURGAPARSAD

Thèse dirigée par
Prof. Maude JIMENEZ et Prof. David BALLOY

Soutenue le 29 mars 2024 devant la commission d'examen composée de :

DR HDR Laurence FOURNAISON	INRAe, Paris-Saclay	Présidente
Pr. Frédéric GUITTARD	Université de Nice	Rapporteur
Dr. HDR Philippe JACQUET	ENSAM, Campus de Cluny	Rapporteur
Dr. Ion-Cosmin GRUESCU	Université de Lille, UMET	Co-encadrant
Pr. David BALLOY	Université de Lille, UMET	Co-directeur de thèse
Pr. Maude JIMENEZ	Université de Lille, UMET	Directrice de thèse

Acknowledgement

Le chemin fût long et semé d'embûche, mais au bout de 42 mois fait de patience et de labeur, sonne le clap de fin ou le glas de la délivrance.

Pour commencer, je tiens à remercier le Docteur Guillaume Delaplace, directeur du laboratoire Unité Matériaux et Transformation, anciennement directeur de l'INRAe de Lille, pour m'avoir donné l'opportunité de rejoindre ces laboratoires où j'ai effectué mes travaux de recherche. Naturellement, je tiens à remercier chaleureusement mes directrice et directeur de thèse, la Professeure Maude Jimenez et le Professeur David Balloy, pour m'avoir recruté.

Merci Maude pour ton efficacité et ton adaptabilité. Je me suis senti compris et accompagné tout au long de la thèse. Je suis content d'avoir eu une directrice aussi insomniaque et branchée à WhatsApp que moi. J'espère avoir un jour ton génie rédactionnel et un quart de l'énergie que tu mets dans ton travail.

Merci David pour tout ce que tu m'as appris en métallurgie avec patience et passion. Ce n'était pas gagné d'avance mais tu y as cru et mis du tien pour que ça marche. J'espère un jour avoir ton niveau de culture des matériaux et ta bonne humeur.

Je remercie mon cher encadrant, Ion-Cosmin Gruescu, le légendaire CMX ! Merci de t'être investit autant dans tous les aspects de ma thèse du début à la fin. Ta droiture et ton perfectionnisme ont parfait ma thèse de la paillasse au manuscrit. J'espère être aussi bienveillant avec mes étudiants et pouvoir supporter le café comme toi un jour.

Je voudrais dire un grand merci à mes collègues. Je sais que je vais en oublier.

Dans l'équipe PIHM, je remercie Christelle et Thomas d'avoir toujours cru en moi et de m'avoir réconforté dans les moments sombres. Je n'oublierai jamais votre dévotion pour la recherche, votre joie de vivre et les retours en voiture jusqu'à Hellemmes. Je remercie aussi, Laurent W, Laurent B, Carolina, Thierry S, Amandine, Océane, Brayan, Helena, Jina, Audrey, Angelina, Anne-Laure, Julie, Christine, Thierry B, Héni. Je remercie mon merveilleux stagiaire Reyan, qui m'a grandement et intelligemment aidé à rattraper du retard.

Dans l'équipe PrEF, je remercie mon acolyte de très longue date, Eric Verret, que je connais maintenant depuis 7 ans. Je te remercie pour ton amitié, ta gentillesse, ta compagnie à l'escalade, ton intelligence et ton humour. Je veux aussi remercier mon frère d'arme, Melvin Dilger, avec qui j'espère encore vivre plein de bataille, tant qu'on ne retourne pas à Lisbonne à pied. Je remercie aussi celle qui m'a tout appris, Dr. Saget Manon, ton expertise et ta bonté ont fait de moi un meilleur

scientifique. Je remercie également Ana Luisa, Philippe et Ulrich. Je remercie aussi Florian de m'avoir aidé sur les manips à froid. Je te confie mes bébés, prends en soin.

Côté C7/Chevreul, je remercie également Nathan, Adrien, Marie-Odile, Matthieu, Xhi, Mingwei, Lotfi, Jihane, Solène, Alban, Soufiane, Sabatino, Salma, Séverine, Mathilde, Fabienne, Sophie D, Ange, Alexandre, Adi, Louis, Sophie V, Pierre, Johan, Guillaume, Igor, Lydia, Gaëlle et Fanny.

Au niveau du MPGM, la première personne à remercier est ma jumelle de thèse avec qui je gambade main dans la main depuis le premier jour, Dr. Aleksandra Cieplak. Tu as été mon soleil pendant toute la thèse et je pense que ça a été réciproque. J'espère que ta vie sera pleine de chien et de poule. Je remercie mon frère et ma sœur de fonderie, Tao et Manisha, avec qui l'expérience de fonderie n'aurait pas été la même. Vous êtes tous les deux des scientifiques hors paires, je vous souhaite naturellement, une belle carrière pleine de métallurgie. On se revoit en Inde et en Chine de toute façon, bon courage pour la fin. Je remercie mes deux grandes sœurs de tricots, Anne-Cécile du pont de Rodrigue et le Pr. Bonvalet. Votre expérience et votre recul sur la recherche m'ont plus d'une fois sauvé de la déprime. Je vous souhaite de super belle chose à vos postes de MCF et avec vos chéris respectifs, ce sont de chouettes types bien que mâles hétéros cis blancs. Je ne crains pas du tout pour vos futurs doctorants, ils seront entre de bonnes mains. Il y en a quatre qui méritent aussi leur quart d'heure de gloire, c'est le quatuor : Thibault aka tipabo, El Marcal, Sojaboy et Couyère. Vous avez mis beaucoup d'ambiance dans le labo, c'était vraiment chouette. Ma super pote à la compote Chloé, je ne t'ai pas connu longtemps, et je pense que c'est mon plus grand regret de cette année. Mais heureusement, tu vas venir à Rouen m'embêter. C'est avec plaisir que tu dormiras sur le paillasson. J'ai déjà fait beaucoup de grand discours alors je vais faire court pour les autres, mais je n'en pense pas moins. Merci à Ana Clara, Renata, Jules, Jorge, Jan, Divyanshu, Rajesh, Michele, Sabrina, Adithya, Yanis, Clément, Charlotte, François, Ingrid, Ludovic, Adil, Imen, Hoang-Long, Jeremy, Jean-Bernard, Rana et Jocelyn. Bien entendu, la petite main (ou plutôt grosse patte) qui aide tout le monde, le meilleur d'entre nous, l'assistant ingénieur Damien Creton. Les différents stagiaires que j'ai suivis, Gidéon, Mohamed, Ivan, Cristina, Joan et Yassine.

Je remercie Mme Marie-Noëlle Avettand-Fénoël pour l'opportunité qu'elle m'a offerte. Grâce à vous j'ai le job de mes rêves. J'espère un jour atteindre votre niveau de connaissance et votre rigueur légendaire.

Dans le reste de l'UMET je remercie Corinne H, Isabelle, Jean, Tiana, Julien L, Anne-Marie, Ahmed, Alexandre F, Simon S et Benoit H. J'en oublie certainement, mais le cœur y est.

Je remercie mes collègues de Manoir Industries Manuel R, Frederic C, Begoña G-F, Benoît J et Mathias C pour leur accueil et leur bienveillance en cette fin de thèse.

Je remercie du fond du chœur, ma chorale avec qui j'ai poussé la chansonnette pendant un an et demi. J'aimerais écrire chaque prénom, hélas, je n'en ai absolument pas le courage, mais je vous adore tous autant que vous êtes. ACDJiste un jour, ACDJiste toujours. Bonsoir.

Je remercie mes amies du club de tricot : Marion, Elodie, Marie, Julie et Nathalie. Merci de m'avoir enseigné cette activité incroyable et de m'avoir tant fait rigoler. Je remercie mes copains de l'escalade : Arthur, Louise, Lucile, Quentin, Adrien, Antoine, Yann, Anthony, Vincent, Antoine, Soufiane, Alban, Justin, Pedro, Benji, Alex, Chloé, Emilie, Florian, Julien, Jordan et Sarah, Elodie et Belline.

Je remercie ceux qui m'ont hébergé dans leur maison le temps que je trouve un emploi et que je termine ma rédaction. Ceux qui font partie du meilleur équipage de l'Espace et des Océans, deux de mes meilleurs amis et leur deux amours, the best crew : Capucine, Charly, Gnoucchi et Kouignette.

Merci Oriane M d'avoir été la photographe de ce jour-ci particulier ! Grâce à toi il sera gravé à jamais dans ma mémoire avec de jolies photos en prime. Je te souhaite de kiffer encore longtemps ce que tu fais si bien avec passion.

Bien entendu tous mes amis proches Séraphine, Apolline, Ryan, Eva, Basile, Helena, Laura, Lina, Max, Lorris, Gabriel, Laurie, Alexandre N, Loïck, Noé, Melvil, Marie, Maryem, Orane, Momo, Patafix, Nuggets, Ricotta, Cindy, Sacha, Sofiane, Valentin, Marion, Muriel, Marine, Marie-Morgane, Laetitia, Thalie, Laeticia, Corentin, Elisa, Romain B, Juju G, Camille H, Alban, Cyril, Julien L, Christopher, Samantha, Céline, Romain, Antinéa, Marie S, Charles C et Tristan R.

Je dois beaucoup à ma famille, ma mère Irène, mon père Omer, ma sœur Karine et mes quatre frères Dylan, Aude, Thomas et Grégory. Mes quatres nièces Naïlly, Chaligri, Kassidy et Icha. Je remercie également les autres membres de ma famille.

Je me remercie aussi moi-même d'avoir cru en ce rêve de gamin de devenir « un savant-fou », un scientifique, un passionné. Je suis content d'avoir été têtu dans mes choix d'étude et d'avoir persévérer dans une science aussi passionnante que celle des matériaux. J'espère l'aimer et l'enrichir encore longtemps.

And when the rain begins to fall

You'll ride my rainbow in the sky

And I will catch you if you fall

You'll never have to ask me why

And when the rain begins to fall

I'll be the sunshine in your life

You know that we can have it all

And everything will be alright

Table of content

Table of figures:

List of abbreviations

α-La	α-lactalbumin
β-Lg	β-lactoglobulin
APPJ	Atmospheric pressure plasma jet
APPP	Atmospheric pressure plasma polymerization
BJT	Binder jet
CAH	Contact angle hysteresis
CAO	Computer-aided design
DED	Direct Energy deposition
EDS	Electron dispersive spectroscopy
HMDSO	Hexamethyldisiloxane
MAM	Metal additive manufacturing
MEX	Material extrusion
MJT	Material jetting
PAM	Polymer additive manufacturing

List of abbreviations

PBF	Powder bed fusion
PHE	Plate heat exchanger
pFOTES	1H,1H,2H,2H-perfluorooctyltriethoxysilane
SEM	Scanning electron microscope
SHL	Sheet lamination
SLIPS	Slippery liquid-infused porous surface
SLM	Selective laser melting
SLS	Selective laser sintering
SS	Stainless steel
VPP	Vat photopolymerization
WAAM	Wire-arc additive manufacturing
WPC	Whey protein concentrate

General introduction

Natural superhydrophobic surfaces are resulting from a long evolution process. Plant and animals perfected surfaces to catch preys, to swim faster, to defend themselves against predators and generally to survive in the wilderness. The understanding of the mechanisms behind the multiple examples of progressive surface engineering has inspired material science. A natural material possesses a precise structure that confers specific functional properties. If it is possible to replicate this particular structure with a different material, maybe the properties will be similar to those of the original material. This creation process is called bio-inspiration. The driving idea of the work which was realized and is presented in this manuscript is to propose an innovative manufacturing method to manufacture a 316L stainless steel bio-inspired surface, architectured from micrometric to nanometric scale.

This manuscript begins with an in-depth examination of superhydrophobic bio-inspired surfaces. Here, the mysteries of nature's designs will be examined, particularly the water-repellent properties from certain plants and animals. By decoding the principles of wettability and contact angles, closely linked to surface texture, this chapter lays the groundwork for understanding how these natural phenomena can inspire technological innovations. Various manufacturing techniques to replicate these features on stainless steel will be discussed. The state-of-the-art analysis of the available technologies, with their advantages and limitations, will motivate the proposed combination of polymer additive manufacturing and stainless steel vacuum-assisted investment casting.

In the second chapter, a transition is made from the theoretical to the practical aspects of manufacturing. The feasibility of stainless steel investment casting at the millimetric scale will be questioned and investigated. To do so, a castability test has been developed and a comparative study to other metallic materials is proposed. Once the castability is proved to be possible at a millimetric scale, the next step will be to manufacture stainless steel surfaces presenting micrometric bio-inspired details.

Chapter three shifts the focus to bio-inspired microtexture manufacturing process. In this chapter, multiple aspects are going to be questioned, from the polymer additive manufacturing

process to the stainless steel casting. It questions the limitations of the technologies. Once manufactured, the surfaces will be characterized in terms of morphology, and more importantly, of wettability. Does the manufacturing process lead to more hydrophobic surfaces than usual flat stainless steel coupons? How could this hydrophobicity further be improved?

The last chapter will introduce an additional nanotexturing technique: the atmospheric pressure plasma polymerization for functionalizing stainless steel microtextured surfaces. The atmospheric pressure technology has been chosen because of its easy scale up at industrial level. This cutting-edge method allows the precise modification of surface properties, enabling the creation of surfaces with enhanced hydrophobicity. The first part of this chapter is dedicated to the understanding of the morphology and the chemical composition of this particular nanoscale coating. In the second part, the surface properties are characterized from a more applicative point of view. The anti-fouling, oil-retention and anti-icing properties of the surfaces are explored.

Throughout the manuscript, several unifying themes emerge. The blend of inspiration from nature with advanced manufacturing and functionalization techniques represents a recurring motive. The pursuit of sustainability, both in terms of manufacturing processes and the lifespan of the materials produced, is another key aspect pointed out along the manuscript. Additionally, the potential applications of these technologies in various sectors – from aerospace to food industry – highlight their versatility and transformative potential.

In conclusion, this manuscript serves as a bridge between the natural world and advanced material science. By exploring the development, functionalization, and application of bio-inspired stainless steel surfaces, we shed light on a field that is at the forefront of innovation. The fusion of chemistry and engineering presented in these chapters offers a glimpse into a future where the boundaries of material capabilities are continually expanding, driven by a blend of inspiration, innovation, and a deep understanding of the natural world.

Chapter 1: Superhydrophobic bio-inspired surfaces and their applications

1 Introduction

Bioinspiration (from the Latin words *bio* meaning "life" and *inspiratio* meaning "breathing in"/ "to inspire") is the development of new materials, devices, processes or structures inspired by biological systems or natural phenomena [1]. This innovation concept is frequently confused with biomimicry, which consists in emulating as much as possible the models, systems and elements of nature to solve complex human issues [2–4]. As an example, bio-inspired lattice structures can help reduce the amount of material necessary for the fabrication and control the mechanical properties of the final object [5].

By applying the concept of bioinspiration to surface engineering, a new generation of materials has been created. In the wilderness exists a large panel of wonderful properties such as iridescence [6], self-healing [7], self-cleaning [8], anti-adhesive [9], anti-fouling [10], anti-icing [11], thermal insulation [12], energy efficiency [13], hydrophilicity or hydrophobicity [14] and has been exploited to enhance the surface performances.

Hydrophobicity (from the Greek words *hudro* or *húdôr* meaning "water" and *phobos* meaning "fear"/ "aversion") is the property of interest that will be developed in this work. In chemistry, it is the ability of a molecule not to fear, but to repel water. In the case of a surface, the adjective hydrophobic describes poor wetting with water. A deep analysis of natural superhydrophobic surfaces such as lotus leaves, has increased the understanding of hydrophobicity [15,16]. The phenomenon has been linked to the particular surface multi-scale texture. Moreover, the biomimicry of this surface texture has also demonstrated a benefit in terms of wetting control. By controlling the interface liquid/solid, multiple new kinds of surfaces, using various materials (polymer, metal, wood, etc.) as substrates, have been designed, such as anti-corrosion [17–20], anti-bacterial [21–23], anti-fouling [24] or anti-icing [25,26] surfaces. The common ground regarding these surfaces is their multi-scale structures, leading to controlled wettability, and in particular superhydrophobicity.

This chapter presents different types of superhydrophobic bio-surfaces and their applications. First of all, a brief detour will be made through the fundamentals of wettability. Secondly, a review of the different examples of superhydrophobic surfaces available in nature will be presented. Then,

a closer examination of how hydrophobic biosurfaces have inspired engineering in metallic surfaces will be provided. In the last part, a particular attention will be dedicated to the stainless steel surfaces manufacturing. The diversity of techniques allowing the texturation of this particular material will be investigated. These three subchapters will lead to a better understanding of the scientific positioning adopted during this PhD thesis work.

2 Fundamentals of wettability

2.1 The successive describing models

Wettability is defined as the attraction of a liquid phase to a solid surface, and it is typically quantified using a contact angle with the solid phase [27]. Three interfaces coexist : liquid/vapor γ_{LV}, vapor/solid γ_{VS} and liquid/solid γ_{LS} (Figure 1a) as Thomas Young first described in 1832 [28]. The different γ are standing for the surface tension between two phases. In this case, two fluids are in contact with the solid surface: the air (vapor) and the drop (liquid) as displayed in Figure 1a. It is a balance between the adhesive forces (liquid/solid) and the cohesive forces (liquid/liquid) [29]. At the (vapor/liquid) interface, the surface tension γ_{LV} maintains the liquid's molecules together. To minimize the surface in contact with the vapor phase, the small amount of liquid will adopt a spherical shape. The wettability of a surface towards a certain liquid can be measured through the contact angle: a single drop of the liquid of controlled volume is dropped on the surface to observe the angle formed at the solid/liquid interface. As mentioned on Figure 1b., the angle measured will qualify the behavior from super hydrophilic for small angles, to superhydrophobic for great angles.

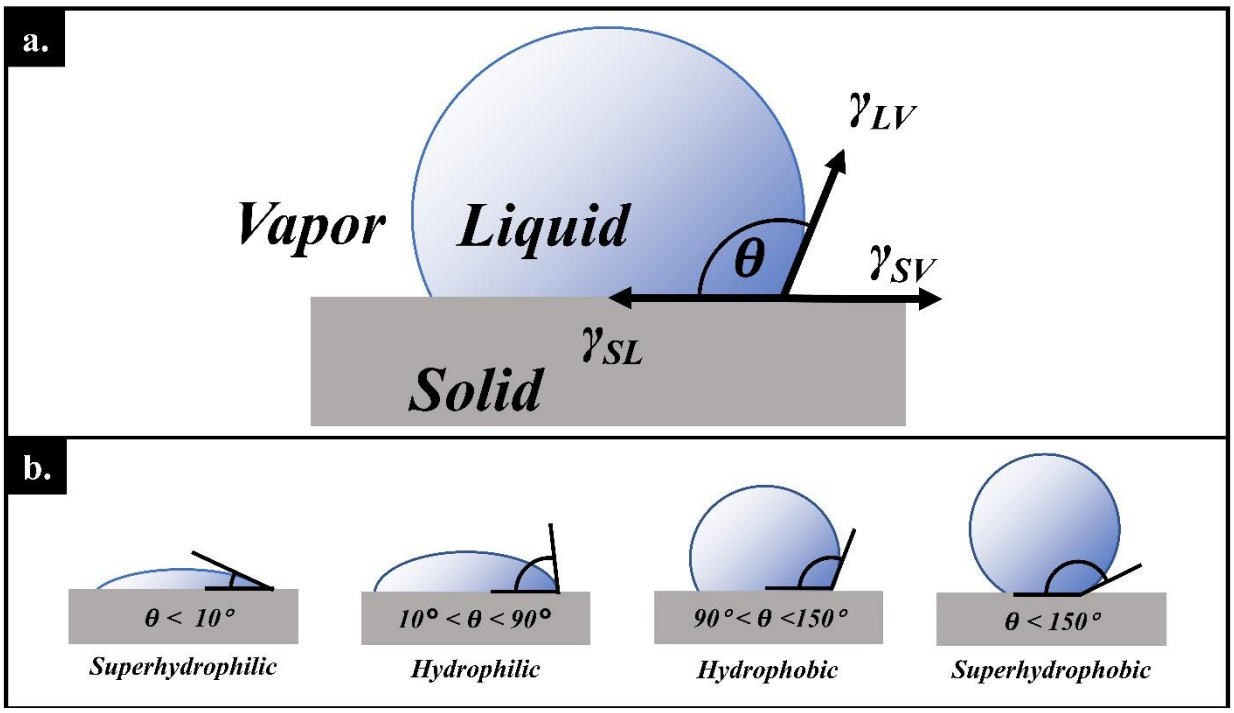

Figure 1. (a) The three coexisting phase in the case of a water drop on a solid substrate in the air (b) 4 subcategories of wetting depending on the contact angle formed between at the liquid/solid interface

The molecules contained in the liquid phase within the droplet have a certain cohesion thanks to intermolecular forces like Van der Walls forces or hydrogen bond (H-bond). Depending on the affinity with the solid and the gas, the angle θ will change.

The wettability measurement can be static, with a single drop of liquid (static contact angle), or dynamic, with a tilted surface, i.e. contact angle hysteresis (CAH), or varying drop volume (maximum drop volume). Equation 1 describes the contact angle through the balance between the three phases mentioned before.

$$\cos\theta_y = \frac{\gamma_{VS} - \gamma_{SL}}{\gamma_{LV}} \quad (1)$$

The model evolved by taking into account the surface roughness with Wenzel, that allowed to partly explain the hydrophobic behavior of some materials [30]. Wenzel quantified in 1936 how

the surface rugosity r affects θ_w , the apparent contact angle (Equation 2). The rugosity factor r is a ratio between the actual rough surface and the surface without any asperities (Equation 3).

$$\cos\theta_w = r\ \cos\theta_y \tag{2}$$

with

$$r = \frac{actual\ surface}{projected\ surface} \tag{3}$$

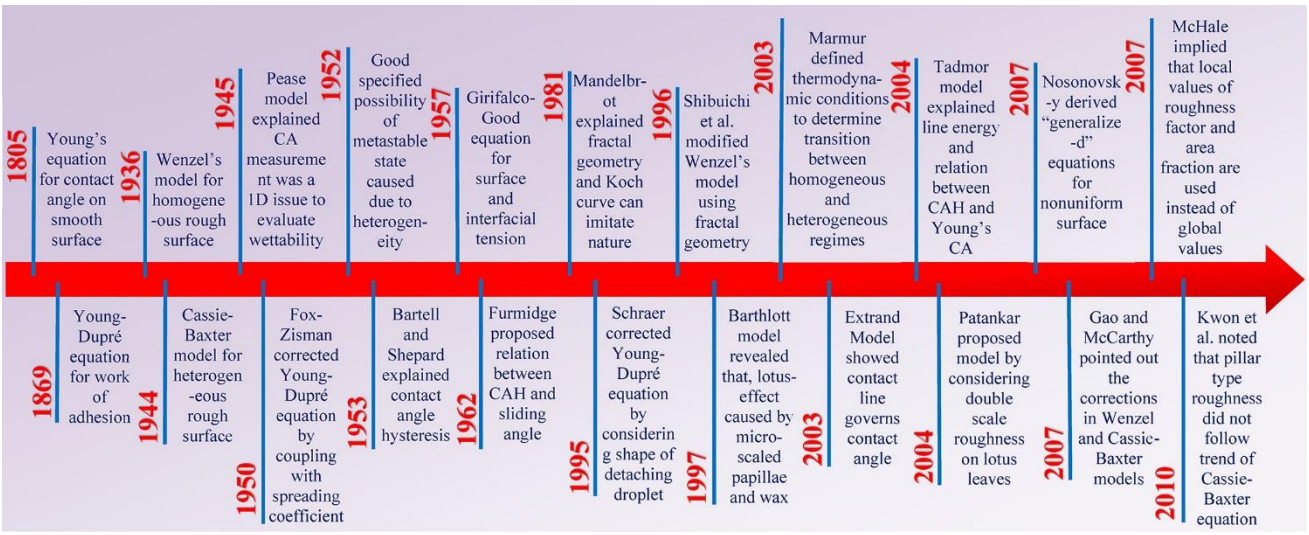

Figure 2. Timeline of key developments of wettability models as described by Parvate et al (2020)

Wenzel and Cassie-Baxter models are fundamental to understanding wettability, but over time, various other theories have emerged. As Parvate et al. (see Figure 2) mentioned in their review about superhydrophobic surfaces. A series of complementary theories appeared between

1945 and 2010 to discuss the surface geometry, the consideration of surface energy or even considering dynamic measurements for the wettability [31].

2.2 Factors influencing wettability

The relationship between a solid and a liquid can be affected by multiple parameters. A liquid will usually show different wetting behaviors when exposed to various solid surfaces. As an example, a drop of water will not behave the same way over ceramics, metals or polymers. From the surface point of view, two main factors affect the wettability: the surface chemistry and the surface morphology [32–34].

On one hand, the chemistry of the surface is of primary importance and will affect the surface wettability significantly. On the other hand, the surface morphology and topology will also affect the liquid/solid interface because the specific surface area fluctuates with the porosity and/or roughness [35]. Other factors such as surface cleanliness, ambient temperature and/or humidity can also affect the wettability [36] (Figure 5). Some of the physical and chemical properties of the fluid are more likely to affect the wettability. For example, the surface tension, the viscosity and the polarity are the motor characteristics of the fluid wettability [37]. As a consequence, wettability between two fluids (for example water and air) and a solid (the surface) is a balance between the intrinsic cohesive forces of the fluids and the surface properties [38]. If the properties of the liquid are matching the substrate properties, the liquid will spread over the surface. A “perfect wetting” is currently admitted when the contact angle is not even measurable because it is approaching zero [39], and these materials are called “superhydrophilic” (Figure 1b). On the contrary, if the surface is not propitious for the liquid to spread because of the chemistry or the morphology of the surface, the liquid will wet less, until reaching very high angles and “superhydrophobicity”, forming spherical drops of liquid on the surface [40] (Figure 1b). Superhydrophobic behavior can also be

assessed by immersing the surface into water and measuring the contact angle formed by air bubbles [41].

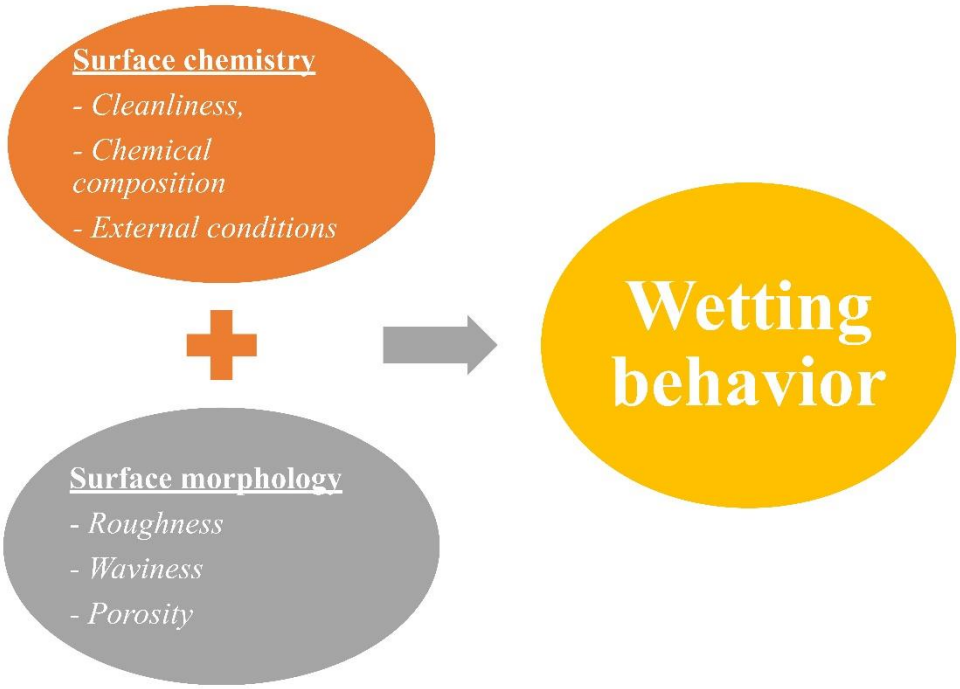

Figure 3. Parameters mitigating the wettability

In particular, wettability is greatly influenced by topology in the context of superhydrophobic surfaces. In 1944, based on Wenzel equation, Cassie and Baxter expressed the apparent angle of a composite material. The following equation (Equation 4) distinguishes the liquid fraction in contact with the solid f_1 and the liquid fraction in contact with the air f_2. Air can be considered as the second material to predict the contact angle of a porous material. The drop does not impregnate the surface completely due to the air trapped in the porosity [42]. The understanding of highly porous materials was thus included in this definition by considering air as a second material.

$$\cos\theta_c = f_1 \cos\theta_1 - f_2 \quad (4)$$

Superhydrophobic surfaces can correspond to Wenzel or Cassie-Baxter models (see Figure 4a.). The difference resides in the drop pinning measured via the sliding angle (SA), i.e. the tilting angle from which the drop starts to slide. When the drop shows a SA above 60 ° or when it is completely pinned to the surface while tilting is applied, it corresponds to a Wenzel state, also known as rose petal effect [43]. Contrarily, when SA is less than 60 °, the surface is in a Cassie-Baxter state, also known as Lotus leaf effect[44] (see Figure 4b.).

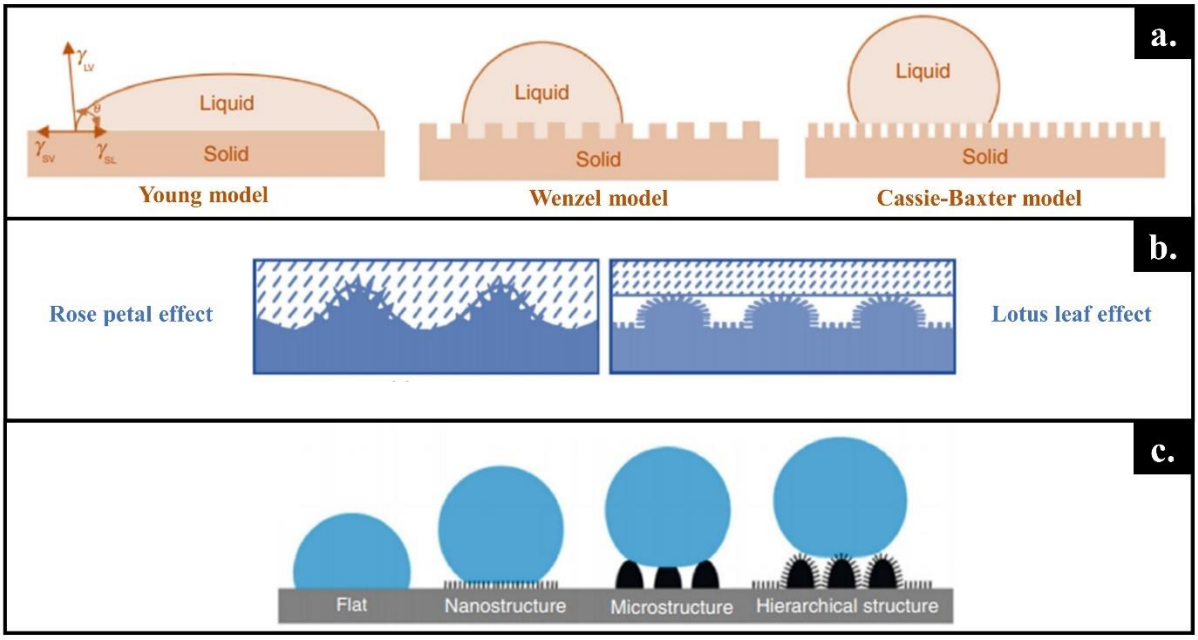

Figure 4. Schematic representation of (a) Young's, Wenzel and Cassie-Baxter models, (b) Rose petal and Lotus leaf effect and (c) influence of different size of texture on a water drop

Superhydrophobic surfaces, such as the one described, are not merely theoretical constructs; they exist in the real world. Cassie and Baxter did their measurement over natural materials such as duck feathers and wool yarn [42]. They conclude their study by saying that the structure of the material was certainly more responsible of the superhydrophobicity than *"any exceptional proofing agent"*. Modern material science specialists are now convinced that hydrophobicity does not only come from the hierarchical surface structure, but also from the chemical surface composition [45]. Before manufacturing new synthetic superhydrophobic surfaces, a closer look to the superhydrophobic surfaces present in nature is mandatory. The next section will be dedicated to their observation.

3 Superhydrophobic biosurfaces in fauna and flora

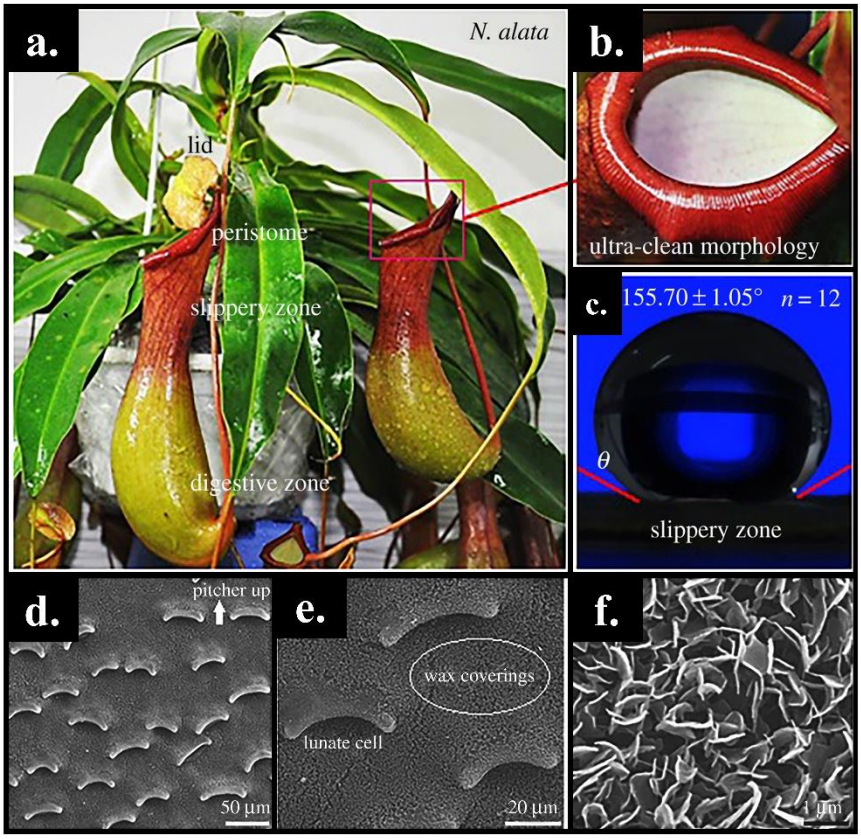

Figure 5. (a) Nepenthes Alata description, (b) Top-view of the self-cleaning pitcher, (c)inner pitcher surface WCA measurement, (d), (e) and (f) SEM imaging of the Nepenthes pitcher at different magnification from the microtexture to the nanotexture (adapted from Wang et al)

Some plant leaves structures have been closely investigated for their hydrophobic behavior. Banana tree, also known as *Musa Acuminata*, possesses stomates and ridges organized to enhance self-cleaning properties [46]. Lotus leaves are very famous for their superhydrophobic hierarchical micro/nanotexture [47,48]. Another well-known example of superhydrophobic plants that inspired slippery liquid infused surfaces are *Nepenthes*, i.e. carnivorous plants possessing a pitcher with a slippery inner surface that can trap insects, composed of a porous structure impregnated with a lubricant [49–53]. Figure 5 displays *Nepenthes Alata* observed at different scales, including Scanning Electron Microscopy (SEM) pictures of the surface texture at different magnification.

Both lotus leaves or nepenthes pitcher have respectively demonstrated remarkable properties such as self-cleanability and anti-fouling activity, respectively [54–56]. Animal scales are another example of amazing materials. For example, fish scales have a double role: they are both protective and shaped to swim faster [57,58]. Multiple species such as snakes, pangolins, crocodiles or lizards adopted the scales as a protective armor [59]. Other animals, such as butterflies and moths developed scales at a micrometric scale that are both iridescent and also show hydrophobic properties thanks to their structural micro-arrangement [60]. Over the last decades, materials science researchers, inspiring from these structures, have created new architectured surfaces. In particular, biomimetic polymer surfaces engineered by copying shark scales architecture are already used to improve hydrodynamics and aerodynamics [61,62]. A similar research inspired from fish scale was conducted to enhance the tribological properties over an aluminum substrate [63].

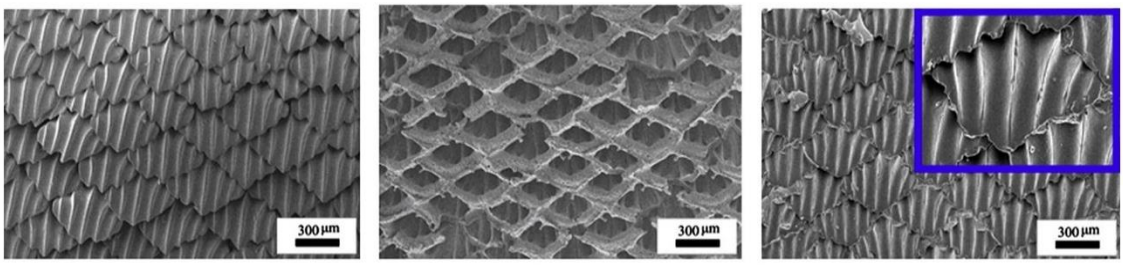

Figure 6. Shark skin replica using a PDMS mold to produce superhydrophobic polymer surface (from Liu et al. 2012)

Superhydrophobic surfaces manufacturing using biomimicry has become a common ground during the past decades. The example of the Nepenthes is well known and described in the literature [51–53,64,65]. The microtexture combined to a nanotexture and impregnated with wax possesses both superhydrophobic and self-cleaning properties. The biomimicry of this surface consists in the manufacturing of a multi-scale texture combined to an oil impregnation. This type of surface is called slippery liquid infused porous surfaces (SLIPS) and presents the same properties than the nepenthes [66]. They can be made on polymer or metallic substrates [3] and the liquid infused can be organic (coconut, black seed oil, etc.) or mineral (silicone, paraffin, krytox, etc.) [67]. The

impregnated phase creates a physical barrier against water to avoid water-contact phenomena such as corrosion [68].

The texture of a surface is defined as a complex combination of waviness, roughness and defects [69]. The waviness is the macro-roughness, which means the shapes observed and measured at scales above 100 µm. The roughness consists of the micro and nano-structures of the surface. In the nature, a great diversity of surface structures with special properties exists among plants and animals. Outstanding abilities such as gecko adhesion [70], shark speed [71], lotus leaves self-cleaning [15], trabecular bone mechanical resistance [72] or butterfly iridescence [73] have respectively inspired non-permanent adhesives [9,74], aircraft surface engineering [75], self-cleaning surface engineering [14], lighter structures [72,76–78] and structural color engineering [73].

This PhD thesis is dedicated to the design of superhydrophobic stainless steel structures, using in particular bio-inspired patterns. The next part will focus on a state of the art of the fabrication of such structures. Usually, to reach such superhydrophobic behavior, a micro/nano-architecture is built-up on a substrate (metallic or polymeric) via mechanical/chemical/physical etching or deposition from liquid suspension to increase the surface roughness [79]. The size of the texturation patterns will provide different wetting behavior to a material. A further chemical modification can be done to improve the hydrophobicity of the micro/nano-structured surface [80].

4 Superhydrophobic stainless steel textured surfaces

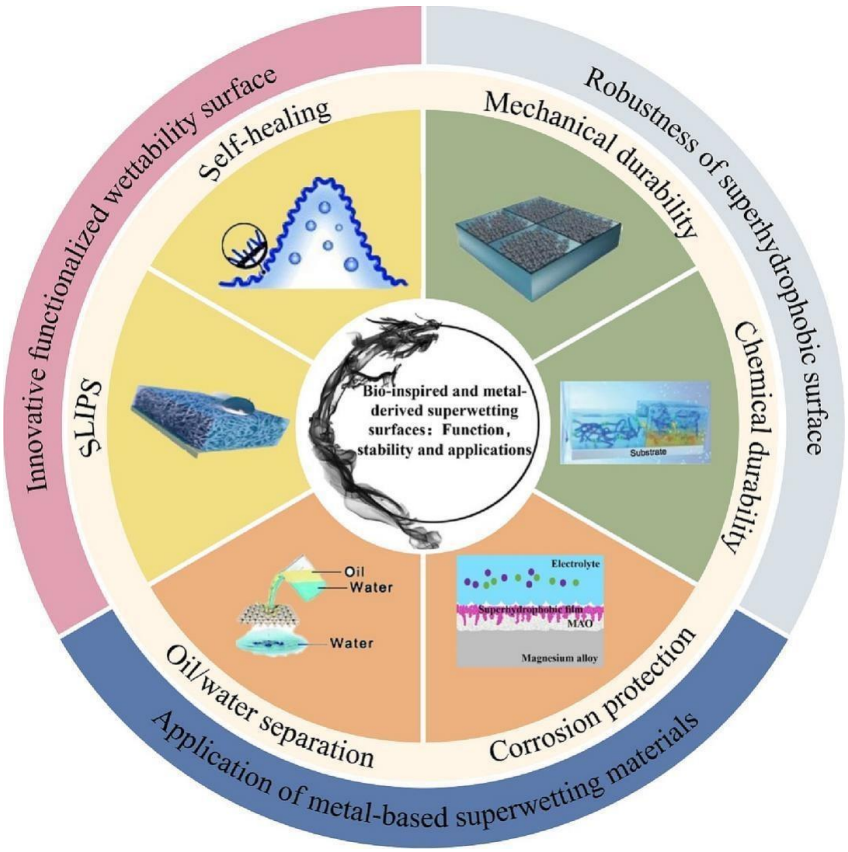

Figure 7. Different purposes of bio-inspired and metal-derived superwetting surfaces (from Wei et al (2023))

Bio-inspired textured stainless steel surfaces refer to surface designs that take inspiration from nature to enhance the properties and performance of stainless steel. These surfaces are engineered to mimic the structures found in plants, animals, or other biological systems, offering unique advantages for various applications [81,82]. Bio-inspired textured surfaces can be designed to affect the wettability, friction, adhesion, or other desired characteristics of stainless steel. By emulating the features found in nature, such as microstructures, hierarchical patterns, these surfaces can exhibit improved functionalities compared to their smooth counterparts [10,83] (Figure 7).

4.1 Generalities about stainless steel

Stainless steel is a type of alloy known for its exceptional corrosion resistance, good mechanical properties and high durability. It is composed primarily of iron, along with varying amounts of chromium, nickel, molybdenum, and other alloying elements. The exact composition of stainless steel can vary depending on the specific grade and intended application [84]. For example, 300 series of steel grades, that contains around 18% chromium and 8% nickel, is mainly prefered for its corrosion resistance [85].

The key element that differentiates stainless steel from regular steel is chromium present in large amount (>10 wt.%). The presence of chromium in stainless steel allows the formation of a protective layer of chromium oxide on the surface, which acts as a barrier against corrosion. This passive film isolates the underlying steel from coming into direct contact with oxygen, moisture, and other corrosive agents, thus making stainless steel highly resistant to rust, stains, and oxidation [86].

The addition of other elements, such as nickel and molybdenum, further enhances the physical and chemical properties of stainless steel : nickel (necessary to transform ferritic steel into austenitic steel) increases the corrosion resistance and imparts ductility [87], while molybdenum improves resistance to pitting and crevice corrosion, especially in harsh environments [88]. In 1948, Anton Schaeffler described the contribution of different elements to the resulting stainless steel microstructure. Some elements such as carbon or manganese are nickel-equivalent (gammagenous or austenite formers). Other elements like molybdenum, silicon, or niobium are (alphagenous or ferrite formers). The diagram represented on Figure 8 maps the main different crystalline phase that stainless steel can adopt depending on the composition.

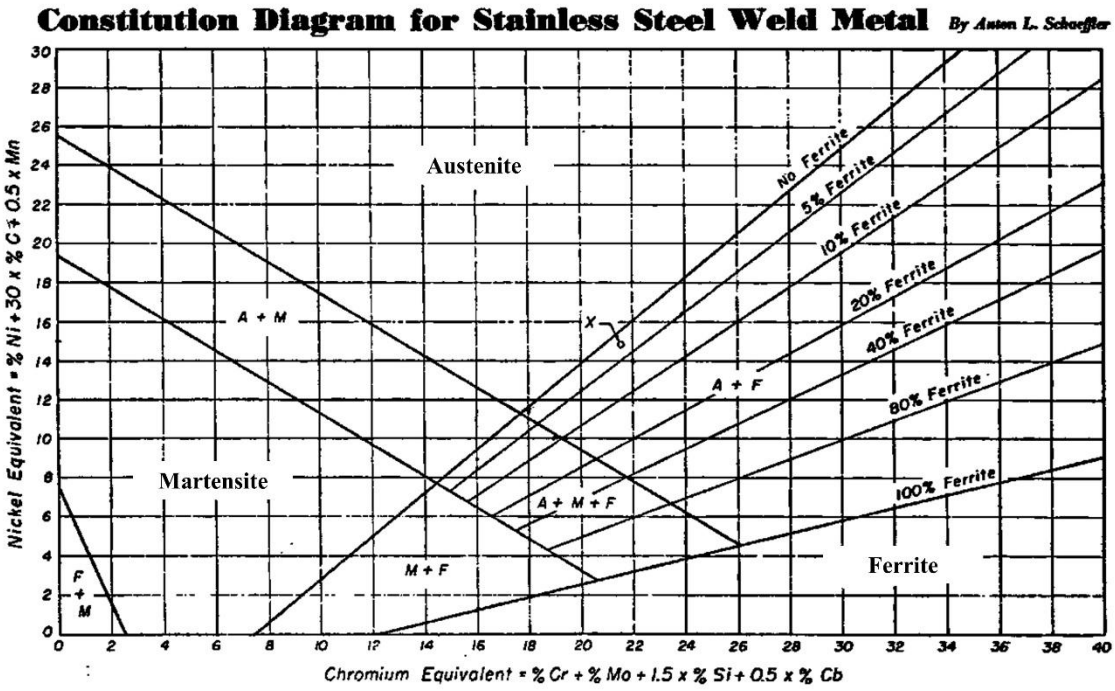

Figure 8. Final version of Schaeffler diagram published in 1949

The three main phases are:

Ferrite is a body-centered cubic (BCC) phase relatively soft and ductile. Ferritic stainless steels, for example AISI 400-series, are used for household items, appliances, sinks, automotive exhaust systems, stoves, etc [89].

Martensite is a body-centered tetragonal phase extremely hard and brittle, contributing to high strength. Martensitic steels, for example AISI 420, are mainly constituting mechanical parts for multiple industries working at high or low temperature [89].

Austenite phase, the last phase presented on the diagram that will interest us during the rest of the work is austenite, a face-centered cubic (FCC) phase, known for the corrosion resistance and the good mechanical properties at high temperature. Austenitic steels, for example AISI 300 series, are the most common grades of stainless steel produced and processed. These grades can be used for the fabrication of communal equipment and various structures or employed in chemical, pharmaceutical, petrochemical, and food industries (tanks...), urban furniture, and extensively in nautical environments [89].

Austenitic stainless steels are known for their high strength and durability, providing structural integrity and longevity to various components and structures. It is non-porous, easy-to-clean, and resistant to bacterial growth, making it widely used in the food and medical industries where cleanliness and hygiene are crucial. The surface finish is easily adjustable from mirror-like to highly rough using polishing or mechanical grinding. Certain grades of stainless steel can withstand high temperatures, making them suitable for applications in heat exchangers, exhaust systems, and fire-resistant structures. Stainless steel is recyclable and can be re-used without loss of its original properties, making it an environmentally friendly material choice. Moreover, the corrosion-resistance property avoids additional coating to the material [90]. Energetically, the SS scrap recycling requires less than a third of the energy used to produce SS from virgin material [91]. In fact, modern industrial stainless steel production is already using second hand stainless steel. Because of its longevity, the amount of stainless steel in end of life collected is not sufficient to able to meet the growing production needs yet. In the coming years, the amount of steel collected will theoretically grow [90].

Due to its versatile properties, stainless steel, under different grades finds application in various industries, including construction, automotive, aerospace, kitchenware, medical devices [92,93], and many others. The following part of the manuscript will focus on 316L stainless steel which is the most common and abundant grade of austenitic stainless steel used in the food processing industries.

Table 1. Chemical composition of 316L stainless steel (weight percentage)

Element	**Fe**	**Cr**	**Ni**	**Mo**	**Mn**	**Si**	**Mn**	**C**	**S**	**P**
(wt %)	Balance	16.0 - 18.0	10.0 - 14.0	2.0 - 3.0	< 2.0	< 1.0	< 2.0	< 0.03	< 0.03	< 0.04
Ref					[94,95]					

Stainless steel surfaces typically exhibit a relatively high surface free energy (34-36 mN/m), which promotes wetting by polar liquids like water. For example, superhydrophobic polymers like polytetrafluoroethylene (PTFE) possess a smaller SFE (21-22 mN/m) [96,97]. The contact angle between water and stainless steel is typically slightly below 90 degrees [32]. Different strategies can be adopted like *top-down* or *bottom-up* to enhance the surface hydrophobicity of the stainless steel.

4.2 Hydrophobic metallic surfaces manufacturing strategies

As Ellinas et al. described in their review about hydrophobic metallic surfaces manufacturing, the different fabrication processes can be classified into two main strategies : the *bottom-up* and the *top-down* [79] strategies. Each term will be defined in the corresponding subchapter.

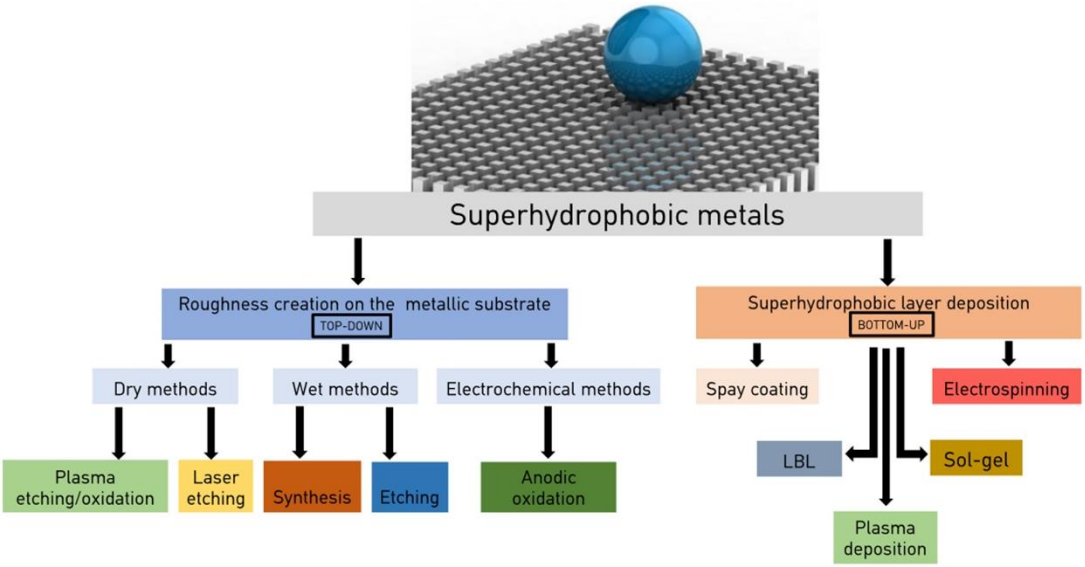

Figure 9. Different strategies for superhydrophobic metals manufacturing [79]

4.2.1 The Bottom-up strategy

The *bottom-up strategy* consists in adding up material to an existing substrate. Most of the time, the material added to the surface is of a different chemical nature than the surface. The deposition can be made through multiple process such as spray coating, electrospinning, sol-gel or

plasma deposition, as mentioned on Figure 9. The process used will depend on the type of coating, the type substrate, the targeted coating thickness and the properties expected.

In the case of this thesis three out of the three conditions are already set. The coating has to be as thin as possible, the substrate is stainless steel and the property expected is hydrophocity. In the modern literature, these conditions have been satisfied using different approaches in a bottom-up strategy. The layers added to increase the hydrophobicity are mostly polymers [55,98] or metallic oxides [99,100]. The surfaces manufactured in a bottom-up strategy are mostly composite materials because the substrate is metallic and the coating is chemically different.

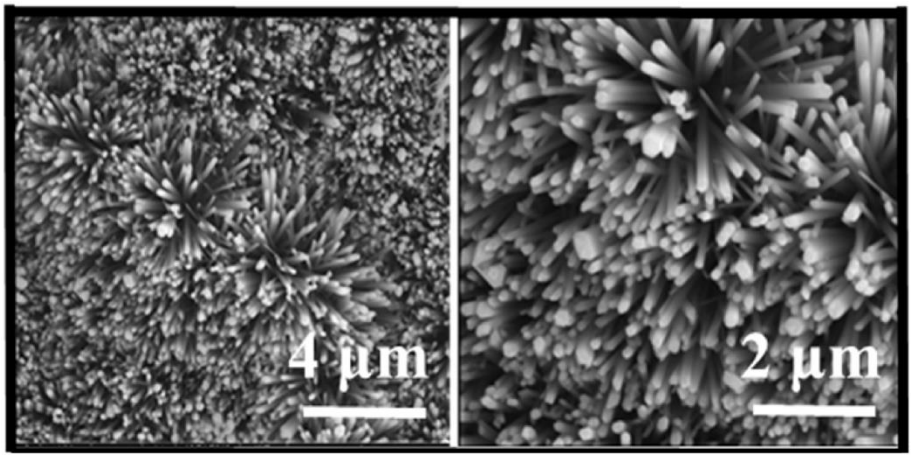

Figure 10. SEM images of zinc oxide (ZnO) coating fabricated through electrodeposition process on a stainless steel substrate from Deng et al (2023).

The additional oxide layer source can be external to the substrate. For hydrophobic applications, the most common oxide are titanium oxides and zinc oxides (see Figure 10) [31,101]. The deposition process can be electrodeposition [16,102], plasma polymerization [103] or sol-gel [104].

If the supplementary layer is made of polymer, it can be synthesized directly on the metallic substrate (spray coating [105], electrospinning [106], etc.) or be shaped on the substrate during the polymerization(embossing [107]). The polymer can be chosen among “commodity polymers” like polymethyl methacrylate (PMMA), polyurethane (PU) and polyethylene (PE), or “engineering polymers” like polytetrafluoroethylene (PTFE) [107].

A large variety of polymer coating have been developed during the last years. The main disadvantage of these kinds of coatings is related to their thermal properties. The polymer layer or the oxide layer are indeed not as thermally conductive as the substrate alone [100,108]. Another drawbacks is the adhesion between the coating and substrate especially in wet environments [109].

The opposite of the *bottom-up* strategy is the *top-down* strategy (see Figure 11), which consists in removing material from an existing substrate via a physical method (like polishing, laser etching, etc.) or a chemical method (e.g. electrochemical etching [110]). These techniques will be detailed in the following part.

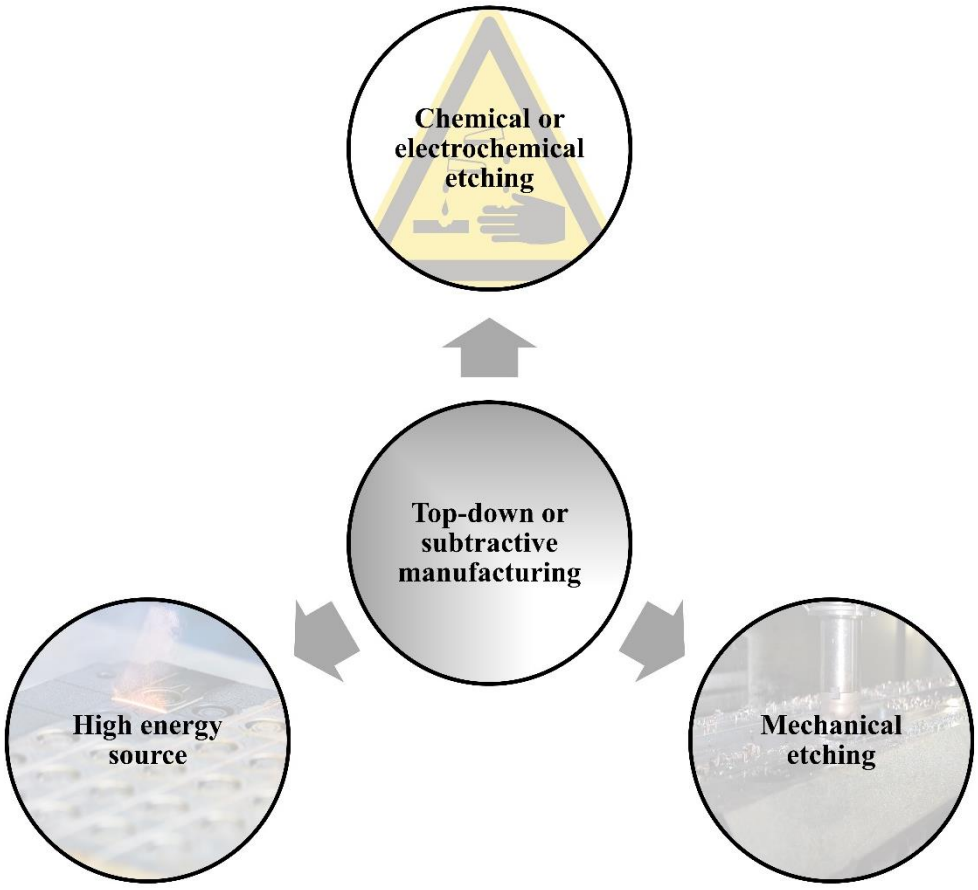

Figure 11. Three main methods of subtractive manufacturing

4.2.2 Subtractive manufacturing or top-down

Removing a layer of material from a stainless steel substrate can be done in multiple ways. This strategy is also called micromachining [111]. In this process, unwanted material is removed from a metal workpiece using: machining, chemicals or non-conventional technologies (e.g. lasers). It allows for precise and intricate designs to be achieved, making it suitable for creating complex metal components with tight tolerances. Subtractive manufacturing methods include milling, turning, drilling, and grinding, each serving specific purposes in metal fabrication [112].

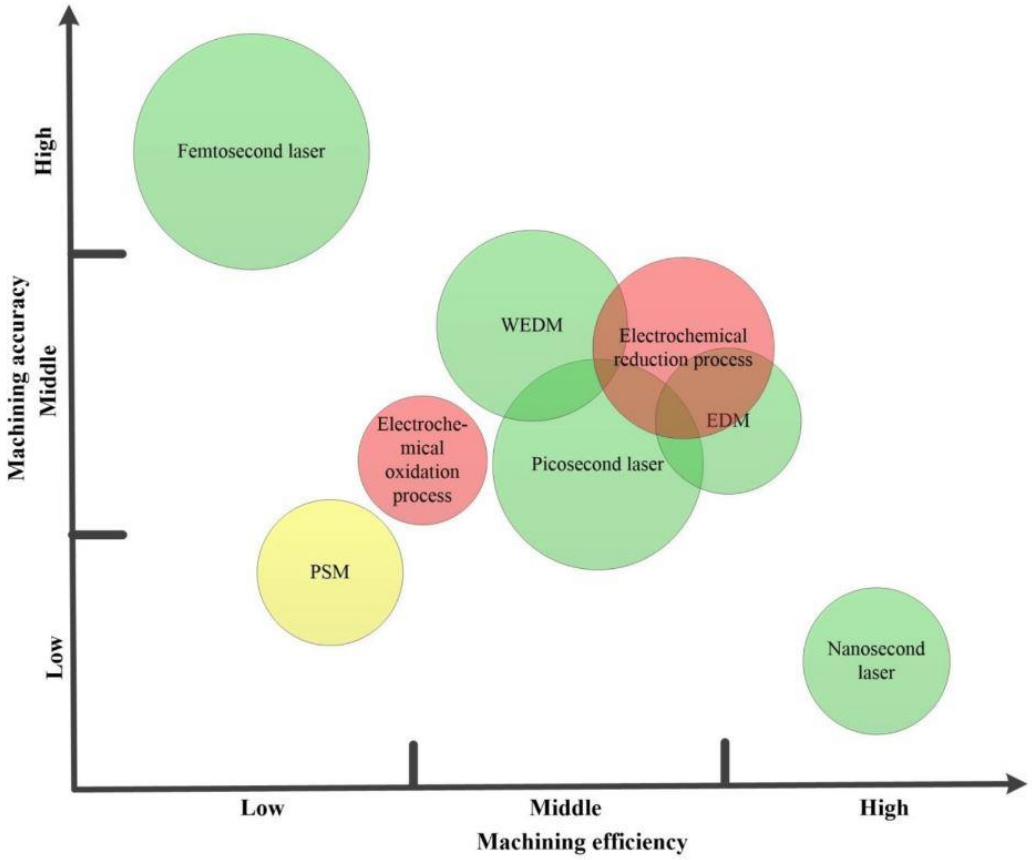

Figure 12. Comparison of various non-conventional machining techniques for superhydrophobic surfaces involves assessing their efficiency, accuracy, cost, and environmental implications. In this comparison, the machining cost is visually represented by the radius of the circle, from Shen et al. (2021)

While subtractive manufacturing offers excellent accuracy and surface finish, it may generate substantial waste material. The metallic chips produced during the process are not easy to recycle because of the residual mix of grease and cooling liquid [113]. The process may also be

time-consuming, particularly for intricate designs, as it involves multiple tool changes and successive passes to achieve the desired final shape, potentially affecting production efficiency and energy consumption. Plus, the tools used for mechanical machining or micromachining have to be replaced frequently. Shen et al (2021) proposes a graphical comparison (see Figure 12) of different machining processes for transform metallic substrate into superhydrophobic surfaces [114]. In this chart electrical discharge machining (EDM), wire electrical discharge machining (WEDM), electrochemical oxidation and reduction, plasma spraying machining (PSM) and three different laser machining technologies are compared. These authors compare the machining efficiency, the machining accuracy the environmental cost and the execution cost. In this study, it is interesting to note that there is a lack of information about the environmental cost classification method. A theoretically perfect technology would be placed in the upper right corner of the chart in a small green circle, but none of the existing technologies could fit these requirements. One interesting fact to mention about the environmental cost of subtractive manufacturing is the specific cost. The more material is removed from a part, the more the specific environmental cost (cost/kg) of the material left increases.

Material can be removed from the substrates physically by high energy sources such as plasma or lasers [115,116]. These processes can effectively turn the substrates into a hydrophobic surface by creating micro and/or nanotexture over the surface. Depending on the laser texturation parameters (current intensity, atmosphere, scanning speed, distance from energy source, etc.), the surface can be hydrophobic or hydrophilic [117]. The resulting hydrophobicity may not be caused only by the texturation but also by the presence of oxide produced during the process [118,119]. It is interesting to note that it is rare to find in the literature a complete characterization of both the surface chemistry, the surface geometry and the wettability. Most of the time, the studies are focusing the optimized process parameter. In the literature, multiple examples of superhydrophobic surfaces manufactured thanks to chemical, physical or mechanical etching have been described [120].

The chemical etching can be a simple etching or an electrochemical etching. The chemical etching occurs when matter is removed from the metallic substrate using an acidic or caustic solution. An additional electrical circuit can be integrated to force redox reactions to happen, in this particular case, it is an electrochemical etching [121]. The generated texture morphology is

strictly dependent on the substrate original microstructure (grain size) because the process is identical to a metallographic analysis. A flat piece of metal is slightly etched to reveal the underlying microstructure. An example of different morphology obtained with different chemical etching is presented on Figure 13. It shows that a same metallic surface won't react in the same way with different chemical solutions, which means the dissolution mechanisms are varying from a solution to another [122]. These chemical based processes are rapid methods to fabricate superhydrophobic surfaces because of their simplicity of execution, efficiency, low cost and easy possibility to scale-up at an industrial level [123]. As mentioned in subsection 4.2.1, superhydrophobic surfaces are synthesized by creating an oxide layer on top of a metallic substrate, but they can be directly generated from the metal using a passivation process [124]. In the case of the stainless steel, the passivation generates chromium and iron oxides in a hierarchical structure that could increase the hydrophobicity. The drawbacks associated to chemical etching are related to the water consumption and the generation of dangerous etching by-products (hexavalent chromium, fluorinated compounds, etc).

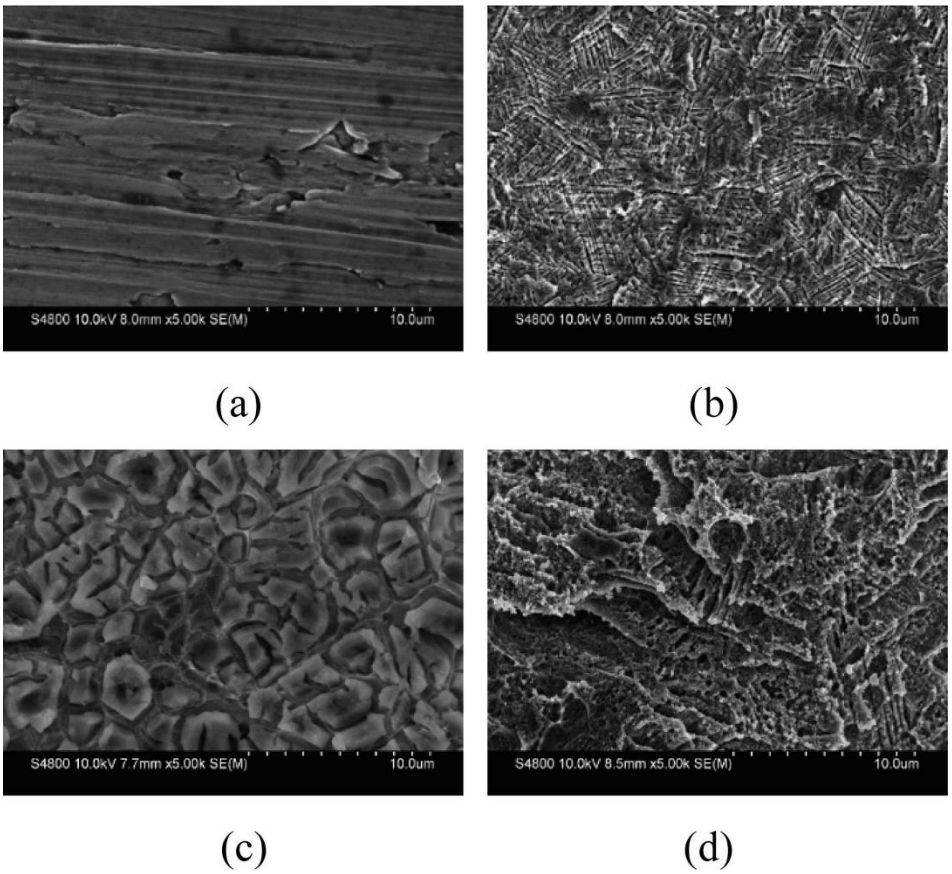

Figure 13. SEM image of three different stainless steel surface chemical etching (a) stainless steel (SS) original sample (b) SS treated with HCl solution (c) SS treated with FeCl3 solution (d) SS treated with HCl and FeCl3 solutions from Zhang et al (2022)

The physical etching can be done using plasma etching/oxidation or laser lithography. Unlike chemical etching, this category of subtractive manufacturing is a dry method, no solvent required to proceed. The idea is to remove material using a powerful source of energy. Laser lithography has been widely explored during the past years to texture stainless steel surface and in order to change the surface wettability [117,118]. Figure 14 from (Tong et al., 2022), displays different texturations realized thanks to a laser over a flat stainless steel substrate [125]. In the same literature review, the mechanism behind the superhydrophobic behavior is explained. The laser oxidizes the metallic surface into active metallic oxides (MO^{2-}), where M can be iron, chromium, nickel or manganese in the case of 316L. These active oxides make the surface temporarily superhydrophilic. The recombination with ambient water transforms the active oxides into metallic hydroxides (MOH). These hydroxides can be used later as preferential location for reactions with acids (steric or lauric acid for example) [125,126]. These acids will be covalently bonded to the

metallic surface to improve the superhydrophobicity. Active oxides can also react with carbon dioxide (CO_2) at a 100°C to produce non-polar carbon that will increase the hydrophobicity of the surface [125]. Laser texturation can also be associated to electrodeposition to nanostructure the laser textured surface [102].

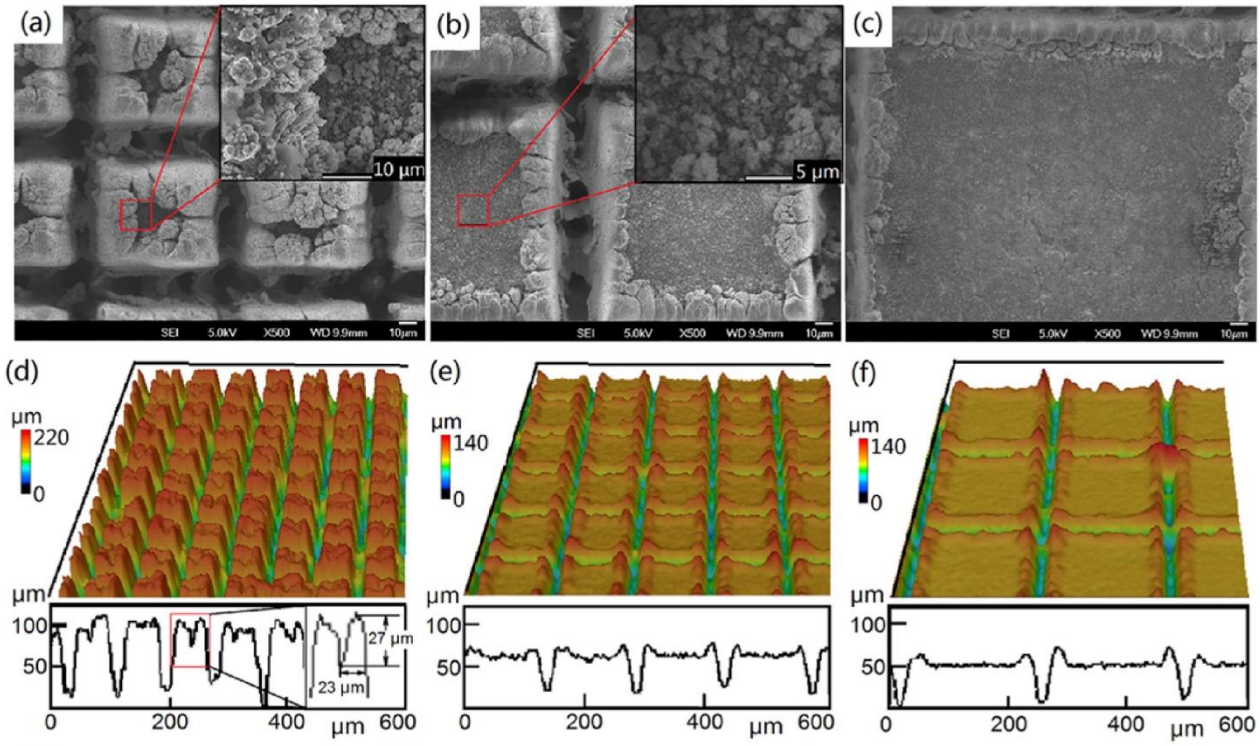

Figure 14. Examples of superhydrophobic laser textured stainless steel from Tong et al (2022)

Material can be removed from a metallic surface using a mechanical force. It exists multiple strategies of mechanical texturing such as sand blasting [127], polishing [128], micromilling [129]. The last scientific article mentioned, written by Abbas et al. (2020), is particularly interesting and representative of how a mechanical micromachining can affect the surface wettability. This work aims at improving the stainless steel hydrophilicity. A result which is not surprising because sand blasting, micromilling and etching are increasing the surface roughness.

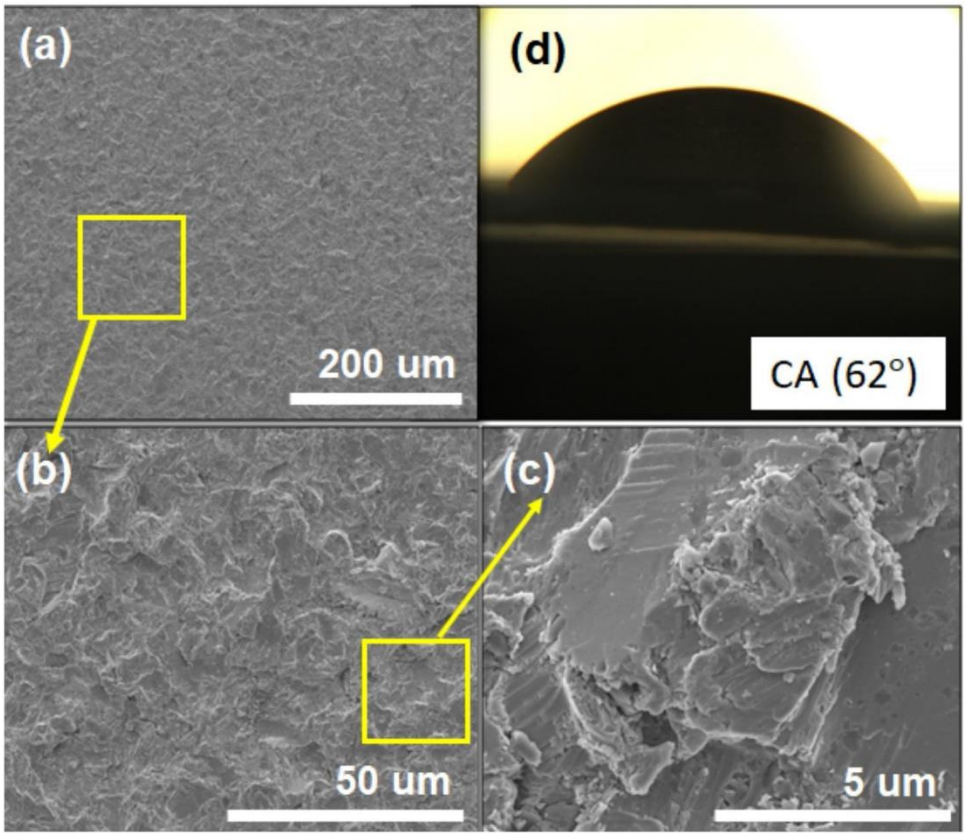

Figure 15. SEM and contact angle images of sand blasted SS-304 surface. (a) Top view of sand blasted SS-304 surface. (b) Blow-up image of area marked in (a). (c) Blow-up image of area marked in (b). (d) Contact angle (θ°) image of a droplet of distilled water on sand blasted SS-304 surface, from Abbas et al. (2020)

No matter which texturation is employed, physical, chemical or mechanical, the microtexture doesn't necessarily leads to hydrophobic properties. The hydrophobicity of the texture created can be enhanced after a chemical treatment that grafts hydrophobic molecules or functions such as halogens or siloxanes [79,119,122,125].

Out of bottom-up and top-down strategies, a family of process originally applied to polymer have emerged and is now applied to metallic powder to manufacture detailed metallic surfaces. The next section will give a better understanding of what is micro-embossing applied to metallic materials.

4.2.3 Micro-embossing

Micro-embossing for stainless steel is a manufacturing process that involves creating microscale patterns or textures at the surface of stainless steel sheets or components by surface plastic deformation. These patterns are typically designed to mimic certain natural or biological structures, hence the term "bio-inspired" or "bio-mimetic" surface texturing. Embossing at a micrometric scale can improve the performance of stainless steel surfaces in several ways (specific surface increase, wettability improvement, etc). Four distinct steps are involved in this technology:

(1) preparing production feedstock (mostly mixtures of powder and binder),

(2) shaping through hot embossing,

(3) debinding,

(4) sintering.

These steps are interconnected and collectively impact the characteristics of the resulting metallic microparts. Textured surfaces have the potential to decrease friction as, in comparison to a flat polished surface, the contact area is reduced. This characteristic renders them valuable in applications where smooth sliding or minimized wear is a critical consideration. Certain microtextures can make stainless steel surfaces water-repellent, which is valuable for anti-fouling, self-cleaning, and anti-icing applications. Texturing can improve tribological properties like wear resistance and lubrication retention [130,131]. This technology is classified as a micromachining process. It can be used to manufacture master mold for microfluidic system [132]. In microfluidic, a master mold is a piece of metal engraved with the negative of the desired system. Polymers can be casted or injected on top of the master mold to reproduce the microfluidic system.

The replicability and surface quality of the finished product are shaped by various factors, including the properties of the powder, composition of the binder, mold material of the, and crucial processing parameters such as temperature, pressure, and holding time. The thermal debinding process has commonly been employed to determine parts suitable for the subsequent sintering step. While the sintering temperature plays a role in shrinkage and final density, the powder's characteristics, embossing pressure, and heating rate are also significant parameters [133].

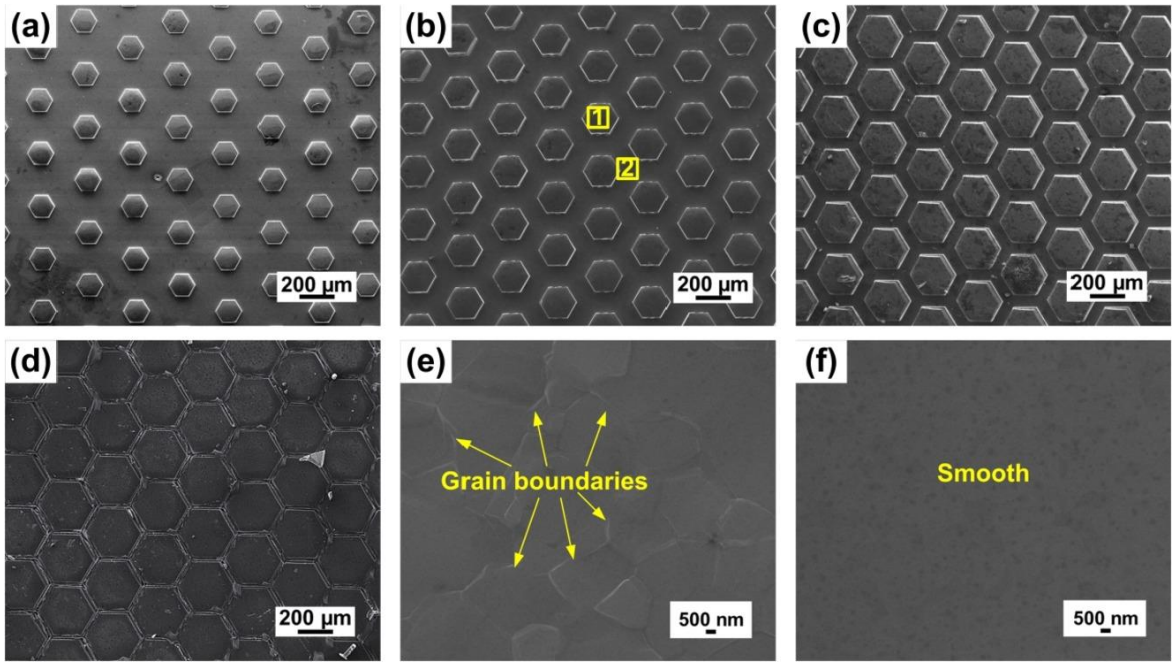

Figure 16. SEM of micro hexagonal pillar patterns after hot micro-embossing on UFG pure aluminum surface with side length of (a) a = 75 µm, (b) a = 105 µm, (c) a = 135 µm, (d) a = 165 µm and large magnification of position (e)1 and (f) 2, from Xu et al. (2019).

The process has been explored for ultra-thin grain aluminum to manufacture superhydrophobic surfaces [134]. Multiple cases of micro-embossing targeting wettability improvement have been found in the literature [134,135] because the sintering temperature is relatively low (300-400 °C). The process can be theoretically be employed with any metallic powder with a reachable sintering temperature. Examples of a few ferrous alloy (including 316L stainless steel) or copper have been reported by Sahli et al. (2013) in two different works to manufacture microfluidics master molds [132,136].

There are two main drawbacks to hot micro-embossing for metallic powder: the feeding material and the generated microstructure. In order to create a microtexture, the stainless steel has to be a thin powder with an particle size range between 3 and 10 µm [133]. This size of atomized powders can represent a safety hazard and the facilities necessary to manipulate them are expensive. The microstructure generated by hot-embossing is porous because the metal bulk is the result of spherical powder grains coalescence [132–134,136]. The porous microstructure can compromise the thermal conductivity and mechanical properties of the part.

4.2.4 Metal additive manufacturing (MAM)

Unlike subtractive manufacturing, additive manufacturing, also known as 3D printing, has revolutionized the production of metal components by layer-by-layer deposition. This innovative technique involves fusing or solidifying metallic powders or wires using lasers, electron beams, or other energy sources [137]. The seven main processes are described by the ISO/ASTM 52900 standard:

- Binder Jetting (BJT),
- Directed Energy Deposition (DED),
- Material Extrusion (MEX),
- Powder Bed Fusion (PBF),
- Sheet lamination (SHL) [138,139]
- Vat photopolymerization (VPP)
- Material jetting (MJT) [140].

Other existing techniques are hybridization of some of aforementioned processes and conventional machining processes [141]. Only four of them (Figure 10) are commonly applied to metals such as stainless steel [138,142,143].

- BJT is a similar technique to MEX where "*liquid bonding agent is selectively deposited to join powder materials*" (see Figure 17b.) [144–146]. The difference between MEX and BJT resides in the formulation of the deposited material.
- DED is a process where "*focused thermal energy is used to fuse materials by melting as they are being deposited*" [146]. A lot of technologies such as wire-arc additive manufacturing (WAAM) [138,147], cladding [148] or powder fed additive manufacturing can be put in this category (see Figure 17d.) [149]. This technology is mostly used to manufacture bigger parts (< 10 cm).
- MEX also known as metal fused deposition modelling (Metal FDM) is *"the process of selectively dispensing material through a nozzle or orifice*" (see Figure 17a.) [146]. The raw material used for the extrusion is a mix of metallic powder and polymer [150,151]. Additional steps are necessary to evacuate the polymer and sinter the metallic particles.

- PBF regroups two other techniques: selective laser sintering (SLS) and selective laser melting (SLM) [152,153]. They are comparable processes "*where thermal energy selectively fuses regions of a powder bed*" (see Figure 17c.) [146].

Table 2. Comparison of the different Metal AM technics

AM method	Compatibility with SS	XY printing resolution	Type of raw material	Ref
BJT	Yes	> 200 µm	Metallic powder mixed with liquid binder	[144]
DED	Yes	250 µm	Wire, metallic powder	[154,155]
MEX	Yes	400µm	Polymeric filament with metallic powder	[156,157]
PBF	Yes	80-250 µm	Metallic powder	[154]

Additive manufacturing offers incomparable design freedom, enabling the creation of complex geometries and internal structures that were previously challenging or impossible to achieve through traditional and/or non-conventional methods. It also minimizes material waste as it only utilizes the required amount of metal for the final product. (it is never the exact amount of material because of technical issues or supporting structure building inherent to complex shapes printing) However, challenges such as slower production speed, post-processing requirements, energy consumption, safety hazard due to the powder and limited material options for high-stress applications remain, but ongoing advancements continue to expand the potential of additive manufacturing in diverse industries, including aerospace, medical, and automotive sectors especially for custom products and small series [143].

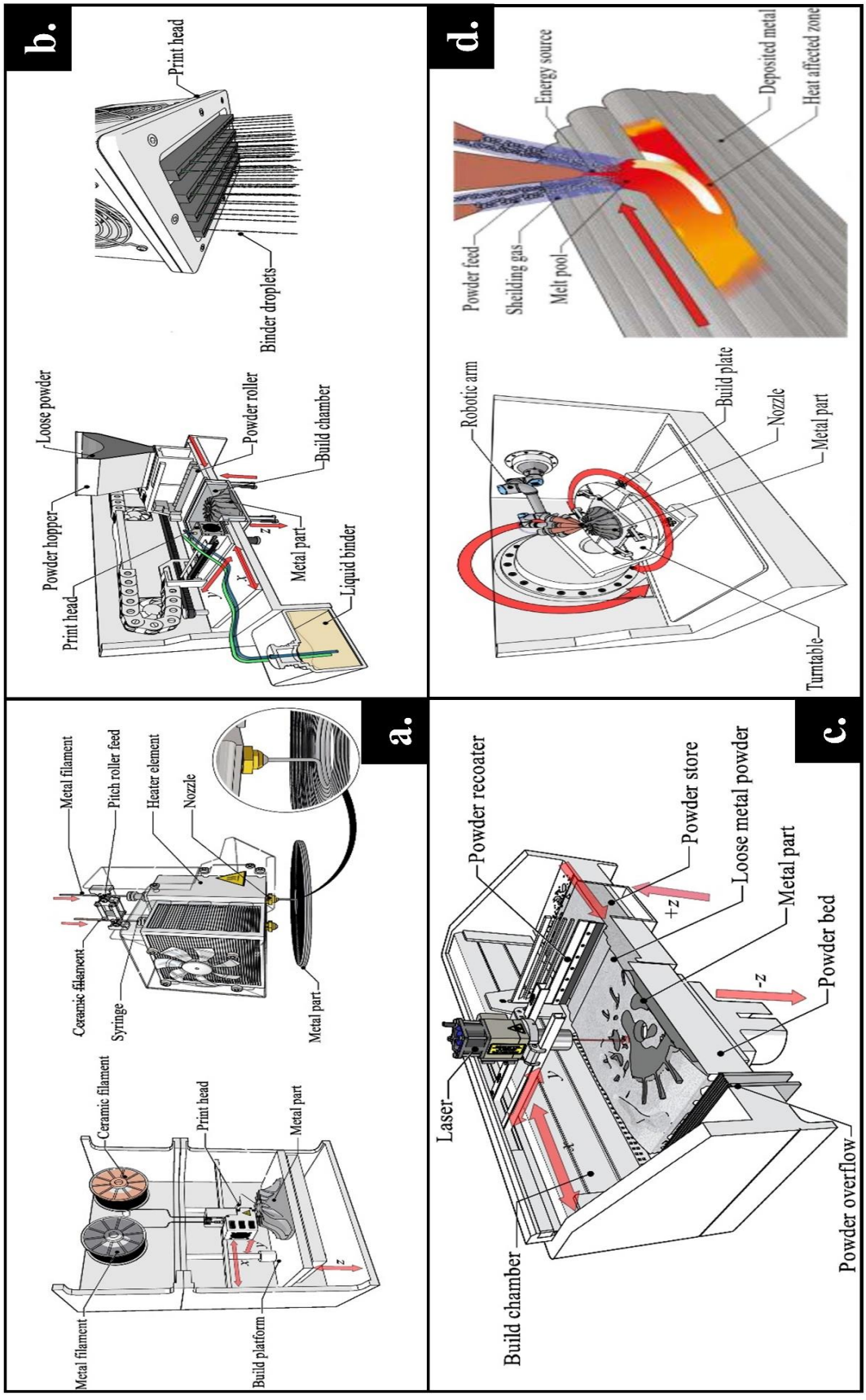

Figure 17. Four main metal additive manufacturing process. Image adapted from Armstrong et al (2022)

Metallic additive manufacturing processes can be relatively slower than traditional subtractive manufacturing methods, making them less suitable for high-volume production. Post-processing steps are often required to achieve desired surface finishes and mechanical or chemical properties, adding additional time and costs to the overall production process [158,159].

More than the production point of view, the precision reachable by the technology is also important to manufacture bio-inspired structures. On that particular point, polymer additive manufacturing (like VPP) is way more suitable to reach submillimetric scale and complex geometry needing high accuracy (resolution between 10 and 80 µm) [154,160–162]. To manufacture a metallic substrate using the polymer additive manufacturing (PAM) accuracy, it is also possible to use metal casting techniques. To carry out this process, it is first necessary to manufacture a ceramic mold based on a pattern that can be polymeric-based. Subsequently, the mold is used to shape the liquid metal into the desired shape. The pattern can be computer-aided designed (CAD) and 3d printed to offer wide prototyping possibilities [163,164]. This process is detailed in the following part.

4.2.5 Metal casting

Metal casting is a manufacturing process that involves pouring molten metal into a mold to create the desired shape. There are various methods of metal casting, including sand casting, investment casting, die casting, and so on. Metal casting allows the production of intricate and complex shapes that might be difficult or expensive to achieve through other manufacturing processes [165]. A wide range of metals and alloys can be used for casting, including steel [166], iron based [167], aluminum [168], bronze [169] or magnesium [165], allowing for flexibility in choosing the right material for specific applications. Casting can be a cost-effective method for producing large quantities of parts, as the initial tooling costs can be offset by the efficiency of producing multiple parts from a single mold [170]. Metal casting can accommodate a broad range of sizes, from small intricate parts to large components. In the case of investment casting (lost wax casting or shell casting), the pattern used can be 3D printed in wax or burnable resin to manufacture the ceramic mold [164]. The three steps common to every investment casting process are represented in Figure 18.

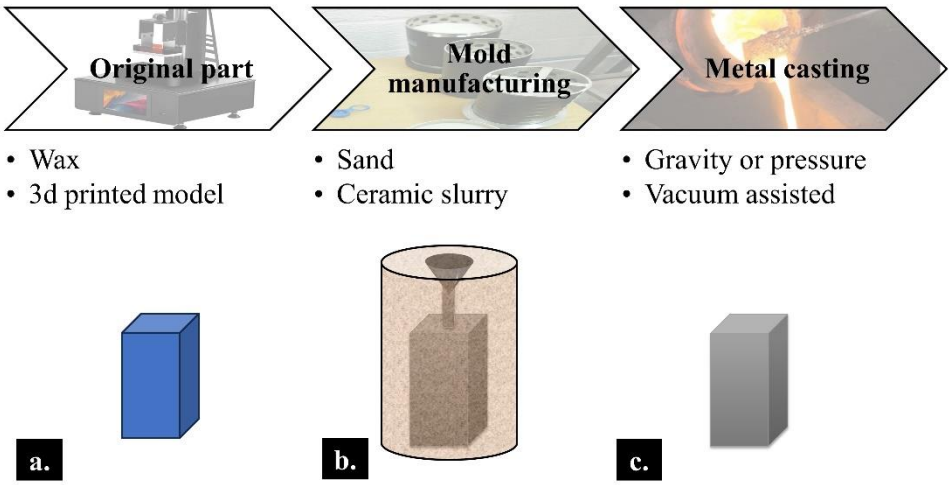

Figure 18. Investment casting (a) Initial pattern, (b) mold manufacturing and (c) liquid metal casting

The pattern and/or mold material and the metal pouring technique can vary depending on the use. Casting can achieve good surface finishes on parts, reducing the need for extensive post-processing. The design of the mold allows for features such as undercuts, draft angles, and textured surfaces to be incorporated into the final product. Achieving tight tolerances can be challenging in metal casting, which might require additional machining or polishing to meet precise specifications [171]. While surface finishes can be good, certain casting methods may still result in some surface imperfections that need to be addressed through secondary processes or improved using numerical foundry simulation to predict the defects [172]. Some casting processes can lead to porosity within the metal, that could affect the mechanical properties and performances of the final part [173]. While a wide range of materials can be used, certain advanced material properties might not be achievable through casting. Creating the molds, patterns, and dies for casting can involve high initial costs compared with some other manufacturing methods. The process of creating molds and patterns can take time, which might impact the overall lead time for production [174]. A raw object taken right after casting does not have the same mechanical properties nor the same geometry that could be forged or made by MAM because the microstructure is completely different depending on the manufacturing method [175,176].

On one hand, some casting processes generate emissions and waste that can have environmental implications, requiring proper disposal and management. But on the other hand, in the case of 316L stainless steel, recasting waste material can cut off a part of the environmental

cost due to the mining and ore transformation [91]. As the need in material is sharply growing and the amount of ore available for mining is limited, recycling the steel already fabricated will become an important challenge [177]. Metal casting is a good shaping method commonly used to obtain intricate geometries but not necessarily hydrophobic surface finish. The following table compares the different casting methods and categorize them following two questions:

- Is the process compatible with stainless steel?
- Is there a proof of feasibility at a submillimetric scale? Is this technology commonly used to manufacture micrometric surface details?

Table 3. Comparison of different common casting processes

	Is SS commonly used with this process?	Proof of feasibility at submillimetric scale	Reference
Investment casting	Yes	No	[178,179]
Die casting	Yes	No	[180]
Sand casting	Yes	No	[178,181]
Permanent mold casting	No	No	[182]
Squeeze casting	No	No	[179]
Centrifugal casting	Yes	No	[179,183]
Vacuum-process casting	Yes	No	[179,184]

The casting methods available to manufacture stainless steel substrates are theoretically numerous, however examples are rare in the literature. In the industrial world, stainless steel investment casting (SSIC) is common and a large number companies are dedicated to steel foundry process [184–188]. Some of them are even proposing to create objects directly from tridimensional files that can be uploaded on the website [189,190]. The casting process able to rise good surface finish, without additional surface machining, suggested by these companies is lost-wax investment casting. Nevertheless, there are no proof of the feasibility concerning casting at a submillimetric scale. The limit in terms of size reachable through SSIC process will constitute one of the main axes of this work.

5 Scientific positioning & conclusion

Finding the best stainless steel shaping is a complex technical issue. As described at the beginning of this chapter, superhydrophobic surfaces possess a multi-scale hierarchical architecture. One of the most important issue to replicate this particular wettability property is the surface roughness. For this reason, in order to choose a process adapted to the stainless steel surfaces manufacturing, multiple parameters have to be considered. The manufacturing process has to:

- be compatible with stainless steel
- be versatile in terms of pattern design
- manufacture at a submillimetric scale

In the previous sections, subtractive manufacturing, micro-embossing, metal additive manufacturing and metal casting have been reviewed to expose their advantages and drawbacks. In the All the subtractive processes allow to reach a submillimetric resolution. For this reason, a lot of examples of superhydrophobic surfaces exist in the literature. In the case of subtractive manufacturing, as reported in section 4.2.2, the surfaces only become superhydrophobic after a chemical functionalization consisting in grafting hydrophobic molecules at the surface. Chemical and electrochemical etching are frequently used to texture stainless steel substrates. Adding a chemical modification to the rough surface also leads to high hydrophobicity [191]. Without chemical functionalization or micro-architectured coating, the substrate would be hydrophilic [192]. Laser or femtolaser texturing is also commonly used to microtexture the steel. It will form shapes similar to the chemical etching but with more oxygen. In this case, no post-functionalization is needed to obtain hydrophobicity, but the energetical cost can go high to obtain hydrophobic surfaces [20,118].

Table 4, a comparison is proposed, considering the criteria mentioned before. All the subtractive processes allow to reach a submillimetric resolution. For this reason, a lot of examples of superhydrophobic surfaces exist in the literature. In the case of subtractive manufacturing, as reported in section 4.2.2, the surfaces only become superhydrophobic after a chemical

functionalization consisting in grafting hydrophobic molecules at the surface. Chemical and electrochemical etching are frequently used to texture stainless steel substrates. Adding a chemical modification to the rough surface also leads to high hydrophobicity [191]. Without chemical functionalization or micro-architectured coating, the substrate would be hydrophilic [192]. Laser or femtolaser texturing is also commonly used to microtexture the steel. It will form shapes similar to the chemical etching but with more oxygen. In this case, no post-functionalization is needed to obtain hydrophobicity, but the energetical cost can go high to obtain hydrophobic surfaces [20,118].

Table 4. Comparison of the different process available for microtexturing a stainless steel substrate

Manufacturing process	Great diversity of pattern formed	Submillimetric precision texturing possible?	Use of chemicals necessary to obtain hydrophobicity	Scalable at industrial level	References
Laser texturing	Yes	Yes	No	No	[93,193–195]
Chemical Etching	No	Yes	Yes	Yes	[122,196,197]
Polishing / Grinding	No	Yes	Yes	Yes	[195,198]
Micro-embossing	No	Yes	No	-	[130]
Metal additive manufacturing	No	Yes	No	Yes	[199–201],
Metal casting	Yes	-	-	Yes	[164,179,202]

The drawback of the chemical etching process also lies in the cost, both in terms of time and energy, to treat a surface that will be chemically oxidized [203]. At an industrial scale, it is also difficult to imagine the used of fluorinated siloxane in great quantity to dip-coat large piece of steel. Moreover, except the cauliflower-like nanoshapes formed during chemical etching, there is no other pattern possible. Concerning the control of the pattern formed, only the laser texturing can allow it because the texturation pattern can be defined.

Micro-embossing of metals, as mentioned in subsection 4.2.3 of this chapter, is a promising technology that can shape metallic powder mixed with organic binders into a microtextured surface.

Metal additive manufacturing (MAM) processes, as discussed in subsection 4.2.4 of this chapter, are able to achieve the micrometric precision, but the surface roughness depends on the deposition technique parameters and the characteristics of the raw materials [158]. Examples of studies reporting hydrophobic stainless steel made thanks to MAM exists. The hydrophobicity is due to the texture created by the remaining powder sticking to the solidified part [204]. . The 316L powder used during the printing processes is expensive, but re-usable when not it hasn't been affected during the process [205] and requires adapted post-treatment facilities to be managed [152]. The main advantage of MAM is the possibility to couple it with CAD in order to design complex tridimensional shapes with more degree of freedom. But numerous issues come with this advantage, especially the minimal resolution and highly specific raw material (metallic powder or wire), that complexify the setting up and the scalability to manufacture a multiscale architecture with bio-inspired patterns.

Metal casting, as described in subsection 4.2.5 of this chapter, seems to counterbalance the lacks of AM as it is a process already widely industrialized and the necessary material can be obtained by recycling waste [91,177]. One reason casting is particularly interesting is that it enables the combination of polymer additive manufacturing (PAM) and vacuum-assisted investment casting. On one side, PAM leads to a smaller resolution and is easier to set up for a cheap investment cost. On the other side, vacuum assisted investment casting is commonly used to reproduce highly complex object with a good surface state. In the literature, no work is reported,

that associate these two processes to obtain stainless steel substrates with an interesting wettability. In the following chapters, multiple technical locks will need to be clarified:

- Firstly, is it possible to cast stainless steel at a submillimetric level? Stainless steel is commonly used to cast bigger objects but not smaller detailed patterns like light alloys could be. Liquid stainless steel is known to be highly viscous and reactive. The list of work describing liquid stainless steel behavior at this scale is short. The absence of information will complexify the setting up of this particular casting.
- Secondly, if stainless steel casting is possible at this scale, is it possible to create a bio-inspired microtexture by combining PAM and SSIC? This association implies a lot of sub-questions concerning the possibility to print a bio-inspired pattern complex enough to have a wettability interest. Even if it is possible to 3D-print such patterns, aren't they too small to be molded with a refractory slurry to cast the metal? Will the liquid stainless steel infiltrate the mold details? Once again, this work would constitute a premier in the literature.
- Finally, the bio-inspired stainless steel substrate obtained will need to be nanotextured to get a multi-scale texture from the microscale to the nanoscale. A quick and simple process that uses as less as possible chemicals and dangerous solvents should be identified.

Chapter 2: Feasibility of vacuum assisted stainless steel casting at millimetric scale

1 Introduction

Lost-wax foundry, also called investment casting (IC), is one of the most ancient metal manufacturing process still used today. It consists in 4 steps : (i) create a pattern in a meltable material such as wax, (ii) immerge the shape in a ceramic slurry to obtain a refractory mold, (iii) cook the dried slurry to evacuate the pattern and solidify the mold [206] and (iv) pour the molten metal in the negative to obtain a metallic part. For centuries, people have carved wax to obtain metallic sculptures, statues and jewelry [207]. Over time, various process improvements have been implemented, and one significant enhancement is the introduction of vacuum during metal pouring in casting. This addition has notably elevated the quality of castings. The improvement is attributed to the evacuation of gas trapped in the mold, increased wettability between the mold and metal, and a reduction in reactions between ambient air and the liquid metal. [181]. Nowadays, this manufacturing technique is particularly appreciated for its great precision and high reachable complexity level [208,209]. IC has been improved in a consequent manner during the last decades thanks to additive manufacturing (AM), computer-aided design (CAD) and casting simulation [164]. It is now even possible to directly print the casting mold in a refractory material [174,210,211]. The quick input of AM in investment casting is noticeable by comparing two review articles dealing with pattern production for investment casting, one written in 2005 [178] and the other from 2020 [164]. The amount of progress achieved in the field in fifteen years is remarkable. As an example of technical prowess, the production of very intricate metallic foams [212] or the controlled solidification of turbine hollow blades [213].

In order to manufacture the stainless steel substrate with a microarchitecture on the surface of interest, a technique called “vacuum assisted lost model casting” (VALMC) was chosen. This technique is not well described in the literature for small stainless steel parts but well known for other light alloys in some specific industries such as jewelry and prosthesis manufacturing. The main advantage of this process is its versatility. Complex shapes such as prosthesis, small metallic prototypes or detailed jewelry can be easily reproduced with a good surface state and geometrical accuracy. In this chapter, the boundaries of this technique will be explored. How to cast millimetric objects with micrometric details in stainless steel? The castability has been investigated and the findings have been categorized in three different sections: the apparatus, the casting conditions and the casted material.

A castability or fluidity test is a shape made to be filled and assess the casting parameters. Two well-known shapes in sand foundry process are the grid pattern [214–220] and the spiral pattern [221–225] (See Figure 19). Compared to other casting techniques such as sand casting (SC), die casting (DC) or centrifugal casting (CC), there are no castability testing systems reported for small scale IC in the literature [221,222,224,226,227]. A lot of examples of experimental and numerical studies can be found in the literature mostly for aluminum-based and titanium-based alloy.

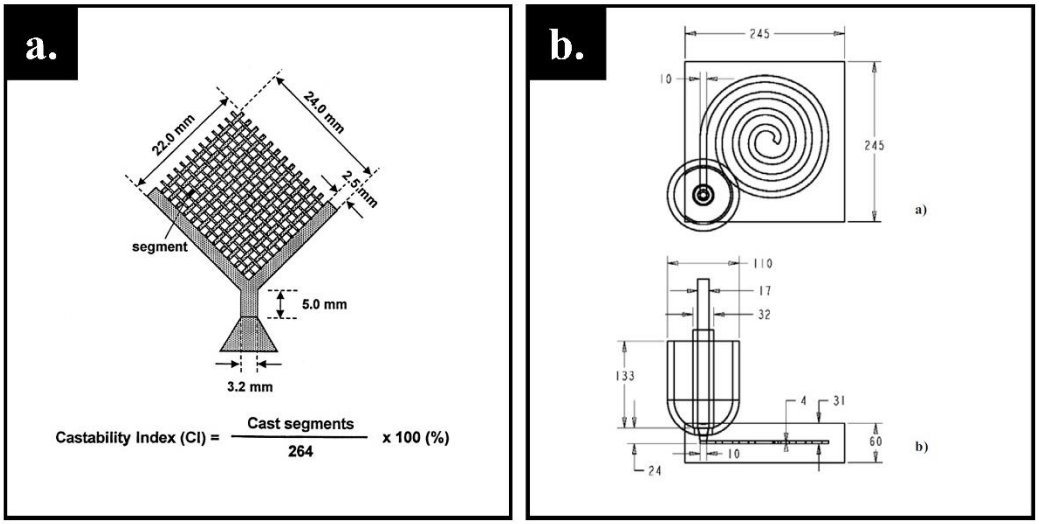

Figure 19. Example of existing castability test patterns (a) mesh pattern used for centrifugal casting from Deac et al. (2018) (b) spiral pattern for sand casting from Di Sabatino et al (2008)

Choosing among the four casting processes to shape a metallic part depends on its requirement specifications. To cast a dental prosthesis or jewelry, fields that require smooth or mirror-like surface states and that are manufactured in small series of high added value , IC and CC are the most common used processes [164]. Jewelry industry will use gold-based and silver-based alloys or steel to manufacture the products. Dentistry manufacturers will focus on biocompatible alloys such as titanium or cobalt based alloys for the mechanical properties and the biocompatibility [228,229]. As an example, automotive and aeronautical manufacturers will cast larger series considering the future mechanical constraints and the weight or the material cost. Each casting process cited earlier can be used in those industries but the alloys reported in the literature are more based on magnesium, aluminum, titanium, nickel or iron [165,230,231].

In the present work, a castability test was developed and tested with three different materials. Generally, castability tests are using large pattern (> 100 mm) but in this study the dimensions are not exceeding a total height of 60 mm and cross section diameters are not exceeding 3 mm. The shape was designed to help manufacturers in the casting parameters assessment for small parts objectively without wasting high valued patterns. The infiltration should depend on the liquid metal properties (viscosity, surface tension, etc.) and the casting parameters (pouring temperature, mold temperature, atmosphere composition, vacuum, etc.). The aim of this work was first to design a small part (total volume < 200 cm^3) that can help the assessment of the casting parameters. The three materials chosen, are not common for vacuum investment casting: pure aluminum (Melting Temperature (MT): 660 °C), pure copper (MT: 1085 °C) and recycled 316L SS (MT: 1370 °C). To anticipate how ferrous material would behave in the equipment, we ran a few tests with grey cast iron, which is a ferrous alloy with a high content of carbon and a lower MT than 316L SS (MT: 1150-1200 °C). The initial goal was not to cast stainless steel, but to understand the behavior of the equipment when metals known for their good castability and with lower melting temperatures were casted.

With the results of these castability tests, a better understanding of the casting parameters will be given to infiltrate the ceramic molds as best as possible with the liquid stainless steel. The ultimate goal is to find an approximate set of parameters to cast bio-inspired microarchitectured in stainless steel.

2 Design and manufacturing

The global scheme of the process is presented in Figure 2. It consists in 3D-printing tridimensional objects that were designed with a CAD software before. Once printed, the shapes are immersed in a ceramic slurry (mainly a mix of silica powder, binding agent and water) to create a ceramic mold. The slurry rests for 2 hours to solidify during a first dry at room temperature. The solidified ceramic mold is placed in an oven for a longer controlled thermal treatment that will

evacuate the printing polymers and leave the negative of the printed shapes inside the mold (see Figure 20).

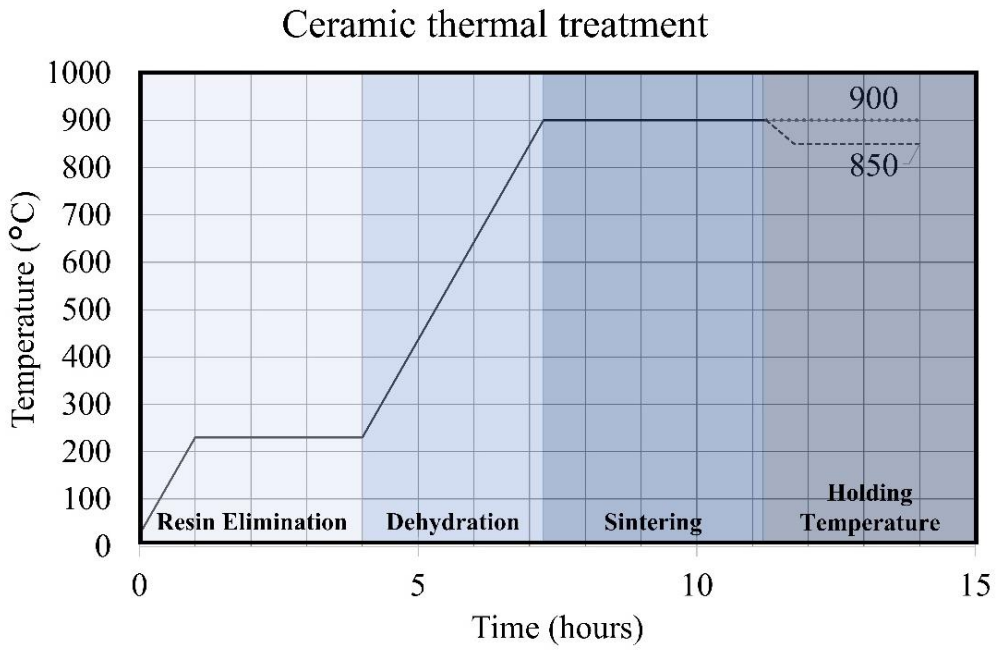

Figure 20. Example of thermal treatment for a ceramic mold before the casting step

When the mold is empty, a liquid metal can be poured inside to replicate the original shape of the 3D-printed model. All the steps mentionned before will be detailed in the following paragraphes.

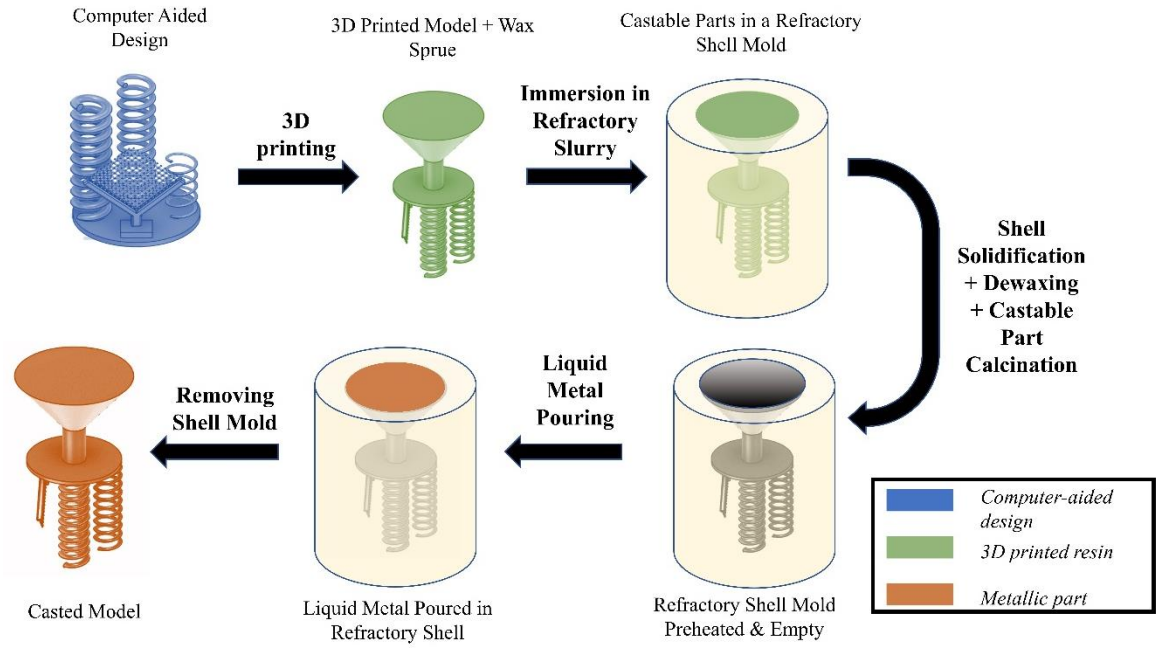

Figure 21. Investment casting process

2.1 3D modeling

The CAD software used for these design is Fusion 360 developed by Autodesk [232]. The castability test patterns were designed to assess the distance a liquid metal can travel through before total solidification. Three springs with various cross section diameters (1 mm, 2 mm and 3 mm) inspired from Deac et al [227] and a grid inspired from Watanabe et al [226] were combined together on a 40 mm circular plate using computer aided design (see Figure 22). The liquid metal should flow through the circular plate before infiltrating the spring and the grid. Table 1 provides the dimensions of the springs. The grid has a 12 x 12 segments network, corresponding to 264 sections to be filled in. The number of sections filled gives a castability rate. The grid cross section diameter is 0.6 mm.

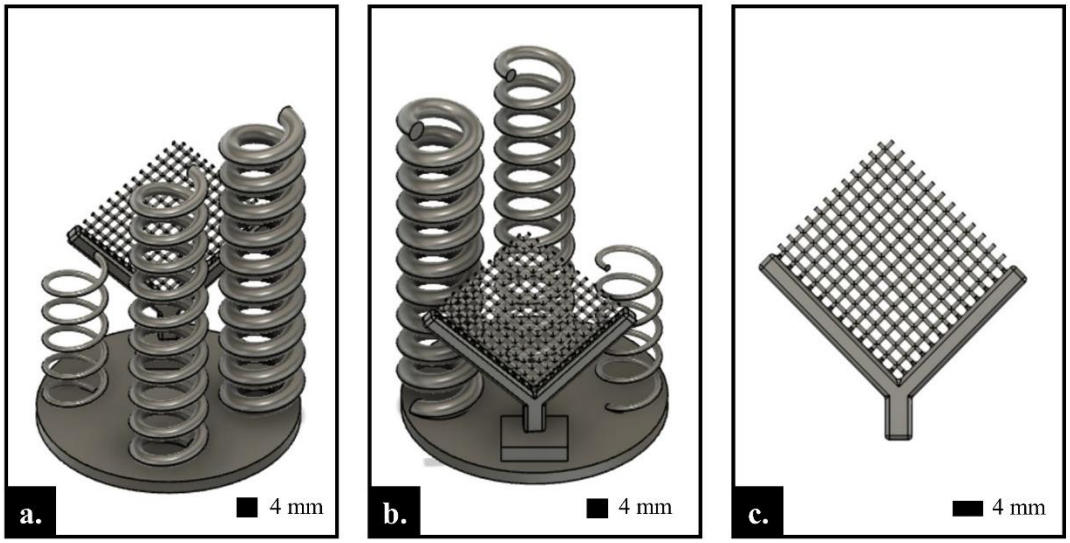

Figure 22. Computer-aided design of the castability test (a) and (b) Castability test from two different point of view (c) grid part of the Castability test isolated.

2.2 3D printing

In vat photopolymerization (VPP), the three-dimensional shape is created by stacking bidimensional layers of material. The 3D model printed is made from liquid resin photopolymerized by a digital 4K screen featuring UV light. A motorized plate moves up and down to superimpose the different layers of the material from the bottom to the top. The liquid resin is the Photocentric© Daylight castable Smokey quartz and the printer is a Liquid Crystal Precision (LC Precision, general scheme presented on Figure 23). The tridimensional model of the castable test previously presented is printed from the circular plate to the top of the springs in one printing step (from the bottom to the top on Figure 22).

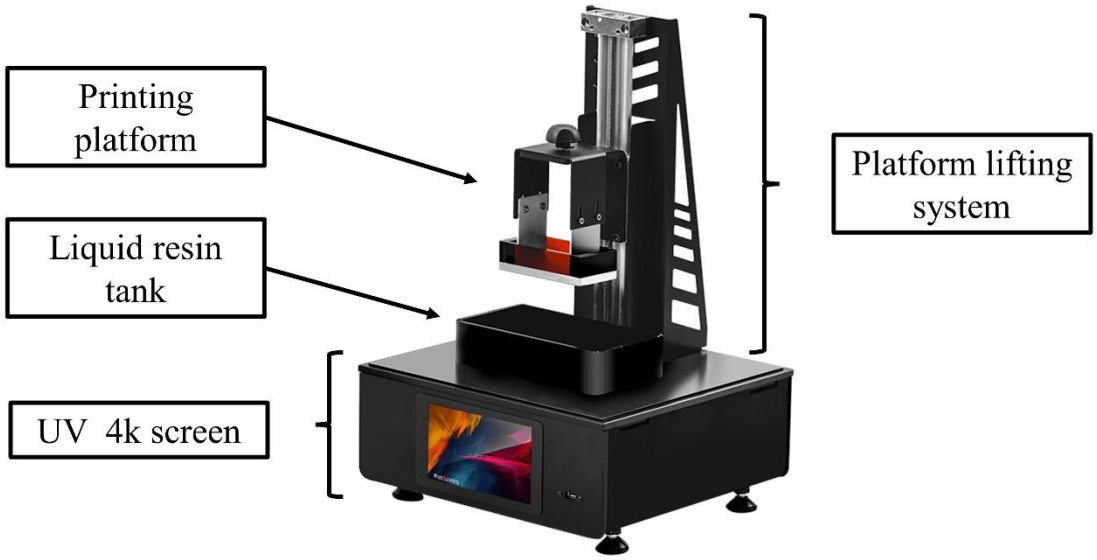

Figure 23. LC precision 3D printer

Table 5. Dimension detail of the designed spring from the CAD software measurement tool

Spring Cross Section Diameter (mm)	**1**	**2**	**3**
Length (mm)	159	380	411
Height (mm)	25	50	50
Radius from revolution axis (mm)	10	10	10
Number of spires	5	10	10

2.3 Refractory Shell

The previous 3D-printed model is put on a 2 cm (diameter) wax stick and placed in a steel cylinder. The bottom of the cylinder is sealed by a rubber with a cone in order to define the pouring cone (Figure 24b.). Water and refractory powder (38:100 water/powder ratio) are mixed in the vacuum investment machine from INDUTHERM to make a refractory slurry (Figure 24a.). The investment powder used for the copper and aluminum molds is Apollo HYDRACAST from GRS. For the stainless steel, the investment powder is Pro HT Platinum from GRS, with a higher thermal resistance. The slurry is poured under vacuum on a vibrating plate in the cylinder to make a mold. The vacuum and the vibration remove the air bubbles generated during the mixing. After 2 hours hardening, the rubber with the conic shape is removed to have a casting cone (Figure 24c.). A heat treatment is done on the mold in an oven to melt the wax, calcinate the resin and dehydrate the refractory material. The heat treatment depends on the refractory chosen and is done in an oven under atmospheric conditions (air and atmospheric pressure). At this step, the steel cylinder contains a refractory material with an empty negative of the desired castability test. Before casting, the mold is maintained at a certain temperature at least 100 °C below the metal melting point to avoid early solidification that could compromise the mold filling. The influence of the mold temperature will be a parameter discussed later in this chapter.

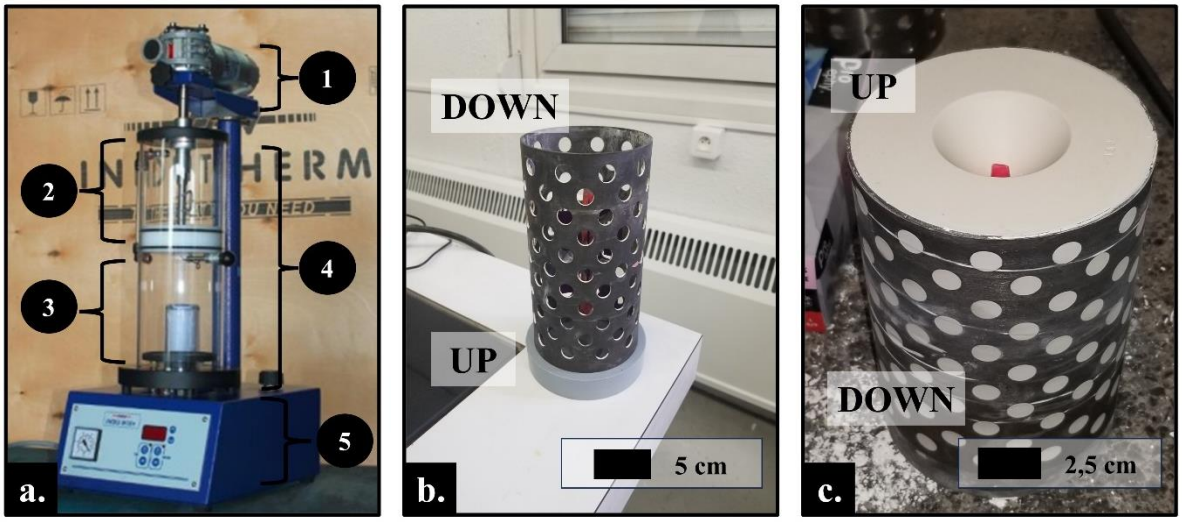

Figure 24. (a) Vacuum mixing machine for the slurry where (1) is a motor for the rotative blade, (2) is the mixing pot where the ceramic powder is mixed to water thanks to a blade, (3) is where the metallic cylinder is placed to receive the ceramic slurry, (4) the previous element are separate and maintained under primary vacuum by one translucid cylinder and (5) is the control station for the vacuum, the rotation speed, vibration intensity and mixing time (b) is a metallic cylinder and a rubber mounting base containing a 3d printed part before filling in the ceramic slurry (c) metallic cylinder filled up with the ceramic slurry after the first dry out at room temperature.

2.4 Casting Process

The hot refractory mold is put in the vacuum casting machine VC480V from INDUTHERM (Figure 25). In this casting machine, the crucible pressure (melting pressure) and the casting chamber pressure can be set separately. The metal is melted thanks to an induction heating in a crucible under argon atmosphere. The crucible can be graphite or a two materials crucible (inner part in alumina and outer part in graphite) to avoid dissolution of the graphite's carbon by the ferrous molten metal. The heating duration and temperature, the vibration of the mold after pouring or the cooling duration are inputs of the casting (detailed list on Figure 25). After pouring the liquid metal, the mold is cooled until the refractory shell reaches a temperature lower than 200°C. For non-ferrous materials, the hot mold is dipped in a water bath to remove the refractory shell. For ferrous materials, the mold is teared apart mechanically after complete cool down to avoid aqueous quenching. Every specimen was then washed with a high pressure water gun set between 5 and 10 bar.

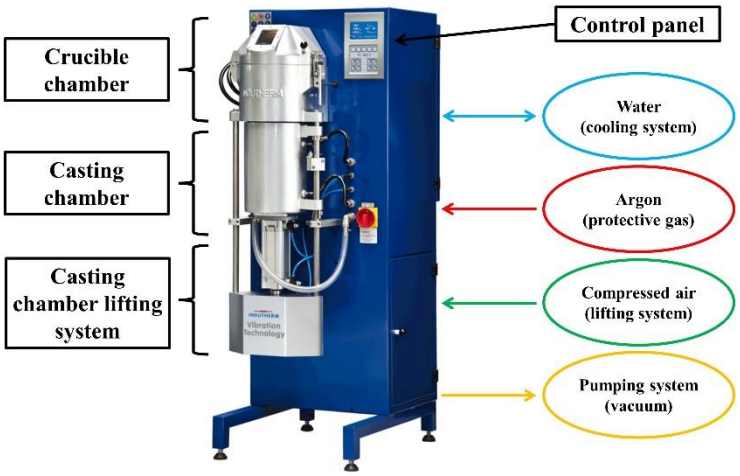

Parameters influencing investment casting
Pressure (casting chamber and crucible chamber)
Number of gas wash
Heating ramp
Cooling duration
Mold vibration after casting
Mold and casting temperatures
Mold insertion before or after metal fusion
Cooling under pressure or not
Mold material
Alloy or metal

Figure 25. Vacuum-assisted investment casting machine, VC480V from Indutherm with a list of parameters that can be set up and influence the casting process

3 Results & Discussion

3.1 Infiltration results

The test parameters and results of the infiltration tests on the 3 metals are summarized in Table 6 and Figure 26. The pure aluminum has completely filled the springs (experiment n°1 in Table 6). The mesh pattern was not casted because it was not molded at first. The part certainly broke during the molding process. The filling of the spring shape is not surprising because aluminum is known for being easy to cast. Numerous scientific papers are describing aluminum casting [168,169,233,234]. Aluminum based materials are light, easy to machine when ductile and highly castable [235]. If the grid had not fell off during the process, it would have been completely filled. Multiple examples of complex network such as periodic cells or foam casted in aluminum exist and are abundant in the literature [236,237].

Table 6. Infiltration results with pure aluminum, pure copper and 316L stainless steel

Casted Metal	Experiment n°	Mold preheating temperature (C°)	Metal casting temperature (C°)	δT (C°)	Mold material	Number of turns filled			Number of grid segments filled	Mass (g)
						1mm	*2mm*	*3mm*		
Aluminum	1	400	740	340	75% $CaSO_4$ + 25% SiO_2	5/5	10/10	10/10	N/A	40
Copper	2	400	1185	785		2/5	4.5/10	7/10	264	96
	3	650	1185	535		2.5/5	8.25/10	10/10	264	102
Stainless Steel	4	800	1550	750		failed				120
	5	800	1550	750	Phosphate bonded silica	0.5/5	1.25/10	3/10	3	120
	6	850	1600	750		1.5/5	4/10	5.5/10	243	75
	7	900	1600	700		1.25	0.5/10	6.5/10	264	117

The same test carried out using pure copper as casted material at two different pre-heating conditions (experiments n°2 and n°3 in Table 6) gave different results. In both cases, the mesh pattern has been completely filled in. This first result supports the hypothesis formulated earlier, concerning the mesh pattern in the aluminum experiment. Concerning the springs, both are less filled than the aluminum one and a slight difference can be noted. The infiltration went deeper for the hotter preheated mold. This result is not surprising as the temperature difference between the melting point and the mold pre-heating temperature will influence the filling. The bigger this temperature difference is, the quicker the liquid metal will solidify in contact with the mold. The same observation has been made for different metals such as titanium alloys [220] or aluminum

alloys [234]. The mass is 6 g higher in the experiment n°3 that in experiment 2, but couldn't exercise enough hydrostatic pressure to push the liquid as much as the infiltration has gone.

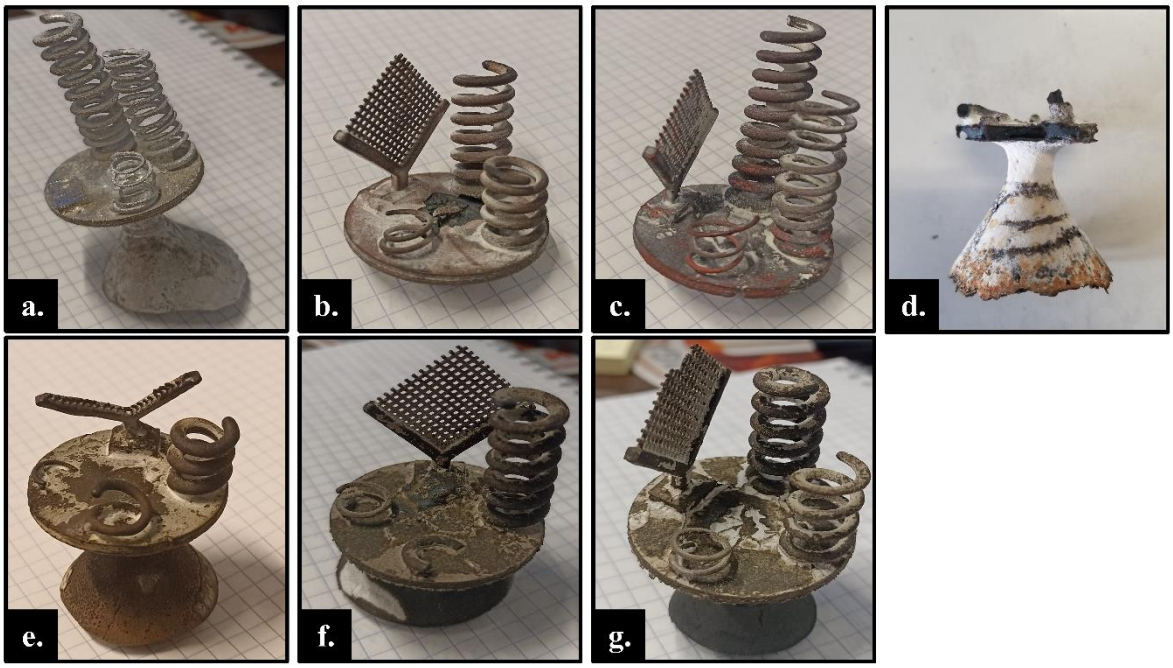

Figure 26. (a) experiment 1, (b) experiment 2, (c)experiment 3, (d) experiment 4, failed stainless steel castability test (condition identical to experiment 5 but in a mold made of gypsum and silica), (e) experiment 5 and (f) experiment 6 and (g) experiment 7

In the last three experiments (experiments n°5/6/7), 316L stainless steel has been casted in a mold in Pro HT Platinum plaster because the calcium sulfate presents in the Apollo HYDRACAST plaster decomposes over 900 °C. An attempt has been made to cast stainless steel into a mold made with Apollo HYDRACAST plaster (gypsum and silica like the mold used for aluminum and copper casting). The resulting castability test is displayed on Figure 26 (f) and is considered as "failed" because the filling is aborted. A thin layer of reaction between the mold and the part has been reported with a strong rotten egg smell. The smell can be attributed to the presence of calcium sulfide (CaS) which is produced when calcium sulfate is decomposed at temperatures above 900 °C [238]. The casting may have been compromised by the reaction between the liquid metal and the mold that generate gases.

Even if some of the small springs cannot be considered, the 3 mm spring and the mesh pattern give a significant result. The higher the temperature, the better the infiltration: a similar

trend was already noticed for the copper CT. The amount of material used is lower in experiment 5 than in experiment 7, which could explain the infiltration difference. Nevertheless, the same amount of material was used in experiments 5 and 76. Only the mold temperature and the liquid metal temperature were significantly different. The castability was sharply improved in the case of experiment 6 because the temperature gap between stainless steel melting point and the mold temperature is smaller. The value δT can be introduced to define the temperature difference between the pre-heated mold and the liquid metal temperature.

$$\delta T = \text{Casting temperature} - \text{Mold temperature} \quad (1)$$

Table 7. Superficial tension and viscosity of the different metals at their respective melting point

Metal	Superficial tension at melting temperature (mN/m)	Viscosity at melting temperature (mPa.s)	References
Aluminum	820 - 860	1.2 - 1.3	[239–241]
Copper	1277 - 1290	3.0 - 4.0	
Stainless steel 316L	1400 - 1600	5.0 - 5.5	[240–243]

The three metals chosen for the experimental part have three distinct superficial tension and viscosity (see Table 7). The higher these values are, the more complicated is the mold infiltration on a long distance. The results are confirming the trend. The aluminum, that is the easiest metal to cast among the three, has entirely filled in the spire patterns. Unfortunately, during the mold manufacturing, some part of the pattern like the grid in the experiment 1 and 1mm and 2 mm spires from experiment 6 may have been broken. This hypothesis is supported by the end of spire shape. The end of the solidified spring should be a round shape at the end but for the 1 mm and 2 mm springs, it is not (see photo (b) on Figure 27). The non-round end of the springs could have been caused by an improper molding. The most valuable information that can be extracted from the

different experiments runned with stainless steel is the castability. It is a proof that small part with millimetric scale cross section diameters can be casted in stainless steel.

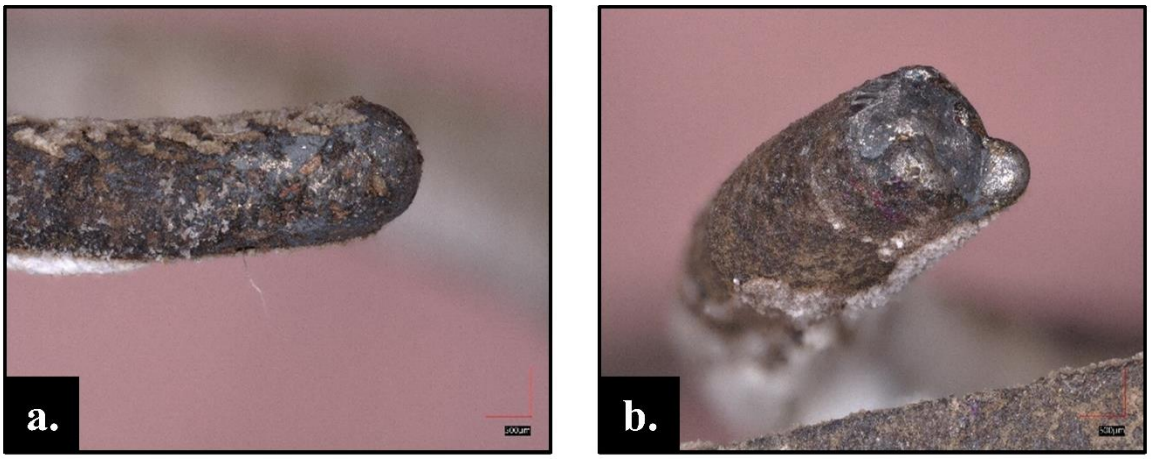

Figure 27. Stainless steel solidified end of 2 mm spiral (a) experiment 6 (b) experiment 7

3.2 Influence of experimental parameters

The investment casting equipment is divided into two parts: the upper part in which the raw material is molten and the lower part where the mold is inserted. Before melting or pouring the liquid metal into the mold, the air contained in the equipment is replaced by argon to create a protective atmosphere. After this purge, the two operations occur under primary vacuum. The upper part is called the melting chamber. It contains a crucible with a hole in the bottom, and a motorized stopper rod to plug the hole during the melting step. Once the metal is completely liquid, the stopper rod can be lifted up to let the liquid flow through the crucible hole. The two following subsections are dedicated to the equipment and to the main parameters influencing the casting process: the mold temperature and the mold/metal interaction. The amount of experiments done is not large whereas a lot of parameters exist that are listed in the literature. A non-exhaustive list of those parameters would be: the pre-heating temperature, the interaction with the mold, the melting crucible nature, the primary vacuum settings, the number of gas purge before casting, the mold cooling speed, the mold granulometry, the casting pressure etc. [242–245].

3.2.1 Influence of the pre-heating temperature

It was a deliberate choice to modify firstly with the preheating temperature (see results presented earlier) because it is easier to set up and appears to affect significantly the casting result. The casting parameters related to the vacuum have been set up to avoid any liquid metal projection during the pouring step. The mold material used was an existing commercialized solution developed for steel casting. The granulometry was extra thin (around 200 nm) and adapted for detail reproduction. A bigger grains size would have implied to have a mold with a rougher surface that could decrease the wettability between the liquid metal and the mold. In the following paragraphs, the influence of the pre-heating temperature, of the melting crucible, of the potential interactions mold/stainless steel is highlighted. The influence of the mold preheating temperature is particularly visible in the case of stainless steel tests. The grid pattern was improperly filled for experiment 6 compared to experiment 7 (see Figure 28). More than the mold temperature, the amount of material was smaller too. For future experiment, the mold temperature and the amount of material will be crucial parameters to look at.

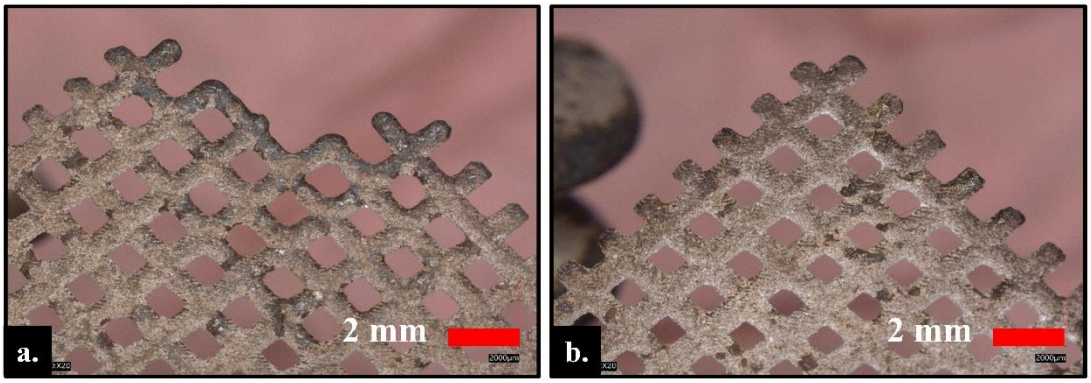

Figure 28. Stainless steel infiltration at two different mold preheating temperature (a) experiment 6, preheating temperature: 850°C (b) experiment 7, preheating temperature: 900°C

3.2.2 The melting crucible

Copper and aluminum were casted in the same graphite crucible. There was no interaction noticed between the graphite and the molten Al or Cu. Ferrous material such as stainless steel can however not be melted in a graphite crucible as the carbon that composes the graphite is soluble in liquid steel. Two tests were conducted to replace the graphite crucible: a graphite crucible coated

with a refractory slurry (see Figure 29 (b)) and a two-parts crucible with an inner part in alumina (see Figure 29 (a)).

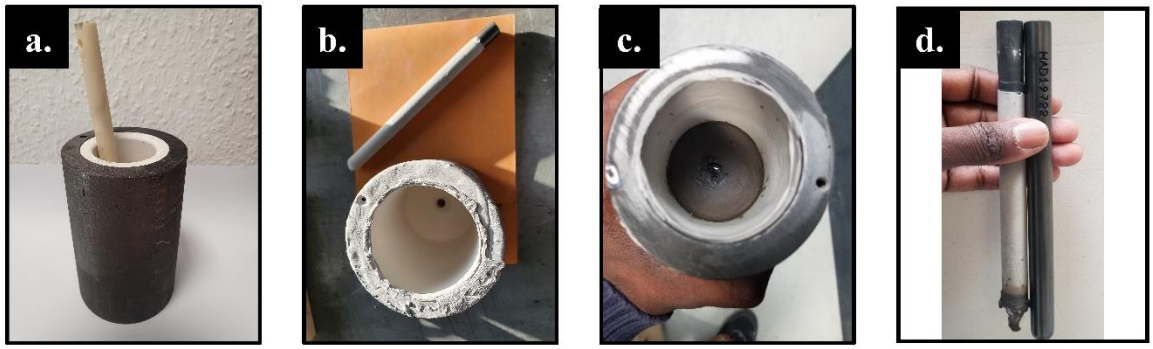

Figure 29. (a) Two-parts crucible outer part in graphite, inner part and rod in alumina, (b) graphite crucible and rod coated with refractory slurry, (c) graphite crucible coated with refractory slurry after one ferrous casting the protective layer is gone in the bottom and the hole is clogged with a residue and (d) the graphite rod coated with the refractory slurry (left) after one ferrous casting compared to an unaltered (right)

The refractory slurry coating the crucible started to crack for temperatures above 900°C. The crucible and the rod were partially dissolved by the liquid stainless steel (see Figure 29 (c) and (d)). The dissolution of the graphite is a risk for the casting equipment and increases sharply the content of carbon in the steel composition. We know the content of carbon was higher because the microstructure of the casted sample was no longer an austenitic microstructure but a chromium enriched cast-iron microstructure. Figure 30 displays the microstructural difference between the sample contaminated by the crucible carbon Figure 30.b and unaltered sample Figure 30.c. The casted stainless steel possesses a microstructure completely different from a thermo-mechanically processed stainless steel (see Figure 30a.) Simply by changing the crucible and stopper rod material, the undesired carbon enrichment could be avoided. Coated graphite was thus replaced by alumina. The same casting executed in the same conditions but using this alumina crucible led to a better filling and the stainless steel chemical composition was not altered.

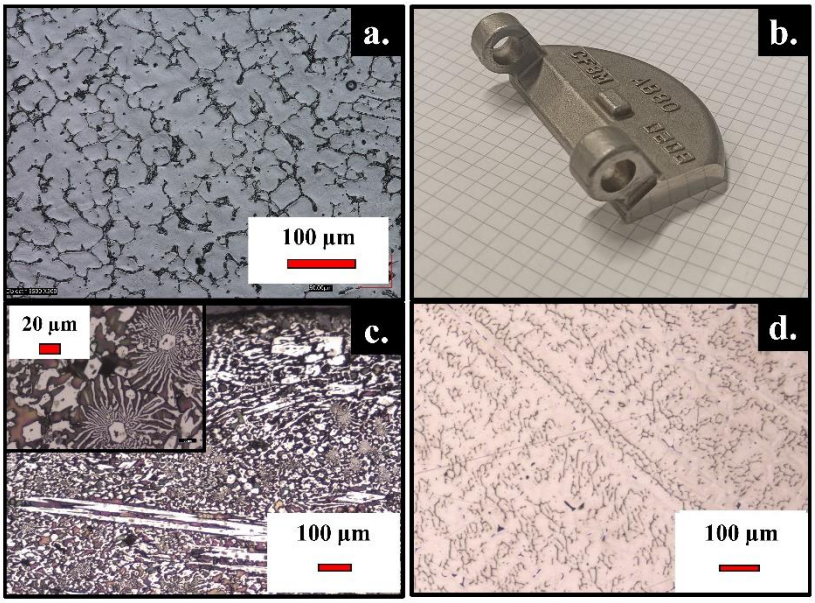

Figure 30. Microstructural optical microscopy observation of (a) a sand casted CF8M austenitic stainless steel, (c) polluted by the crucible carbon during the casting step, (d) 316L stainless steel casted in an alumina crucible and (b) is the sand casted CF8M austenitic stainless steel part

Since the interactions have been limited in the upper part of the castability equipment, other interactions were observed in the lower part. When the liquid metal is getting in contact with the mold, reaction can occur. The first tests executed with aluminum and copper were casted in a mold made of calcium sulfate and silica as mentioned in Table 6. The sample made of aluminum was not presenting any mold residue at the surface. On the contrary, the copper and the stainless steel presented a rougher aspect because of the mold residue remaining on the casted surface (as shown on Figure 31). It is common to have mold residue trapped at the surface of the casted part [246]. The potential interactions of the mold with stainless steel are detailed in the next paragraph.

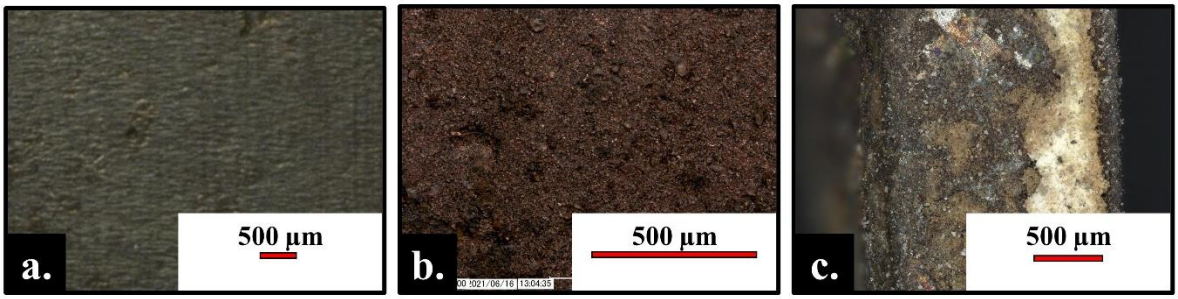

Figure 31. Optical microscopy observation of different casted samples surface: (a) aluminum, (b) copper and (c) 316L stainless steel

3.2.3 Interactions mold/liquid stainless steel

The surface state can indicate if a reaction occurs or not. Usually when steel is casted, a mill scale, i.e. an oxide layer, appears at its surface. In this work, the melting was carried out under a protective atmosphere and under a primary vacuum, helping to reduce oxide formation [247]. In the industry, a reduction agent such as coke can be added to capture the oxygen that could compromise the chemical composition [248]. A closer look to the surface of the casted part can give a first clue about the reaction that occurred between the liquid metal and the mold.

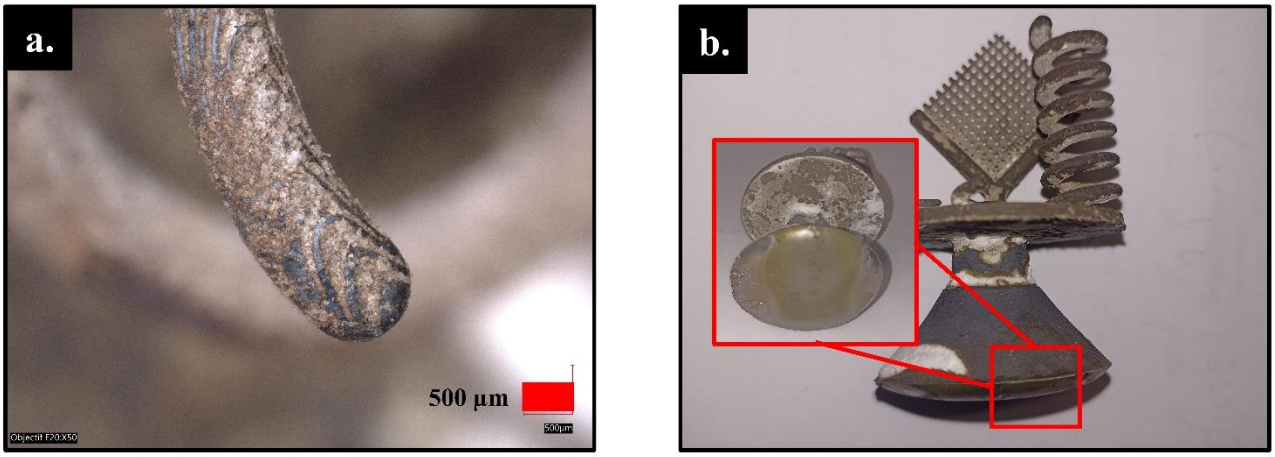

Figure 32. (a) Tip of the 1mm stainless steel spring casted during experiment 5 and (b) difference of color between the top of the casting cone and the side in contact with the mold

On Figure 32.a, the visual aspect of one of the springs, i.e. the 1 mm stainless steel from experiment 5, is presented. The metal appears dark and white grains are embedded between the layers. The layer aspect is due to the original pattern that was made of 3D-printed resin. The layers, here seen from the front and the top, are set up to be 50 µm layers. It is a major result in this study because it constitutes a proof of small details reproduction using stainless steel vacuum casting.

The alternation between the dark metallic material and the white grains indicates that the metal has infiltrated small details such as the pattern roughness. Especially at the end of the 1mm spring, this result indicates that the infiltration of detailed surfaces with 3D-printed pattern could be possible. Nevertheless, a reaction occurred during the process because the surface finish has a different color than the original metal. The silica mold can react with a liquid metal; for example, a reaction with copper has been documented [249]. It is also documented that stainless steel like 304L stainless steel can react with alumina substrates [250]. Plus, at high temperature, oxide formation has also been studied in the case of 316L stainless steel [251,252].

As shown on Figure 32.b, the stainless steel which was not directly in contact with the mold has a shiny aspect as it would be expected for a ferrous material. Consequently, a reaction between silica and 316L stainless steel, although never reported yet, could be possible. In the next chapter, further chemical analysis will be presented, giving a better understanding of what oxide is formed at the surface and if it does not compromise the chemical composition of the alloy.

4 Conclusion

At the outset of this section, several technological challenges related to the micrometric casting of stainless steel were emphasized. These challenges encompassed the reactivity of stainless steel, the high surface tension in its liquid state, and its ability to infiltrate submillimetric details. Overcoming these obstacles is imperative to ensure the feasibility of casting stainless steel at a micrometric scale, which is essential for achieving precise geometries.

To evaluate the casting process, two designs were proposed: springs ranging from 1 to 3 mm in diameter and a mesh. Through various casting experiments conducted in this section, several

conclusions can be drawn. Initially, a comparison was made with two other metals, aluminum and copper, to comprehend the casting process at a lower working temperature. Aluminum, known for its ease of casting, successfully filled the different spring patterns. Copper faced more challenges but underscored the significance of mold preheating temperature. Adapting certain elements of the apparatus, including modifying the crucible and mold material, facilitated the casting of 316L stainless steel at a millimetric scale.

Additionally, the 3D printed patterns used in the experiment retained surface marks from the manufacturing process. Despite being constituted of 50 µm resin layers, the patterns effectively captured micrometric details, allowing liquid stainless steel to infiltrate them during casting.

This finding paves the way for the next phase: proving the concept that surfaces with micrometric biomimetic-inspired design can be casted in stainless steel. The upcoming section will introduce a new set of technological challenges, with a specific focus on managing the formation of oxides on the stainless steel surface during casting. Identifying the composition of this oxide layer and efficiently eliminating it will be a crucial aspect in the forthcoming steps of the study.

Chapter 3: Bio-inspired and recycled 316L stainless steel surfaces prototyped by coupling digital light processing and investment vacuum casting

This section is adapted from an article entitled "Bio-inspired and recycled 316L stainless steel surfaces prototyped by coupling digital light processing and investment vacuum casting" submitted in Journal of Manufacturing processes in 2023

1 Introduction

In the previous section, the feasibility of casting stainless steel at a macroscopic scale has been explored. The previous results have proved the possibility to infiltrate sub-millimetric shapes. This section aims at producing stainless steel surfaces microtextured with bio-inspired patterns.

Micro-architectured stainless steel surfaces are usually manufactured with a top-down strategy (removing matter from the substrate), or a bottom-up strategy (adding matter over a substrate) [79]. Main pathways are: **(i)** micromachining, i.e. a subtractive manufacturing process relatively expensive and long to achieve. Simple micropatterns like holes or channels can be obtained using laser ablation [111,193], solid tools [79,253] or electrochemical micromachining [254]. Although laser texturing is an efficient, but high energy consuming method to carve in a metallic substrate, it has the disadvantage to form undesired oxides over 316L stainless steel [81,118] and wettability of the substrates obtained is difficult to control; **(ii)** Common metallic additive manufacturing processes for stainless steel, such as Selective Laser Melting (SLM) and Selective Laser Sintering (SLS), that have the disadvantage of giving poor surface state and a relatively low precision [149,158,255–257]. Some techniques such as micro-SLA or micro-SLS can manufacture objects under 100 µm, nevertheless the raw material, the post-process equipment and the precise optical system are very expensive [258]. On the contrary, polymer additive manufacturing processes are much precise (< 50µm), as technology has been existing since a longer time, and the raw printing materials are cheaper [256,259–261].

Another way to micro-texture a metallic surface is micro-casting but stainless steel casting for under micrometric details constitutes a technical challenge due to its high surface tension, high dynamic viscosity and high working temperature (1600°C). Usually, studies focus on lower melting point alloys like gold-based alloys [262]. Stainless steel molding is usually used for bigger parts made by injection molding [263]. Scientific researches about steel investment casting are thus quite rare [208]. In the previous chapter, the feasibility of stainless steel casting has been explored,

particularly the reproduction of small details. The aim of the present chapter is to investigate micro-detailed stainless steel surfaces manufacturing via vacuum assisted investment casting.

Nowadays, thanks to the recent advances in additive manufacturing and computer aided-design (CAD), modern science is able to replicate the natural microarchitectures to create materials with interesting properties [61,261]. In this work, polymer additive manufacturing (vat photopolymerization) and investment vacuum casting were coupled to design stainless steel microtextured surfaces. The process, used in jewelry [207] and prosthesis manufacturing [264], allows to directly create a microtextured substrate. This section is articulated in three different sub-sections: the printability of micrometric patterns, the molding process and the wettability characterization of the substrate. Different shapes were designed, bio-inspired (fish scale, drops, honeycomb) or not (simple grid, peaks). All surfaces were carefully characterized in terms of waviness, morphology and wettability.

2 Printability of micrometric patterns

2.1 First benchtest, VPP dimensional limitations exploration

First of all, to obtain a microtexture through the foundry process, it is necessary to print the texture in a polymeric material. What is the low limit of the 3D printing process in terms of size? Is it possible to print different shapes (cylinders, parallelepiped, etc.)? In this section an overview of the polymer pattern printability will be given.

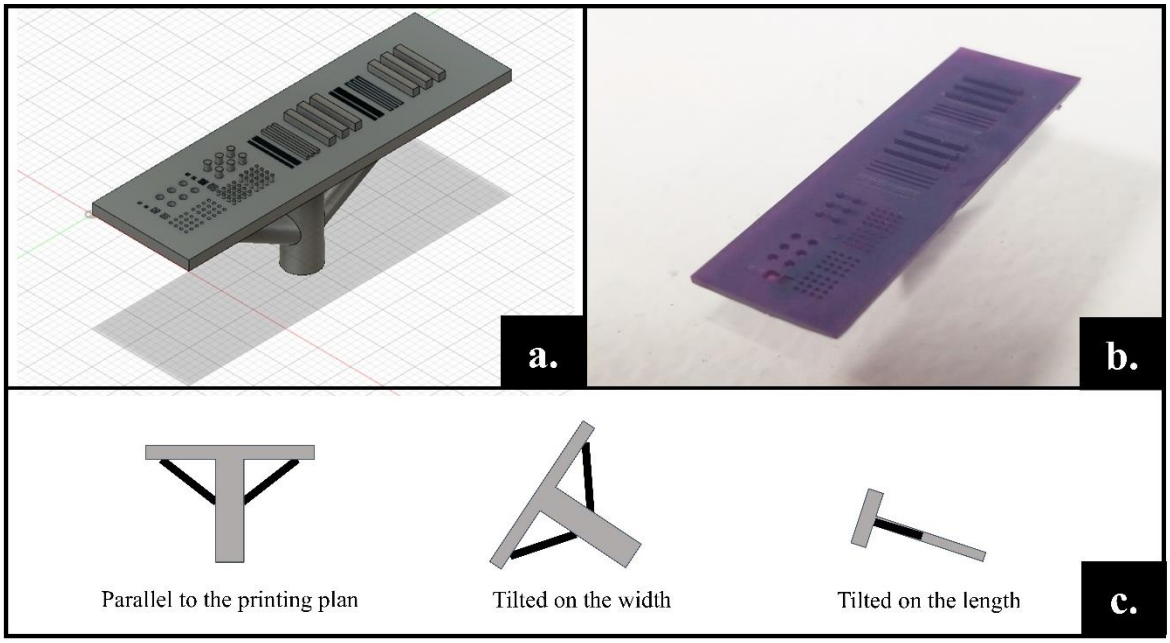

Figure 33. Benchtest n°1 (a) CAD version, (b) SLA-3D printed version (c) three different printing directions

The two techniques related to vat photopolymerization (VPP) used during this work to print the pattern were stereolithography (SLA) and digital light processing (DLP). Both technologies consist in liquid resin polymerization/curing thanks to a light source, respectively a liquid crystal display (LCD) screen (DLP) and a laser (SLA), both emitting UV-light. To manufacture an object, the 3D printer will superimpose layers of cured material. Three test benches have been developed to assess the printing possibilities of the printers. The preliminary tests were executed with the SLA printer to determine the smallest size of printable object.

The Z axis precision is the thickness of the polymerized layer. This value can be adjusted at 25, 50 and 100 µm in the printing parameters. In this work, every layer was 50 µm thick and exposed to UV light for 50 seconds. This duration and this layer size is a good compromise in terms on printing duration and quality. The samples obtained were coupons (2x20x15 mm^3) ramified in three points to be assembled as a sprue using a wax stick (see Figure 33).

The first bench test was printed in three different positions using the SLA printer: parallel to the printing directing, tilted on the length and tilted on the width as shown on Figure 33. The tilting was investigated to see if the combination of the x-y resolution with the z axis resolution could improve the printing. Cylindrical and parallelepipedal bumps and holes of multiple sizes were designed (50, 100, 200 and 400 µm, as diameter for the cylinders or side length for the parallelepiped). The printability of a pattern can vary depending on the distance with the closest shape, so different spacing have also been investigated (200 or 500 µm).

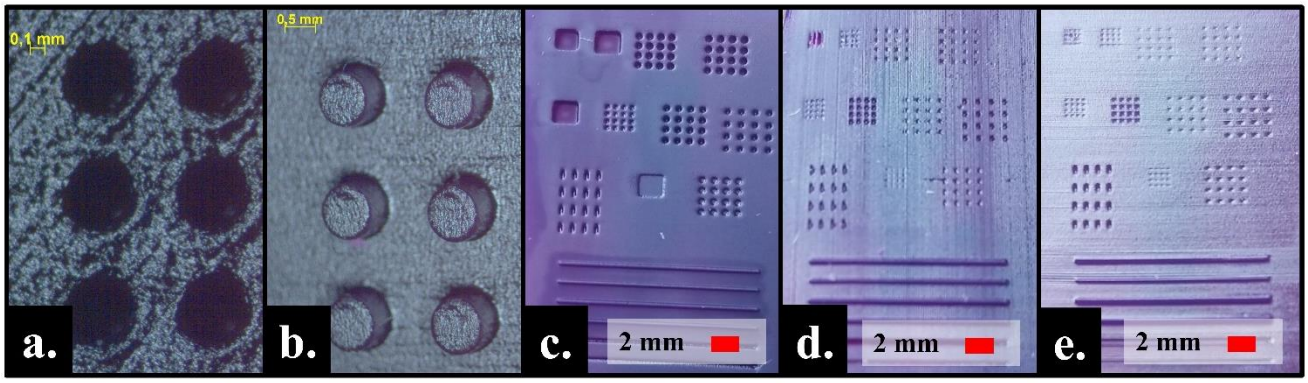

Figure 34. Examples of (a) 400 µm holes, (b) 400 µm cylinders. Bench test printed (c) parallel to the printing plan, (d) tilted on the length and (e) tilted on the width

Different conclusions came out of the printing results:

- Shapes with a dimension bigger than 400 µm were always successfully printed, no matter the printing direction
- 50 µm shapes and holes were not printable
- 100 µm shapes and holes were printable with at least 500 µm spacing between the shapes
- The smoothest surface state was given by the sample printed parallel to the printing plan. With the other direction, the layers are visible on the shapes.

The printability between holes and bumps smaller than 100µm has already been reported for VPP techniques using similar LCD screens [265]. Using these results, the size range between 50

µm and 100 µm has to be explored with a 500 µm spacing. The spacing has not been changed for the moment.

2.2 Second benchtest, micrometric scale printing improvement

A second bench test has been designed to assess the printability of this range size with one intermediary size (75 µm) and one bigger size (150 µm) (see Figure 35a. and b.). A size evaluation after printing has been performed to assess the dimensional accuracy of the printed shapes (round and squared). The main interest here is to evaluate the size distortion during the 3D printing step for difference size of objects.

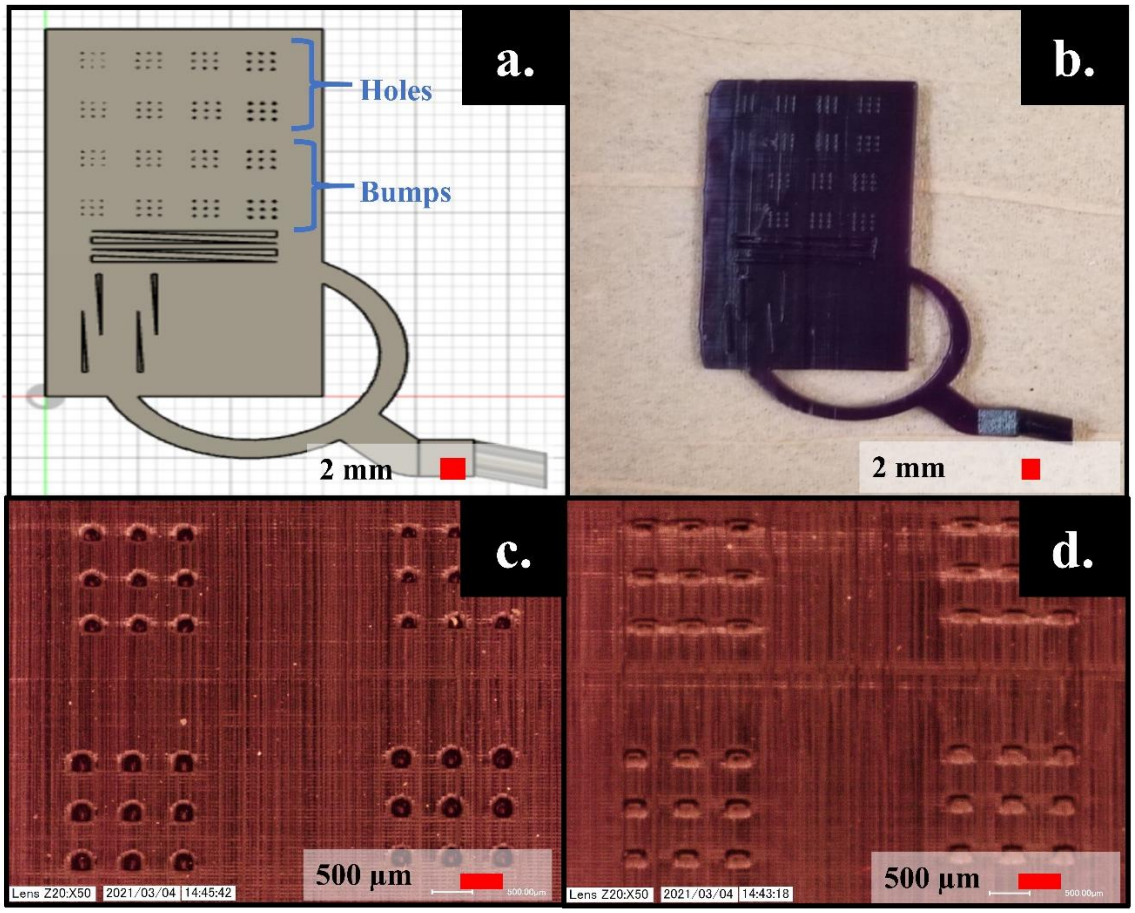

Figure 35. Benchtest n°2 (a) CAD version and (b) SLA-3D printed version, optical microscopy image of the 100/150 µm (c) bumps and (d) holes

The holes were all printed and only the 50 µm bumps did not appear no matter the printing direction. The dimensions measurement revealed the lack of accuracy for every object size. Table 8 gives the average size increase for the bumps and holes (squared and round) of every size. Based on the printed object measurements, the relative difference from the original dimension is calculated as shown by Equation 2:

$$Relative\ difference = \frac{(object\ size - original\ dimension)}{original\ dimension} \quad (2)$$

The relative difference for every type of shape (bumps and holes) at difference sizes (50, 75, 100 and 150) is plotted on Figure 36. The trend confirms the hypothesis formulated before, under 200 µm, the smaller a shape is designed, the less accurately the dimension are reproduced.

Table 8. Holes and bumps mean dimensions values on benchtest n°2

	Shape extruded	**50 µm**	**75 µm**	**100 µm**	**150 µm**
Holes	Round	149	160	158	224
	Squared	125	146	163	195
Bumps	Round	-	125	149	257
	Squared	-	169	182	227

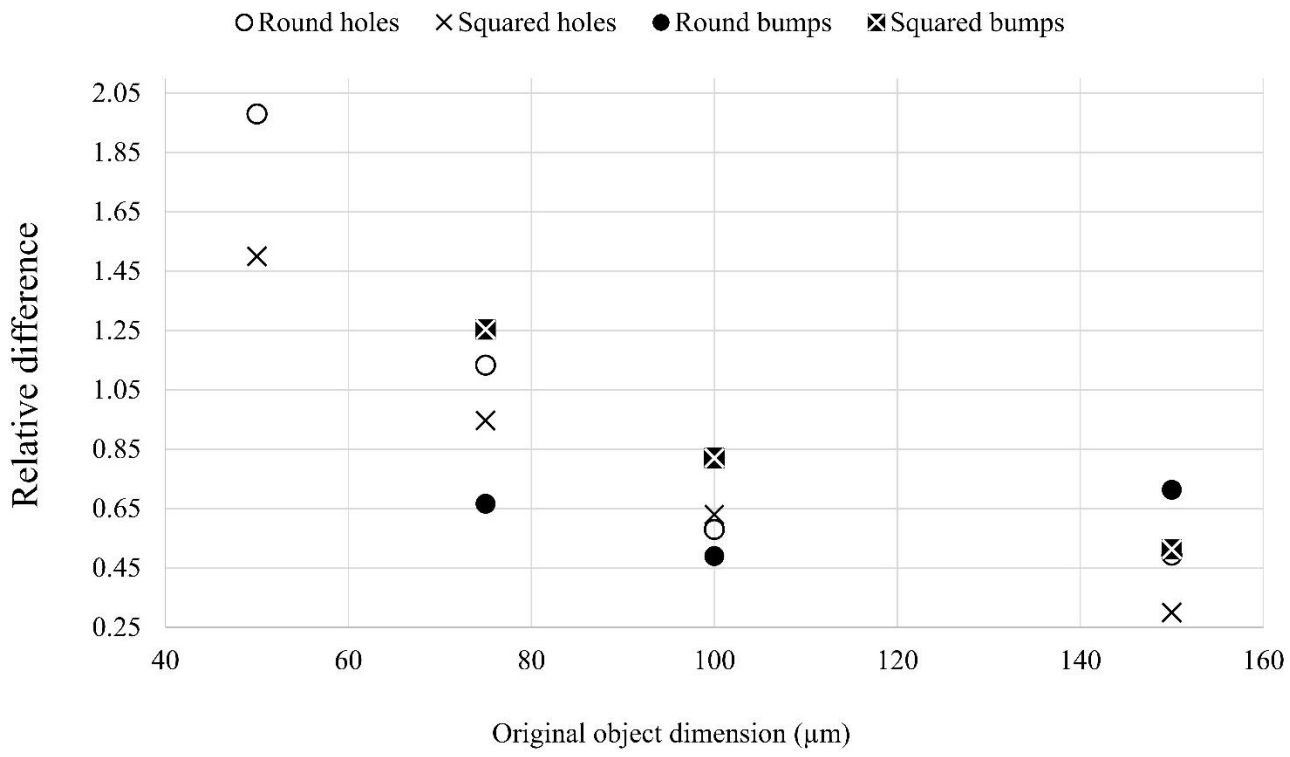

Figure 36. Relative difference between the original dimension of the 3d designed objects (holes and bumps) and the dimension of the printed objects

Regarding the results, a few remarks can be done:

- Any of the printed object dimensions were not below 125 µm, no matter the original size
- The bigger a shape is, the more accurate it is
- The 50 µm bumps were not printed
- 75 and 100 µm round bumps shapes give better results than other shapes

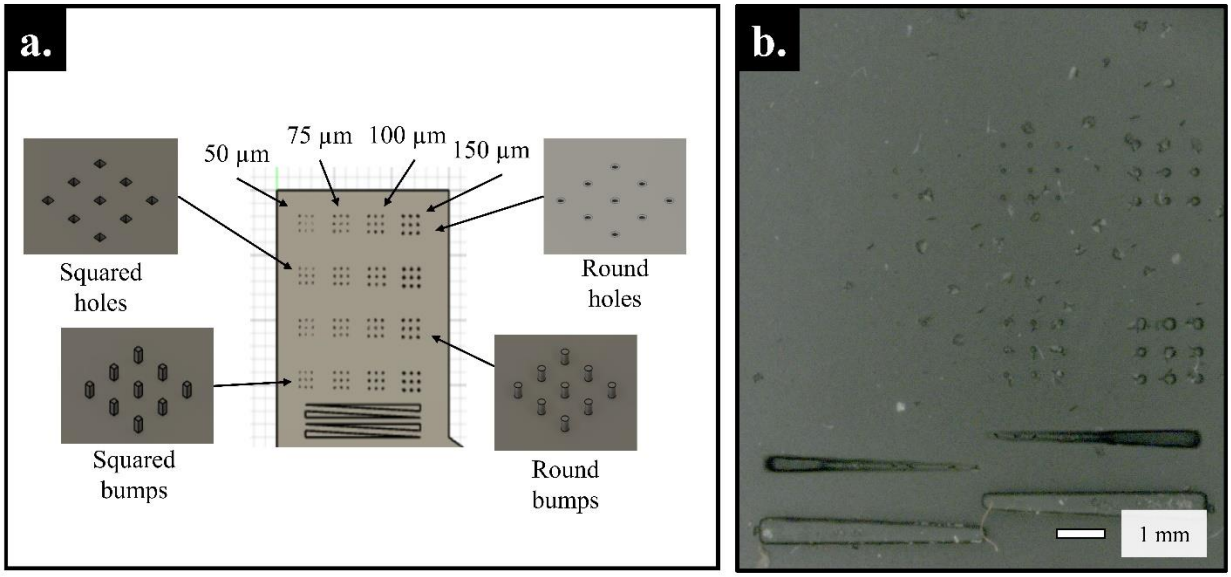

Figure 37. (a) Detailed description of benchtest n°2 and (b) benchtest n°2 with printed DLP

These two aforementioned experiments were executed in the same printing conditions on the SLA printer. The same experiment (benchtest n°2) was run on the DLP printer to compare (see Figure 37b.). The DLP printer showed a more accurate result. On the DLP printed benchtest n°2, 75 and 100 µm bumps came out respectively with 93 µm and 131 µm, which is slightly better the SLA printer because closer to the original dimension designed. Unfortunately, none of the holes were printed with the DLP printer. For the small objects, coming out of the surface, the DLP printing seems to give better results.

2.3 Third benchtest, SLA vs DLP

A third benchtest with has been designed with bigger object (< 200 µm) to compare the two printers. The samples were printed in the same direction with comparable layer thickness (50 µm).

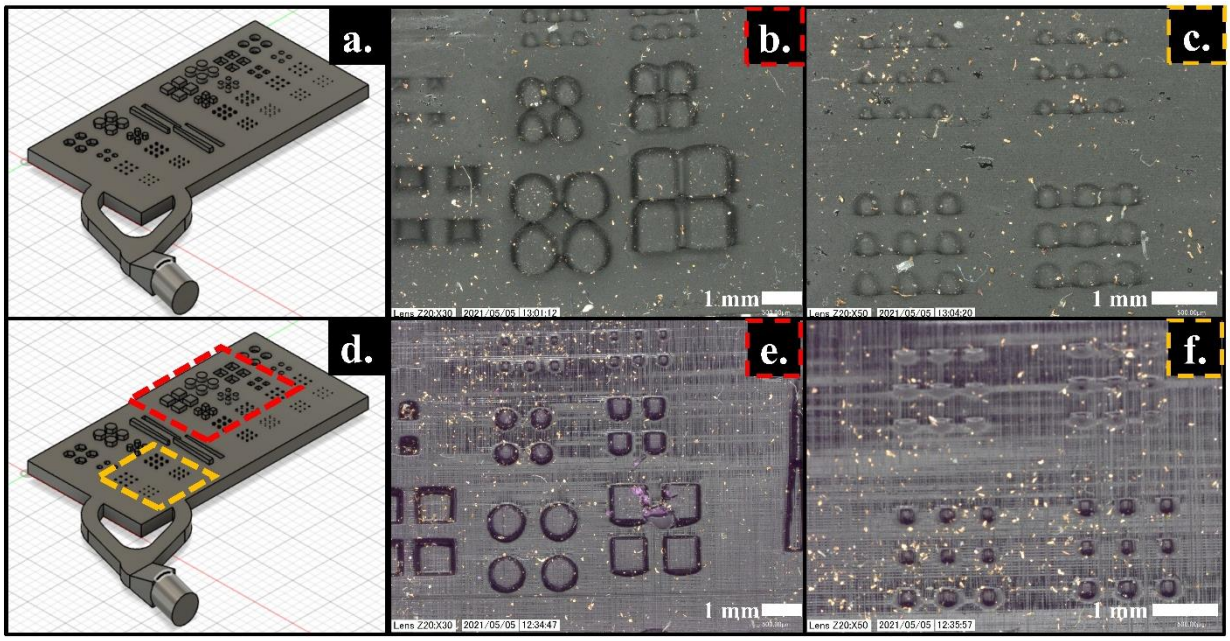

Figure 38. (a) & (b) Benchtest n°3 CAD design, (b) & (c) DLP printed, (e) & (f) SLA printed

Figure 38a. presents the benchtest n°3 where different size of bumps and holes were designed to be printed. This benchtest is not necessarily to compare the printed object sizes but their aspects and more importantly, the duration of the printing. Even if in terms of size, the DLP printed benchtest (see Figure 38b. and c.) seems less accurate than the SLA printed (Figure 38e. and f.), the visual aspect is less sharp and more organic.

One other important technical point is the printing duration. To print 10 samples, the DLP printer took 5.5 hours where the SLA printer took 12h to complete the same task. For batch printing, the DLP is more adapted than the SLA., because the DLP printing duration depends on the batch total height where the SLA printing duration depends on the number of objects to print. DLP printers are polymerizing layer by layer every object at the same time, unlike the SLA printers for to polymerize the layer objects after objects.

From the three different benchtests, a lot of lessons have been learned in order to design and print better bio-inspired microtextures. From benchtest n°1, a better understanding of what a SLA printer can manufacture in terms of size was given. Around 100 µm, the shapes and holes require more spacing to be printed. Benchtest n°2 was designed to explore the printing between 50 and 200 µm. DLP printer showed a better accuracy than SLA. Benchtest n°3 gave a visual comparison for bigger objects between the DLP and SLA printing. After these tests, the DLP has been chosen to pursue for the smoother visual aspect and its great printing speed adapted to batch printing. From all the benchtest, bumps (objects coming out of the printed surface) were printed better than the holes (objects with the printed surface).

Knowing the printing technical boundaries, the next step toward bio-inspired microtexture printing can begin. The printed objects will have to be around 100 µm, round-like and designed like a bump (coming out of the printed surface). For the moment, the only shapes printed were isolated shapes of difference size. If the next step is to print a bio-inspired microtexture, the printed objects are going to be reproduced all over the printed surface as a pattern. The next section is a printing parameters exploration that will focus on pattern printing.

2.4 DLP printing parameter exploration

Benchtests showed that one of the main differences between the CAD images and the real printed patterns concerns the sizes of the patterns printed (Figure 39). This size distortion may be due to two phenomena during polymerization: laser accuracy and the over-exposure to UV-light. Understanding the laser movement during the printing seems a complicated task To have a better control over the object printing, the SLA printing has been replaced by DLP.

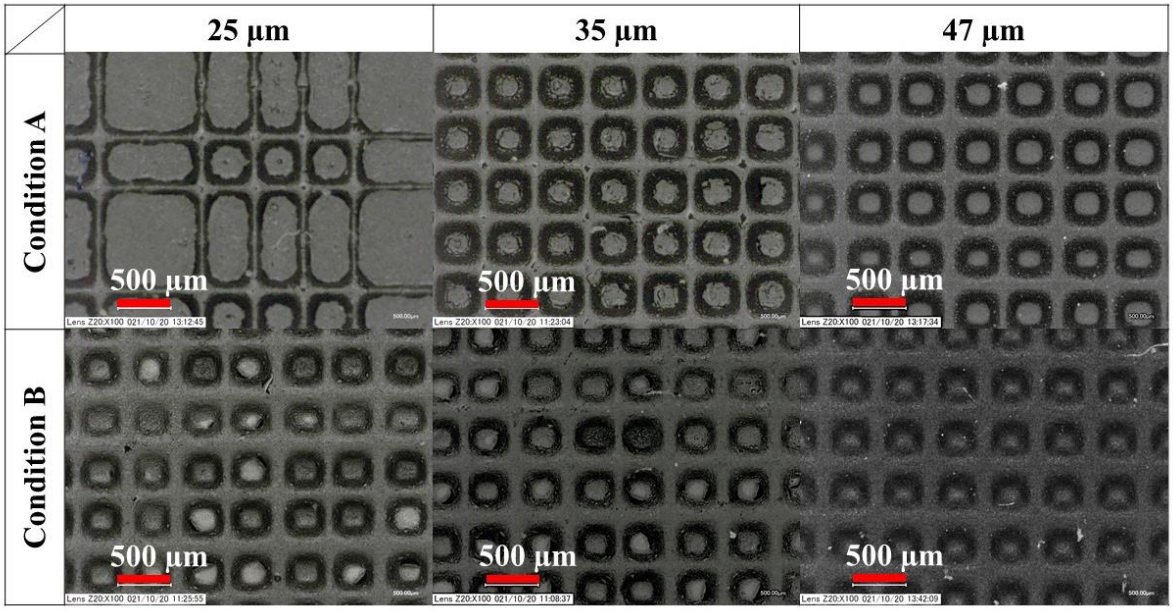

Figure 39. Grid pattern of different wall thicknesses (25 µm, 35 µm and 47 µm) printed with two different conditions (A and B)

The 3D printed parts were made with *Daylight precision castable* resin for jewelry from Photocentric. The polymer is mentioned as "acrylates" by the resin fabricant. The 3D printer was a DLP printer LC-Precision from Photocentric. Thanks to a liquid crystal display (LCD) screen featuring UV light, liquid ink is polymerized into solid polymer. The 3D printer has a X-Y precision of 47 µm which is the size of a pixel on the LCD screen (5.5' diagonal inch and 2560x1440 resolution). The size of a pixel is calculated using Equation 1:

$$Pixel\ size = \frac{Screen\ diagonal\ in\ inches}{\sqrt{Width\ in\ pixels^2 + Height\ in\ pixels^2}} \times 25.4 \qquad (1)$$

To test these hypotheses, grid patterns were printed with wall thickness of 50% (25 µm), 75% (35 µm) and 100% of the pixel size of the 3D printer 4K screen in the xy plane (47 µm). A grid pattern is composed of perpendicular walls designed with a certain thickness. Figure 39 presents the results for three wall thicknesses (25, 35 and 47 µm) and the two printing conditions detailed below.

These walls are designed to be 200 µm along the z axis. Condition A is 50 µm thickness of the printed layer and 50 s for the polymerization time per layer; condition B is 100 µm thickness of the printed layer and 100 s for the polymerization time per layer. For exposure time below 50 s, the parts were not well polymerized enough. When the grid pattern is printed, the 4K screen will display a grid. If the information to display is covering a sufficient part of a pixel, it will be lit. This may explain the loss of information for the 25 µm grid printed with condition A. Condition B leads to obvious better result because of the longer polymerization duration. As the exposure time is doubled compare to condition A, it might be sufficient to polymerize every part of the grid completely. It has been indeed demonstrated in the literature that the size of the object photopolymerized grows with the exposure time.[266]

With 35µm wall size, condition A leads to patterns printed in a more uniform manner over the surface. The longer the exposure time gets, the more liquid resin is polymerized to form the pattern, as seen with condition B.

At 47 µm wall size, for both conditions, the squares composing the grid are lengthened is one direction. The rectangular aspect of the cells is due to directional thickening of grid walls. The thickening is omnipresent in condition B, therefore the pattern is much affected by a long exposure time. At 35µm in condition A, some of the grid walls were not printed at all. The exposure time may have been too low to polymerize properly the liquid resin. Consequently, in the following part of the work, condition A was chosen to print the coupons and ensure correct pattern printing for thin interconnected objects such as the grid.

3 From CAD to resin printing

Further printing experiments were then carried out using the optimized printing parameters reported in previous paragraph. Five different patterns were chosen, bio-inspired (honeycomb and fish scales) or not (grid pattern) and designed using CAD (Figure 40). The fish scales in particular have been chosen for a

potential sliding improvement in a turbulent flow [62,63,267]. The patterns can be separated into two categories: the "nets" (honeycomb and grid - Figure 40 (d) and (e)) and the "repeated objects" (Long scale, short scale and Drop-like scale - Figure 40 (a), (b) and (c)). The printed patterns look similar to those originally created on the CAD software. During the printing step, the main aspect is still preserved but the layer-by-layer process affects the shapes (Figure 41). Two main differences can be observed between the CAD version of the patterns and the printed version of the pattern. First, all the scales (Long, short and drop-like) which are designed to be separated objects seem to merge after printing, i.e. the separation between each element is less clear. Secondly, all the patterned surfaces printed seem "rounder" than the original 3d sketch. The UV-light coming from a pixel during the photopolymerization is indeed not a uniform square but an asymmetrical conical distribution. It is described as more intense in the center of the pixel and fading on the edges. The stair-stepping aspect of the small printed objects has already been reported in the literature [164,265]. This aspect could be attenuated by increasing the gap between the liquid resin vat and the screen [265].

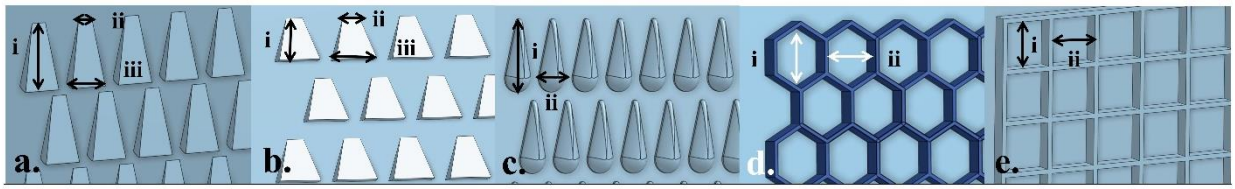

Dimensions (µm)	i	ii	iii	Height
a.	1000	200	500	340
b.	500	200	500	175
c.	1340	500	-	300
d.	500	430	-	200
e.	470	470	-	150

Figure 40. Designed patterns on a CAD software (a) Long fish scale, (b) Short fish scale, (c) Drop-like fish scale, (d) Honeycomb and (e) Grid pattern

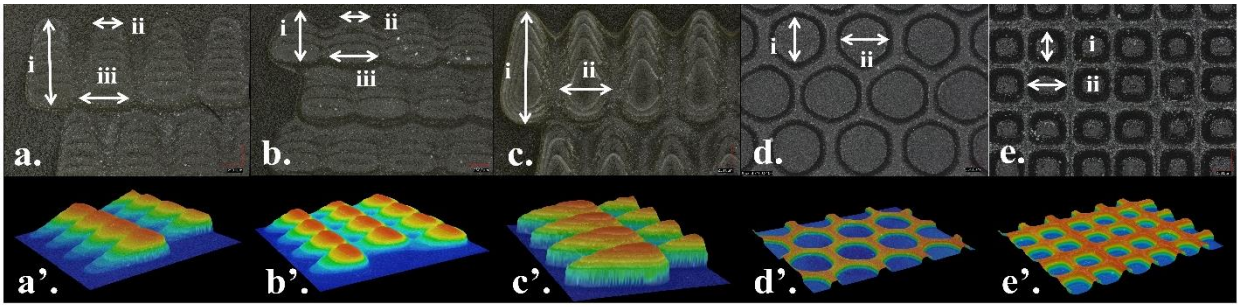

Dimensions (µm)	i	ii	iii	Height
a.	1056 ± 17	306 ± 29	605 ± 38	325 ± 17
b.	647 ± 8	273 ± 41	625 ± 26	194 ± 6
c.	1465 ±	3689 ± 15	-	395 ± 16
d.	596 ± 18	575 ± 25	-	173 ± 20
e.	345 ± 24	345 ± 24	-	150 ± 32

Figure 41. 3D printed patterns (a and a') Long fish scale, (b and b') Short fish scale, (c and c') Drop-like fish scale, (d and d') Honeycomb and (e and e') Grid pattern

4 From resin printing to stainless steel casting

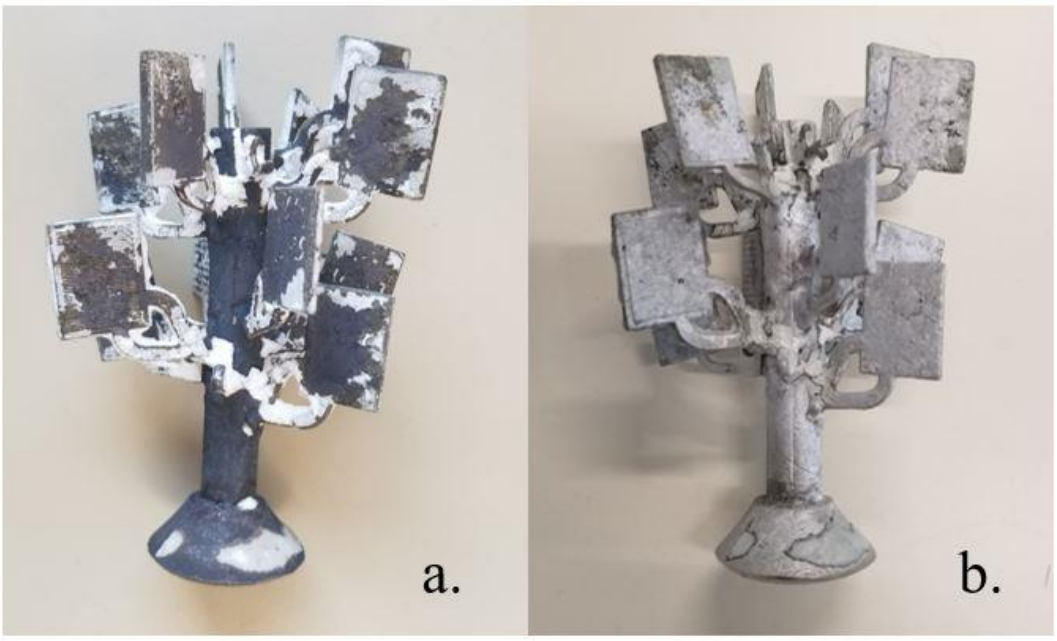

Figure 42. Sample assembled in a sprue after the casting: (a) before chemical etching (b) after chemical etching.

4.1 Oxide layer formation after stainless steel casting

After casting, the coupon surfaces are appearing visually dark with a lot of persistent mold residue at the surface (Figure 42). A chemical etching is mandatory to remove the dark layer and the mold residue. The casted parts were immersed for 5 minutes in an acidic aqueous solution (15%vol HCl (hydrochloric acid 37% from Normapur), 12%vol H_2SO_4 (sulfuric acid 95% from Normapur) and 5%vol HNO_3 (nitric acid 65% from Fluka)) at 80 °C to remove the mill skin and residual silica from the mold. This chemical etching is inspired from a French technical article "Décapage en milieu aqueux" written by M. Depétris-Wéry in 2019 for *Technique de l'ingénieur* [268]. After etching, the surfaces were rinsed in an ultrasonic bath of deionized water at room temperature for 30 minutes.

In the previous chapter, the hypothesis of a reaction between the liquid stainless steel and the ceramic mold has been formulated. To prove this theory, two analysis have been performed, x-ray diffraction (XRD) and EDS analysis. The first analysis will give structural information about the crystal phase and the second will inform the chemical composition of the different phase.

Theoretically, if there was no reaction between the liquid stainless steel and the ceramic mold, the crystal phase should be an addition of austenite and the mold. If a new phase has been created, signals different should appear. On Figure 43, the XRD diffractogram of the as-cast coupon is compared to the raw stainless steel and the ceramic mold powder. The signal coming from the austenite are clear, but other crystal phases are also present but not related to the ceramic mold.

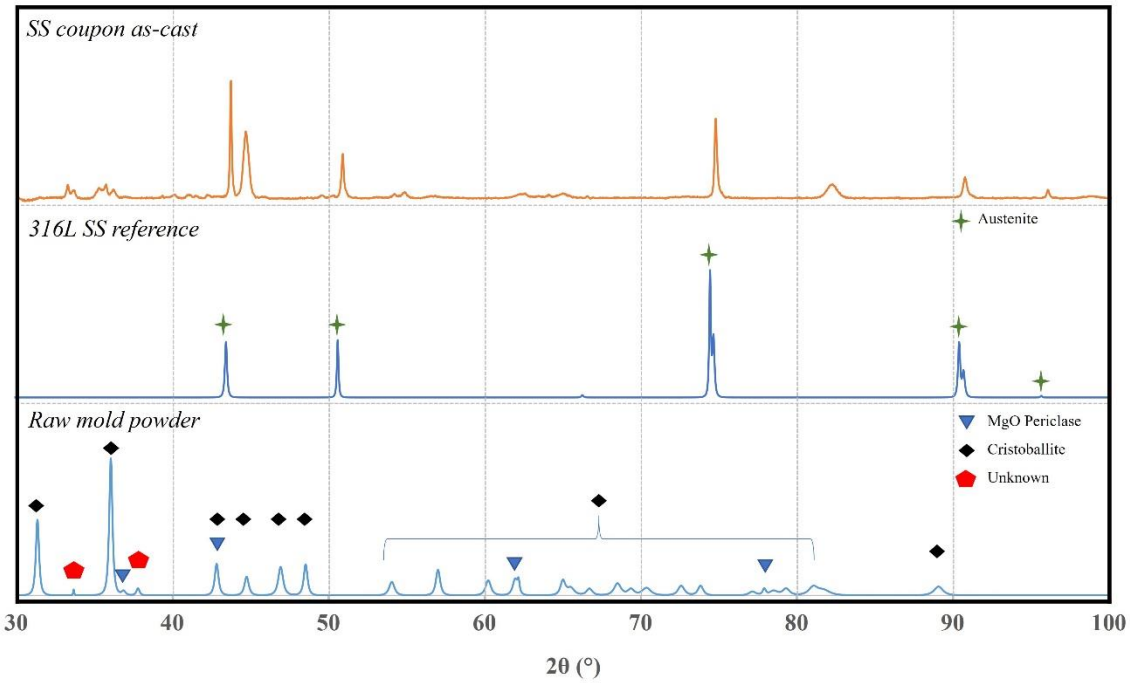

Figure 43. XRD of a coupon as-cast, 316L SS before melting as a reference and the ceramic mold powder.

The different signals of the SS as-cast diffractogram, other than the one from the obvious austenite, could be from other steel phase (α-ferrite, sigma, martensite or bainite). The sample as-cast can be compared to a sample chemically etched to distinguish the signal coming from the bulk (metallic) and the signal coming from the dark oxide layer probably formed. On Figure 44, a comparison between the original stainless steel (raw foundry material), a coupon as-cast and two coupons chemically etched to remove the dark oxide layer is presented. After etching, the signals not coming from the austenite are disappearing, even the α-ferrite. It proves that the phases were essentially concentrated in the dark oxide layer formed during the casting at the sample's surfaces. The etched coupons were taken from two different batch to confirm the trend. It is interesting to note that some of the signal from the austenite, especially (220) and (222), vary in terms of intensity. It can be due to the sample orientation. A casted sample is highly directional because of the oriented solidification, which induce preferential orientation of the grains.

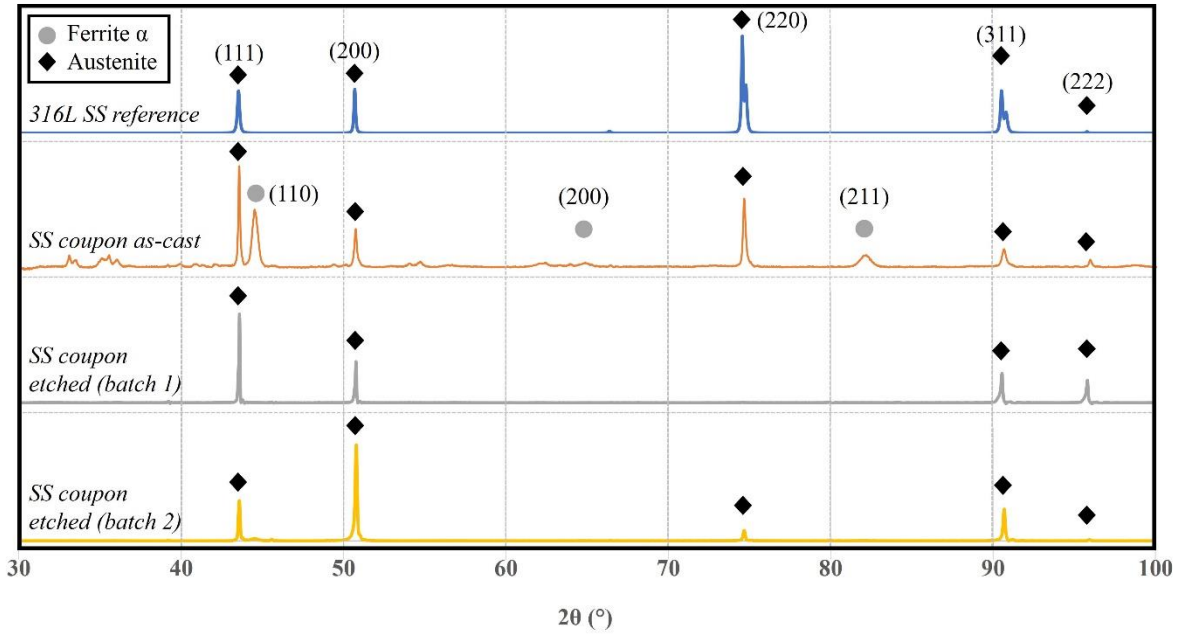

Figure 44. XRD comparison between 316L SS as a ref, a coupon as cast, and two different coupon after etching

A cross section SEM-EDS analysis of the casted coupon before chemical etching reveals a composite external layer (Figure 45). Different phases can be observed (see Figure 45b). The dark part (see point A) is essentially composed of silica (SiO_2) and the bright part (see points B & C) is a chromium-iron oxide layer.

The remaining silica is coming from the mold. On Figure 45 (analyse A), the silica grains, mentioned before, trapped in the surface layer are still distinguishable. The chromium rich oxide (analyse B) is probably generated when the liquid metal infiltrates the ceramic mold grains. This oxide layer is mainly composed of chromium and manganese oxides from the metal or silica as well as titanium and magnesium oxides traces (identified with an EDS analysis) from the mold (analyses B and C). The formation of chromium oxides from austenitic stainless steel at high temperature is a well described phenomenon [251]. The external layer of the stainless steel contains oxygen but also silicon (see Figure 45 points D and E). These two elements diffuse in the stainless steel surface, a behavior also observed when a material or a coating rich in silicon (like the silica

mold in the present process) is in contact with a hot ferrous material [269–271]. The oxide layer removal via chemical etching is thus necessary to reach the stainless steel underneath.

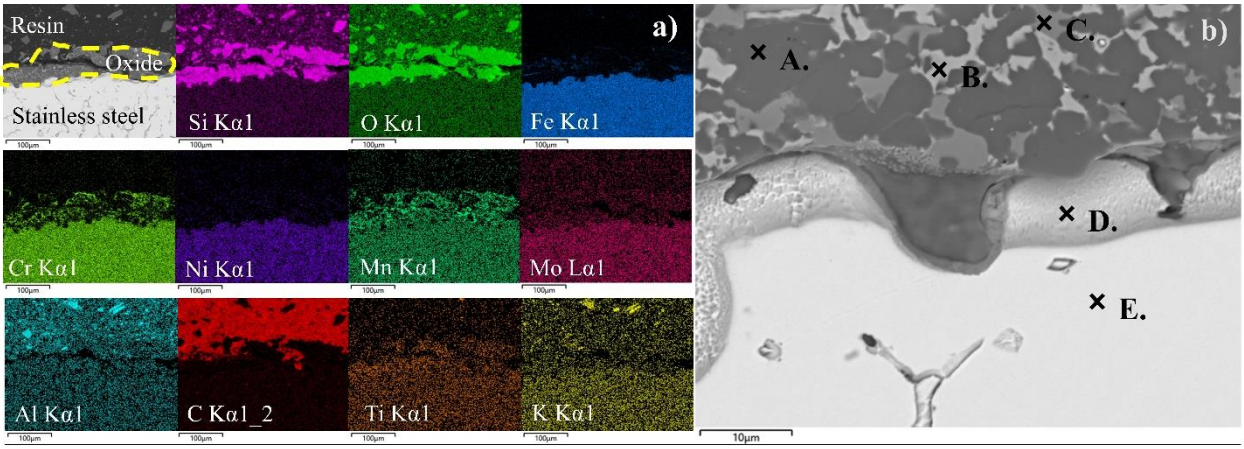

At.%	Cr	Fe	Mg	Mn	Mo	Ni	O	Si	Ti
A.	-	-	-	-	-	-	68.2	31.8	-
B.	18.8	0.9	1.4	8.5	-	-	59.5	7.7	2.8
C.	1.4	-	-	8.2	-	-	61.4	20.5	1.2
D.	15.7	59.4	-	0.8	0.7	8.2	9.1	6.1	-
E.	18.1	67.2	-	0.7	1.0	9.3	1.4	1.4	-

Figure 45. EDS-SEM cross section element analysis (at. %) of the stainless steel oxidation layer (a) with an element mapping and (b) the atomic percentage in the different phases: A. is the silica from the mold, B and C are the oxides formed during the casting when the liquid metal touches the mold, D is the surface of the stainless steel enriched with oxygen and silicon, E is the stainless steel with less oxygen and silicon.

With EDS and XRD analysis, it is possible to sketch a hypothetical mechanism happening when the liquid stainless steel enters in contact with the ceramic mold to form the dark oxide layer. On Figure 46, a schematic description of the mechanism is proposed. It is divided in three phases: before contact, the infiltration and after the complete solidification. When the liquid stainless steel enters in contact with the mold, it will fill the spaces between the mold grains. During the infiltration, the liquid metal will cool down and solidify. The infiltrated metal will be oxidized and element such as silicon and oxygen are going to diffuse into the bulk. Comparable mechanisms

have been reported in the literature for austenitic steels. For example Al-Si coatings, in contact with a austenitic steel during hot stamping (700-800 °C), generates Si and Al diffusion [272,273].

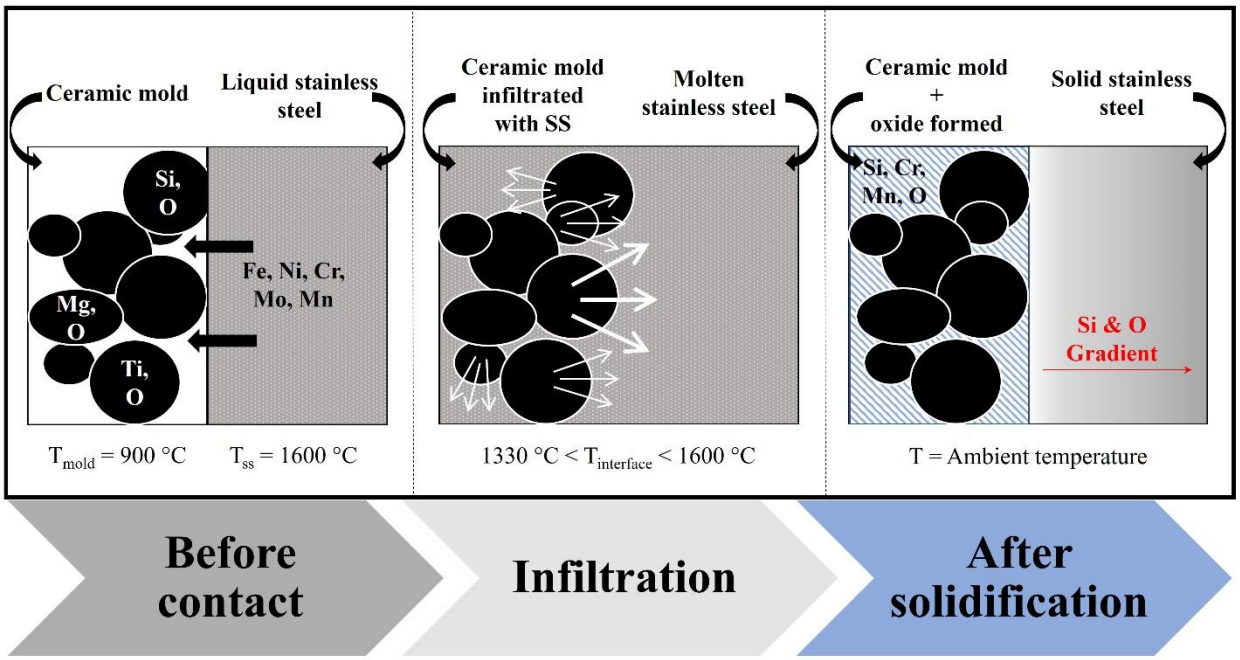

Figure 46. Hypothetical mechanism of the dark oxide layer formation

A diffusion simulation study based on thermodynamics, such as Diffusion Controlled TRAnsformation (DICTRA), could constitute an interesting outlook for this observation. It could confirm or deny the hypothetical diffusion mechanism explained earlier.

Once the oxide layer removed thanks to the chemical etching, the substrates reveal the bio-inspired microtexture mold during the investment casting step. After etching, microscopic analyses were carried out on the samples obtained and are presented on Figure 47. Patterns are obtained at the stainless steel surface, that correspond to the initial resin printed patterns, but not as smooth and uniform as in the resin version.

4.2 Patterns molding

Visually, the pattern is well reproduced for drop-like fish scale, long fish scale and short fish scale. The honeycomb and grid patterns are similar to the reference one (coupon without pattern). The fish scales, composed of single objects replicated all over the surface, were casted in a more precise way (8. a, b and c) than grid and honeycomb patterns. In fact, these patterns have been well molded locally but not all over the coupon (Figure 8 d & e). In the author's opinion, it could be explained by the fact that they are conceived as networks and form one single object coming out of the coupon surface.

The layer-by-layer aspect has faded, especially on the long and short fish scales. The drop-like fish scale, which is the biggest pattern in term of dimensions, has kept the layer by layer aspect of the resin version.

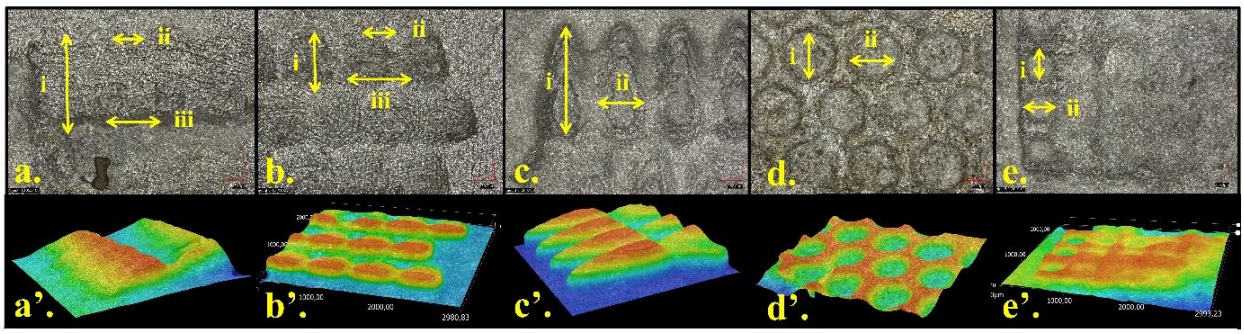

Dimensions (µm)	i	ii	iii	Height
a.	1030 ± 17	244 ± 26	552 ± 59	288 ± 12
b.	527 ± 17	212 ± 12	659 ± 29	138 ± 18
c.	1401 ± 33	675 ± 17	-	386 ± 25
d.	518 ± 20	548 ± 22	-	194 ± 17
e.	345 ± 21	345 ± 21	-	137 ± 16

Figure 47. Stainless steel molded patterns (a and a') Long fish scale, (b and b') Short fish scale, (c and c') Drop-like fish scale, (d and d') Honeycomb and (e and e') Grid pattern

Not surprisingly, the bigger the topography, the easier the moldability. This drop-like fish scale pattern was used to estimate qualitatively the loss of precision between the CAD design and

the obtained pattern after etching (Figure 48f. to h.). The 50 µm stair appearance of the printed shapes is still recognizable after casting and chemical etching.

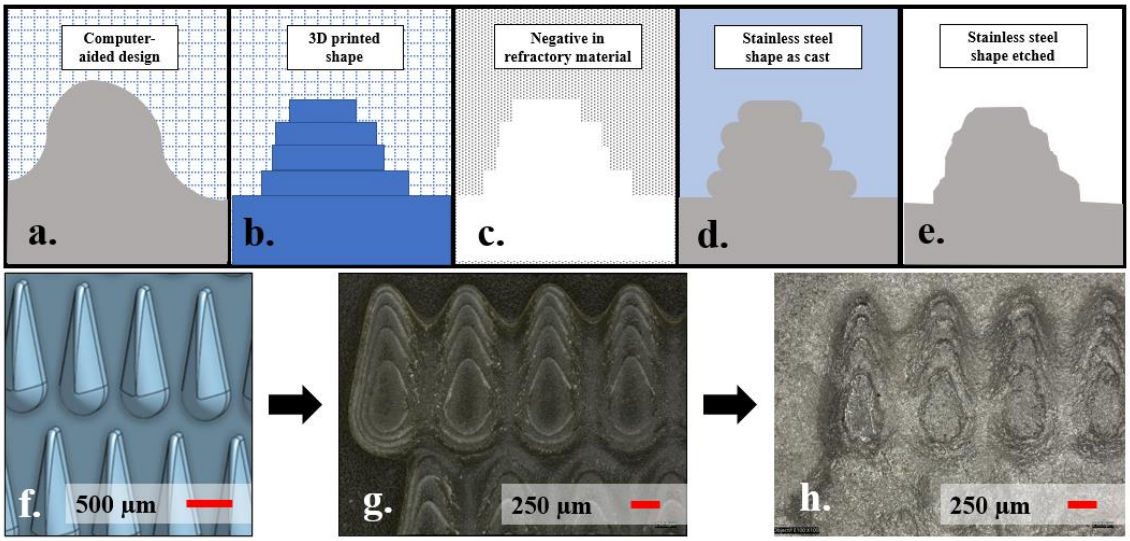

Figure 48. Representation of the information loss along the manufacturing process (a) and (f) computer-aided design of a curvy detail, (b) and (g) layer-by-layer interpretation of the detail, (c) investment powder molded as a negative of the detail printed, (d) stainless steel casted shape, (e) and (h) metallic detail after chemical etching.

The shapes designed in 3D (Figure 48a.) are sliced into multiple layers for the printing (Figure 48b.). During this interpretation step, a part of the information is lost. Thus, curves are printed as "stairs". The refractory material that envelops the 3d-printed resin to create the mold will fit the shapes as much as the granulometry and viscosity of the slurry can allow. Because the ceramic slurry is a commercial product for jewelry with a strict procedure, no variation on that part was possible. During the slurry drying and dewaxing step, some distortion of the final dimension could appear (Figure 48c.). Then, during the casting, the liquid metal infiltration into the mold

details is limited by the liquid stainless steel surface tension and the wettability between the liquid metal and the mold material. At last, when steel solidifies, it slightly retracts. The volume occupied by the liquid steel in the pattern is slightly bigger than the volume of the solidified part as the molten stainless steel is less dense than the solidified material (Figure 48d.) [243]. During the last step, the chemical etching applied in the surface post-treatment to remove the oxide layer and the mold residue also smoothens the stair aspect of the shapes (Figure 48e.). As an example of the evolution of the pattern versus process steps, Figure 48 (f-h) shows the loss of precision between the CAD design and the obtained pattern after etching, for the drop-like fish scale.

In order to characterize more precisely the information loss, the waviness was measured with a optical microscope before and after casting. Both the linear (Ra, Rz) and superficial (Sa, Sz) waviness were quantified after the printing step and after the post-casting etching step.

$$Change\ percentage = \frac{X_{polymer} - X_{metal}}{X_{polymer}} \times 100 \quad (1)$$

Where $X = \{Ra, Rz, Sa, Sz\}$

A comparison percentage (Equation 1) was defined to assess the change between the polymer and the metallic version of the pattern, quantifying the evolution of the waviness parameters (Ra, Sa, Rz, Sz) before and after the casting process. The metallic versions, if molded correctly, will possess smaller roughness parameters. In general, the values are in a range between 30 and 50 µm for the metallic version of the patterns.

Table 9 shows that the waviness of the metallic version of the patterns is decreasing. In particular, the z parameters for the maximum heights (Rz and Sz) after casting are decreasing. These results, in accordance with microscopic observations, show that the patterns are less pronounced and less homogeneous than in the 3D-printed polymer version. A positive change percentage is when the polymer roughness is superior to the metallic roughness, which is normal

during a molding process. In Table 1, a pattern presenting a negative change percentage for most of the parameters means that it is not molded correctly. This is the case for example of the grid and honeycomb patterns, that were visually smooth and that show mostly negative percentages (red/yellow code in Table 1).

Table 9. Change percentage of the roughness parameter (Ra, Sa, Rz, Sz) between the polymer and the metallic version of the different patterns (Green (>10 %), Yellow (between -10 % and 10 %), Red (<-10 %)

	Drop like fish scale	Short fish scale	Long fish scale	Honeycomb	Grid
Ra	37.4	9.0	42.9	-31.0	-10.3
Rz	51.5	51.1	50.4	5.6	16.5
Sa	24.1	-9.0	47.5	-73.0	-25.0
Sz	68.4	28.9	62.4	-0.4	-27.6

The same decrease is observable for Ra and Sa values except for honeycomb and grid patterns. It means that a general height flattening occurs during the casting process. The general aspect of the pattern is fading along the process. Optical microscopy allowed us to compare the polymer and the metallic version of the pattern but is limited when the surface is flat compared to a profilometer.

In the following sections, a profilometer using interferometry, a more accurate method of roughness characterization will be used. Note that it could not be used to compare the polymer and the metallic coupons as it can only detect metallic shiny materials.

More than the loss of information during the casting process, another interesting point concerns the dendrite formation during the solidification. The substrates presented in the current article are indeed featuring dendrites at the surface. Usually, dendrites are formed when the metal solidification is slow, oriented and controlled. They can be oriented in one direction. For example, when austenitic stainless steels are welded or during controlled solidification, the part solidified after melting will present oriented dendrites following the heat flux [274–276]. It is reported that only the combination of a solidification rate higher than 0.01mm/s and temperature gradient lower

than 100°C/mm will form equiaxed dendrites [277]. Moreover, most of the time, the dendrites are grown over a pre-existing substrate. In the present work, the dendrites formed during the casting process are coming from the substrate material: the microtexture and the substrate are one continuous material. Dendrites are thus randomly dispersed on the samples, which might explain the high standard deviations observed in terms of roughness and wettability. It adds another textured layer to the micro-textured surfaces and changes the surface state. This texture is in that case due to the slow cooling down after casting [276]. As observed on Figure 49a, the dendrites are not oriented in one direction but randomly dispersed in the coupon.

The various patterns developed in this study show the possibilities that emerge through the fusion of polymer additive manufacturing and vacuum-assisted investment casting. The fabricated surfaces exhibit two distinct levels of complexity: the 3D-printed waviness and the roughness (dendrites) that emerge during solidification (see Figure 49b. and c.). Different surface elements contribute to alterations in surface chemistry and texture, thereby influencing wettability. In the following section, the wettability of each sample is assessed, with the objectives to isolate the different surface components to determine their contributions to wettability.

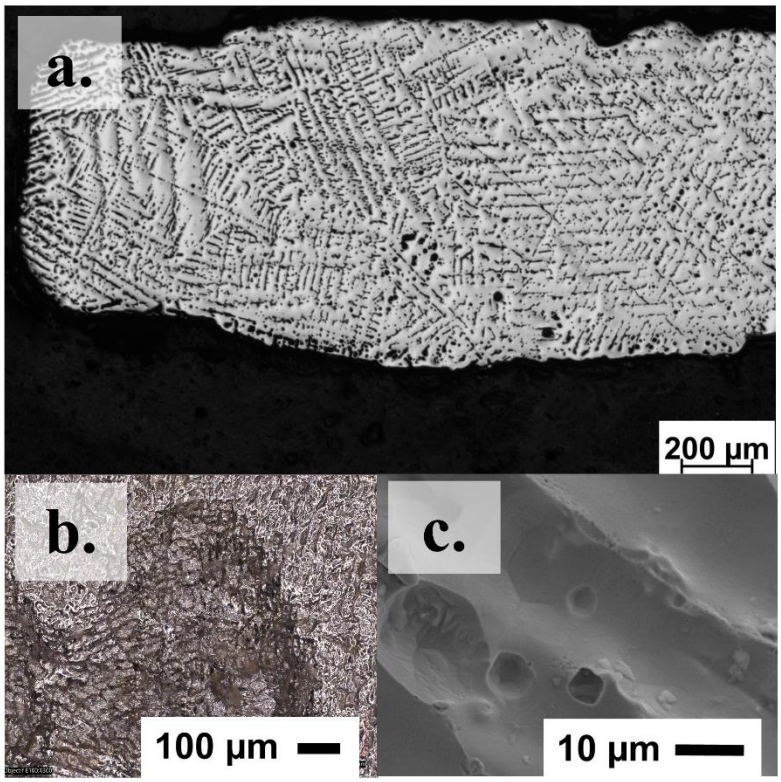

Figure 49. a) Dendritic microstructure of a coupon cross section, b) Optical microscope observation of the short fish scale pattern with a dendritic aspect of the surface and c) SEM observation of the dendritic surface presenting a "wavy"/non-flat aspect at the micrometric scale

4.3 Effect of the bio-inspired texture on the wettability

The water contact angle (WCA) results are depicted in Figure 50. Various substrates are compared, including micro-textured surfaces, a commercially flat stainless steel (2R), native or etched in conditions identical to the casted samples, and a reference stainless steel produced using the same foundry process but lacking microtexture. When compared to the flat commercial 316L stainless steel etched under the same conditions as the casted samples (WCA: 59.2° ± 1.3), all micro-textured surfaces exhibit higher mean WCA values (Long fish scale: 112.4° ± 19.6; Short fish scale: 81.7° ± 23.9; Drop-like fish scale: 83.0° ± 15.9). Surfaces manufactured via the same

foundry process but not textured ("Virgin" sample) demonstrate greater hydrophilicity (WCA= 41.2 ± 17.3), underscoring the significant impact of micro-texture on wettability. Figure 50 proposes a plotting of the previous values.

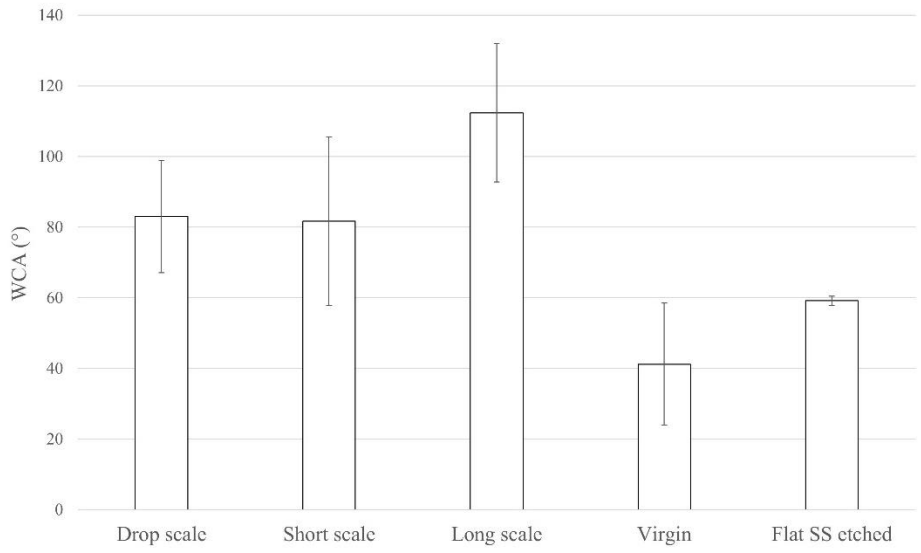

Figure 50. Water contact angle of 3 different fish scale patterns compared to a virgin coupon (no pattern but flat molded stainless)

The designed microtextured surfaces are collectively more hydrophobic than commercial stainless steel plates (etched under similar conditions) or stainless steel plates manufactured through the lost-wax foundry process. However, significant standard deviation is observed for casted surfaces, indicating some degree of inhomogeneity. This inhomogeneity may stem from the random dispersion of dendrites on the surface (refer to Figure 10b) as observed previously. It is worth noting that the dendritic surfaces studied for wetting properties in literature used different dendrite sizes (>1 µm) and substrate materials (gold, silver, copper) compared to our work, making direct comparisons challenging [278–280], In our work, the impact of microtexturation on

wettability is clear, as the dendritic surface alone exhibits hydrophilicity. It is not possible to fully comprehend the separate contribution of 3D printed microtexture and the dendritic texture formed during solidification on surface wettability. A surface solely with 3D printed microtexture and without the additional dendritic texture due to solidification could be manufactured.

An increasing roughness is supposed to increase the contact angle. Here the etching is unveiling the stainless steel grains, which will induce second-order effects in the wettability [281] leading to a more hydrophilic surface. Chemically, a stainless steel surface exposed to hot acidic solution will more likely form chromium trihydroxide ($Cr(OH)_3$) which is more likely to enhance hydrophilic behavior due to the H-bonds formation [282]. Further chemical analysis of the surface could be an interesting outlook to have a better understanding of the surface chemistry. For now, there is no clear evidence that the surface chemistry contributes more than the surface morphology to the apparent microtextured sample hydrophobicity.

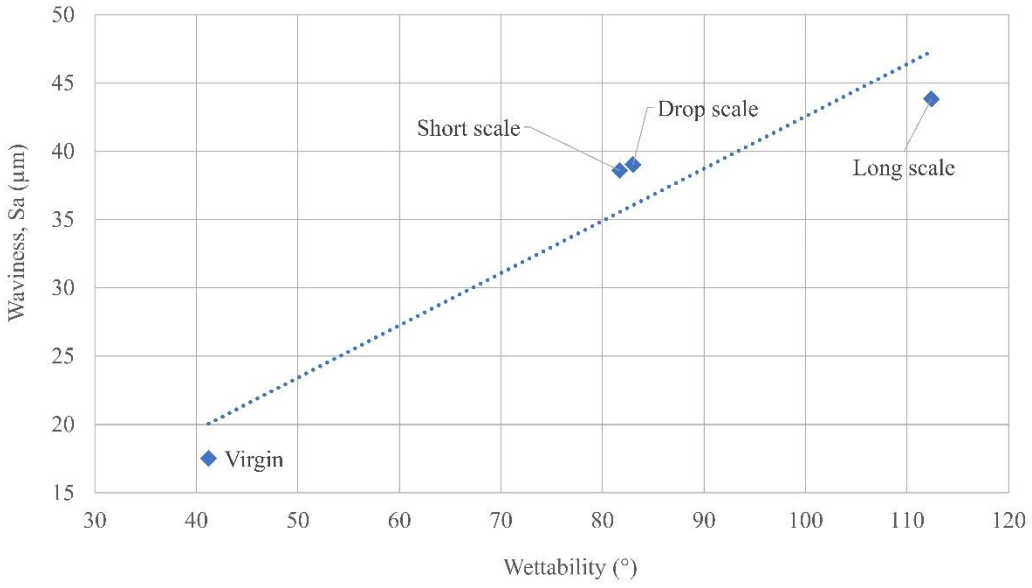

Figure 51. Comparison of the water contact angle with the surface waviness mean values for the different patterns

The parallel between surface waviness and wettability has already been studied by other research groups. Misyura & al. compared these two parameters through laser textured substrates but there is no clear link between them [283]. In addition, the surface chemistry or surface free energy has been considered. The same conclusion was drawn by Lugscheider & al. when they tried to identify a correlation between different multiple physical vapor deposition (PVD) coatings over the same substrate [284]. Wettability and waviness can even be differentiated and considered as separate parameters like Bogacz & al. did to assess the impact of each parameter in the fouling of a laminar flow [32]. In the present work, the rougher a surface is, the higher the WCA is. An attempt of linear correlation between waviness and WCA is featured on Figure 51. However, the trend needs to be considered carefully because both the wettability and the waviness possess wide standard deviation values.

5 Conclusion

In this section, we have explored the innovative concept of bio-inspired microtexturing on stainless steel. This was achieved through the integration of Digital Light Processing (DLP) and vacuum-assisted investment casting. The focus was on creating intricate patterns, reminiscent of different fish scales and honeycombs, on surfaces made from 100% recycled stainless steel. Despite the technical complexities associated with stainless steel investment casting at a millimetric scale, our work has demonstrated its feasibility.

The process involved in this work was investigated, with particular attention to the loss of detail through various stages of investment casting. This was quantified using waviness measurements, providing valuable insights into the limitations and potential improvements of the process. An important discovery in our research was the presence of an oxide layer on the as-cast austenitic stainless steel. An acidic treatment was employed to remove this layer, revealing a dendritic microstructure underneath. This microstructure, combined with the printed microtextures, endowed the surfaces with a notable hydrophobic property.

A significant takeaway from this research is the validation of controlled microtexturing on stainless steel. While the process is indeed complex and resource-intensive, it represents a significant step forward in the field of metallic additive manufacturing. This opens up new possibilities for creating varied and customizable hydrophobic stainless steel structures with high practical value.

The hydrophobic behavior of the microtextured stainless steel surfaces obtained in this section could be enhanced with a coating. The aim of this coating would be to add a nanotexture on top of the microtexture. As explained from the example of plants leaves in the first chapter, the combination of asperities at multiple scale can result into superhydrophobic behavior, the so-called *lotus leaf effect*. The following section will be dedicated to the nanotexturation of the stainless steel substrates.

Chapter 4: Stainless steel functionalization by atmospheric pressure plasma polymerization

1 Introduction

In the previous section, hydrophobic stainless steel surfaces have been manufactured. The metallic substrates fabricated have been analyzed and possess a microtexture that presents interesting wettability properties. To reach higher levels of hydrophobicity, it is however necessary to add another level of complexity in terms of architecture. In the first chapter, the hierarchical size distribution of asperities and objects from micro to nanoscale was shown as a crucial factor to improve the hydrophobicity. In the current section, the study will focus on the nanotexturation using atmospheric pressure plasma polymerization (APPP) of organosilanes.

As mentioned in the first chapter, hydrophobicity and hydrophilicity describe how a drop of water behaves when in contact with a solid substrate [29]. The angle formed at the liquid/solid interface characterizes the wettability of a liquid over a specific surface. In the case of liquid water, if the contact angle is under 90°, the surface is hydrophilic [40]. For an angle between 90° and 150°, the surface is considered hydrophobic [121,285]. Above an angle of 150°, the surface is considered as superhydrophobic or ultrahydrophobic [286,287]. Superhydrophobic and ultrahydrophobic are similar terms that can be differentiated by the water contact angle measurement. For the superhydrophobic surface, a water contact angle can be measured but not in the case of ultrahydrophobic surface, as the drop will systematically go off. A superhydrophobic surface is generally architectured at a microscale and/or a nanoscale [288,289]. Not only the surface texture affects the wettability but also the surface chemistry. The presence of oil or hydrophobic functions can enhance the hydrophobicity of a surface [17,290]. The creation of this type of surface has been inspired by the structure of plant leaves [47]. One of the most renowned example of hydrophobic leaf structure is the lotus leaf [44]. The idea of impregnating the surface by a lubricant also comes from nature. From the fishes' skin mucus [291] to the nepenthes' pitcher [50,64], a fair number of natural surfaces have improved their "water sliding ability" through lubrication.

Consequently, mimicking the structure and the chemistry of organic surfaces has become a serious challenge for modern materials science [292]. Water-repellency for a metallic substrate can have a different purpose because the presence of water can be an issue, especially for metallic materials where water can be a vector of corrosion [293], fouling [21] or bacterial contamination [294]. Not only liquid water but also ice formation can constitute a problem in aeronautics [295]

and food industry [296] over metallic surfaces. Some superhydrophobic surfaces have shown promising anti-icing results [25].

To manufacture this kind of surfaces on metallic substrates, two different strategies can be used. The first is a *top-down* one, which consists in removing material from the substrates. It can be done mechanically (polishing or grinding) [195], physically (laser texturing) [193] or chemically (etching) [121,122]. The interest of these processes resides in the roughness creation that can be paired with a chemical functionalization or oil infusion [17,66,297]. The second strategy is *bottom-up* and encompasses adding material to the existing substrates. It can be a coating, nanoparticles growth, plasma or vapor deposition (chemical or physical) [79]. Both strategies have been explored during the past decades to manufacture more and more complex surfaces. Although this strategy is effective at the laboratory scale, the inherent loss of material, time-consuming techniques or large amount of chemicals used are obstacles to an industrial upscale. In a greener approach, the reduction of material loss and chemical use has become a significant issue for modern processes. The nanotexturing process that will be presented in this section is part of the bottom-up strategies. APPP presents multiple advantages regarding surface hydrophobization: the amount of precursor necessary is limited and no solvent nor any vacuum system are required [116,298–301].

In the present work, following the microtexturing approach presented in the previous section, a closer look will be given to the nanotexturation process. Stainless steel substrates have been microtextured through a process associating polymer additive manufacturing and vacuum assisted casting. The microtextured surface is nanotextured thanks to the APPP of two different organosiloxane precursors: hexamethyldisiloxane (HMDSO) and 1H,1H,2H,2H-perfluorooctyltriethoxysilane (pFOTES). The wettability was assessed through a goniometer and water contact angle (WCA) measurements. Observations of the surface were made with numerical microscopy (NM) and scanning electron microscopy (SEM). All experimental conditions and results obtained are presented in the next section.

2 Atmospheric pressure plasma

The substrate manufacturing process has been detailed in the previous section. Roughness and wettability of the raw surfaces are also described.

2.1 Generalities about plasma surface treatments

The word plasma designates an ionized gas, a high energy state firstly described as "radiant matter" by Sir William Crookes in 1879 [302]. He was trying to put a name on "the particles constituting the cathode stream" in a vacuum. For him, it was nor liquid, nor solid and nor gaseous but consisted in "something smaller than the atom". The word plasma came later with the work of Irving Langmuir, after almost five decades in 1928, when he published "Oscillations in ionized gas", an article about mercury low-pressure arc [303]. His eminent workmate, Levi Tonks revealed later that the word *plasma* probably takes inspiration from the blood plasma [304]. It can be considered as the fourth state of matter because a phase transition is possible when energy is brought to a gas. This state appears to be completely different from the three other states of matter: solid, liquid and gaseous (see Figure 52).

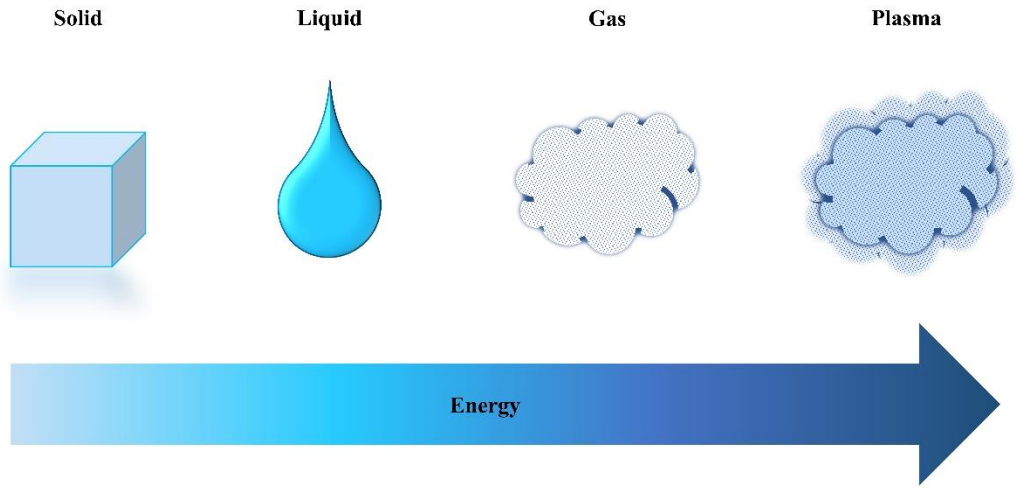

Figure 52. Four states of matter

Since the early discoveries of the early 20th century, different plasmas have been discovered or identified. They can be differentiated in two categories: natural plasma and artificial plasma. Multiple natural phenomena, like lightening or aurora borealis (see Figure 53 (a) and (b)) are examples of natural plasmas [305,306]. A part of the atmosphere of Earth, called the ionosphere, is made of dense plasma and located between the mesosphere and the exosphere (see Figure 53 (c)). The gas of this atmosphere layer is continuously ionized by the solar wind [307]. In the universe, 99% the objects observable, such as the stars, are in a plasma state [308]. Mankind has succeeded to reproduce this state of matter in various controlled environments and is able to utilize it for different purposes.

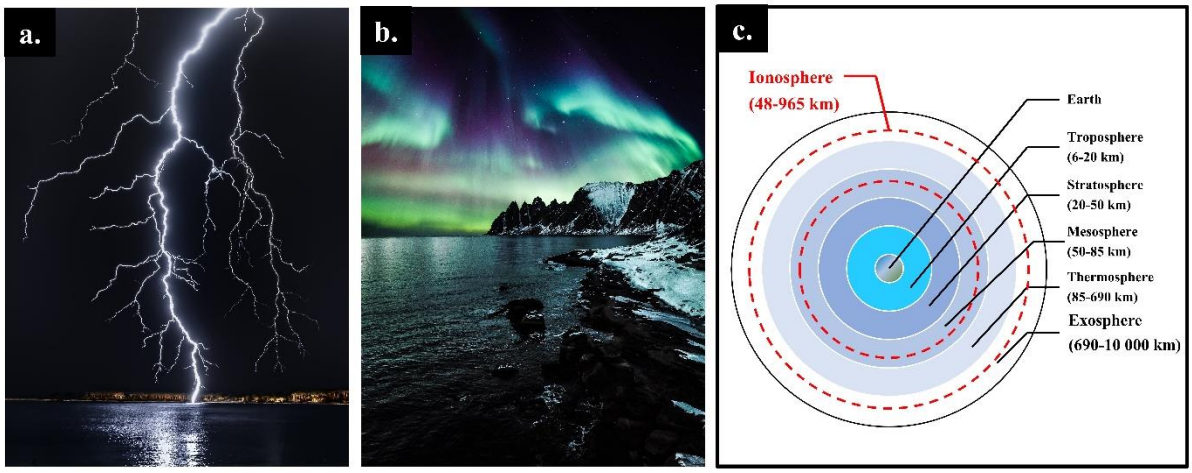

Figure 53.Examples of natural plasma: (a) lightnings (b) aurora borealis and (c) representation of the ionosphere among the different layer of Earth atmosphere

The knowledge about plasma has evolved from pure observation of an ionized gas phenomenon to an entire family of applied technics that can propel a satellite [309], produce energy [310], weld metallic materials [311] and even modify materials surface [299]. This last category will be the one that interests us in the rest of this section.

Nowadays, the different plasma processes can be used to modify a material. Two different types of plasmas exist to modify a surface: the low-pressure (LP) cold plasma and the atmospheric pressure cold plasma (APP) [312]. These technologies can have different purposes:

- *Plasma treatments*: The use of inert gases (helium or argon) under a plasma form can generates reactive ions or radicals at the substrate surface that will be more reactive. This enhancement will create a better adhesion for coating or dye molecules [313,314]. Other techniques like plasma enhanced chemical vapor deposition (PECVD) or physical vapor deposition (PVD) or atomic layer deposition (ALD) can directly generate controlled thin layers of material (oxides, nitrides, sulfides or tellurides) on a substrate to change its chemical, physical and/or mechanical properties [315–319].
- *Plasma etching*: The plasma being a source of high energy, more than modifying the substrate matter, it can also remove material from its surface. It can be used in different applications such as microelectronics or surface engineering as a nanofabrication process for hard materials like metals, oxides or even diamond [320,321].
- *Plasma polymerization*: The association of molecules and a plasma can induce a polymerization. It can occur in two different ways: the plasma state polymerization or the plasma-induced polymerization [322]. In the first case, the monomers are in a plasma state under vacuum and will form a layer of polymerized material. In the other case, the monomers contained in a condensed phase (liquid or solid) are polymerized thanks to a plasma. The molecules injected in the plasma discharge are fragmented by the ions contained in the plasma, and recombined into a "plasma – polymer". It can be done using a large diversity of molecules to manufacture films and/or nanoparticles [323]. Through this particular polymerization method, not only organic monomers can be polymerized but also inorganic molecules such as Hexamethyldisiloxane (HMDSO) [324–326].

The following part will focus on plasma polymerization. The nanotexture added to the microtextured stainless steel will be obtained through an atmospheric pressure plasma polymerization of organosiloxane precursors. This process is interesting for different reasons:

- it is a solvent free process,

- the amount of precursor used is small (5 mL maximum for one layer over 20×20 cm^2),

- it is executed at atmospheric pressure,

- the carrier gas (industrial grade nitrogen) is not expensive and safe,

The principle and apparatus are presented in the following section.

2.2 APPP principle

The plasma polymerization was carried out using an ULS Lab-Scan (Ultra-Light System), i.e. an atmospheric pressure plasma torch (APPT) from Acxys Technologies (France). The surfaces were treated in two steps: activation and functionalization. The activation is done by passing the torch four times over the surface to clean the surface from organic residue and remove the thin oxide layer. The functionalization was carried out with two different precursors, hexamethyldisiloxane (HMDSO) and 1H,1H,2H,2H-perfluorooctyltriethoxysilane (pFOTES) (as shown on Figure 54). The precursors are nebulized into the plasma thanks to a syringe pump NE-300, New Era Pump System (United States) at flow rate of 60 g/h for HMDSO and 20 g/h for pFOTES. The carrier gas (N2) flow rate is 6L/min for HMDSO and 2 L/min for pFOTES. Both steps were processed with D = 20 mm from the surface, 1550 W of power (frequency = 80 kHz) and industrial nitrogen flow of 60 L/min.

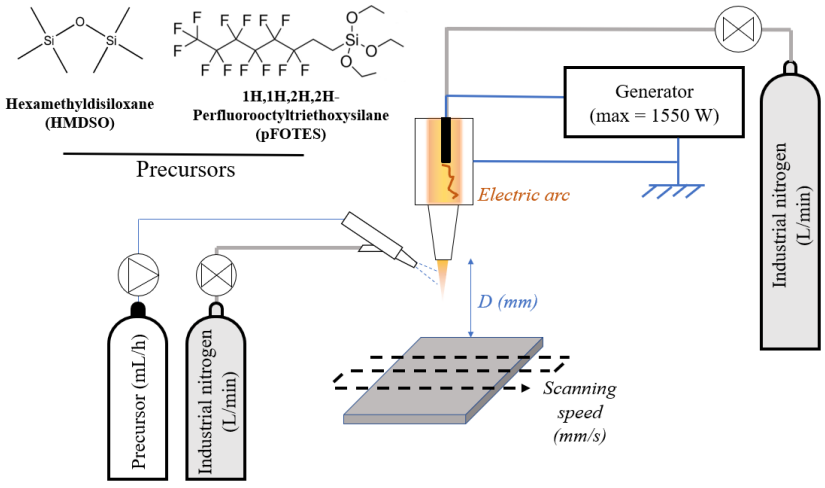

Figure 54. Atmospheric pressure plasma setting

The chosen parameters were explored during previous work in the laboratory [103]. The parameters are known to be effective on commercial flat 316L stainless steel substrates. On a flat surface, in the same conditions, only the association of the two precursors (HMDSO and pFOTES) can result into superhydrophobic surfaces.

2.3 Coating's morphology and composition

The objects formed during this coating step were observed using scanning electron microscopy (SEM). The observations were first carried out on a non-coated sample and secondly on a coated sample to compare the structure at the nanoscale. On Figure 55, pictures (a) and (b) are made at a microscale magnification, and the difference is subtle.

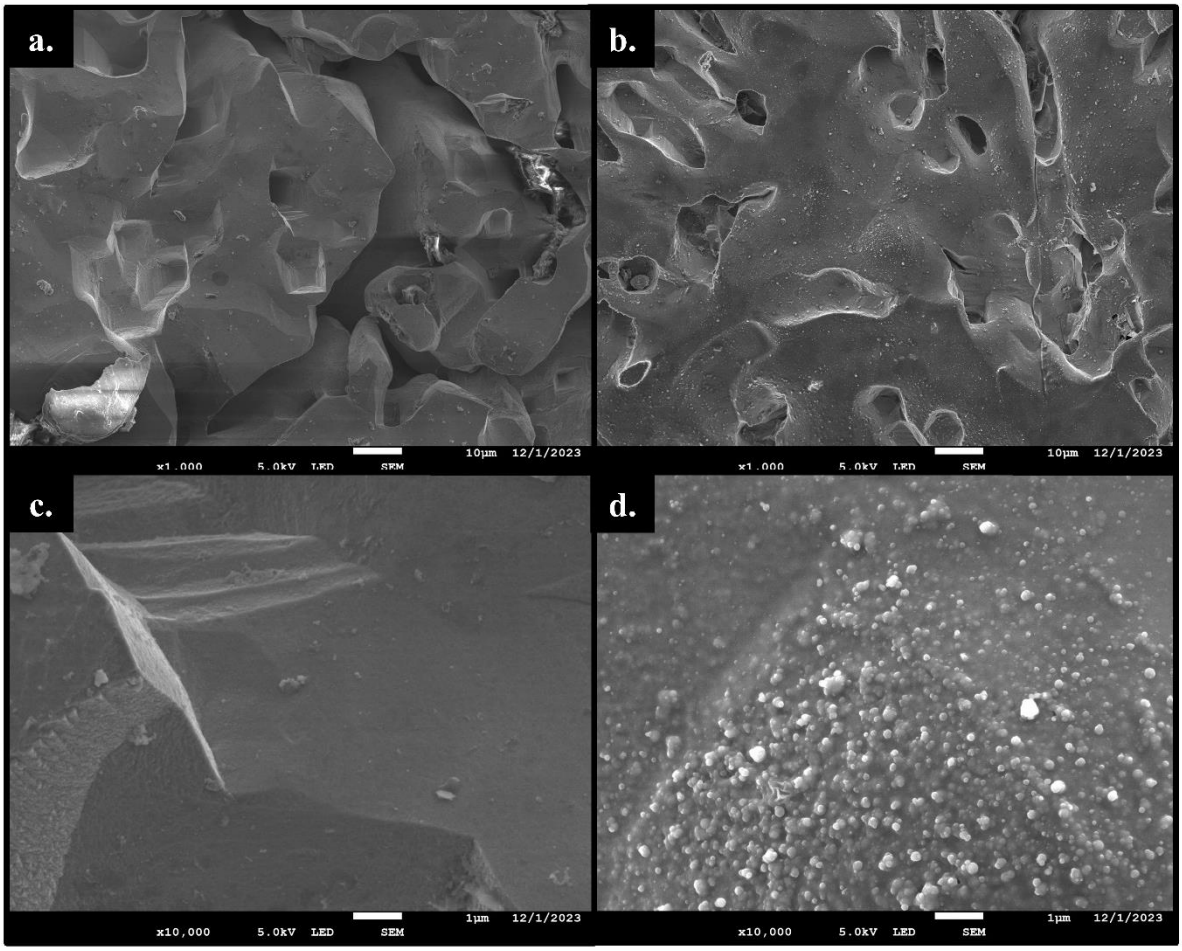

Figure 55. SEM observation of the textured stainless steel from the foundry process (a) & (c) uncoated and (b) & (d) coated.

The surface presents more *"dusty"* objects observable on the coated sample. A higher magnification (x10,000) gives a more precise idea of the coating morphology (the scale bars are representing 1 µm). The coating seems to be composed of nanometric spherical beads (see Figure 55, (d)). At this scale, an EDS analysis would not be pertinent as the interaction sphere created by the electron beam is way larger (a few micrometers large at 15 kV) than the particles observed. The chemical composition cannot be estimated quantitatively using SEM-EDS at this scale. Nevertheless, a qualitative chemical analysis is possible and preferable because the surface is highly rough. As it is schematically explained on Figure 56, the high roughness and the substrate composition can interfere a lot with the EDS analysis. The light elements Kα signal coming from

the coating at the bottom of the roughness profile will be absorbed by the substrate which contains heavier elements.

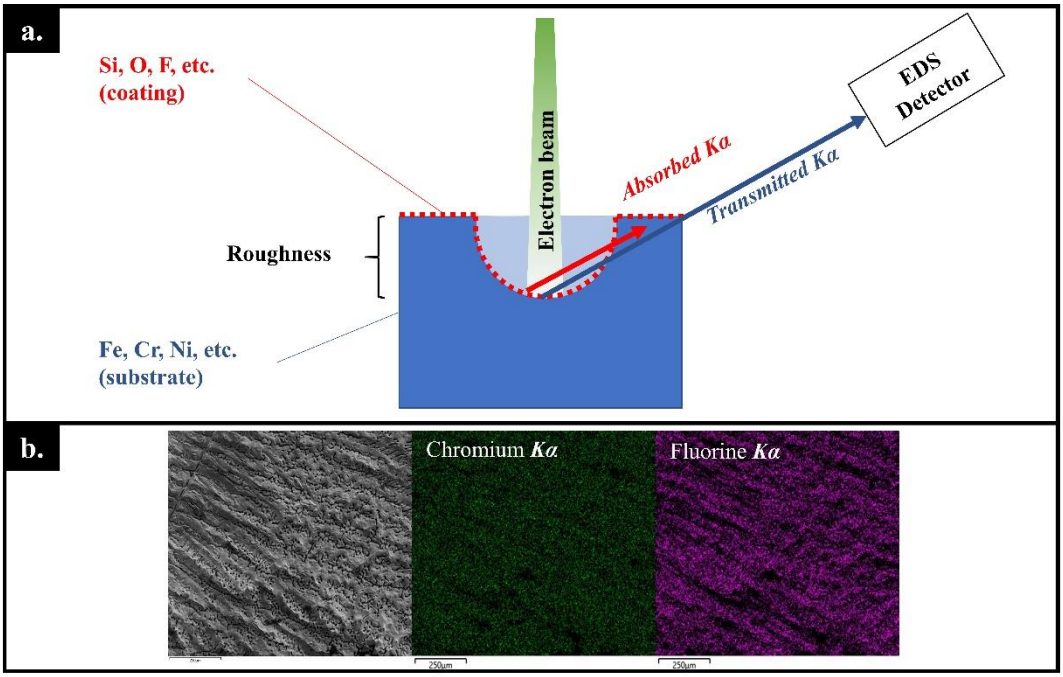

Figure 56. (a) Schematic explanation of how the roughness interferes with EDS analysis of a coating on a rough surface (b) EDS difference between a heavy element like Chromium and a lighter element like fluorine

EDS mapping can give an idea about the coating composition. A Fourier-transform infrared spectroscopy (FTIR) is more commonly used to determine the different chemical bonds created during a coating step. Nonetheless, the high roughness of the stainless steel substrate could not enable the collection of a proper spectrum.

The expected composition of the coating should be directly related to the original atomic composition of the molecule. In the case of HMDSO, the coating should increase the amount of silicon, carbon and oxygen at the surface. Because the coating is not conductive, a thin layer of carbon has been deposited at the surface to allow the observation. Silicon and oxygen are two light elements that can be easily found on a stainless steel surface. For these reasons, the HMDSO coating has not been investigated in terms of composition. On the contrary, the polymerized pFOTES possesses fluorine functions that could be easily detected and attributed to the coating

formation. In the following table (see Table 10), two macroscopic EDS mappings are compared before and after pFOTES APPP.

Table 10. EDS mapping comparison between a coated and an uncoated stainless steel textured sample

Sample	Elements	Fe	Cr	Ni	O	Mo	Si	Mn	F	Other undetected elements
Textured stainless steel without coating	(% at.)	62.5	17.2	8.1	8.6	0.9	1.2	1.0	0	0.5
	(% at. /Fe % at.)	1	0.28	0.13	0.14	0.01	0.02	0.02	0	0.01
Textured stainles steel with APPP coating	(% at.)	47.3	13.2	6.5	14.3	0.8	4.3	0.9	12.6	0.1
	(% at. /Fe % at.)	1	0.28	0.14	0.3	0.02	0.09	0.02	0.27	0

In addition to a simple atomic percentage distribution of the different elements, a normalization based on the iron content has been made to see if a drastic change is remarkable. The pFOTES molecule is atomically composed of silicon, carbon, oxygen and fluorine. The carbon content is ignored because, as mentioned before, the sample has been coated with a thin carbon layer to become conductive. The amount of the three other elements increases sharply, fact that confirms the deposition of a polymerized nanostructured pFOTES. On Figure 57, a SEM image of the pFOTES coating at high magnification is presented to highlight the nanometric size of the polymerized particles. Consequently, after this deposition step, the stainless steel substrate is textured at multiple scales (millimetric, micrometric and nanometric). This high complexity should theoretically be associated to hydrophobic properties. In the next section, the wettability of the manufactured surface will be questioned.

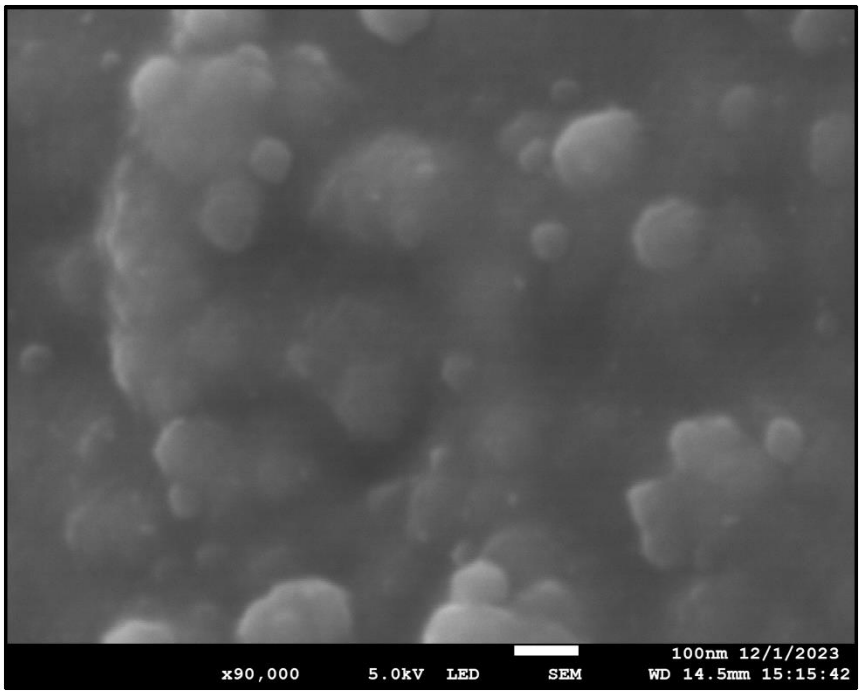

Figure 57. SEM image of the pFOTES coating on a microtextured stainless steel substrate at high magnification

3 Wettability improvement

Without coating, the three different patterns obtained in the previous chapter present three different roughness and 3 different WCA. Table 11 gathers the WCA measurements performed on the different substrates (commercial 316L stainless steel, molded stainless steel without pattern ("virgin") and 3 different stainless steel molded patterns). The molded microtextured surfaces are more hydrophobic than a stainless steel surface molded without patterns (Virgin). On the contrary, 316L stainless steel coupon with a 2R finish has a mean WCA higher than that of two of the molded patterns (drop-like scale and short fish scale).

3.1 HMDSO atmospheric pressure plasma polymerization

Due to its surface geometry, the long scale pattern displays natural hydrophobicity without any coating (WCA: 112°). Nevertheless, after an APPP of HMDSO, the WCA mean values increase for all the molded samples more than the commercial stainless steel coupons. Except for the short fish scale pattern, the WCA values of the molded patterns coated with plasma polymerized

HMDSO are between 101.7° and 109.1° which is higher than the commercial stainless steel covered with the same coating (94.4°). The hydrophobicity of the 2R SS coupon and of the long fish scale pattern slightly decreases but it is important to note the high standard deviations that translate the heterogeneity of the different samples. Every molded sample, microtextured or not, seems to be more homogeneous after coating as the standard deviation decreased. The importance of the texture is slight but noticeable, the mean WCA of the 2R SS and virgin sample are less than that of the microtextured samples.

A previous study had been conducted by the team on flat stainless steel, that reported a higher contact angle for HMDSO APPP (107.7 ± 3.1) [103]. Two things differ from this previous experiment: the HMDSO injection system used was different and the bare substrate contact angle was 20° higher than in our case. This difference can be caused by the initial surface state and the precursor injection system.

3.2 pFOTES atmospheric pressure plasma polymerization

The pFOTES APPP leads to different results on the stainless steel molded surfaces: no water drop was able to remain on the surface, they systematically went off the surface. The same experiment was carried out with a polytetrafluoroethylene (PTFE) needle to reduce the adhesion between the water drop and the needle, but the surfaces were still ultra-hydrophobic.

This result is interesting when compared to the commercial 2R stainless steel coated with the same process, which presents a WCA of 133°. Similar results (138.8 ± 3) were reported earlier by *Saget et al*. on stainless steel for pFOTES APPP [103]. However, to obtain ultra-hydrophobic flat stainless steel samples, these researchers had to combine a layer of HMDSO and one of pFOTES. In our case, one layer of pFOTES on the micro-textured samples is enough to reach the same result.

Table 11. Water contact angle comparison of 2R stainless steel and the textured surface (with and without pattern), without coating, coated with plasma polymerized HMDSO and plasma polymerized pFOTES (N/D: not determined, which means the angle was not measurable).

	Wettability (°)		
	Without coating	HMDSO coating	pFOTES coating
2R SS	101.7 ± 2.5	94.4 ± 3.4	133.3 ± 3.6
Virgin	41.2 ± 17.3	101.6 ± 7.7	N/D
Drop like fish scale	78.0 ± 23.9	107.1 ± 8.8	N/D
Short fish scale	81.7 ± 23.9	118.6 ± 11.22	N/D
Long fish scale	112.4 ± 19.6	109.1 ± 12.6	N/D

The APPP pFOTES coating seems to be particularly interesting in terms of wettability. One interesting observation has been made during SEM imaging of APPP pFOTES coating over the microtextured stainless steel, the particle formed are mostly present on the highest points of the roughness (see Figure 58). The high standard deviation for the non-coated indicates a lack of homogeneity coming from the surface morphology or chemistry. After coating, the different standard deviations are smaller, which indicates a homogenization thanks to the coating. Even if the standard deviation decreased after coating, the values are still more significant than a flat 2R stainless steel coupon. The lack of homogeneity could affect the wettability properties, the stability or the performances of the coated material.

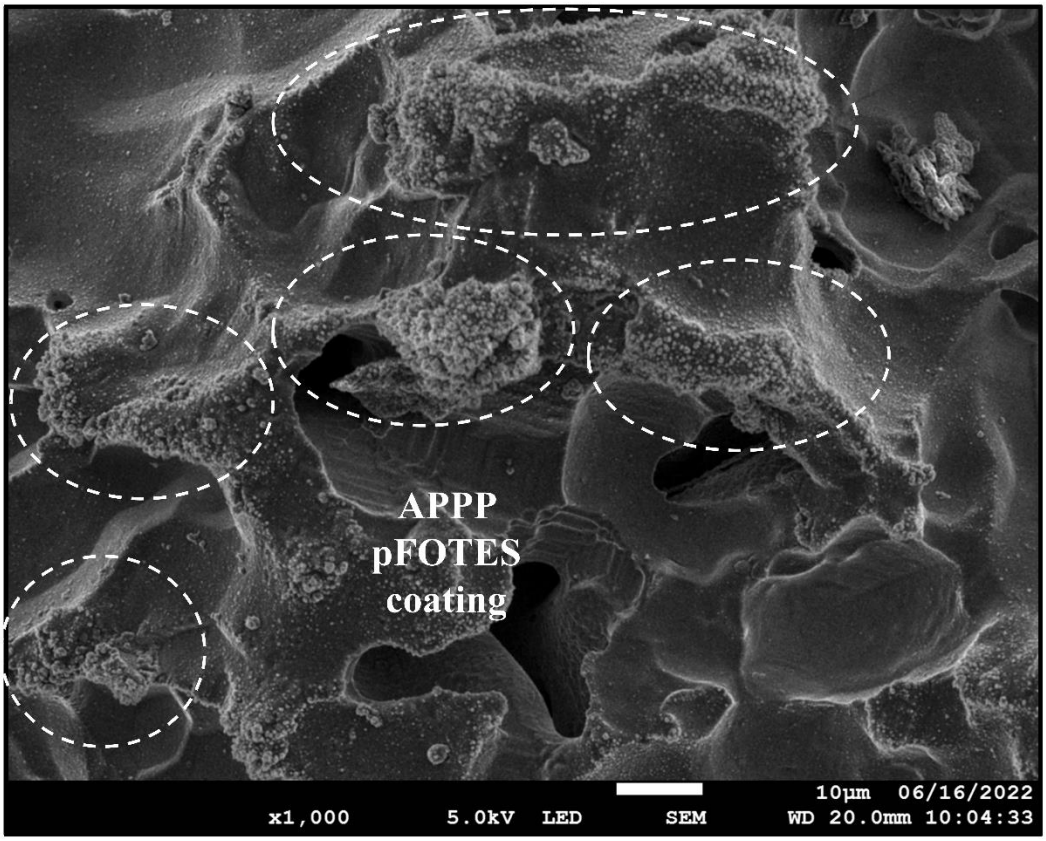

Figure 58. Inhomogeneous aspect of the particles formed during the APPP pFOTES coating

In the next section, the stability of the coating along time will be determined by measuring the WCA after 6 months ageing.

Preliminary remark: due the small quantity of samples available for both the ageing test and the application tests (antifouling and anti-icing) the different textures have been mixed and sorted out by coating. Gathering the samples into two categories (textured + HMDSO and textured + pFOTES) was possible because the wettability properties were considered similar enough for a coating over a microtextured surface. From 6 samples of each microtexture, we obtained 18 samples of each coating available for the next tests.

3.3 Durability of the coated samples

The ageing was carried out at room temperature in a closed container.Three different microtextures were not coated to take into account the ageing of the metallic material alone. A set of 2R and microtextured surfaces were coated with HMDSO and pFOTES and their WCA was measured 24h after surface treatment. The samples were then set aside during 6 months before measuring the WCA a second time. Both WCA values (t+24h and t+6 months) are compared in Table 12.

Compared to the measurements done before ageing, all the values evolved, showing the unstability of the coating along great period of time. Not only the coating, but the microtextured material also is evolving: the WCA values under 100° seem to increase and the values above 100° seems to decrease. The convergence of these WCA values could be the proof of chemical or structural surface evolution over the metallic microtextured surface. This assumption is weak because of the diversity of sample available. The difference cannot come from the number of samples as the ageing experiment is conducted with almost the same number of specimens per condition than before ageing (4 sample per condition before and 3 after ageing). One argument in favor of homogeneization is the standard deviation decrease for every non-coated microtextured stainless steel surface. Before ageing, standard deviations were significantly great compared to the actual WCA values. After ageing, these values are decreasing. For the APPP coated samples, 2R and microtextured stainless steel surfaces, a WCA decrease is observed. Along a great period of time, the process is not stable. A more periodic study of this ageing with closer measurement along time would be interesting to understand the ageing kinetics. The WCA evolution coupled to a chemical quantification of the surface functions (Fourier transform infrared spectroscopy or x-ray photoelectron spectroscopy for example), could lead to a better understanding of the mechanism responsible for this decrease.

Table 12. WCA measurement after 6 months ageing at room temperature at atmospheric pressure

Wettability (°)			
	Without coating	**HMDSO coating**	**pFOTES coating**
2R SS	101.7 ± 2.5	94.4 ± 3.4	133.3 ± 3.6
Virgin	41.2 ± 17.3	101.6 ± 7.7	N/D
Drop like fish scale	78.0 ± 23.9	107.1 ± 8.8	N/D
Short fish scale	81.7 ± 23.9	118.6 ± 11.22	N/D
Long fish scale	112.4 ± 19.6	109.1 ± 12.6	N/D
Wettability after 6 months ageing (°)			
2R SS		84.9 ± 2.8	121.0 ± 5.05
Drop like fish scale	98.6 ± 8.5		
Short fish scale	99.3 ± 2.9		
Long fish scale	105.2 ± 10.3		
Textured + HMDSO		100.2 ± 8.8	
Textured + pFOTES			121.0 ± 5.0

The instability along time aside, a superhydrophobic behavior has been observed for some of the APPP coated microtextured surfaces. It could be interesting to assess the usefulness of this property. As mentioned in the first chapter, 316L stainless steel is a common alloy in the food industry and keeping them clean or easy to be cleaned is a critical issue. The superhydrophobic behavior of the material designed previously could be interesting in that case.

4 Applications and properties

The surfaces manufactured in this work present two main advantages. They are highly rough and superhydrophobic. In the literature, as mentioned in chapter 1, this type of surface can be used for different purposes, for example anti-fouling, anti-icing, anti-corrosion or even SLIPS manufacturing. During this section, the properties of these surfaces will be explored.

4.1 Anti-fouling property

Fouling is an accumulation of unwanted substances or deposits on a surface. It can occur in a chemical reactor, during industrial processes, in the sea or in a pipeline [327,328]. Different types of fouling can be distinguished depending on the nature of the deposit. For example, marine bio-fouling refers to the accumulation of microorganisms, algae, plants or small animals on surfaces immersed in water. It can also occur on ship hulls, underwater structures or water intake systems [98]. Dairy fouling also appears in industrial food processes such as pasteurization or other dairy product transformations [329,330]. This particular type of fouling will be discussed in the following part.

4.1.1 Dairy fouling formation

Raw milk is a complex biological fluid essential for young mammal growth. Mainly composed of water, it also contains lipids, proteins, amino acids, vitamins and minerals [331]. The most abundant proteins in bovine milk are caseins, accounting for 75 - 80 %. The 20 % left are whey proteins like β-Lactoglobulin (β-Lg), α-Lactalbumin (α-La), bovine serum albumin, immunoglobulin and lactoferrin [332]. The proteins contained in the milk are heat sensitive and can be degraded when heated up. The pasteurization process, an essential step in the dairy transformation industries, designed to eliminate harmful bacteria in food particles and beverages, was initially developed by the French chemist and biologist Louis Pasteur in 1864 [333]. It involves subjecting every particle of milk or milk product to elevated temperatures for a brief period within appropriately designed and operated equipment, extending the refrigerated shelf life to two weeks or more. This method uses heat to eradicate potentially harmful micro-organisms, ensuring the safety of various food items such as milk, milk products, eggs, and fruit juices [330,334,335].

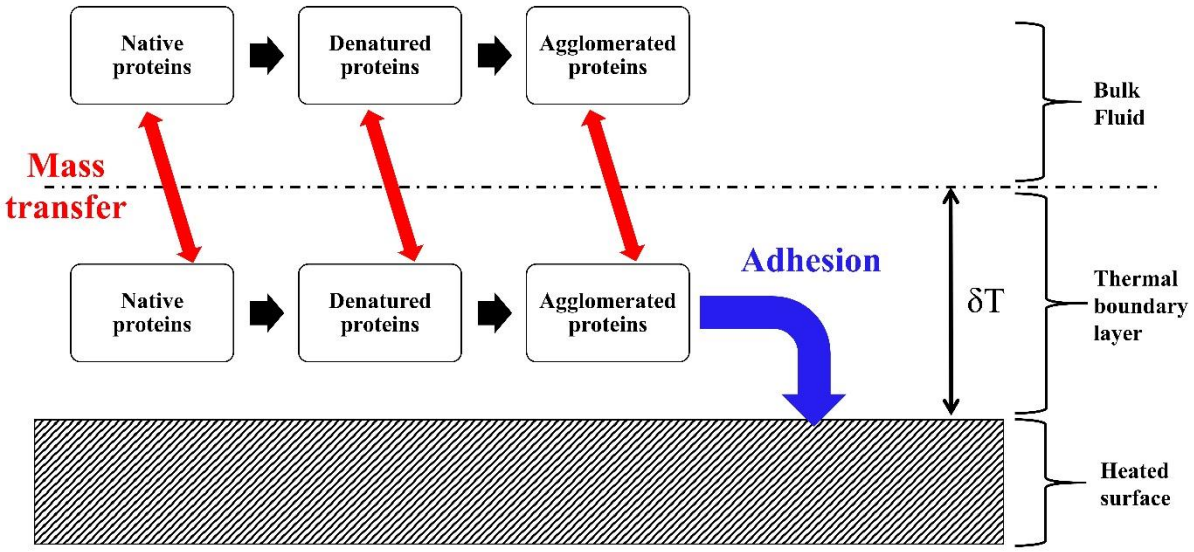

Figure 59. Fouling formation mechanism simplified (from Georgiadis and Macchietto, 1998)

One of the side effects caused by the thermal treatment of the raw milk is the protein denaturation [335]. Even if the exact fouling mechanism is not completely understood, the chemical composition of the undesired deposit suggests his origin. Mainlytwo types of dairy-fouling exist: the mineral fouling or the protein fouling. The first one, also called type B fouling or milk-stone, contains 30 - 40 % of minerals, 50 – 70 % proteins and 4 – 8 % of fat. This type of fouling is hard, compact and can be obtained at high temperature (above 110 °C). The second one, also called type A fouling, contains around 50% of proteins, mainly β-Lg [329,336]. A simplified mechanism of the type A fouling is proposed on Figure 59. First, the native β-Lg in the bulk fluid turns into a denatured β-Lg. There is a constant protein mass transfer between the bulk fluid and the thermal boundary layer for every step of the protein denaturation.. The protein mechanism aside, the concentration of minerals, especially calcium dissolved in the milk, plays a major role in fouling formation [337].

Dairy fouling is an important issue because the accumulation of this un-desired layer constitutes a biohazard [338]. Moreover, in a heating system such as a pasteurization unit, for example heat exchanger plates, the additional fouling may affect the pressure system and the plates

thermal conductivity. These two parameters generate a higher energy consumption [335] and cleaning in place procedures also account for important water, detergents and energy consumption.

4.1.2 Dairy fouling elimination by cleaning-in-place procedures

Dairy fouling elimination can be made chemically using sodium hydroxide (NaOH) solution washes. The alkaline washes are associated to multiple running water and slightly acidic solution washes to evacuate most of the fouling [327]. Those classical cleaning in place (CIP) processes consume a large amount of water, which increases the environmental impact of dairy industry.

Three different parameters are involved in the fouling formation: the milk composition, the pasteurization conditions and the exchange surface properties. In order to avoid fouling formation, it could be possible to change the milk composition or modify the pasteurization process. Nevertheless, none of those two solutions are easy to play with. The last parameter, i.e. the exchange surface properties, can be modified to avoid or to reduce the fouling formation through two mechanisms: anti-fouling and fouling release [338,339]. On one hand, an anti-fouling surface will inhibit the residue formation. On the other hand, a fouling-release surface can let the fouling deposit but will ease the cleaning process. The two mechanisms are schematically explained on Figure 60. In the literature, these two phenomena are well known to occur on superhydrophobic surfaces [17,21,292,328,340,341]. Earlier in this chapter, surfaces with superhydrophobic properties were developed. The possible anti-fouling properties of these surfaces will thus be tested in the following section.

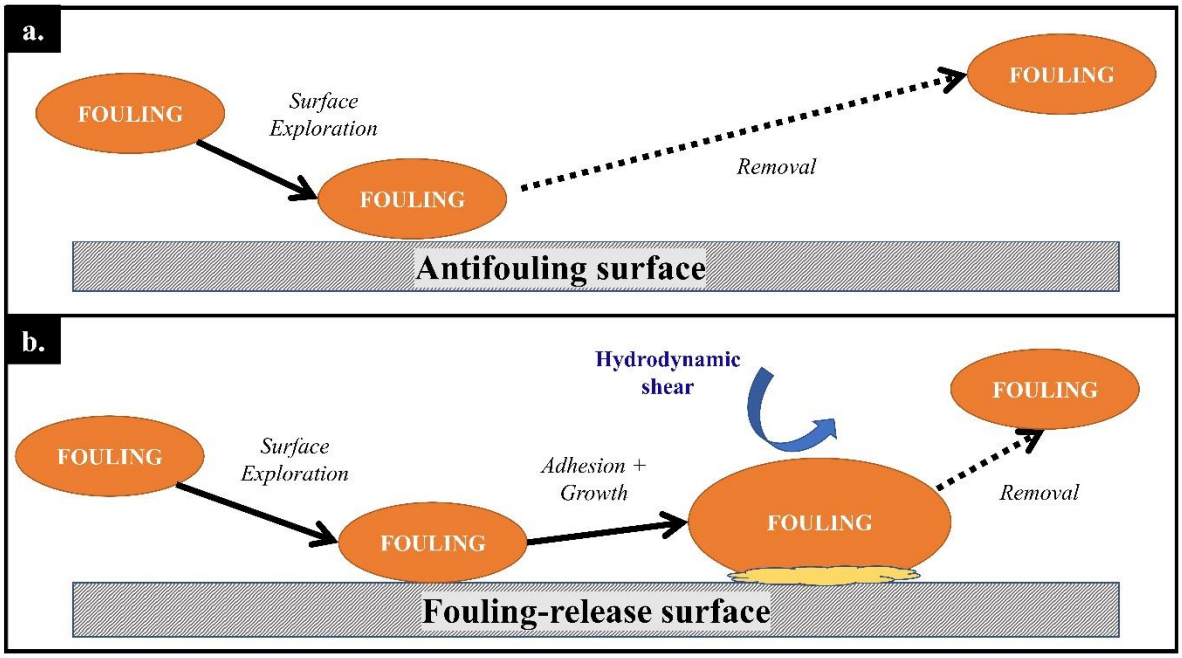

Figure 60. Schematic explanations of the anti-fouling and fouling-release mechanisms

4.1.3 Anti-fouling and fouling release performances

Surface fouling is emulated thanks to a semi-pilot pasteurization system where the raw milk is replaced by a model fluid to get more repeatable results. As β-Lactoglobulin (β-Lg) and calcium constitute the primary components of dairy fouling deposits, a model fluid was prepared using whey protein concentrate (WPC) powder (Promilk 852 FB1, 80% protein in dry state, Ingredia, France) and $CaCl_2$ (Sigma Aldrich). The model fluid consists of a 1% WPC solution, and the calcium concentration is adjusted to 100 ppm by the addition of $CaCl_2$. This specific calcium concentration was selected to prevent overpressure or blockage in the plate heat exchangers (PHEs) while maximizing the duration of the fouling runs. A total of 325 liters of model fluid were prepared for each fouling run. WPC and $CaCl_2$ were first rehydrated and dissolved separately under stirring in reverse osmosis water for 1.5 hours, followed by a 30-minute mixing period. The preparation of the model fluid was conducted at room temperature.

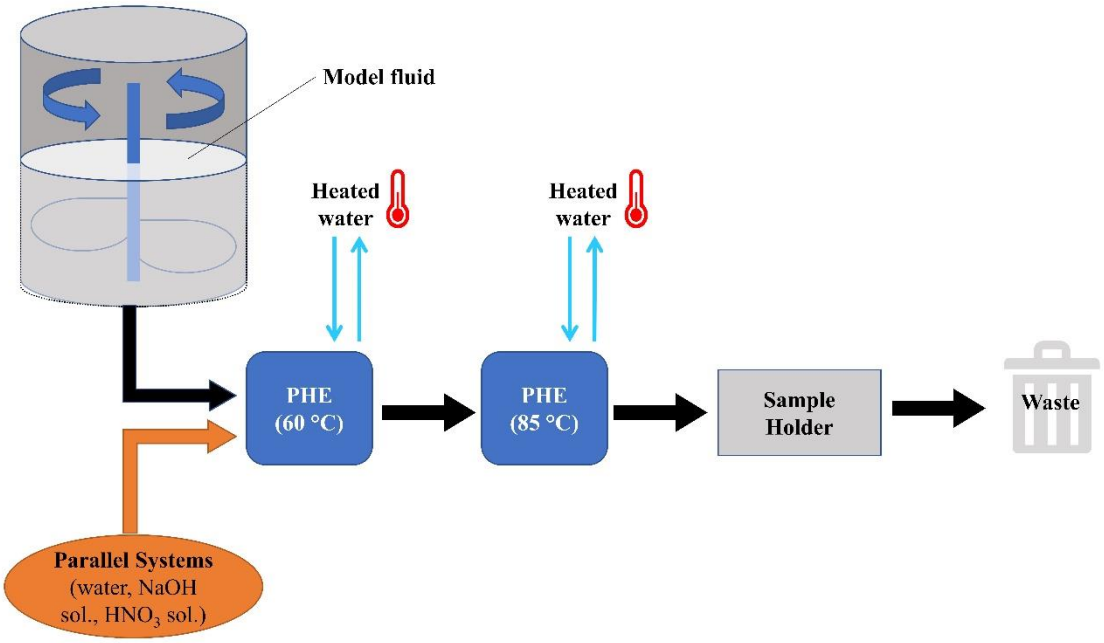

Figure 61. Simplified representation of the pasteurization pilot plant

Fouling tests were conducted using a scaled-down version (approximately 1/10) of an industrial pasteurization system. This system includes a stirred tank, a volumetric pump (PCM, France), and two plate heat exchangers (V7 models from Alfa-Laval-Vicarb, France) arranged in a counter-current configuration. PHE 1 consists of 10 passes, each with a single channel, and preheats the treated fluid from room temperature to 60°C. PHE 2 consists of 5 passes, each with a single channel, and raises the model fluid temperature to 85°C, a commonly used temperature in traditional pasteurization processes. In both plate heat exchangers, the space between consecutive plates is 3.93 mm. The samples were placed at the end of this system to be in contact with the hot processed model fluid. A simplified representation of the pasteurization system is proposed on Figure 61.

The samples tested are those developed in this last chapter, i.e. microtextured and plasma-coated substrates. During this test, two main aspects were compared: the influence of the surface roughness and of the coatings. Table 13 gathers the results of this test performed on three different roughnesses (from the less rough to the roughest surface: mirror-like, 2R and microtextured

surfaces) and 2 different APPP coatings (HMDSO and pFOTES). The fouling test was conducted the day after coating to minimize the ageing impact. The samples were fouled for one hour with hot model fluid and rinsed for 20 minutes with hot water (both at 85 °C), the rinsing step allowing to evaluate the fouling-release properties of the surfaces. The samples were dried for one week in a cold storage (dried air with temperature maintained around 4 °C). They were observed with an optical microscope and the results are presented in Table 13.

The mirror-like surfaces, i.e. the less rough surfaces, industrially polished by the manufacturer as flat as possible, did not demonstrate good anti-fouling properties. A non-neglectable amount of dried milk protein remained in the case of both the non-coated and HMDSO-coated mirror polished surfaces. Similar behavior was observed for the 2R coated samples, which are 2 mm thick 316L stainless steel coupons. The non-coated and HMDSO coated 316L samples were covered with residual milk proteins (white deposit). The color is completely different compared to the sample before fouling. The 2R sample coated with pFOTES is more punctual, and not uniform as it is for the mirror like or the 2R samples. Unlike the 2R and the mirror-like samples, the color of the substrate did not change after fouling for the microtextured samples. In the same way, the mirror-like surface coated with the pFOTES is less affected but not completely clean. The punctual aspect of the dairy fouling is however stronger over all the textured surfaces. The dried milk proteins seem to be inlaid into the surfaces' crevices.

These results are not surprising regarding previous studies conducted by the group a couple years ago. Zouaghi et al (2018) demonstrated that the surface roughness is a favorable ground for fouling development compared to mirror-like surfaces. Effect that can be minimized by a coating presenting fluorinated functions at the surface.

The fouling experiment conclusions are not in favor of the coated microtextured materials. Since organic compounds such as milk proteins seem to have an affinity with the surface roughness, maybe this drawback in terms of fouling can be turned into an advantage. As mentioned in the first chapter of this manuscript, a rough surface can become a slippery liquid-infused porous surface (SLIPS) when impregnated with a lubricant. In the next section, the lubricant retention capacity of this surface will be explored. Because of the small quantity of sample available, the lubricant retention study has been reduced to only a few surfaces: non-coated 2R stainless steel, 2R SS with

APPP pFOTES, non-coated microtextured SS surfaces and microtextured SS surfaces with APPP pFOTES. These four conditions will help in understanding the individual contributions of each surface component: the material, microtexture, and the APPP coating.

Table 13. Different surfaces (mirror-like, 2R and microtextured) after a fouling test

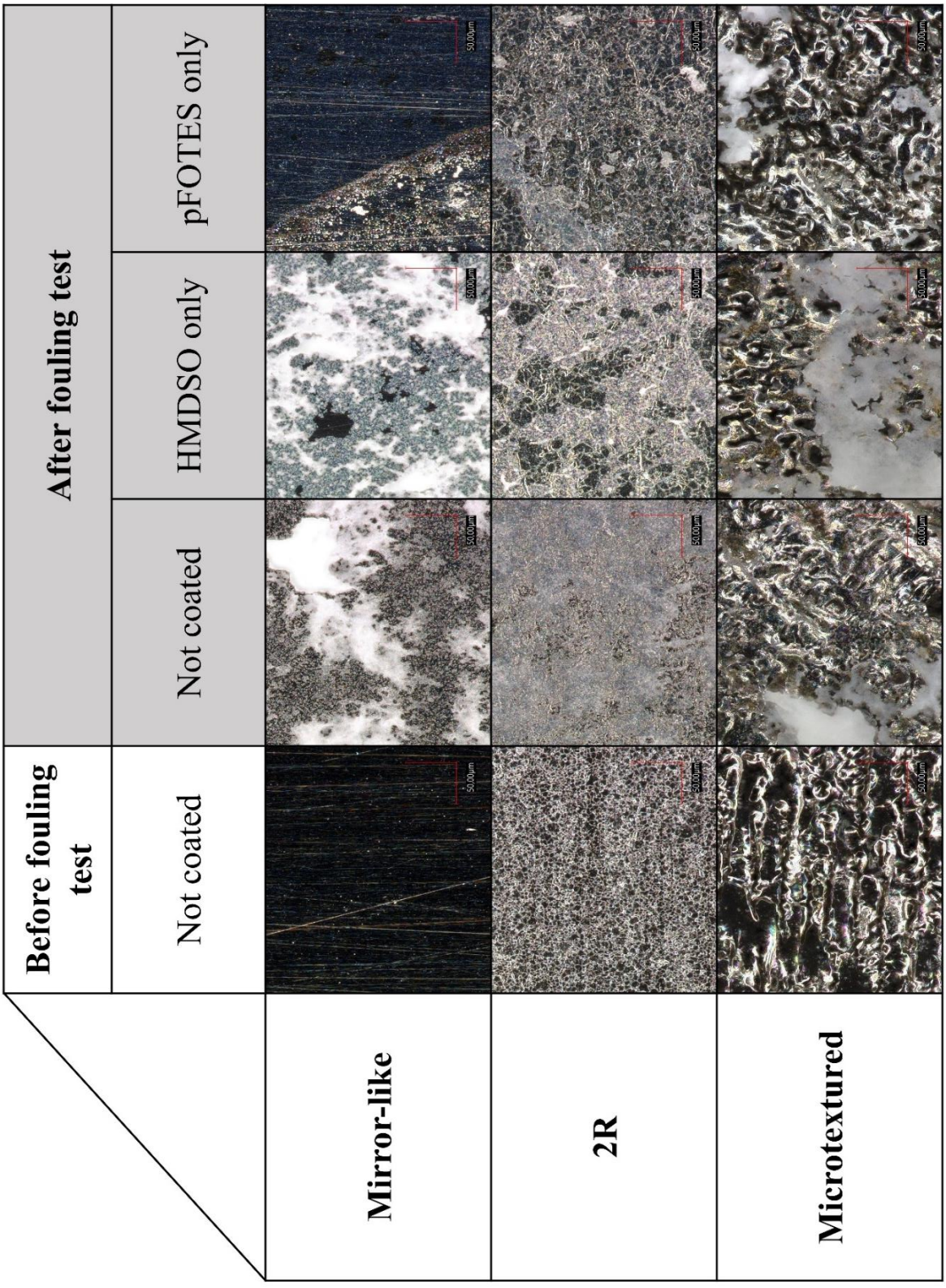

4.2 Lubricant retention property

The lubricant impregnation, represented on Figure 62, is divided in three steps: the flat impregnation, the first adsorption and the second adsorption. The adsorption steps are executed with the samples placed vertically in absorbent paper, in an oven set at 37.5 °C. The main interest is to remove as much lubricant as possible with the absorbent paper. At this temperature, coconut oil is more than 10 °C above its melting point (around 25 °C) [67].

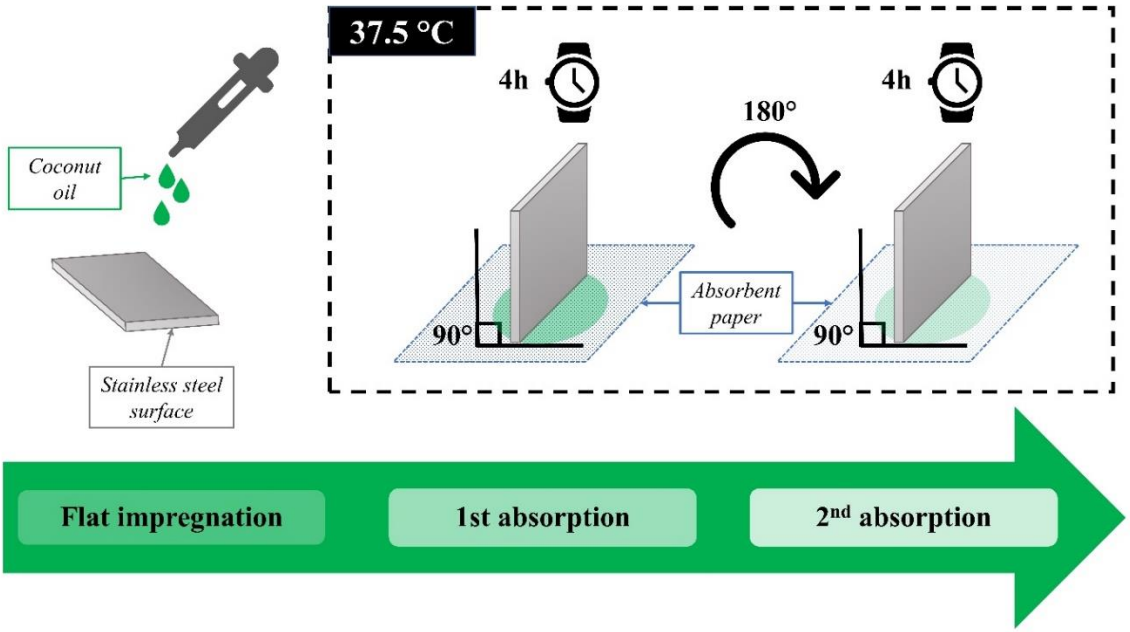

Figure 62. Lubricant impregnation procedure for stainless steel surfaces

The sample weight is measured before and after to determine the amount of lubricant deposited on the surface. The lubricant retention experiment was conducted with coconut-oil on four type of samples:

- non-coated 2R stainless steel
- 2R SS with APPP pFOTES

- non-coated microtextured SS surfaces
- microtextured SS surfaces with APPP pFOTES

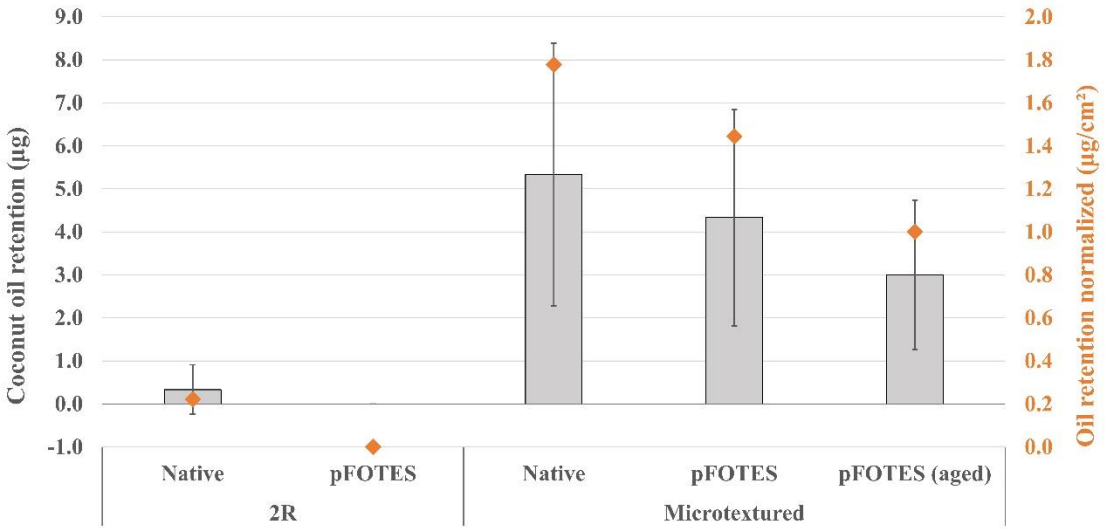

Figure 63. Coconut oil retention measurements (bar chart). Weight of oil measured after impregnation in µg, (dot chart) superficial oil retention (µg/cm²)

On Figure 63, the coconut oil retention has been assessed and presented with two key values: the amount of oil retained (grey bar chart in µg) and the amount of oil retained divided by the surface area (dot chart in µg/cm²). Effectively, the microtextured surfaces present a better lubricant retention than the non-textured stainless steel surfaces. Concerning the APPP pFOTES coating, it seems to have slightly decreased the oil retention for the 2R samples and the microtextured surface. This result is surprising because in the literature, substrates are commonly treated with fluorinated molecules comparable to pFOTES before lubricant impregnation to improve the oil retention [67]. Even if the pFOTES coated microtextured surface is less impregnated than the non-coated microtextured sample, it is much more impregnated than both the 2R samples (coated and non-coated). Previously, the coating ageing has been mentioned. With coconut oil successfully infused in the microtextured material, the surface can be considered as a LIS. It could be considered as a SLIPS if a low sliding angle is measured during a dynamic WCA measurement. Further

characterization would be necessary to determine if the oil is permanently trapped in the structure or would be gone after a single wash.

As coconut oil melting temperature is relatively low, it would not be interesting to test its performances in a hot system such as the pasteurization process from 4.1. Application tests where the lubricant remains in the solid state could be interesting to explore. In the literature, LIS and SLIPS are known for their anti-icing properties, which are low temperature systems [342]. It could be insightful to characterize the wettability behavior of these surfaces at low temperature. The next subsection will assess the anti-icing efficiency of different stainless steel surfaces to understand the contribution of each constituting element: the roughness, the APPP pFOTES coating and the oil impregnation. The microtextured surface will be compared to 2R stainless steel, uncoated and APPP pFOTES coated, with and without coconut oil impregnation.

4.3 Anti-icing property

The formation of frost and ice on equipment surfaces in winter environments can lead to economic, energy, material, and even human losses. The accumulation and adherence of ice can occur on various structures, including airplanes, ships, power lines, offshore oil platforms, and wind turbines, among others [295,296,343]. Managing and preventing such ice-related issues is crucial in mitigating the associated risks and ensuring the safe and efficient operation of these diverse structures. Advanced anti-icing technologies and proactive measures play a pivotal role in addressing these challenges and enhancing overall operational resilience in cold climates.

4.3.1 Ice formation and issues related

Ice theoretically requires two elements to be formed: water and low temperature. Pure water at atmospheric pressure (1 bar) is supposed to freeze at 0 °C. It is a phase transformation of liquid (or vapor) water into the solid state. The process of water freezing represents a spontaneous phase transition, wherein the reduction in temperature is accompanied by a decrease in the system's Gibbs

free energy [344]. As presented on Figure 64, when clusters of molecules (or embryos) attain a specific size (the critical size) and achieve stability, they act as nuclei, initiating growth and leading to the formation of ice crystals [345]. Multiple factors can favorize the ice nuclei formation, for example, a rough surface, nanoparticles from air pollution, etc. [346–348]. Nucleation is commonly triggered by the presence of air pollutants and foreign particles, that can lower the free energy at the interface, consequently enhancing nucleation potential [344].

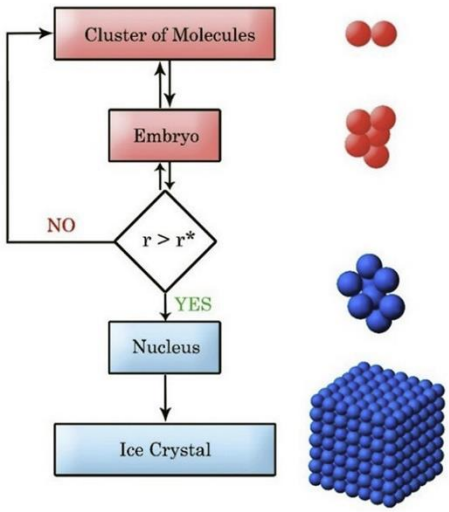

Figure 64. Illustration depicting the formation of ice crystals, where r and r represent respectively the radius and critical radius of an embryo, from Azimi Yancheshme et al. (2020)*

The accumulation of ice can have several adverse effects on various aspects, particularly in the aviation and structural engineering domains. In aviation, the aerodynamic performance of an aircraft can be significantly compromised due to ice build-up on its surface. This accumulation not only alters the airflow around the aircraft, potentially leading to decreased lift and increased drag, but also poses a safety risk [295]. Moreover, in structural engineering, the additional load caused by the weight of accumulated ice can potentially lead to damage or structural failure. This is particularly concerning for buildings, bridges, or any other structures that are exposed to freezing conditions. The increased weight from ice accumulation can exceed the designed load capacity, resulting in structural stress and potential damage [349].

Additionally, in various systems such as cooling systems, the components can be vulnerable to damage when ice forms. The formation of ice can obstruct or impair the functioning of crucial components, reducing the efficiency of the system and potentially causing long-term damage [343]. Due to all these reasons, anti-icing and defrosting technologies have become crucial investigation fields to explore. During the last decade, a growing number of scientific studies with different approaches were published targeting ice mitigation [344]. The next section will briefly present them.

4.3.2 Anti-icing strategies

In the literature a few strategies have been reported to minimize ice formation on a solid surface [344,350]. As summarized on Figure 65, the strategies can intervene:

- before the ice formation, when the cold water is still liquid
- during solidification, when the liquid water is freezing to the solid state
- after solidification, when the crystals are already formed

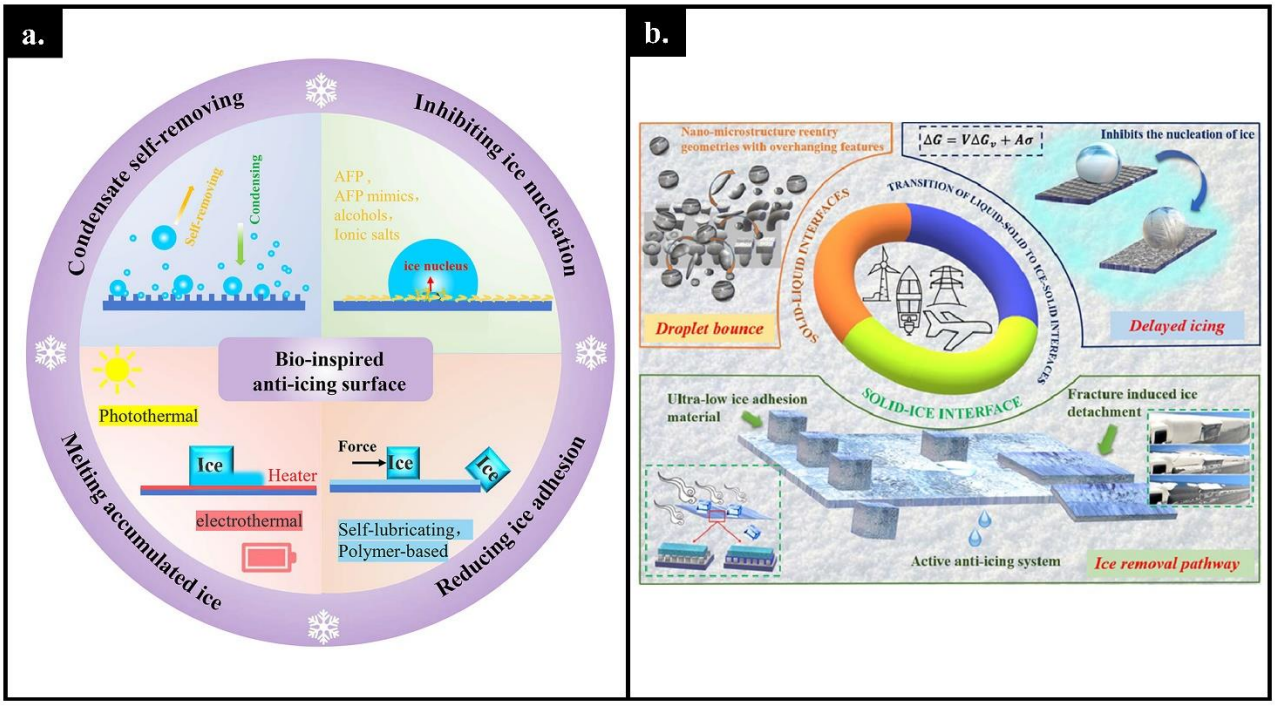

Figure 65. Different anti-icing surface strategies (a) review about bio-inspired technologies from Jiang et al. (2022) and (b) from Zhao et al. (2023)

It is interesting to note that the strategies combating ice formation are similar to the one used against fouling, explained in section 4.1 of the current chapter. Ice crystals and fouling are both undesired deposits. In the literature, there are example of surfaces that demonstrate both properties [351].

The undesired deposit can be avoided by repelling the liquid at the surface thanks to superhydrophobic properties. If it is already formed, surface engineering can ease the elimination step. Nevertheless, recent studies are warning about the link between superhydrophobicity and icephobicity. Superhydrophobic coatings, while limiting water droplet attachment, do not prevent water condensation on their surface. This condensation and subsequent freezing play a key role in macroscopic ice formation. Experimental studies show a freezing front on superhydrophobic surfaces that acts as a seed for attached water droplets' freezing upon contact. Superhydrophobicity slows down, but does not eliminate the condensation and freezing processes [352,353]. The efficiency of this strategy can be assessed through dynamic water contact angle or water drop bouncing over a cooled down surface.

Another strategy consists in the nucleation inhibition (Figure 65a.), which can be executed by grafting molecules with anti-freezing properties directly over the surface. It can be alcohols function, anti-freezing proteins or salts that will delay the icing mechanism. This delay can be in terms of temperature with a lower supercooling temperature or a longer freezing time. The supercooling state is a metastable state at a temperature below the melting point. Nucleation takes place spontaneously in supercooled water, occuringat a nucleation temperature that may vary stochastically below the melting temperature. The ice nucleation temperature in pure water consistently remains below 0°C at atmospheric pressure [354,355].

Two other strategies are focused on ice crystals already formed: ice adhesion reduction and accumulated ice melting (see Figure 65). Ice adhesion reduction is a passive mechanism that can facilitate the ice removal [101]. It is the strategy used for SLIPS, the lubricant layer helps ice sliding. On the contrary, accumulated ice melting is an active ice elimination method that can use photothermal heating or induce fractures to eliminate ice caps.

In this thesis, the surfaces created through the stainless steel foundry process are rough and hydrophobic. Combined to an APPP coating, the SS surfaces are becoming superhydrophobic for a certain period of time. Additionally, the roughness and the bio-inspired microtexture, created through the stainless steel investment casting process, has demonstrated good oil retention properties. In the following section, the main objective will be the anti-icing characterization of the different surfaces created previously.

4.3.3 Anti-icing characterization

The anti-icing characterization proposed in this thesis, is a first approach and is not a complete icephobicity analysis. A complete analysis would include mechanical tests to assess ice adhesion and dynamic water contact angle measurement. The lacks of this study could constitute the next investigation step for future work. In this work, the goniometer mentioned in the previous chapter has been instrumented with thermally isolated chamber containing a Pelletier thermoelectric cooling plate.

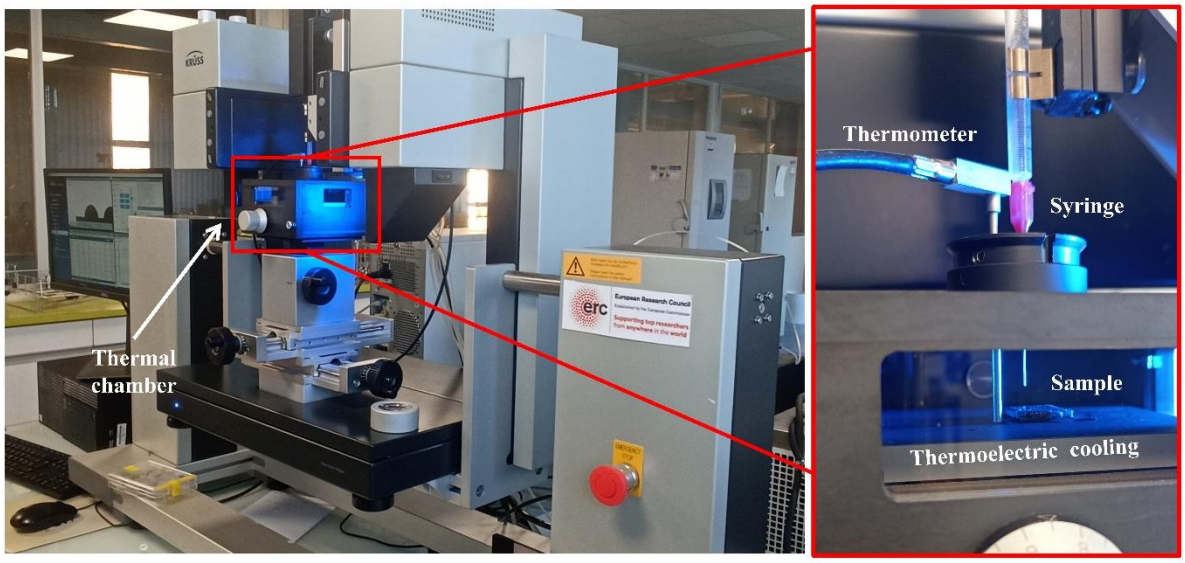

Figure 66. Instrumented goniometer for anti-icing characterization

Thanks to this apparatus on Figure 66, WCA measurement can be done while cooling down the surface. The thermal connection between the sample and the thermoelectric plate is established thanks to a 50:50 ethanol/water solution. A 5 µL water drop is deposited on the analyzed surface preheated at 26 °C. After 30 seconds, a quick surface cooling down is programmed. The goniometer is set up to take one measurement per degree Celsius lost during the cooling between 24 °C and -20 °C. Multiple values are coming out of this experiment:

- the WCA
- the freezing delay
- the supercooling temperature

During this experiment, different aspects of the material were compared. The surface microtexture, the APPP pFOTES coating and the coconut oil impregnation. The combination of the different parameters gives 8 different types of sample. It is important to mention that the ambient humidity was not controlled during the icing tests but estimated between 30 and 35 %. It is also important to highlight the quick cooling down, as it reduces the evaporation influence on the WCA measurements.

The first interesting phenomenon occuring to a water drop during the cooling down is the change in shape. Before freezing, most of the WCA will decrease, mainly because the surface free energy is increased when the surface temperature goes down.

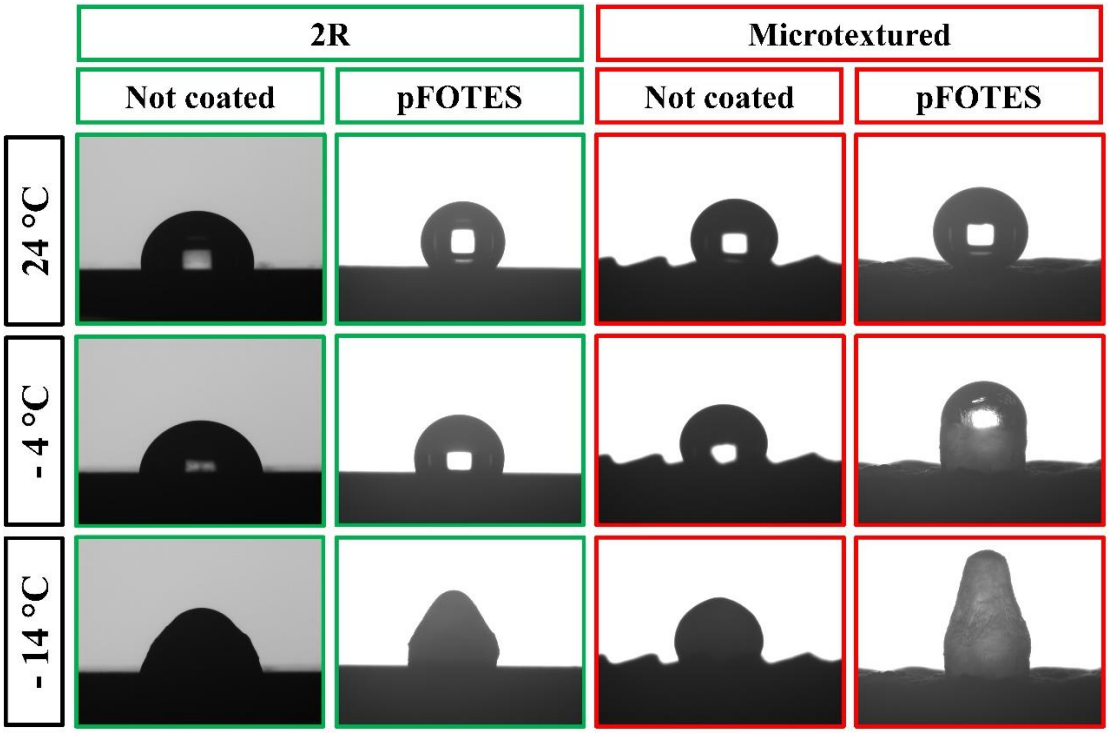

Figure 67. WCA image at 3 different temperature (24, -4 and -14 °C) for 2R and microtextured surfaces with uncoated and coated with APPP pFOTES

Figure 67 represents the evolution of the WCA during the cooling down for 4 types of surface, 2R and microtextured stainless steel, both uncoated and coated. For each surface except the microtextured stainless steel coated with APPP pFOTES, the freezing starts under -4 °C. The WCA slightly changes, it is essential to plot the evolution of the WCA during the cooling down until freezing. Before that, it could be interesting to take a look at a water drop evolution during freezing for the same surface than before, but impregnated with coconut oil. Figure 68 presents this evolution at 4 different temperature (24, 8, -8 and -16 °C). The interesting phenomenon to point out here is how the oil layer is behaving. In the case of the 2R samples (uncoated or APPP pFOTES coated), the oil layer is simply deposited on the surface. At 8 °C, the water drop is no longer

translucent but blurred, especially on the non-coated sample, where the drop is divided in two phases. At this temperature, the coconut oil is solid. The phenomenon is slightly visible on the -8 °C image of the non-coated microtextured sample. Fortunately, it is less visible on the impregnated pFOTES-coated microtextured sample. This observation can be seen as a proof of stronger bond between the surface and the oil thanks to the coating. One of the main issues coming from SLIPS is the lubricant attachment to the substrate and the probable release into the fluid in contact. For now, the stronger bond observed is a interesting remark but would need further investigation to be proved.

The image observations are already giving us different information about the probable anti-icing surface behavior. A closer look to the different key values measured during the cooling down could improve our understanding.

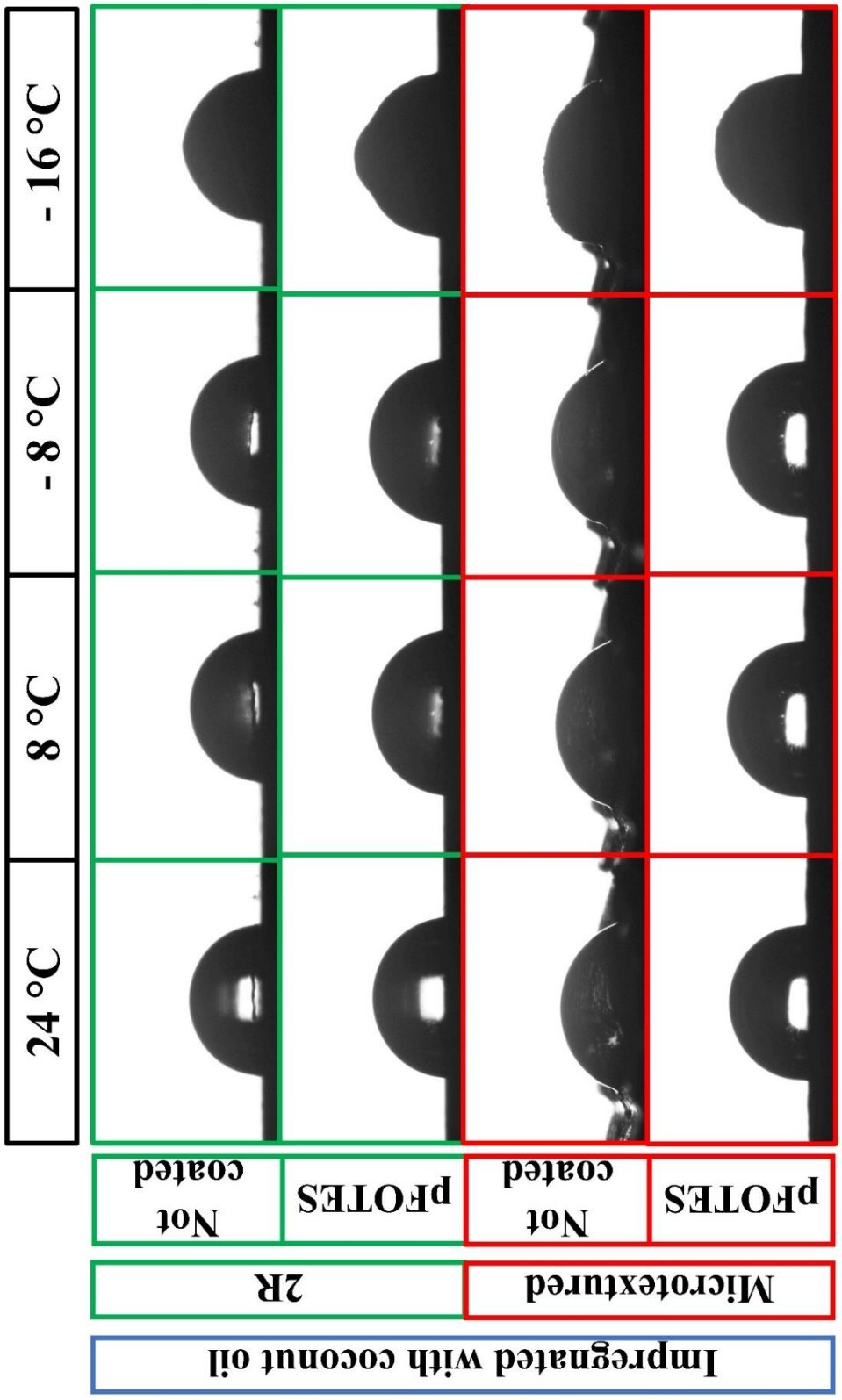

Figure 68. WCA evolution at different temperature (24, 8, -8 and -16 °C) for 4 impregnated samples 2R and microtextured stainless steel (uncoated and APPP pFOTES coated)

For each sample, the cooling speed has been evaluated by plotting the temperature during the cooling down duration. The average cooling speeds for the 2R samples (between 0.16 and 0.19 °C/s) are slightly lower than the microtextured sample cooling down speed (between 0.18 and 0.20 °C/s). As presented on Figure 69, the temperature profiles versus time are similar and evolve the same way, which means the cooling down speeds are comparable for the different samples. The slight difference could not come from difference from the sample thermal conductivity. In chapter 3, the microstructure difference between a thermomechanically processed stainless steel (2R) and as-cast (microtextured) has been highlighted. But no significative differences have been reported, between stainless steel as-cast and thermomechanically processed, because of the manufacturing process and/or the microstructure in the literature [175]. The only difference left that could explain the different thermal speed is the size of the sample, more precisely, the surface in contact with the thermoelectrical plate. In the case of the as-cast microtextured samples, the contact surface is 300 mm² and 150 mm² for the 2R samples. Having a greater exchange area could explain these slight differences.

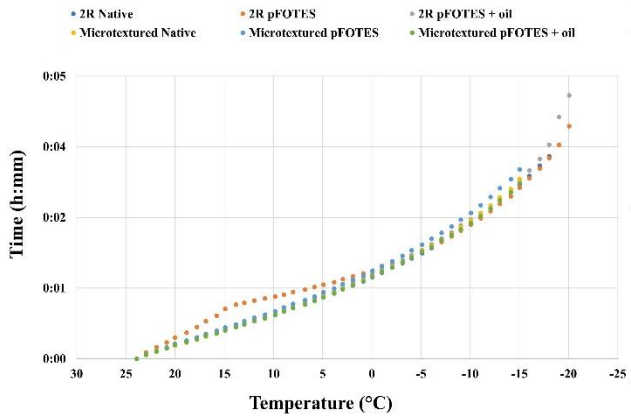

Average cooling down speed (°C/s)		
2R	**Native**	0.19 ± 0.011
	Native + oil	0.18 ± 0.011
	PFOTES	0.18 ± 0.013
	PFOTEs + oil	0.16 ± 0.008
Microtextured	**Native**	0.20 ± 0.021
	Native + oil	0.20 ± 0.008
	PFOTES	0.20 ± 0.016
	PFOTES + oil	0.18 ± 0.017

Figure 69. Evolution of the temperature along time during the cooling down for different samples with the average cooling down speed

The measurements of the cooling down speed of the different samples are becoming even more interesting when we compare it to the supercooling temperature and the freezing delay. The supercooling temperature as mentioned in subsection 4.3.1, is a temperature below the melting point where phase transition will occur spontaneously. The freezing delay here is the duration measured between 24°C and supercooling temperature, when the water drop becomes solid.

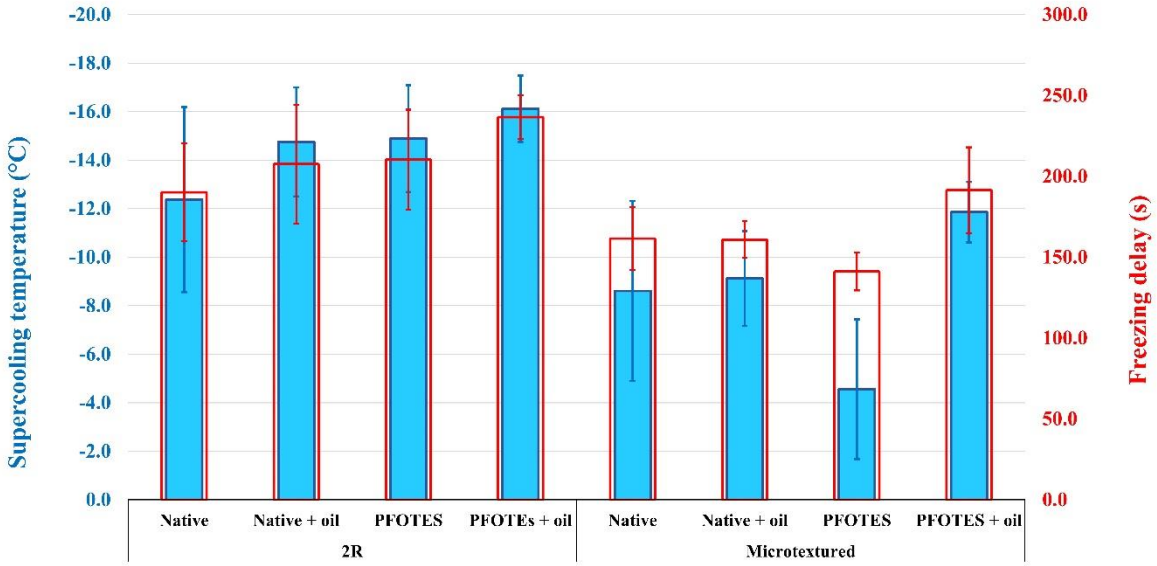

Figure 70. Supercooling temperature and freezing delay for 2R and microtextured sample, influence of the APPP pFOTES coating and the oil impregnation

Figure 70 represents the supercooling temperature and the freezing delay. It compares the 2R to the microtextured samples, the coated to the uncoated (native) and the impregnated to the not impregnated samples. As mentioned in subsection 4.3.1, the surface roughness improves ice nucleation, that occurs earlier on the microtextured surfaces than on the 2R sample. For the 2R sample, the coating and the oil impregnation are both increasing the supercooling temperature and the freezing delay. The improvement brought by the oil impregnation is even more significant for the microtextured pFOTES samples. The supercooling temperature and the freezing delaying for the oil impregnated APPP pFOTES sample are comparable to the 2R native stainless steel values.

From the icing point of view, it is an interesting result to have a rough surface with surface modifications (coating + impregnation), that compensate the initial roughness drawback. Another aspect that could be interesting to look at is the evolution of the WCA along temperature. From the optical observation made earlier, a WCA decrease can be expected during the cooling down. Is this decrease affected by the APPP coating and/or the oil impregnation?

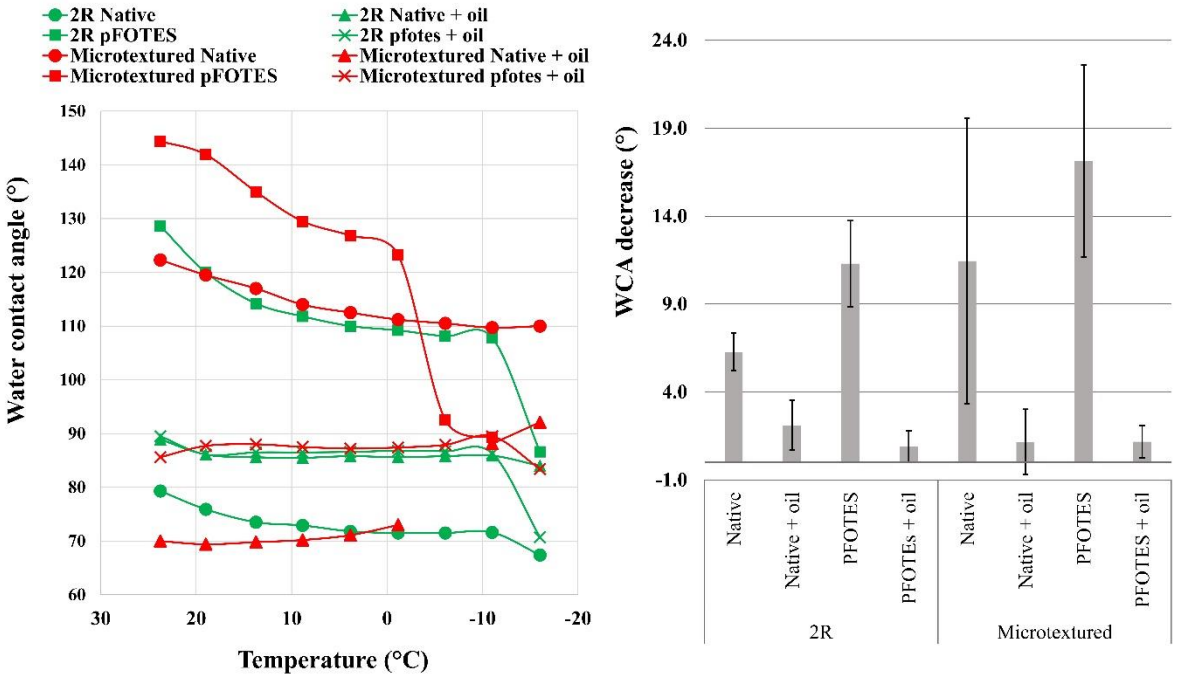

Figure 71. Water contact angle evolution during surface cooling down (left) and Subtraction between the initial WCA (at 24 °C) and the final WCA (1 °C before solidification) (right)

On Figure 71, the WCA of different samples are plotted during the cooling down. For the hydrophobic samples at 24 °C (for example microtextured SS coated and uncoated without oil impregnation or 2R SS APPP pFOTES coated), the angle decrease is particularly high. This phenomenon is attenuated but noticeable at smaller angles (for example 2R native not impregnated). This angle decrease can be due to the moisture condensation at the surface increasing with the low temperature [356]. For every impregnated sample, the WCA decrease is strongly weakened. The impregnated samples with the best contact angle and the smaller decrease along temperature are the microtextured APPP pFOTES coated surfaces. Recent studies concerning LIS

and SLIPS for anti-icing application have already reported their efficiency, especially for properties not explored in the present work such as ice mechanical adhesion or self-healing [357,358]. Further characterizations, such as impregnation longevity or adhesion tests will be required to confirm the anti-icing interest of the microtextured surface developed.

5 Conclusion

In this chapter, several surfaces were manufactured from the bio-inspired microtextured stainless steel substrates created in the Chapter 3. A nanoscale coating was manufactured using organosilane atmospheric pressure plasma polymerization. The main interest of this technique is to add a nanostructure to the microtextured surface using a small amount of precursor and a cheap plasmageneous gas (industrial nitrogen). At first, two molecules were explored as precursors, i.e. hexamethyldisiloxane (HMDSO) and 1H,1H,2H,2H-perfluorooctyltrietoxysilane (pFOTES). Because of a lack of samples, the bio-inspired architecture characteristic was set aside and the samples were gathered as microtextured stainless steel samples. These microtextured samples coated with the APPP pFOTES demonstrated ultrahydrophobic behavior. Unfortunately, after 6 months ageing in atmospheric conditions, the surfaces wettability properties evolved. The APPP pFOTES coated microtextured surfaces evolved from ultrahydrophobic to highly hydrophobic surfaces, proving instability along long period of time.

In the second part of this chapter, the potential applications of the ultrahydrophobic manufactured surface were explored. At each step, the microtextured samples were compared to 2R or mirror-like stainless steel substrates coated with similar precursors.

The first application was anti-fouling, more specifically dairy fouling. A model-fluid composed of whey protein (β-Lactoglobulin) and calcium salt ($CaCl_2$) was placed in a semi-pilot installation to reproduce the milk pasteurization conditions. The hot model-fluid was placed directly in contact with the tested surfaces. The microtextured surfaces were less and not uniformly fouled like the 2R or mirror-like samples. The milk protein agglomerates were particularly present in the surface roughness. Even if the fouling test was not a success, the experiment gave a clue for the next step.

This apparent affinity between organic agglomerates and the roughness motivated the second application test, i.e. oil impregnation to design liquid infused surfaces.

The oil impregnation experiment was conducted with less samples. The measurements were focused on a few types of samples to get a better understanding of each element's contribution. The different elements compared were the roughness (2R and microtextured) and the coating (native and APPP pFOTES coated) with one set of samples aged for 1 month and freshly coated. Thanks to their roughness, the microtextured samples (uncoated and coated) demonstrated a better oil retention rate, especially the uncoated batch. The impregnation of the microtextured surfaces resulted in liquid infused surfaces (LIS) manufacturing. Because of its low melting temperature (25 °C), the anti-fouling properties of the LIS was considered unnecessary and replaced by an anti-icing property assessment.

The anti-icing properties were assessed using an instrumented goniometer equipped with a thermoelectrical plate and an isolated chamber. The evolution of WCA was studied during cooling down to estimate if the surface engineered during this chapter had an interest. Different results came out of these experiments. First, the impregnation seems to be more stable in the coated microtextured samples and does not migrate in the water drop during the cooling down. Second, the oil layer increases the freezing delay for a surface. Finally, the impregnation avoids contact angle decrease during cooling down. These three points are evidences that will require further investigation to confirm the true anti-icing interest of the designed surfaces. The characterizations carried out were not considering several crucial aspects important to anti-icing characterization such as mechanical adhesion or humidity influence.

While these results present compelling evidence, further investigations are imperative to confirm the genuine anti-icing potential of the designed surfaces. Overall, this chapter lays the groundwork for continued research into the optimization and practical applications of the bio-inspired microtextured surfaces with nanoscale coatings.

General conclusion

This work aimed at designing and prototyping bio-inspired surfaces with superhydrophobic properties by combining additive manufacturing, investment casting and atmospheric pressure plasma coating. The proposition made was at a crossroad of three different materials science subfields: additive manufacturing, metallurgy and surface treatment.

The first chapter explored the intricacies of bioinspired surface engineering, with a particular focus on the development of superhydrophobic stainless steel surfaces. We have delved into the fundamental principles of wettability, examined nature's fascinating superhydrophobic biosurfaces, and discussed various manufacturing strategies that draw inspiration from these natural phenomena. The potential applications of this research are vast, ranging from enhancing industrial processes to creating innovative materials with improved properties. Looking ahead, future research could further optimize these metallic additive manufacturing techniques, explore new bioinspired designs, and expand the application scope of superhydrophobic surfaces. This exploration not only contributes to the field of material science but also opens doors to interdisciplinary collaborations, harnessing the synergy between nature's wisdom and human ingenuity.

The second chapter explores the practicality of vacuum-assisted investment casting for creating detailed millimetric scales stainless steel parts. It begins by outlining the investment casting process, emphasizing its historical significance and recent advancements, including the integration of polymer 3D printing. The chapter then explores the experimental setup designed to test the castability of different metals, focusing on stainless steels' unique challenges. Through a series of experiments, it evaluates how various parameters, such as mold preheating temperature and material choice, affect the casting outcome. The findings underscore the potential to cast intricate stainless steel components, paving the way for further research on micrometric bioinspired designs and oxide layer management in casting processes.

The third chapter explores the feasibility and methodology for creating hydrophobic stainless steel surfaces with biomimetic microtextures using vacuum-assisted investment casting and vat photopolymerization (VPP). It demonstrates the technical challenges and solutions in

mimicking natural hydrophobic structures at a micro-scale on stainless steel. The chapter explores the detailed process of designing, creating, and evaluating the effectiveness of these textures in emulating the superhydrophobic properties found in nature. Through rigorous testing and surface analysis, it concludes that such surfaces offer promising applications in terms of superhydrophobic surface engineering and could be enhanced by a nanotexturation or a coating.

The fourth and final chapter examines the functionalization of bio-inspired microtextured stainless steel surfaces with nanoscale coatings via atmospheric pressure plasma polymerization (APPP), using organosilane precursors to enhance hydrophobicity. It investigates APPP's advantages, including minimal precursor use and cost-effectiveness, demonstrating ultrahydrophobic behavior on coated surfaces. However, a noted instability over six months suggests further research into durability. The chapter evaluates potential applications, including anti-fouling and anti-icing, highlighting the complex interplay between surface texture, chemical coating, and performance. Despite promising results, the need for comprehensive durability and efficacy studies is emphasized for future industrial applications.

In summary, this work integrates additive manufacturing, investment casting, and atmospheric pressure plasma coating to develop bio-inspired, superhydrophobic surfaces. Initial chapters discuss bioinspired engineering and superhydrophobicity fundamentals, highlighting potential applications and future research directions for optimizing techniques and designs. Subsequent chapters detail vacuum-assisted investment casting for stainless steel parts and creating hydrophobic surfaces with microtextures. Finally, surface functionalization via plasma polymerization to enhance hydrophobicity, and coconut oil impregnation, pointing to promising industrial applications despite some durability concerns.

Outlooks

During the past three years, the main challenge was to continuously develop new processes and to adapt existing processes. The knowledge acquired through this multidisciplinary work inspired the research teams to create new projects or to change their angle of attack. From this work, multiple scientific projects were born or inspired, mainly following the two main parts: stainless steel investment casting and the nanotextured surface engineering.

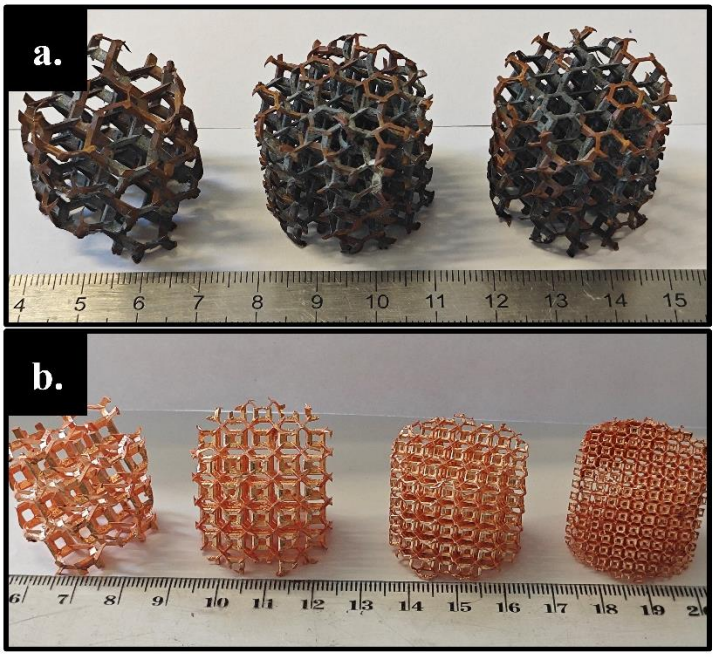

Figure 72. Pure copper foams manufactured by associating additive manufacturing and investment casting (a) as-cast sample before etching and (b) after chemical etching, from Tao AN thesis work.

About the castability tests designed during second chapter, the copper casting knowledge basis co-evolved with another project which consisted in the development of pure copper foams (see Figure 72). This manufacturing process was also a combination of polymer additive manufacturing and vacuum-assisted investment casting. Multiple steps, such as the post-casting chemical etching, the ceramic slurry manufacturing and casting parameters were inspired from the first copper castability tests and the 316L stainless steel investment casting procedure. These foams are of complex organized geometry that will be used to develop breaking pads. The next step of the manufacturing process is to sinter steel powder within the structure to create a bimetallic material.

Thanks to the procedure established to cast 316L stainless steel, the research team knowledge evolved about ferrous material casting. Cast iron foams associating additive manufacturing and vacuum-assisted investment casting were developed in the frame of the PhD thesis of Michele Zemo (see Figure 73). The casting parameters, the crucible materials and the ceramic slurry manufacturing were also inspired by the stainless steel investment casting procedure

developed during this work. The stainless steel infiltration test mentioned during the second chapter was the first ferrous material casting proof of concept at a millimetric scale. These structures were developed to create composite materials by polymer flash sintering within the metallic structure.

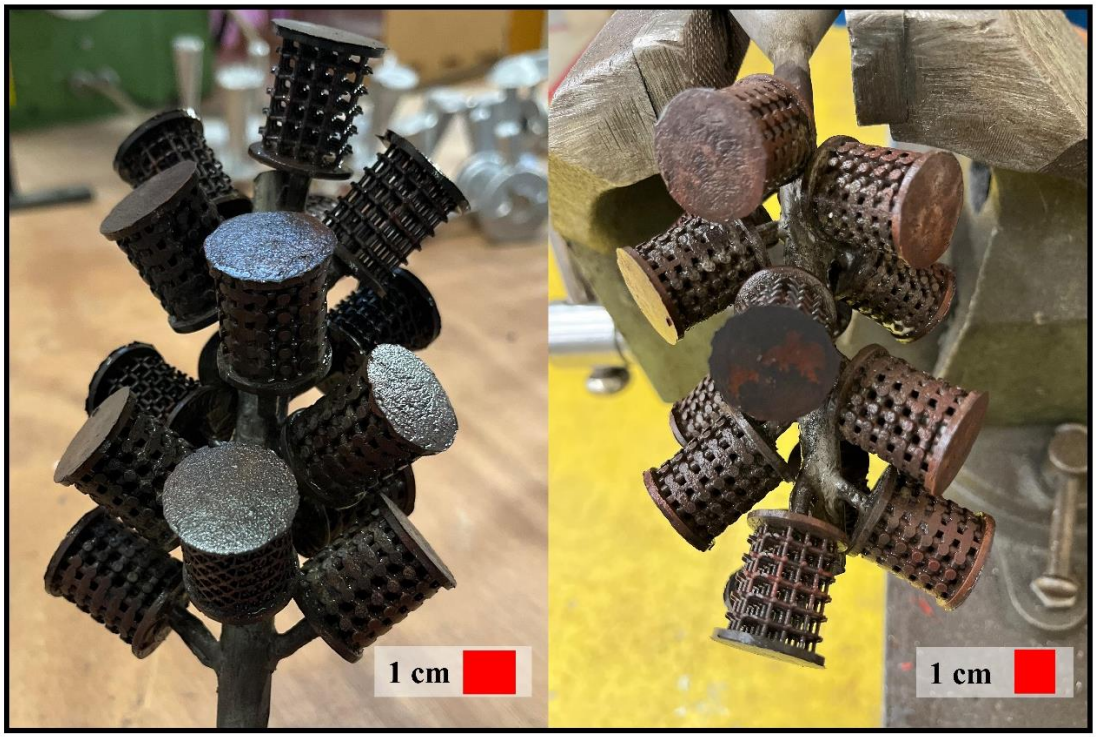

Figure 73. Cast iron foams manufactured by associating additive manufacturing and investment casting as-cast sample before etching, from Michele ZEMO-FOTEU thesis work.

On the surface engineering side, side-work not mentioned in this manuscript, about SLIPS toward anti-icing properties and surface microtexturing, inspired new scientific collaboration. The first results obtained in the last chapter, i.e. the vegetable oil retention increased by the plasma treatment, will be part of the future investigation. Through different partnerships, a more complete anti-icing characterization, including adhesion tests and dynamic water contact angle, will be possible. This scientific collaboration has been materialized by a financial grant (ANR COOLISSE-AAPG2023, Biomimetic Anti-Icing surfaces for eco efficient ice-slurry generators) from French national scientific research agency.

Scientific valorization

Publications:

K. Dourgaparsad, I-C Gruescu, R. Rasoli, D. Balloy, M. Jimenez, Bio-inspired and recycled 316L stainless steel surfaces prototyped by coupling vat photopolymerization and investment vacuum casting, Journal of manufacturing processes, status: submitted under review

M. Saget, N. Nuns, P. Supiot, C. Foissac, S. Bellayer, K. Dourgaparsad, P.-A. Royoux, G. Delaplace, V. Thomy, Y. Coffinier, M. Jimenez, Ultra-hydrophobic biomimetic transparent bilayer thin film deposited by atmospheric pressure plasma, Surfaces and Interfaces 42;A, 103398 (2023), [doi:10.1016/j.surfin.2023.103398]

Communications:

K. Dourgaparsad, M. Saget, D. Balloy, C. Gruescu, M. Jimenez, Superhydrophobic bio-inspired micro-architectured stainless steel surfaces, Oral communication, Société Française du Génie des procédés (SFGP), Webinar, February 2024

K. Dourgaparsad, M. Saget, S. Zouaghi, N. Nuns, S. Bellayer, M. Grunlan, V. Thomy, Y. Coffinier, D. Balloy, C. Gruescu, G. Delaplace, M. Jimenez, Surface engineering of stainless steel for dairy fouling management, Oral communication, Nature Inspired Creativity Engineers, Nice, France, Juin 2023

K. Dourgaparsad, M. Saget, D. Balloy, C. Gruescu, M. Jimenez, Superhydrophobic bio-inspired micro-architectured stainless steel surfaces, Oral communication, Surfaces, Interfaces and Coating Technologies, Lisboa, Portugal, Avr 2023

K. Dourgaparsad, M. Jimenez, D. Balloy, C. Gruescu, Fabrication de surfaces uniformément microtexturées en acier inoxydable : de la fabrication additive polymère à la fonderie à cire perdue, Oral communication, Matériaux 2022, Lille, France, Oct 2022

References:

[1] C. Sanchez, H. Arribart, M.M. Giraud Guille, Biomimetism and bioinspiration as tools for the design of innovative materials and systems, Nat. Mater. 4 (2005) 277–288. https://doi.org/10.1038/nmat1339.

[2] C. Huang, Z. Guo, Fabrications and Applications of Slippery Liquid-infused Porous Surfaces Inspired from Nature: A Review, J. Bionic Eng. 16 (2019) 769–793. https://doi.org/10.1007/s42235-019-0096-2.

[3] M. Villegas, Y. Zhang, N. Abu Jarad, L. Soleymani, T.F. Didar, Liquid-Infused Surfaces: A Review of Theory, Design, and Applications, ACS Nano 13 (2019) 8517–8536. https://doi.org/10.1021/acsnano.9b04129.

[4] S. Arango-Santander, Bioinspired Topographic Surface Modification of Biomaterials, Materials 15 (2022) 2383. https://doi.org/10.3390/ma15072383.

[5] X. Zhang, L. Jiang, X. Yan, Z. Wang, X. Li, G. Fang, Regulated multi-scale mechanical performance of functionally graded lattice materials based on multiple bioinspired patterns, Mater. Des. 226 (2023) 111564. https://doi.org/10.1016/j.matdes.2022.111564.

[6] M. Thomé, L. Nicole, S. Berthier, Multiscale Replication of Iridescent Butterfly Wings, Mater. Today Proc. 1 (2014) 221–224. https://doi.org/10.1016/j.matpr.2014.09.026.

[7] H. Tian, Y. Zhan, L. Tian, J. Sun, Corrosion resistance self-healing coating with bioinspired interfacial structure, Prog. Org. Coat. 174 (2023) 107303. https://doi.org/10.1016/j.porgcoat.2022.107303.

[8] J. Ren, R. Kong, Y. Gao, L. Zhang, J. Zhu, Bioinspired adhesive coatings from polyethylenimine and tannic acid complexes exhibiting antifogging, self-cleaning, and antibacterial capabilities, J. Colloid Interface Sci. 602 (2021) 406–414. https://doi.org/10.1016/j.jcis.2021.06.032.

[9] W. Wang, Y. Liu, Z. Xie, Gecko-Like Dry Adhesive Surfaces and Their Applications: A Review, J. Bionic Eng. 18 (2021) 1011–1044. https://doi.org/10.1007/s42235-021-00088-7.

[10] T. Sullivan, I. O'Callaghan, Recent Developments in Biomimetic Antifouling Materials: A Review, Biomimetics 5 (2020) 58. https://doi.org/10.3390/biomimetics5040058.

[11] K. Yang, Q. Liu, Z. Lin, Y. Liang, C. Liu, Investigations of interfacial heat transfer and phase change on bioinspired superhydrophobic surface for anti-icing/de-icing, Int. Commun. Heat Mass Transf. 134 (2022) 105994. https://doi.org/10.1016/j.icheatmasstransfer.2022.105994.

[12] Z. Shao, Y. Wang, H. Bai, A superhydrophobic textile inspired by polar bear hair for both in air and underwater thermal insulation, Chem. Eng. J. 397 (2020) 125441. https://doi.org/10.1016/j.cej.2020.125441.

[13] S. Shashwat, K.T. Zingre, N. Thurairajah, D.K. Kumar, K. Panicker, P. Anand, M.P. Wan, A review on bioinspired strategies for an energy-efficient built environment, Energy Build. 296 (2023) 113382. https://doi.org/10.1016/j.enbuild.2023.113382.

[14] K. Koch, W. Barthlott, Superhydrophobic and superhydrophilic plant surfaces: an inspiration for biomimetic materials, Philos. Trans. R. Soc. Math. Phys. Eng. Sci. 367 (2009) 1487–1509. https://doi.org/10.1098/rsta.2009.0022.

[15] F. Yang, Z. Guo, Characterization of Micro-Morphology and Wettability of Lotus Leaf, Waterlily Leaf and Biomimetic ZnO Surface, J. Bionic Eng. 12 (2015) 88–97. https://doi.org/10.1016/S1672-6529(14)60103-7.

[16] E. Celia, T. Darmanin, E. Taffin de Givenchy, S. Amigoni, F. Guittard, Recent advances in designing superhydrophobic surfaces, J. Colloid Interface Sci. 402 (2013) 1–18. https://doi.org/10.1016/j.jcis.2013.03.041.

[17] R. Deng, T. Shen, H. Chen, J. Lu, H.-C. Yang, W. Li, Slippery liquid-infused porous surfaces (SLIPSs): a perfect solution to both marine fouling and corrosion?, J. Mater. Chem. A 8 (2020) 7536–7547. https://doi.org/10.1039/D0TA02000A.

[18] L. Feng, H. Zhang, Z. Wang, Y. Liu, Superhydrophobic aluminum alloy surface: Fabrication, structure, and corrosion resistance, Colloids Surf. Physicochem. Eng. Asp. 441 (2014) 319–325. https://doi.org/10.1016/j.colsurfa.2013.09.014.

[19] X. Han, W. Dou, S. Chen, S. Zhu, Y. Pu, H. Li, W. Wang, W. Li, Stable slippery coating with structure of tubes and pyramids for inhibition of corrosion induced by microbes and seawater, Surf. Coat. Technol. 388 (2020) 125596. https://doi.org/10.1016/j.surfcoat.2020.125596.

[20] M. Saqib, N. Beshchasna, R. Pelaccia, A. Roshchupkin, I. Yanko, Y. Husak, S. Kyrylenko, B. Reggiani, G. Cuniberti, M. Pogorielov, J. Opitz, L. Orazi, Tailoring surface properties, biocompatibility and corrosion behavior of stainless steel by laser induced periodic surface treatment towards developing biomimetic stents, Surf. Interfaces 34 (2022) 102365. https://doi.org/10.1016/j.surfin.2022.102365.

[21] W. DeFlorio, S. Liu, A.R. White, T.M. Taylor, L. Cisneros-Zevallos, Y. Min, E.M.A. Scholar, Recent developments in antimicrobial and antifouling coatings to reduce or prevent contamination and cross-contamination of food contact surfaces by bacteria, Compr. Rev. Food Sci. Food Saf. 20 (2021) 3093–3134. https://doi.org/10.1111/1541-4337.12750.

[22] P. Fernández-Gómez, I. Muro-Fraguas, R. Múgica-Vidal, A. Sainz-García, E. Sainz-García, M. González-Raurich, A. Álvarez-Ordóñez, M. Prieto, M. López, M. López, P. Toledano, Y. Sáenz, A. González-Marcos, F. Alba-Elías, Development and characterization of anti-biofilm coatings applied by Non-Equilibrium Atmospheric Plasma on stainless steel, Food Res. Int. 152 (2022) 109891. https://doi.org/10.1016/j.foodres.2020.109891.

[23] R. Múgica-Vidal, E. Sainz-García, I. Muro-Fraguas, A. Sainz-García, A. González-Marcos, M. López, B. Rojo-Bezares, P. Toledano, Y. Sáenz, F. Alba-Elías, Inhibition of biofilm

formation on polystyrene substrates by atmospheric pressure plasma polymerization of siloxane-based coatings, Plasma Process. Polym. 18 (2021) 2100097. https://doi.org/10.1002/ppap.202100097.

[24] H. Pérez, G. Vargas, R. Silva, Use of Nanotechnology to Mitigate Biofouling in Stainless Steel Devices Used in Food Processing, Healthcare, and Marine Environments, Toxics 10 (2022) 35. https://doi.org/10.3390/toxics10010035.

[25] S. Heydarian, R. Jafari, G. Momen, Recent progress in the anti-icing performance of slippery liquid-infused surfaces, Prog. Org. Coat. 151 (2021) 106096. https://doi.org/10.1016/j.porgcoat.2020.106096.

[26] T. Wu, W. Xu, K. Guo, H. Xie, J. Qu, Efficient fabrication of lightweight polyethylene foam with robust and durable superhydrophobicity for self-cleaning and anti-icing applications, Chem. Eng. J. (2020) 127100. https://doi.org/10.1016/j.cej.2020.127100.

[27] P.S. Birak, C.T. Miller, Dense non-aqueous phase liquids at former manufactured gas plants: Challenges to modeling and remediation, J. Contam. Hydrol. 105 (2009) 81–98. https://doi.org/10.1016/j.jconhyd.2008.12.001.

[28] T. Young, An essay on the cohesion of fluids, Abstr. Pap. Print. Philos. Trans. R. Soc. Lond. 1 (1997) 171–172. https://doi.org/10.1098/rspl.1800.0095.

[29] J. Jeevahan, M. Chandrasekaran, G. Britto Joseph, R.B. Durairaj, G. Mageshwaran, Superhydrophobic surfaces: a review on fundamentals, applications, and challenges, J. Coat. Technol. Res. 15 (2018) 231–250. https://doi.org/10.1007/s11998-017-0011-x.

[30] R.N. Wenzel, RESISTANCE OF SOLID SURFACES TO WETTING BY WATER, Ind. Eng. Chem. 28 (1936) 988–994. https://doi.org/10.1021/ie50320a024.

[31] S. Parvate, P. Dixit, S. Chattopadhyay, Superhydrophobic Surfaces: Insights from Theory and Experiment, J. Phys. Chem. B 124 (2020) 1323–1360. https://doi.org/10.1021/acs.jpcb.9b08567.

[32] W. Bogacz, M. Lemanowicz, M.H. Al-Rashed, D. Nakonieczny, T. Piotrowski, J. Wójcik, Impact of roughness, wettability and hydrodynamic conditions on the incrustation on stainless steel surfaces, Appl. Therm. Eng. 112 (2017) 352–361. https://doi.org/10.1016/j.applthermaleng.2016.10.076.

[33] F. Borgioli, E. Galvanetto, T. Bacci, Influence of surface morphology and roughness on water wetting properties of low temperature nitrided austenitic stainless steels, Mater. Charact. 95 (2014) 278–284. https://doi.org/10.1016/j.matchar.2014.07.006.

[34] O. Çakır, Study of Etch Rate and Surface Roughness in Chemical Etching of Stainless Steel, Key Eng. Mater. 364–366 (2008) 837–842. https://doi.org/10.4028/www.scientific.net/KEM.364-366.837.

[35] E.E. Ubuo, I.A. Udoetok, A.T. Tyowua, I.O. Ekwere, H.S. Al-Shehri, The Direct Cause of Amplified Wettability: Roughness or Surface Chemistry?, J. Compos. Sci. 5 (2021) 213. https://doi.org/10.3390/jcs5080213.

[36] M. Mantel, J.P. Wightman, Influence of the surface chemistry on the wettability of stainless steel, Surf. Interface Anal. 21 (1994) 595–605. https://doi.org/10.1002/sia.740210902.

[37] H.-J. Jacobasch, K. Grundke, A. Augsburg, T. Gietzelt, S. Schneider, Wetting of solids by liquids with low and high viscosity, in: J.B. Rosenholm, B. Lindman, P. Stenius (Eds.), Trends Colloid Interface Sci. XI, Steinkopff, Darmstadt, 1997: pp. 44–54. https://doi.org/10.1007/BFb0110961.

[38] E.C. Donaldson, W. Alam, Wettability, Elsevier, 2013.

[39] J. Drelich, E. Chibowski, D.D. Meng, K. Terpilowski, Hydrophilic and superhydrophilic surfaces and materials, Soft Matter 7 (2011) 9804. https://doi.org/10.1039/c1sm05849e.

[40] D.V. Antonov, A.G. Islamova, P.A. Strizhak, Hydrophilic and Hydrophobic Surfaces: Features of Interaction with Liquid Drops, Materials 16 (2023) 5932. https://doi.org/10.3390/ma16175932.

[41] M.A.Q. Siddiqui, S. Ali, H. Fei, H. Roshan, Current understanding of shale wettability: A review on contact angle measurements, Earth-Sci. Rev. 181 (2018) 1–11. https://doi.org/10.1016/j.earscirev.2018.04.002.

[42] A.B.D. Cassie, S. Baxter, Wettability of porous surfaces, Trans. Faraday Soc. 40 (1944) 546. https://doi.org/10.1039/tf9444000546.

[43] C. Wang, R. Shao, G. Wang, S. Sun, Hierarchical hydrophobic surfaces with controlled dual transition between rose petal effect and lotus effect via structure tailoring or chemical modification, Colloids Surf. Physicochem. Eng. Asp. 622 (2021) 126661. https://doi.org/10.1016/j.colsurfa.2021.126661.

[44] H.J. Ensikat, P. Ditsche-Kuru, C. Neinhuis, W. Barthlott, Superhydrophobicity in perfection: the outstanding properties of the lotus leaf, Beilstein J. Nanotechnol. 2 (2011) 152–161. https://doi.org/10.3762/bjnano.2.19.

[45] A. Satdive, S. Tayde, B. Toksha, D. Kundu, J. Naik, C. Hazra, S. Joshi, A. Chatterjee, Superhydrophobic hybrid nanocomposites: Mapping the current research trends and recent advances, Chem. Eng. Sci. 278 (2023) 118941. https://doi.org/10.1016/j.ces.2023.118941.

[46] H.A. Hassan, M.J. Ghazali, C. Meric, C.H. Azhari, Wettability Effect of the Surface Morphologies of Musa Acuminata Leaves, BioResources 14 (2019) 8331–8344. https://doi.org/10.15376/biores.14.4.8331-8344.

[47] X. Gou, Z. Guo, Superhydrophobic Plant Leaves with Micro-line Structures: An Optimal Biomimetic Objective in Bionic Engineering, J. Bionic Eng. 15 (2018) 851–858. https://doi.org/10.1007/s42235-018-0072-2.

[48] G. Wang, Z. Guo, W. Liu, Interfacial effects of superhydrophobic plant surfaces: A review, J. Bionic Eng. 11 (2014) 325–345. https://doi.org/10.1016/S1672-6529(14)60047-0.

[49] L. Wang, S. Zhang, S. Li, S. Yan, S. Dong, Inner surface of *Nepenthes* slippery zone: ratchet effect of lunate cells causes anisotropic superhydrophobicity, R. Soc. Open Sci. 7 (2020) 200066. https://doi.org/10.1098/rsos.200066.

[50] S. Miguel, A. Hehn, F. Bourgaud, Nepenthes: State of the art of an inspiring plant for biotechnologists, J. Biotechnol. 265 (2018) 109–115. https://doi.org/10.1016/j.jbiotec.2017.11.014.

[51] L. Wang, Q. Zhou, Nepenthes pitchers: surface structure, physical property, anti-attachment function and potential application in mechanical controlling plague locust, Chin. Sci. Bull. 59 (2014) 2513–2523. https://doi.org/10.1007/s11434-014-0383-6.

[52] M. Riedel, A. Eichner, H. Meimberg, R. Jetter, Chemical composition of epicuticular wax crystals on the slippery zone in pitchers of five Nepenthes species and hybrids, Planta 225 (2007) 1517–1534. https://doi.org/10.1007/s00425-006-0437-3.

[53] L. Gaume, S.N. Gorb, N. Rowe, Function of epidermal surfaces in the trapping efficiency of Nepenthes alata pitchers, New Phytol. 156 (2002) 479–489. https://doi.org/10.1046/j.1469-8137.2002.00530.x.

[54] S. Zouaghi, T. Six, S. Bellayer, Y. Coffinier, M. Abdallah, N.-E. Chihib, C. André, G. Delaplace, M. Jimenez, Atmospheric pressure plasma spraying of silane-based coatings targeting whey protein fouling and bacterial adhesion management, Appl. Surf. Sci. 455 (2018) 392–402. https://doi.org/10.1016/j.apsusc.2018.06.006.

[55] Z. He, X. Lan, Q. Hu, H. Li, L. Li, J. Mao, Antifouling strategies based on super-phobic polymer materials, Prog. Org. Coat. 157 (2021) 106285. https://doi.org/10.1016/j.porgcoat.2021.106285.

[56] C. Wuang, Z. Guo, Fabrications and Applications of Slippery Liquid-infused Porous Surfaces Inspired from Nature: A Review, J. Bionic Eng. 16 (2019) 769–793. https://doi.org/10.1007/s42235-019-0096-2.

[57] M.K. Islam, P.J. Hazell, J.P. Escobedo, H. Wang, Biomimetic armour design strategies for additive manufacturing: A review, Mater. Des. 205 (2021) 109730. https://doi.org/10.1016/j.matdes.2021.109730.

[58] D.K. Wainwright, G.V. Lauder, Mucus Matters: The Slippery and Complex Surfaces of Fish, in: S.N. Gorb, E.V. Gorb (Eds.), Funct. Surf. Biol. III, Springer International Publishing, Cham, 2017: pp. 223–246. https://doi.org/10.1007/978-3-319-74144-4_10.

[59] W. Yang, I.H. Chen, B. Gludovatz, E.A. Zimmermann, R.O. Ritchie, M.A. Meyers, Natural Flexible Dermal Armor, Adv. Mater. 25 (2013) 31–48. https://doi.org/10.1002/adma.201202713.

[60] D. Zhang, W. Zhang, J. Gu, T. Fan, Q. Liu, H. Su, S. Zhu, Inspiration from butterfly and moth wing scales: Characterization, modeling, and fabrication, Prog. Mater. Sci. 68 (2015) 67–96. https://doi.org/10.1016/j.pmatsci.2014.10.003.

[61] G. Liu, Z. Yuan, Z. Qiu, S. Feng, Y. Xie, D. Leng, X. Tian, A brief review of bio-inspired surface technology and application toward underwater drag reduction, Ocean Eng. 199 (2020) 106962. https://doi.org/10.1016/j.oceaneng.2020.106962.

[62] M. Muthuramalingam, L.S. Villemin, C. Bruecker, Streak formation in flow over biomimetic fish scale arrays, J. Exp. Biol. (2019) jeb.205963. https://doi.org/10.1242/jeb.205963.

[63] Z. Lian, J. Xu, Y. Wan, Y. Li, Z. Yu, Q. Liu, H. Yu, Tribological properties of fish scale inspired underwater superoleophobic hierarchical structure in aqueous environment, Mater. Res. Express 4 (2017) 106504. https://doi.org/10.1088/2053-1591/aa8c32.

[64] M.J. Benz, E.V. Gorb, S.N. Gorb, Diversity of the slippery zone microstructure in pitchers of nine carnivorous Nepenthes taxa, Arthropod-Plant Interact. 6 (2012) 147–158. https://doi.org/10.1007/s11829-011-9171-2.

[65] L. Wang, S. Dong, Q. Zhou, Slippery Surface of Nepenthes alata Pitcher: The Role of Lunate Cell and Wax Crystal in Restricting Attachment Ability of Ant Camponotus japonicus Mayr, J. Bionic Eng. 13 (2016) 373–387. https://doi.org/10.1016/S1672-6529(16)60310-4.

[66] Z. Shi, Y. Xiao, R. Qiu, S. Niu, P. Wang, A facile and mild route for fabricating slippery liquid-infused porous surface (SLIPS) on CuZn with corrosion resistance and self-healing properties, Surf. Coat. Technol. 330 (2017) 102–112. https://doi.org/10.1016/j.surfcoat.2017.09.053.

[67] W. Yao, L. Wu, L. Sun, B. Jiang, F. Pan, Recent developments in slippery liquid-infused porous surface, Prog. Org. Coat. 166 (2022) 106806. https://doi.org/10.1016/j.porgcoat.2022.106806.

[68] W. Yan, S. Xue, B. Xiang, X. Zhao, W. Zhang, P. Mu, J. Li, Recent advances of slippery liquid-infused porous surfaces with anti-corrosion, Chem. Commun. 59 (2023) 2182–2198. https://doi.org/10.1039/D2CC06688B.

[69] P. Sahoo, T.Kr. Barman, ANN modelling of fractal dimension in machining, in: Mechatron. Manuf. Eng., Elsevier, 2012: pp. 159–226. https://doi.org/10.1533/9780857095893.159.

[70] J.-S. Kwak, T.-W. Kim, A review of adhesion and friction models for gecko feet, Int. J. Precis. Eng. Manuf. 11 (2010) 171–186. https://doi.org/10.1007/s12541-010-0020-5.

[71] Y. Liu, G. Li, A new method for producing “Lotus Effect” on a biomimetic shark skin, J. Colloid Interface Sci. 388 (2012) 235–242. https://doi.org/10.1016/j.jcis.2012.08.033.

[72] A. Du Plessis, A.J. Babafemi, S.C. Paul, B. Panda, J.P. Tran, C. Broeckhoven, Biomimicry for 3D concrete printing: A review and perspective, Addit. Manuf. 38 (2021) 101823. https://doi.org/10.1016/j.addma.2020.101823.

[73] L. Feng, F. Wang, H. Luo, B. Qiu, Review of recent advancements in the biomimicry of structural colors, Dyes Pigments 210 (2023) 111019. https://doi.org/10.1016/j.dyepig.2022.111019.

[74] A. Davoudinejad, M.M. Ribo, D.B. Pedersen, A. Islam, G. Tosello, Direct fabrication of bio-inspired gecko-like geometries with vat polymerization additive manufacturing method, J. Micromechanics Microengineering 28 (2018) 085009. https://doi.org/10.1088/1361-6439/aabf17.

[75] G.N. S, B.R.R. J, Performance enhancement of futuristic airplanes by nature inspired biomimetic fish scale arrays—A design approach, Biomim. Intell. Robot. 2 (2022) 100045. https://doi.org/10.1016/j.birob.2022.100045.

[76] S.E. Naleway, M.M. Porter, J. McKittrick, M.A. Meyers, Structural Design Elements in Biological Materials: Application to Bioinspiration, Adv. Mater. 27 (2015) 5455–5476. https://doi.org/10.1002/adma.201502403.

[77] U.G.K. Wegst, H. Bai, E. Saiz, A.P. Tomsia, R.O. Ritchie, Bioinspired structural materials, Nat. Mater. 14 (2015) 23–36. https://doi.org/10.1038/nmat4089.

[78] A. Du Plessis, C. Broeckhoven, I. Yadroitsava, I. Yadroitsev, C.H. Hands, R. Kunju, D. Bhate, Beautiful and Functional: A Review of Biomimetic Design in Additive Manufacturing, Addit. Manuf. 27 (2019) 408–427. https://doi.org/10.1016/j.addma.2019.03.033.

[79] K. Ellinas, P. Dimitrakellis, P. Sarkiris, E. Gogolides, A Review of Fabrication Methods, Properties and Applications of Superhydrophobic Metals, Processes 9 (2021) 666. https://doi.org/10.3390/pr9040666.

[80] Q. Yang, J. Cao, R. Ding, K. Zhan, Z. Yang, B. Zhao, Z. Wang, V. Ji, The synthesis and mechanism of superhydrophobic coatings with multifunctional properties on aluminum alloys surface: a review, Prog. Org. Coat. 183 (2023) 107786. https://doi.org/10.1016/j.porgcoat.2023.107786.

[81] L. Lu, W. Yao, Y. Xie, K. Li, Z. Wan, Study on the wettability of biomimetic stainless-steel surfaces inspired by Bauhinia Linn. leaf, Surf. Coat. Technol. 405 (2021) 126721. https://doi.org/10.1016/j.surfcoat.2020.126721.

[82] S. Zouaghi, S. Bellayer, V. Thomy, T. Dargent, Y. Coffinier, C. Andre, G. Delaplace, M. Jimenez, Biomimetic surface modifications of stainless steel targeting dairy fouling mitigation and bacterial adhesion, Food Bioprod. Process. 113 (2019) 32–38. https://doi.org/10.1016/j.fbp.2018.10.012.

[83] Y. Liu, X. He, C. Yuan, P. Cao, X. Bai, Antifouling applications and fabrications of biomimetic micro-structured surfaces: A review, J. Adv. Res. (2023) S2090123223002357. https://doi.org/10.1016/j.jare.2023.08.019.

[84] S. Astafurov, E. Astafurova, Phase Composition of Austenitic Stainless Steels in Additive Manufacturing: A Review, Metals 11 (2021) 1052. https://doi.org/10.3390/met11071052.

[85] M. Kaladhar, K.V. Subbaiah, C.H.S. Rao, Machining of austenitic stainless steels - a review, Int. J. Mach. Mach. Mater. 12 (2012) 178. https://doi.org/10.1504/IJMMM.2012.048564.

[86] C.W. Kovach, High-performance stainless steels, Nickel Development Institute, Toronto, Ont, 2000.

[87] H. Li, Z. Jiang, Z. Zhang, Y. Yang, Effect of Grain Size on Mechanical Properties of Nickel-Free High Nitrogen Austenitic Stainless Steel, J. Iron Steel Res. Int. 16 (2009) 58–61. https://doi.org/10.1016/S1006-706X(09)60011-X.

[88] J.L. Polo, E. Cano, J.M. Bastidas, An impedance study on the influence of molybdenum in stainless steel pitting corrosion, J. Electroanal. Chem. 537 (2002) 183–187. https://doi.org/10.1016/S0022-0728(02)01224-X.

[89] J.-L. Fanchon, Guide pratique des sciences et technologies industrielles: dessin industriel, éléments de construction, organisation - méthodes d'analyse, matériaux - automatisme - schématisation, Edition mise à jour conformément aux normes en vigueur, AFNOR, Paris, 2014.

[90] B. Rossi, Discussion on the use of stainless steel in constructions in view of sustainability, Thin-Walled Struct. 83 (2014) 182–189. https://doi.org/10.1016/j.tws.2014.01.021.

[91] J. Johnson, B.K. Reck, T. Wang, T.E. Graedel, The energy benefit of stainless steel recycling, Energy Policy 36 (2008) 181–192. https://doi.org/10.1016/j.enpol.2007.08.028.

[92] K. Bordjih, J.-Y. Jouzeau, D. Mainard, E. Payan, J.-P. Delagoutte, P. Netter, Evaluation of the effect of three surface treatments on the biocompatibility of 316L stainless steel using human differentiated cells, Biomaterials 17 (1996) 491–500. https://doi.org/10.1016/0142-9612(96)82723-2.

[93] J.D. Majumdar, A. Kumar, S. Pityana, I. Manna, Laser Surface Melting of AISI 316L Stainless Steel for Bio-implant Application, Proc. Natl. Acad. Sci. India Sect. Phys. Sci. 88 (2018) 387–403. https://doi.org/10.1007/s40010-018-0524-4.

[94] P.S. Korinko, S.H. Malene, Considerations for the weldability of types 304L and 316L stainless steel, Pract. Fail. Anal. 1 (2001) 61–68. https://doi.org/10.1007/BF02715336.

[95] R. Venugopalan, Medical Device Materials Iii, ASM International, 2006.

[96] A.S. Grenadyorov, A.A. Solovyev, K.V. Oskomov, E.V. Yakovlev, M.O. Zhulkov, AISI 316L stainless steel modification by surface alloy and a-C:H:SiOx coating synthesis, Vacuum 204 (2022) 111369. https://doi.org/10.1016/j.vacuum.2022.111369.

[97] C.I. Pereni, Q. Zhao, Y. Liu, E. Abel, Surface free energy effect on bacterial retention, Colloids Surf. B Biointerfaces 48 (2006) 143–147. https://doi.org/10.1016/j.colsurfb.2006.02.004.

[98] S. Pourhashem, A. Seif, F. Saba, E.G. Nezhad, X. Ji, Z. Zhou, X. Zhai, M. Mirzaee, J. Duan, A. Rashidi, B. Hou, Antifouling nanocomposite polymer coatings for marine applications: A review on experiments, mechanisms, and theoretical studies, J. Mater. Sci. Technol. 118 (2022) 73–113. https://doi.org/10.1016/j.jmst.2021.11.061.

[99] V.S. Saji, Superhydrophobic surfaces and coatings by electrochemical anodic oxidation and plasma electrolytic oxidation, Adv. Colloid Interface Sci. 283 (2020) 102245. https://doi.org/10.1016/j.cis.2020.102245.

[100] A. Fattah-alhosseini, M. Molaei, N. Attarzadeh, K. Babaei, F. Attarzadeh, On the enhanced antibacterial activity of plasma electrolytic oxidation (PEO) coatings that incorporate particles: A review, Ceram. Int. 46 (2020) 20587–20607. https://doi.org/10.1016/j.ceramint.2020.05.206.

[101] Y. Deng, F. Xu, Z. Yin, M. Xue, Y. Chen, P. He, J. Wu, J. Ou, F. Wang, Y. Luo, Z. Hong, Controllable fabrication of superhydrophobic alloys surface on 304 stainless steel substrate for anti-icing performance, Ceram. Int. 49 (2023) 25135–25143. https://doi.org/10.1016/j.ceramint.2023.05.044.

[102] Y. Wang, G. Zhang, Z. Liu, S. Zheng, L. Zhu, Z. He, Robust and durable superhydrophobic coating prepared via a combined method of laser marking and electrodeposition, J. Mater. Res. Technol. 26 (2023) 477–486. https://doi.org/10.1016/j.jmrt.2023.07.085.

[103] M. Saget, N. Nuns, P. Supiot, C. Foissac, S. Bellayer, K. Dourgaparsad, P.-A. Royoux, G. Delaplace, V. Thomy, Y. Coffinier, M. Jimenez, ULTRA-HYDROPHOBIC BIOMIMETIC TRANSPARENT BILAYER THIN FILM DEPOSITED BY ATMOSPHERIC PRESSURE PLASMA, Surf. Interfaces (2023) 103398. https://doi.org/10.1016/j.surfin.2023.103398.

[104] A.O. Ijaola, P.K. Farayibi, E. Asmatulu, Superhydrophobic coatings for steel pipeline protection in oil and gas industries: A comprehensive review, J. Nat. Gas Sci. Eng. 83 (2020) 103544. https://doi.org/10.1016/j.jngse.2020.103544.

[105] M.-J. Su, S. Bai, Y. Luo, G.-W. Chu, B.-C. Sun, Y. Le, J.-F. Chen, Controllable wettability on stainless steel substrates with highly stable coatings, Chem. Eng. Sci. 195 (2019) 791–800. https://doi.org/10.1016/j.ces.2018.10.025.

[106] W. Song, X. Zhao, Z. Jin, L. Fan, X. Ji, J. Deng, J. Duan, Poly(vinyl alcohol) for multi-functionalized corrosion protection of metals: A review, J. Clean. Prod. 394 (2023) 136390. https://doi.org/10.1016/j.jclepro.2023.136390.

[107] Jaishree, A. Bhandari, N. Khatri, Y.K. Mishra, M.S. Goyat, Superhydrophobic coatings by the hot embossing approach: recent developments and state-of-art applications, Mater. Today Chem. 30 (2023) 101553. https://doi.org/10.1016/j.mtchem.2023.101553.

[108] Z. Yan, D. Zhou, Q. Zhang, Y. Zhu, Z. Wu, A critical review on fouling influence factors and antifouling coatings for heat exchangers of high-salt industrial wastewater, Desalination 553 (2023) 116504. https://doi.org/10.1016/j.desal.2023.116504.

[109] V. Sharma, V. Sharma, M.S. Goyat, A. Hooda, J.K. Pandey, A. Kumar, R. Gupta, A.K. Upadhyay, R. Prakash, J.B. Kirabira, P. Mandal, P.K. Bhargav, Recent progress in nano-oxides and CNTs based corrosion resistant superhydrophobic coatings: A critical review, Prog. Org. Coat. 140 (2020) 105512. https://doi.org/10.1016/j.porgcoat.2019.105512.

[110] W.T. Choi, K. Oh, P.M. Singh, V. Breedveld, D.W. Hess, Wettability control of stainless steel surfaces via evolution of intrinsic grain structures, J. Mater. Sci. 51 (2016) 5196–5206. https://doi.org/10.1007/s10853-016-9821-y.

[111] V.K. Jain, R. Balasubramaniam, R.G. Mote, M. Das, A. Sharma, A. Kumar, V. Garg, B. Kamaliya, Micromachining: An overview (Part I), J. Micromanufacturing 3 (2020) 142–158. https://doi.org/10.1177/2516598419895828.

[112] J. Airao, B. Chaudhary, V. Bajpai, N. Khanna, An Experimental Study of Surface Roughness Variation in End Milling of Super Duplex 2507 Stainless Steel, Mater. Today Proc. 5 (2018) 3682–3689. https://doi.org/10.1016/j.matpr.2017.11.619.

[113] L. Simon, C.A.M. Moraes, R.C.E. Modolo, M. Vargas, D. Calheiro, F.A. Brehm, Recycling of contaminated metallic chip based on eco-efficiency and eco-effectiveness approaches, J. Clean. Prod. 153 (2017) 417–424. https://doi.org/10.1016/j.jclepro.2016.11.058.

[114] D. Shen, W. Ming, X. Ren, Z. Xie, X. Liu, Progress in Non-Traditional Processing for Fabricating Superhydrophobic Surfaces, Micromachines 12 (2021) 1003. https://doi.org/10.3390/mi12091003.

[115] G. Annamaria, B. Massimiliano, V. Francesco, Laser polishing: a review of a constantly growing technology in the surface finishing of components made by additive manufacturing, Int. J. Adv. Manuf. Technol. 120 (2022) 1433–1472. https://doi.org/10.1007/s00170-022-08840-x.

[116] P. Dimitrakellis, E. Gogolides, Hydrophobic and superhydrophobic surfaces fabricated using atmospheric pressure cold plasma technology: A review, Adv. Colloid Interface Sci. 254 (2018) 1–21. https://doi.org/10.1016/j.cis.2018.03.009.

[117] M.R. Pratheesh Kumar, S.T. Siddeswar, S. Elanchezian, K. Yogesh, T. Dharun, Experimental investigation on the superhydrophobic property of laser micromachined stainless steel 316L surface, Mater. Today Proc. (2023). https://doi.org/10.1016/j.matpr.2023.10.038.

[118] C. Sciancalepore, L. Gemini, L. Romoli, F. Bondioli, Study of the wettability behavior of stainless steel surfaces after ultrafast laser texturing, Surf. Coat. Technol. 352 (2018) 370–377. https://doi.org/10.1016/j.surfcoat.2018.08.030.

[119] S. Ahlawat, A. Singh, P.K. Mukhopadhyay, R. Singh, V.P. Dhamgaye, S.K. Dixit, K.S. Bindra, Analyte enrichment and sensitive detection over nanosecond laser textured stainless steel superhydrophobic surfaces, Mater. Chem. Phys. 302 (2023) 127755. https://doi.org/10.1016/j.matchemphys.2023.127755.

[120] M. Benčina, I. Junkar, A. Vesel, M. Mozetič, A. Iglič, Nanoporous Stainless Steel Materials for Body Implants—Review of Synthesizing Procedures, Nanomaterials 12 (2022) 2924. https://doi.org/10.3390/nano12172924.

[121] S. Zhu, W. Deng, Y. Su, Recent advances in preparation of metallic superhydrophobic surface by chemical etching and its applications, Chin. J. Chem. Eng. 61 (2023) 221–236. https://doi.org/10.1016/j.cjche.2023.02.018.

[122] Y. Zhang, Z. Zhang, J. Yang, Y. Yue, H. Zhang, Fabrication of superhydrophobic surface on stainless steel by two-step chemical etching, Chem. Phys. Lett. (2022) 139567. https://doi.org/10.1016/j.cplett.2022.139567.

[123] W. Liu, S. Wang, G. Wang, J. Zhang, C. Zhou, Investigation on the differences of surface cleaning properties of series of superhydrophobic aluminum alloys, Colloids Surf. Physicochem. Eng. Asp. 651 (2022) 129614. https://doi.org/10.1016/j.colsurfa.2022.129614.

[124] J. Song, W. Huang, J. Liu, L. Huang, Y. Lu, Electrochemical machining of superhydrophobic surfaces on mold steel substrates, Surf. Coat. Technol. 344 (2018) 499–506. https://doi.org/10.1016/j.surfcoat.2018.03.061.

[125] W. Tong, D. Xiong, Direct laser texturing technique for metal surfaces to achieve superhydrophobicity, Mater. Today Phys. 23 (2022) 100651. https://doi.org/10.1016/j.mtphys.2022.100651.

[126] A.M. Escobar, N. Llorca-Isern, O. Rius-Ayra, Identification of the mechanism that confers superhydrophobicity on 316L stainless steel, Mater. Charact. 111 (2016) 162–169. https://doi.org/10.1016/j.matchar.2015.11.026.

[127] M. Alonso Frank, A.R. Boccaccini, S. Virtanen, A facile and scalable method to produce superhydrophic stainless steel surface, Appl. Surf. Sci. 311 (2014) 753–757. https://doi.org/10.1016/j.apsusc.2014.05.152.

[128] X. Li, M. Xi, W. Guo, G. Xu, W. Luo, Q. Zhu, Y. Li, H. Yu, T. Chang, Y. Zhang, Z. Zhang, T. Sun, Two-Step Chemical Mechanical Polishing of Stainless Steel, ECS J. Solid State Sci. Technol. 11 (2022) 044001. https://doi.org/10.1149/2162-8777/ac5eae.

[129] M. Abbas, M.T. Mehran, M.-W. Moon, J.Y. Byun, S.H. Kim, Wettability control of modified stainless steel surfaces for oxide catalyst carrier slurry coating, J. Ind. Eng. Chem. 91 (2020) 330–339. https://doi.org/10.1016/j.jiec.2020.08.017.

[130] A.H. Cannon, Investigating wetting characteristics on microstructured surfaces for superhydrophobicity and metal microcasting, (n.d.). https://www.academia.edu/30135643/Investigating_wetting_characteristics_on_microstructured_surfaces_for_superhydrophobicity_and_metal_microcasting (accessed September 1, 2021).

[131] A. Cannon, M. Maguire, R. Hulseman, W. King, Manufacturing Microstructured Surfaces for Automotive Applications, (2015).

[132] M. Sahli, J.-C. Gelin, T. Barriere, Characterisation and replication of metallic micro-fluidic devices using three different powders processed by hot embossing, Powder Technol. 246 (2013) 284–302. https://doi.org/10.1016/j.powtec.2013.05.026.

[133] E.W. Sequeiros, O. Emadinia, M.T. Vieira, M.F. Vieira, Development of Metal Powder Hot Embossing: A New Method for Micromanufacturing, Metals 10 (2020) 388. https://doi.org/10.3390/met10030388.

[134] J. Xu, Q. Su, D. Shan, B. Guo, Sustainable micro-manufacturing of superhydrophobic surface on ultrafine-grained pure aluminum substrate combining micro-embossing and surface modification, J. Clean. Prod. 232 (2019) 705–712. https://doi.org/10.1016/j.jclepro.2019.05.394.

[135] R.A. Hulseman, D. Mammarella, A.H. Cannon, W.P. King, Method of manufacturing products having a metal surface, US8814954B2, 2014. https://patents.google.com/patent/US8814954B2/en?oq=US8814954B2 (accessed October 9, 2023).

[136] M. Sahli, C. Millot, J.-C. Gelin, T. Barrière, The manufacturing and replication of microfluidic mould inserts by the hot embossing process, J. Mater. Process. Technol. 213 (2013) 913–925. https://doi.org/10.1016/j.jmatprotec.2012.11.007.

[137] C. Tan, R. Li, J. Su, D. Du, Y. Du, B. Attard, Y. Chew, H. Zhang, E.J. Lavernia, Y. Fautrelle, J. Teng, A. Dong, Review on field assisted metal additive manufacturing, Int. J. Mach. Tools Manuf. 189 (2023) 104032. https://doi.org/10.1016/j.ijmachtools.2023.104032.

[138] R.F.V. Sampaio, J.P.M. Pragana, I.M.F. Bragança, C.M.A. Silva, C.V. Nielsen, P.A.F. Martins, Modelling of wire-arc additive manufacturing – A review, Adv. Ind. Manuf. Eng. 6 (2023) 100121. https://doi.org/10.1016/j.aime.2023.100121.

[139] Z. Fan, K. Bai, C. Chen, The application of ultrasound in Joining: Principles, processes and properties, J. Manuf. Process. 101 (2023) 269–299. https://doi.org/10.1016/j.jmapro.2023.05.094.

[140] A. Elkaseer, K.J. Chen, J.C. Janhsen, O. Refle, V. Hagenmeyer, S.G. Scholz, Material jetting for advanced applications: A state-of-the-art review, gaps and future directions, Addit. Manuf. 60 (2022) 103270. https://doi.org/10.1016/j.addma.2022.103270.

[141] J.P.M. Pragana, R.F.V. Sampaio, I.M.F. Bragança, C.M.A. Silva, P.A.F. Martins, Hybrid metal additive manufacturing: A state–of–the-art review, Adv. Ind. Manuf. Eng. 2 (2021) 100032. https://doi.org/10.1016/j.aime.2021.100032.

[142] A.H. Alami, A. Ghani Olabi, A. Alashkar, S. Alasad, H. Aljaghoub, H. Rezk, M.A. Abdelkareem, Additive manufacturing in the aerospace and automotive industries: Recent trends and role in achieving sustainable development goals, Ain Shams Eng. J. 14 (2023) 102516. https://doi.org/10.1016/j.asej.2023.102516.

[143] M. Armstrong, H. Mehrabi, N. Naveed, An overview of modern metal additive manufacturing technology, J. Manuf. Process. 84 (2022) 1001–1029. https://doi.org/10.1016/j.jmapro.2022.10.060.

[144] S. Mirzababaei, S. Pasebani, A Review on Binder Jet Additive Manufacturing of 316L Stainless Steel, J. Manuf. Mater. Process. 3 (2019) 82. https://doi.org/10.3390/jmmp3030082.

[145] A. Mostafaei, A.M. Elliott, J.E. Barnes, F. Li, W. Tan, C.L. Cramer, P. Nandwana, M. Chmielus, Binder jet 3D printing—Process parameters, materials, properties, modeling, and challenges, Prog. Mater. Sci. 119 (2021) 100707. https://doi.org/10.1016/j.pmatsci.2020.100707.

[146] ISO/ASTM 52900:2021(en), Additive manufacturing — General principles — Fundamentals and vocabulary, (n.d.). https://www.iso.org/obp/ui/en/#iso:std:iso-astm:52900:ed-2:v1:en (accessed October 24, 2023).

[147] K. Li, W. Chen, N. Gong, H. Pu, J. Luo, D.Z. Zhang, L.E. Murr, A critical review on wire-arc directed energy deposition of high-performance steels, J. Mater. Res. Technol. 24 (2023) 9369–9412. https://doi.org/10.1016/j.jmrt.2023.05.163.

[148] A.U.H. Mohsan, M. Zhang, D. Wang, S. Zhao, Y. Wang, C. Chen, J. Zhang, State-of-the-art review on the Ultrasonic Vibration Assisted Laser Cladding (UVALC), J. Manuf. Process. 107 (2023) 422–446. https://doi.org/10.1016/j.jmapro.2023.10.066.

[149] N. Haghdadi, M. Laleh, M. Moyle, S. Primig, Additive manufacturing of steels: a review of achievements and challenges, J. Mater. Sci. 56 (2021) 64–107. https://doi.org/10.1007/s10853-020-05109-0.

[150] N.K. Bankapalli, V. Gupta, P. Saxena, A. Bajpai, C. Lahoda, J. Polte, Filament fabrication and subsequent additive manufacturing, debinding, and sintering for extrusion-based metal additive manufacturing and their applications: A review, Compos. Part B Eng. 264 (2023) 110915. https://doi.org/10.1016/j.compositesb.2023.110915.

[151] X. Ang, J.Y. Tey, W.H. Yeo, K.P.Y. Shak, A review on metallic and ceramic material extrusion method: Materials, rheology, and printing parameters, J. Manuf. Process. 90 (2023) 28–42. https://doi.org/10.1016/j.jmapro.2023.01.077.

[152] K. Fellah, M.H. Mechkouri, H. Azzouzi, K. Reklaoui, Effects of 316L Steel Powder Recycling on Manufactured Parts by Selective Laser Melting Process: A Review, in: K. Zarbane, Z. Beidouri (Eds.), Proc. CASICAM 2022, Springer Nature Switzerland, Cham, 2023: pp. 73–80. https://doi.org/10.1007/978-3-031-32927-2_7.

[153] A. Amado, M. Schmid, G. Levy, K. Wegener, Advances in SLS Powder Characterization, (2011). https://doi.org/10.26153/TSW/15306.

[154] M. Srivastava, S. Rathee, V. Patel, A. Kumar, P.G. Koppad, A review of various materials for additive manufacturing: Recent trends and processing issues, J. Mater. Res. Technol. 21 (2022) 2612–2641. https://doi.org/10.1016/j.jmrt.2022.10.015.

[155] A. Saboori, A. Aversa, G. Marchese, S. Biamino, M. Lombardi, P. Fino, Microstructure and Mechanical Properties of AISI 316L Produced by Directed Energy Deposition-Based Additive Manufacturing: A Review, Appl. Sci. 10 (2020) 3310. https://doi.org/10.3390/app10093310.

[156] S. Spiller, S.O. Kolstad, N. Razavi, Fabrication and characterization of 316L stainless steel components printed with material extrusion additive manufacturing, Procedia Struct. Integr. 42 (2022) 1239–1248. https://doi.org/10.1016/j.prostr.2022.12.158.

[157] C. Zhang, Y. Yuan, C. Shi, J. Chen, Material extrusion-based fabrication of 316L stainless steel: analysis of debinding and sintering, mechanical properties, and corrosion resistance, Int. J. Adv. Manuf. Technol. 129 (2023) 587–599. https://doi.org/10.1007/s00170-023-12309-w.

[158] J. Fu, H. Li, X. Song, M.W. Fu, Multi-scale defects in powder-based additively manufactured metals and alloys, J. Mater. Sci. Technol. 122 (2022) 165–199. https://doi.org/10.1016/j.jmst.2022.02.015.

[159] Q. Liu, J. Lu, Z. Luo, J. Yi, M. He, Y. Zhao, S. Wang, Enhancing corrosion resistance of additively manufactured 316L stainless steel by fabricating pillar arrays, Mater. Des. 230 (2023) 111940. https://doi.org/10.1016/j.matdes.2023.111940.

[160] K. Li, T. Yang, N. Gong, J. Wu, X. Wu, D.Z. Zhang, L.E. Murr, Additive manufacturing of ultra-high strength steels: A review, J. Alloys Compd. 965 (2023) 171390. https://doi.org/10.1016/j.jallcom.2023.171390.

[161] F. Zhang, L. Zhu, Z. Li, S. Wang, J. Shi, W. Tang, N. Li, J. Yang, The recent development of vat photopolymerization: A review, Addit. Manuf. 48 (2021) 102423. https://doi.org/10.1016/j.addma.2021.102423.

[162] K. Zhang, Q. Meng, Z. Qu, R. He, A review of defects in vat photopolymerization additive-manufactured ceramics: Characterization, control, and challenges, J. Eur. Ceram. Soc. (2023). https://doi.org/10.1016/j.jeurceramsoc.2023.10.067.

[163] W.P. Ryan-Johnson, L.C. Wolfe, C.R. Byron, J.K. Nagel, H. Zhang, A Systems Approach of Topology Optimization for Bioinspired Material Structures Design Using Additive Manufacturing, Sustainability 13 (2021) 8013. https://doi.org/10.3390/su13148013.

[164] M. Mukhtarkhanov, A. Perveen, D. Talamona, Application of Stereolithography Based 3D Printing Technology in Investment Casting, Micromachines 11 (2020) 946. https://doi.org/10.3390/mi11100946.

[165] A.A. Luo, A.K. Sachdev, D. Apelian, Alloy development and process innovations for light metals casting, J. Mater. Process. Technol. 306 (2022) 117606. https://doi.org/10.1016/j.jmatprotec.2022.117606.

[166] I.N. Hollis, STEEL CASTINGS, J. Am. Soc. Nav. Eng. 1 (2009) 193–206. https://doi.org/10.1111/j.1559-3584.1889.tb05750.x.

[167] S. Boonmee, D. Stefanescu, Casting Skin Management in Compacted Graphite Iron - Part I: Effect of Mold Coating and Section Thickness, in: Trans. Am. Foundry Soc, 2013: pp. 435–448.

[168] Y.-C. Cheng, G.-Y. Yang, S.-L. Lü, S.-J. Liu, W.-Q. Jie, Study on microstructures and mechanical properties of plaster mould casting aluminum alloy under the condition of vacuum pressurizing solidification and vacuum solidification, Zhuzao/Foundry 63 (2014) 10–14.

[169] G. Baumeister, B. Okolo, J. Rögner, Microcasting of Al bronze: influence of casting parameters on the microstructure and the mechanical properties, Microsyst. Technol. 14 (2008) 1647–1655. https://doi.org/10.1007/s00542-008-0605-4.

[170] A. Hamasaiid, M.S. Dargusch, G. Dour, The impact of the casting thickness on the interfacial heat transfer and solidification of the casting during permanent mold casting of an A356 alloy, J. Manuf. Process. 47 (2019) 229–237. https://doi.org/10.1016/j.jmapro.2019.09.039.

[171] E. Aykac, M. Turkmen, Investigation of the Biocompatibility of Laser Treated 316L Stainless Steel Materials, Coatings 12 (2022) 1821. https://doi.org/10.3390/coatings12121821.

[172] H. Ding, X. Jin, T. Chen, H. Li, Study on Casting Defect Control of Austenitic 304 Complex Structural Parts, Int. J. Met. 17 (2023) 1427–1438. https://doi.org/10.1007/s40962-022-00865-y.

[173] J. Singh, R. Singh, H. Singh, Surface roughness prediction using Buckingham's Pi-theorem for SS-316L hip implant prepared as rapid investment casting, Mater. Today Proc. 5 (2018) 18080–18088. https://doi.org/10.1016/j.matpr.2018.06.142.

[174] T. Sivarupan, N. Balasubramani, P. Saxena, D. Nagarajan, M. El Mansori, K. Salonitis, M. Jolly, M.S. Dargusch, A review on the progress and challenges of binder jet 3D printing of sand moulds for advanced casting, Addit. Manuf. 40 (2021) 101889. https://www.sciencedirect.com/science/article/pii/S2214860421000543 (accessed September 13, 2022).

[175] S. Eshkabilov, I. Ara, I. Sevostianov, F. Azarmi, X. Tangpong, Mechanical and thermal properties of stainless steel parts, manufactured by various technologies, in relation to their microstructure, Int. J. Eng. Sci. 159 (2021) 103398. https://doi.org/10.1016/j.ijengsci.2020.103398.

[176] M. Blair, Cast Stainless Steels, in: ASM Handbook Committee (Ed.), Prop. Sel. Irons Steels High-Perform. Alloys, ASM International, 1990: pp. 908–929. https://doi.org/10.31399/asm.hb.v01.a0001047.

[177] L.D.D. Harvey, Iron and steel recycling: Review, conceptual model, irreducible mining requirements, and energy implications, Renew. Sustain. Energy Rev. 138 (2021) 110553. https://doi.org/10.1016/j.rser.2020.110553.

[178] C.M. Cheah, C.K. Chua, C.W. Lee, C. Feng, K. Totong, Rapid prototyping and tooling techniques: a review of applications for rapid investment casting, Int. J. Adv. Manuf. Technol. 25 (2005) 308–320. https://doi.org/10.1007/s00170-003-1840-6.

[179] P. Kapranos, C. Carney, A. Pola, M. Jolly, 5.03 - Advanced Casting Methodologies: Investment Casting, Centrifugal Casting, Squeeze Casting, Metal Spinning, and Batch Casting, in: S. Hashmi, G.F. Batalha, C.J. Van Tyne, B. Yilbas (Eds.), Compr. Mater. Process., Elsevier, Oxford, 2014: pp. 39–67. https://doi.org/10.1016/B978-0-08-096532-1.00539-2.

[180] P. Kapranos, Current State of Semi-Solid Net-Shape Die Casting, Metals 9 (2019) 1301. https://doi.org/10.3390/met9121301.

[181] A.S. Chaus, M. Bračík, M. Sahul, M. Dománková, Microstructure and properties of M2 high-speed steel cast by the gravity and vacuum investment casting, Vacuum 162 (2019) 183–198. https://doi.org/10.1016/j.vacuum.2019.01.041.

[182] M. Ahmadein, A.H. Elsheikh, N.A. Alsaleh, Modeling of cooling and heat conduction in permanent mold casting process, Alex. Eng. J. 61 (2022) 1757–1768. https://doi.org/10.1016/j.aej.2021.06.048.

[183] A.D. Pradeep, T. Rameshkumar, Review on centrifugal casting of functionally graded materials, Mater. Today Proc. 45 (2021) 729–734. https://doi.org/10.1016/j.matpr.2020.02.764.

[184] European Investment Casters' Federation, Eur. Invest. Casters' Fed. (n.d.). https://eicf.org/ (accessed November 6, 2023).

[185] Barron Industries | Metal Foundry | Precision Investment Casting, Barron Ind. (n.d.). https://www.barron-industries.com/ (accessed November 6, 2023).

[186] Home - Manufacturer of Precision Casting and Machining Components, Impro Precis. (n.d.). https://www.improprecision.com/ (accessed November 6, 2023).

[187] Investment Casting Foundry | Investment Casting Company | Manufacturer Hollister, California, Am. Cast. Co. (n.d.). https://americancastingco.com/ (accessed November 6, 2023).

[188] CFS Foundry - Investment Casting & Die Casting Company, (2023). https://www.investmentcastchina.com/ (accessed November 6, 2023).

[189] A propos de Sculpteo et de l'impression 3D, Sculpteo (n.d.). https://www.sculpteo.com/fr/about/ (accessed November 6, 2023).

[190] On-Demand Manufacturing for Enterprise Scale Businesses | Xometry, (n.d.). https://www.xometry.com/xometry-enterprise/ (accessed November 6, 2023).

[191] W.T. Choi, K. Oh, P.M. Singh, V. Breedveld, D.W. Hess, Hydrophobicity and Improved Localized Corrosion Resistance of Grain Boundary Etched Stainless Steel in Chloride-Containing Environment, J. Electrochem. Soc. 164 (2017) C61. https://doi.org/10.1149/2.1271702jes.

[192] J. Qu, C. Yu, R. Cui, J. Qin, H. Wang, Z. Cao, Preparation of super-hydrophobic and corrosion resistant colored films on chemically etched 304 stainless steel substrate, Surf. Coat. Technol. 354 (2018) 236–245. https://doi.org/10.1016/j.surfcoat.2018.09.022.

[193] W. Ma, M. Zhao, J. Zhao, Z. Guo, Y. Cui, H. Li, Preparation of superamphiphobic stainless steel surface by laser and perfluorooctanoic acid treatment, Opt. Laser Technol. 154 (2022) 108321. https://doi.org/10.1016/j.optlastec.2022.108321.

[194] Y. Wang, Z. Zhang, J. Xu, H. Yu, One-step method using laser for large-scale preparation of bionic superhydrophobic & drag-reducing fish-scale surface, Surf. Coat. Technol. 409 (2021) 126801. https://doi.org/10.1016/j.surfcoat.2020.126801.

[195] S. Zouaghi, T. Six, N. Nuns, P. Simon, S. Bellayer, S. Moradi, S.G. Hatzikiriakos, C. André, G. Delaplace, M. Jimenez, Influence of stainless steel surface properties on whey protein fouling under industrial processing conditions, J. Food Eng. 228 (2018) 38–49. https://doi.org/10.1016/j.jfoodeng.2018.02.009.

[196] N.U. Taskin, F. Ordu, Effect of etching duration on roughness and wettability of different carbon steel substrates, Mater. Chem. Phys. 257 (2021) 123746. https://doi.org/10.1016/j.matchemphys.2020.123746.

[197] M. Stöver, M. Renke-Gluszko, T. Schratzenstaller, J. Will, N. Klink, B. Behnisch, A. Kastrati, R. Wessely, J. Hausleiter, A. Schömig, E. Wintermantel, Microstructuring of

stainless steel implants by electrochemical etching, J. Mater. Sci. 41 (2006) 5569–5575. https://doi.org/10.1007/s10853-006-0257-7.

[198] E. Łyczkowska-Widłak, P. Lochyński, G. Nawrat, Electrochemical Polishing of Austenitic Stainless Steels, Materials 13 (2020) 2557. https://doi.org/10.3390/ma13112557.

[199] D. D'Andrea, Additive Manufacturing of AISI 316L Stainless Steel: A Review, Metals 13 (2023) 1370. https://doi.org/10.3390/met13081370.

[200] J. Sun, W. Wang, Z. Liu, B. Li, K. Xing, Z. Yang, Study on selective laser melting 316L stainless steel parts with superhydrophobic surface, Appl. Surf. Sci. 533 (2020) 147445. https://doi.org/10.1016/j.apsusc.2020.147445.

[201] W. Huang, B. Nelson, R. Mullennex, D. Kokabi, H. Hu, C. Eluchie, H. Hu, A. Samanta, H. Ding, Superhydrophobic surface processing for selective laser melting of metal parts, Procedia CIRP 108 (2022) 418–423. https://doi.org/10.1016/j.procir.2022.03.065.

[202] G. Kaur, A. Marmur, S. Magdassi, Fabrication of superhydrophobic 3D objects by Digital Light Processing, Addit. Manuf. 36 (2020) 101669. https://doi.org/10.1016/j.addma.2020.101669.

[203] A. S. , D.W.R. D. , A. Jain, J. Kandasamy, M. Singhal, Laser processing techniques for surface property enhancement: Focus on material advancement, Surf. Interfaces 42 (2023) 103293. https://doi.org/10.1016/j.surfin.2023.103293.

[204] A. Nouri, A. Rohani Shirvan, Y. Li, C. Wen, Additive manufacturing of metallic and polymeric load-bearing biomaterials using laser powder bed fusion: A review, J. Mater. Sci. Technol. 94 (2021) 196–215. https://doi.org/10.1016/j.jmst.2021.03.058.

[205] T. Delacroix, F. Lomello, F. Schuster, H. Maskrot, J.-P. Garandet, Influence of powder recycling on 316L stainless steel feedstocks and printed parts in laser powder bed fusion, Addit. Manuf. 50 (2022) 102553. https://doi.org/10.1016/j.addma.2021.102553.

[206] T. Phetrattanarangsi, C. Puncreobutr, A. Khamkongkaeo, C. Thongchai, B. Sakkomolsri, S. Kuimalee, P. Kidkhunthod, N. Chanlek, B. Lohwongwatana, The behavior of gypsum-bonded investment in the gold jewelry casting process, Thermochim. Acta 657 (2017) 144–150. https://doi.org/10.1016/j.tca.2017.09.008.

[207] L.B. Hunt, The long history of lost wax casting, Gold Bull. 13 (1980) 63–79. https://doi.org/10.1007/BF03215456.

[208] S. Pattnaik, D.B. Karunakar, P.K. Jha, Developments in investment casting process—A review, J. Mater. Process. Technol. 212 (2012) 2332–2348. https://doi.org/10.1016/j.jmatprotec.2012.06.003.

[209] M. Sigirisetty, Role of Additive Manufacturing in Investment Casting Process, Int. J. Res. Appl. Sci. Eng. Technol. 10 (2022) 278–286. https://doi.org/10.22214/ijraset.2022.41227.

[210] M. Upadhyay, T. Sivarupan, M. El Mansori, 3D printing for rapid sand casting—A review, J. Manuf. Process. 29 (2017) 211–220. https://doi.org/10.1016/j.jmapro.2017.07.017.

[211] A. Curodeau, E. Sachs, S. Caldarise, Design and fabrication of cast orthopedic implants with freeform surface textures from 3-D printed ceramic shell, J. Biomed. Mater. Res. 53 (2000) 525–535. https://doi.org/10.1002/1097-4636(200009)53:5<525::AID-JBM12>3.0.CO;2-1.

[212] G. Costanza, M.E. Tata, G. Trillicoso, Al foams manufactured by PLA replication and sacrifice, Int. J. Lightweight Mater. Manuf. 4 (2021) 62–66. https://doi.org/10.1016/j.ijlmm.2020.07.001.

[213] S. Ren, K. Bu, S. Mou, R. Zhang, B. Bai, Control of dimensional accuracy of hollow turbine blades during investment casting, J. Manuf. Process. 99 (2023) 548–562. https://doi.org/10.1016/j.jmapro.2023.05.077.

[214] G.L. Adabo, G.R. de Paula, F. Nogueira, L.M.G. Fais, O. Peitl, A quality assessment of titanium castings produced in an experimental short-heating-cycle investment, Mater. Res. 17 (2014) 420–426. https://doi.org/10.1590/S1516-14392013005000194.

[215] R.A. Kaminski, K.J. Anusavice, T. Okabe, P.K. Morse, P.E. Casteel, Castability of silver-base fixed partial denture alloys, J. Prosthet. Dent. 53 (1985) 329–332. https://doi.org/10.1016/0022-3913(85)90503-7.

[216] W. Naylor, B. Moore, R. Phillips, C. Goodacre, C. Muñoz, Comparison of two tests to determine the castability of dental alloys, Int. J. Prosthodont. 3 (1990) 413–24.

[217] K. Tajima, S. Matsuda, S. Kitajima, Y. Yokoyama, H. Kakigawa, Y. Kozono, Efficacy of gas purging for titanium casting, Dent. Mater. J. 13 (1994) 206–213. https://doi.org/10.4012/dmj.13.206.

[218] G. Ramesh, P. Ariga, T. Padmanabhan, R. Subramanian, Evaluation and comparison of castability between an indigenous and imported Ni-Cr alloy, Indian J. Dent. Res. 22 (2011) 733. https://doi.org/10.4103/0970-9290.93471.

[219] K.J. Qiu, Y. Liu, F.Y. Zhou, B.L. Wang, L. Li, Y.F. Zheng, Y.H. Liu, Microstructure, mechanical properties, castability and in vitro biocompatibility of Ti–Bi alloys developed for dental applications, Acta Biomater. 15 (2015) 254–265. https://doi.org/10.1016/j.actbio.2015.01.009.

[220] P.C.G. Oliveira, G.L. Adabo, R.F. Ribeiro, S.S. Rocha, The effect of mold temperature on castability of CP Ti and Ti–6Al–4V castings into phosphate bonded investment materials, Dent. Mater. 22 (2006) 1098–1102. https://doi.org/10.1016/j.dental.2005.09.004.

[221] W.-D. Kim, Y.-S. Na, Y.-T. Hyun, S.-W. Kim, J.-W. Park, J.-H. Kang, C.-Y. Kang, S.-E. Kim, A Study on Fluidity and Metal-Mold Reaction of Titanium Alloys, Sci. Adv. Mater. 9 (2017) 1929–1936. https://doi.org/10.1166/sam.2017.2822.

[222] M. Di Sabatino, L. Arnberg, Castability of aluminium alloys, Trans. Indian Inst. Met. 62 (2009) 321–325. https://doi.org/10.1007/s12666-009-0049-2.

[223] P. Popielarski, J. Hajkowski, R. Sika, Z. Ignaszak, Archives of Metallurgy and Materials, (2019). https://doi.org/10.24425/AMM.2019.130110.

[224] J. Shin, T. Kim, D. Kim, D. Kim, K. Kim, Castability and mechanical properties of new 7xxx aluminum alloys for automotive chassis/body applications, J. Alloys Compd. 698 (2017) 577–590. https://doi.org/10.1016/j.jallcom.2016.12.269.

[225] P. Giordano, Fluidity of Aluminium Foundry Alloys: Development of a Testing Procedure, (n.d.). https://core.ac.uk/reader/228810383 (accessed July 21, 2021).

[226] I. Watanabe, M. Woldu, K. Watanabe, T. Okabe, Effect of casting method on castability of titanium and dental alloys, J. Mater. Sci. Mater. Med. 11 (2000) 547–553. https://doi.org/10.1023/A:1008972018025.

[227] C. Deac, A. Gligor, L. Tarnu, Considerations on determining the castability of dental casting alloys, MATEC Web Conf. 178 (2018) 04009. https://doi.org/10.1051/matecconf/201817804009.

[228] M.F.F.A. Hamidi, W.S.W. Harun, M. Samykano, S.A.C. Ghani, Z. Ghazalli, F. Ahmad, A.B. Sulong, A review of biocompatible metal injection moulding process parameters for biomedical applications, Mater. Sci. Eng. C 78 (2017) 1263–1276. https://doi.org/10.1016/j.msec.2017.05.016.

[229] M. Roach, Base Metal Alloys Used for Dental Restorations and Implants, Dent. Clin. North Am. 51 (2007) 603–627. https://doi.org/10.1016/j.cden.2007.04.001.

[230] Y.K. Hu, W.M. Mao, J. Jing, X.M. Cheng, The High-Temperature Mechanical Properties of EN 1.4509 Stainless Steel Cast Using Investment Casting, J. Mater. Eng. Perform. 28 (2019) 6603–6613. https://doi.org/10.1007/s11665-019-04353-z.

[231] H. Najafi, J. Rassizadehghani, S. Norouzi, Mechanical properties of as-cast microalloyed steels produced via investment casting, Mater. Des. 32 (2011) 656–663. https://doi.org/10.1016/j.matdes.2010.08.007.

[232] Fusion 360 | Logiciel 3D de CAO, de FAO, d'IAO et de conception de circuits imprimés basé sur le cloud | Autodesk, (n.d.). https://www.autodesk.fr/products/fusion-360/overview (accessed December 29, 2023).

[233] K. Fedorov, K. Fayazbakhsh, C. Ravindran, Surface roughness and dimensional tolerances in A319 alloy samples produced by rapid investment casting process based on fused filament fabrication, Int. J. Adv. Manuf. Technol. 119 (2022) 4423–4437. https://doi.org/10.1007/s00170-021-08644-5.

[234] M. Di Sabatino, F. Syvertsen, L. Arnberg, A. Nordmark, An improved method for fluidity measurement by gravity casting of spirals in sand moulds, Int. J. Cast Met. Res. 18 (2005) 59–62. https://doi.org/10.1179/136404605225022865.

[235] S. Li, X. Yue, Q. Li, H. Peng, B. Dong, T. Liu, H. Yang, J. Fan, S. Shu, F. Qiu, Q. Jiang, Development and applications of aluminum alloys for aerospace industry, J. Mater. Res. Technol. 27 (2023) 944–983. https://doi.org/10.1016/j.jmrt.2023.09.274.

[236] F. Gallien, V. Gass, A. Mortensen, Investment casting of periodic aluminum cellular structures using slurry-cast table salt moulds, Mater. Des. 215 (2022) 110488. https://doi.org/10.1016/j.matdes.2022.110488.

[237] C. Ji, H. Huang, T. Wang, Q. Huang, Recent advances and future trends in processing methods and characterization technologies of aluminum foam composite structures: A review, J. Manuf. Process. 93 (2023) 116–152. https://doi.org/10.1016/j.jmapro.2023.03.015.

[238] M. de Beer, J.P. Maree, L. Liebenberg, F.J. Doucet, Conversion of calcium sulphide to calcium carbonate during the process of recovery of elemental sulphur from gypsum waste, Waste Manag. 34 (2014) 2373–2381. https://doi.org/10.1016/j.wasman.2014.07.010.

[239] J.M. Molina, R. Voytovych, E. Louis, N. Eustathopoulos, The surface tension of liquid aluminium in high vacuum: The role of surface condition, Int. J. Adhes. Adhes. 27 (2007) 394–401. https://doi.org/10.1016/j.ijadhadh.2006.09.006.

[240] L.-D. LUCAS, Viscosité des principaux métaux et métalloïdes, Ref TIP551WEB - Étude Propr. Métaux (1984). http://www.techniques.ingenieur.fr/base-documentaire/materiaux-th11/bases-de-donnees-materiaux-metalliques-42584210/viscosite-des-principaux-metaux-et-metalloides-m66/ (accessed March 29, 2021).

[241] L. Battezzati, A.L. Greer, The viscosity of liquid metals and alloys, Acta Metall. 37 (1989) 1791–1802. https://doi.org/10.1016/0001-6160(89)90064-3.

[242] L. Cheng, L. Zhang, Y. Ren, Wettability between 304 stainless steel and refractory materials, J. Mater. Res. Technol. 9 (2020) 5784–5793. https://doi.org/10.1016/j.jmrt.2020.03.103.

[243] H. Fukuyama, H. Higashi, H. Yamano, Thermophysical Properties of Molten Stainless Steel Containing 5 mass % B4C, Nucl. Technol. 205 (2019) 1154–1163. https://doi.org/10.1080/00295450.2019.1578572.

[244] B.U.E. Klotz, T. Drago, The Role of Process Parameters in Platinum Casting, Platin. Met. Rev. 55 (2011) 20–27. https://doi.org/10.1595/147106711X540373.

[245] J. Campbell, The 10 Rules for good castings, in: Complete Cast. Handb., Elsevier, 2011: pp. 605–737. https://doi.org/10.1016/B978-1-85617-809-9.10010-6.

[246] J. Campbell, Molds and cores, in: Complete Cast. Handb., Elsevier, 2011: pp. 155–186. https://doi.org/10.1016/B978-1-85617-809-9.10004-0.

[247] J. Campbell, Melting, Remelting, and Casting for Clean Steel, Steel Res. Int. 88 (2017) 1600093. https://doi.org/10.1002/srin.201600093.

[248] A. Babich, D. Senk, Coke in the iron and steel industry, in: New Trends Coal Convers., Elsevier, 2019: pp. 367–404. https://doi.org/10.1016/B978-0-08-102201-6.00013-3.

[249] I. Goto, K. Kurosawa, T. Matsuki, Effect of 3D-printed sand molds on the soundness of pure copper castings in the vicinity of as-cast surfaces, J. Manuf. Process. 77 (2022) 329–338. https://doi.org/10.1016/j.jmapro.2022.03.020.

[250] W. Yan, A. Schmidt, S. Dudczig, T. Wetzig, Y. Wei, Y. Li, S. Schafföner, C.G. Aneziris, Wettability phenomena of molten steel in contact with alumina substrates with alumina and alumina-carbon coatings, J. Eur. Ceram. Soc. 38 (2018) 2164–2178. https://doi.org/10.1016/j.jeurceramsoc.2017.12.001.

[251] H. Buscail, S.E. Messki, F. Riffard, S. Perrier, R. Cueff, E. Caudron, C. Issartel, Characterization of the oxides formed at 1000°C on the AISI 316L stainless steel—Role of molybdenum, Mater. Chem. Phys. 111 (2008) 491–496. https://doi.org/10.1016/j.matchemphys.2008.04.054.

[252] M. Da Cunha Belo, M. Walls, N.E. Hakiki, J. Corset, E. Picquenard, G. Sagon, D. Noël, Composition, structure and properties of the oxide films formed on the stainless steel 316L in a primary type PWR environment, Corros. Sci. 40 (1998) 447–463. https://doi.org/10.1016/S0010-938X(97)00158-3.

[253] J.T. Ok, E. Lopez-On˜a, H. Wong, S. Park, Effect of Surface Wetting of Micro/Nano Ratchets on Leidenfrost Liquid Drop Motion, in: ASME 2009 7th Int. Conf. Nanochannels Microchannels Minichannels, ASMEDC, Pohang, South Korea, 2009: pp. 1037–1041. https://doi.org/10.1115/ICNMM2009-82173.

[254] A. Kumar, M. kumar, A. Alok, M. Das, Surface Texturing by Electrochemical Micromachining: A Review, IOP Conf. Ser. Mater. Sci. Eng. 804 (2020) 012011. https://doi.org/10.1088/1757-899X/804/1/012011.

[255] B. Bhushan, M. Caspers, An overview of additive manufacturing (3D printing) for microfabrication, Microsyst. Technol. 23 (2017) 1117–1124. https://doi.org/10.1007/s00542-017-3342-8.

[256] M. Vaezi, H. Seitz, S. Yang, A review on 3D micro-additive manufacturing technologies, Int. J. Adv. Manuf. Technol. 67 (2013) 1721–1754. https://doi.org/10.1007/s00170-012-4605-2.

[257] Y. Wang, Y. Zhou, L. Lin, J. Corker, M. Fan, Overview of 3D additive manufacturing (AM) and corresponding AM composites, Compos. Part Appl. Sci. Manuf. 139 (2020) 106114. https://doi.org/10.1016/j.compositesa.2020.106114.

[258] Z. Huang, G. Shao, L. Li, Micro/nano functional devices fabricated by additive manufacturing, Prog. Mater. Sci. 131 (2023) 101020. https://doi.org/10.1016/j.pmatsci.2022.101020.

[259] P. Jagadeesh, M. Puttegowda, S.M. Rangappa, K. Alexey, S. Gorbatyuk, A. Khan, M. Doddamani, S. Siengchin, A comprehensive review on 3D printing advancements in polymer composites: technologies, materials, and applications, Int. J. Adv. Manuf. Technol. 121 (2022) 127–169. https://doi.org/10.1007/s00170-022-09406-7.

[260] T.D. Ngo, A. Kashani, G. Imbalzano, K.T.Q. Nguyen, D. Hui, Additive manufacturing (3D printing): A review of materials, methods, applications and challenges, Compos. Part B Eng. 143 (2018) 172–196. https://doi.org/10.1016/j.compositesb.2018.02.012.

[261] H. Shams, K. Basit, M.A. Khan, S. Saleem, A. Mansoor, Realizing surface amphiphobicity using 3D printing techniques: A critical move towards manufacturing low-cost reentrant geometries, Addit. Manuf. 38 (2021) 101777. https://doi.org/10.1016/j.addma.2020.101777.

[262] L. Borasi, E. Casamenti, R. Charvet, C. Dénéréaz, S. Pollonghini, L. Deillon, T. Yang, F. Ebrahim, A. Mortensen, Y. Bellouard, 3D metal freeform micromanufacturing, J. Manuf. Process. 68 (2021) 867–876. https://doi.org/10.1016/j.jmapro.2021.06.002.

[263] L. Ammosova, K. Mönkkönen, M. Suvanto, Precise fabrication of microtextured stainless steel surfaces using metal injection moulding, Precis. Eng. 62 (2020) 89–94. https://doi.org/10.1016/j.precisioneng.2019.11.012.

[264] M.N.A. Aziz, Rusnaldy, P. Munyensanga, S.A. Widyanto, Paryanto, Application of lost wax casting for manufacturing of orthopedic screw: a review, Procedia CIRP 78 (2018) 149–154. https://doi.org/10.1016/j.procir.2018.08.304.

[265] Y. Shan, A. Krishnakumar, Z. Qin, H. Mao, Reducing lateral stair-stepping defects in liquid crystal display-based vat photopolymerization by defocusing the image pattern, Addit. Manuf. 52 (2022) 102653. https://doi.org/10.1016/j.addma.2022.102653.

[266] K. Kowsari, B. Zhang, S. Panjwani, Z. Chen, H. Hingorani, S. Akbari, N.X. Fang, Q. Ge, Photopolymer formulation to minimize feature size, surface roughness, and stair-stepping in digital light processing-based three-dimensional printing, Addit. Manuf. 24 (2018) 627–638. https://doi.org/10.1016/j.addma.2018.10.037.

[267] G.N. S, B.R.R. J, Performance enhancement of futuristic airplanes by nature inspired biomimetic fish scale arrays—A design approach, Biomim. Intell. Robot. 2 (2022) 100045. https://doi.org/10.1016/j.birob.2022.100045.

[268] M. Depetris-Wery, Décapage en milieu aqueux, Tech. L'Ingénieur (2019). https://www.techniques-ingenieur.fr/base-documentaire/materiaux-th11/traitements-de-surface-des-metaux-controle-et-preparation-42362210/decapage-en-milieu-aqueux-m1455/ (accessed October 2, 2019).

[269] A.L. Cabrera, J.F. Kirner, Formation of silicon diffusion coatings on ferrous alloys from their reaction with silane, Surf. Coat. Technol. 39–40 (1989) 43–51. https://doi.org/10.1016/0257-8972(89)90039-X.

[270] E. Frutos, P. Adeva, J.L. González-Carrasco, P. Pérez, Oxidation behavior of AISI 316 steel coated by hot dipping in an Al–Si alloy, Surf. Coat. Technol. 236 (2013) 188–199. https://doi.org/10.1016/j.surfcoat.2013.09.046.

[271] P. Hussain, A. Isnin, Joining of austenitic stainless steel and ferritic stainless steel to sialon, J. Mater. Process. Technol. 113 (2001) 222–227. https://doi.org/10.1016/S0924-0136(01)00640-9.

[272] V. Rohr, M. Schütze, E. Fortuna, D. n. Tsipas, A. Milewska, F. j. Pérez, Development of novel diffusion coatings for 9–12 % Cr ferritic-martensitic steels, Mater. Corros. 56 (2005) 874–881. https://doi.org/10.1002/maco.200503918.

[273] Z. Wang, N.A. Xu, M.X. Huang, Phase transformation and carbon profile at the interface between Al-Si coating and steel substrate in a press-hardened steel, Materialia 20 (2021) 101268. https://doi.org/10.1016/j.mtla.2021.101268.

[274] G. Rajamurugan, P.K. Ghosh, K. Prabu, D. Dinesh, S.M. Vinukumar, Dendrite Morphological Analysis on SMA, GMA, and PGMA Welding of Dissimilar 304LN Austenitic Stainless Steel and Micro-alloyed Steel, Trans. Indian Inst. Met. 73 (2020) 595–611. https://doi.org/10.1007/s12666-020-01871-6.

[275] J.W. Fu, Y.S. Yang, J.J. Guo, J.C. Ma, W.H. Tong, Formation of two-phase coupled microstructure in AISI 304 stainless steel during directional solidification, J. Mater. Res. 24 (2009) 2385–2390. https://doi.org/10.1557/jmr.2009.0282.

[276] S.N. Lekakh, R. O'malley, M. Emmendorfer, B. Hrebec, Control of Columnar to Equiaxed Transition in Solidification Macrostructure of Austenitic Stainless Steel Castings, ISIJ Int. 57 (2017) 824–832. https://doi.org/10.2355/isijinternational.ISIJINT-2016-684.

[277] M. Tümer, C. Schneider-Bröskamp, N. Enzinger, Fusion welding of ultra-high strength structural steels – A review, J. Manuf. Process. 82 (2022) 203–229. https://doi.org/10.1016/j.jmapro.2022.07.049.

[278] C.H. Kung, B. Zahiri, P.K. Sow, W. Mérida, On-demand oil-water separation via low-voltage wettability switching of core-shell structures on copper substrates, Appl. Surf. Sci. 444 (2018) 15–27. https://doi.org/10.1016/j.apsusc.2018.02.238.

[279] A. Taleb, C. Mangeney, V. Ivanova, Electrochemical synthesis using a self-assembled Au nanoparticle template of dendritic films with unusual wetting properties, Nanotechnology 22 (2011) 205301. https://doi.org/10.1088/0957-4484/22/20/205301.

[280] P. Wang, D. Zhang, R. Qiu, Extreme wettability due to dendritic copper nanostructure via electrodeposition, Appl. Surf. Sci. 257 (2011) 8438–8442. https://doi.org/10.1016/j.apsusc.2011.04.126.

[281] V. Hejazi, A.D. Moghadam, P. Rohatgi, M. Nosonovsky, Beyond Wenzel and Cassie–Baxter: Second-Order Effects on the Wetting of Rough Surfaces, Langmuir 30 (2014) 9423–9429. https://doi.org/10.1021/la502143v.

[282] C. Peng, T. Izawa, L. Zhu, K. Kuroda, M. Okido, Tailoring Surface Hydrophilicity Property for Biomedical 316L and 304 Stainless Steels: A Special Perspective on Studying Osteoconductivity and Biocompatibility, ACS Appl. Mater. Interfaces 11 (2019) 45489–45497. https://doi.org/10.1021/acsami.9b17312.

[283] S.Y. Misyura, G.V. Kuznetsov, D.V. Feoktistov, R.S. Volkov, V.S. Morozov, E.G. Orlova, The influence of the surface microtexture on wettability properties and drop evaporation, Surf. Coat. Technol. 375 (2019) 458–467. https://doi.org/10.1016/j.surfcoat.2019.07.058.

[284] E. Lugscheider, K. Bobzin, M. Möller, The effect of PVD layer constitution on surface free energy, Thin Solid Films 355–356 (1999) 367–373. https://doi.org/10.1016/S0040-6090(99)00543-X.

[285] Y. Wei, F. Wang, Z. Guo, Bio-inspired and metal-derived superwetting surfaces: Function, stability and applications, Adv. Colloid Interface Sci. 314 (2023) 102879. https://doi.org/10.1016/j.cis.2023.102879.

[286] F. Sotoudeh, S.M. Mousavi, N. Karimi, B.J. Lee, J. Abolfazli-Esfahani, M.K.D. Manshadi, Natural and synthetic superhydrophobic surfaces: A review of the fundamentals, structures, and applications, Alex. Eng. J. 68 (2023) 587–609. https://doi.org/10.1016/j.aej.2023.01.058.

[287] N.J. Shirtcliffe, G. McHale, S. Atherton, M.I. Newton, An introduction to superhydrophobicity, Adv. Colloid Interface Sci. 161 (2010) 124–138. https://doi.org/10.1016/j.cis.2009.11.001.

[288] A. Cannon, Investigating wetting characteristics on microstructured surfaces for superhydrophobicity and metal microcasting, (2010).

[289] A. Chakraborty, A.T. Mulroney, M.C. Gupta, Superhydrophobic Surfaces by Microtexturing: A Critical Review, in: K.L. Mittal (Ed.), Prog. Adhes. Adhes., 1st ed., Wiley, 2021: pp. 621–649. https://doi.org/10.1002/9781119846703.ch14.

[290] W. Ma, M. Zhao, J. Zhao, Z. Guo, Y. Cui, H. Li, Preparation of superamphiphobic stainless steel surface by laser and perfluorooctanoic acid treatment, Opt. Laser Technol. 154 (2022) 108321. https://doi.org/10.1016/j.optlastec.2022.108321.

[291] D.K. Wainwright, G.V. Lauder, Chaptre 10, Mucus Matters: The Slippery and Complex Surfaces of Fish, in: Funct. Surf. Bioogy III Divers. Phys. Phenom., Springer, 2017.

[292] Y. Liu, X. He, C. Yuan, P. Cao, X. Bai, Antifouling applications and fabrications of biomimetic micro-structured surfaces: a review, J. Adv. Res. (2023) S2090123223002357. https://doi.org/10.1016/j.jare.2023.08.019.

[293] Preparation and anti-corrosion Properties of SiO2@MWCNTs@PFOTES Superhydrophobic Coatings on Magnesium Alloy, Int. J. Electrochem. Sci. (2022) ArticleID:220129. https://doi.org/10.20964/2022.01.31.

[294] P. Wang, Z. Lu, D. Zhang, Slippery liquid-infused porous surfaces fabricated on aluminum as a barrier to corrosion induced by sulfate reducing bacteria, Corros. Sci. 93 (2015) 159–166. https://doi.org/10.1016/j.corsci.2015.01.015.

[295] Q. He, K. Li, Z. Xu, J. Wang, X. Wang, A. Li, Research progress on construction strategy and technical evaluation of aircraft icing accretion protection system, Chin. J. Aeronaut. (2023) S1000936123002339. https://doi.org/10.1016/j.cja.2023.07.003.

[296] Z. Zhu, Y. Zhang, D.-W. Sun, Biomimetic modification of freezing facility surfaces to prevent icing and frosting during freezing for the food industry, Trends Food Sci. Technol. 111 (2021) 581–594. https://doi.org/10.1016/j.tifs.2021.02.034.

[297] S. Yang, R. Qiu, H. Song, P. Wang, Z. Shi, Y. Wang, Slippery liquid-infused porous surface based on perfluorinated lubricant/iron tetradecanoate: Preparation and corrosion protection application, Appl. Surf. Sci. 328 (2015) 491–500. https://doi.org/10.1016/j.apsusc.2014.12.067.

[298] A.S.M. de Freitas, C.C. Maciel, J.S. Rodrigues, R.P. Ribeiro, A.O. Delgado-Silva, E.C. Rangel, Organosilicon films deposited in low-pressure plasma from hexamethyldisiloxane — A review, Vacuum 194 (2021) 110556. https://doi.org/10.1016/j.vacuum.2021.110556.

[299] C. Tendero, C. Tixier, P. Tristant, J. Desmaison, P. Leprince, Atmospheric pressure plasmas: A review, Spectrochim. Acta Part B At. Spectrosc. 61 (2006) 2–30. https://doi.org/10.1016/j.sab.2005.10.003.

[300] D. Merche, N. Vandencasteele, F. Reniers, Atmospheric plasmas for thin film deposition: A critical review, Thin Solid Films 520 (2012) 4219–4236. https://doi.org/10.1016/j.tsf.2012.01.026.

[301] A. Schutze, J.Y. Jeong, S.E. Babayan, J. Park, G.S. Selwyn, R.F. Hicks, The atmospheric-pressure plasma jet: a review and comparison to other plasma sources, IEEE Trans. Plasma Sci. 26 (1998) 1685–1694. https://doi.org/10.1109/27.747887.

[302] W. Crookes, Modern Views on Matter: The Realization of a Dream, Science 17 (1903) 993–1003. https://doi.org/10.1126/science.17.443.993.

[303] I. Langmuir, Oscillations in Ionized Gases, Proc. Natl. Acad. Sci. U. S. A. 14 (1928) 627–637. https://www.jstor.org/stable/85270 (accessed November 20, 2023).

[304] L. Tonks, The Birth of "Plasma," Am. J. Phys. 35 (1967) 857–858. https://doi.org/10.1119/1.1974266.

[305] C. Cimarelli, K. Genareau, A review of volcanic electrification of the atmosphere and volcanic lightning, J. Volcanol. Geotherm. Res. 422 (2022) 107449. https://doi.org/10.1016/j.jvolgeores.2021.107449.

[306] D. Siingh, R.P. Singh, S. Kumar, T. Dharmaraj, A.K. Singh, A.K. Singh, M.N. Patil, S. Singh, Lightning and middle atmospheric discharges in the atmosphere, J. Atmospheric Sol.-Terr. Phys. 134 (2015) 78–101. https://doi.org/10.1016/j.jastp.2015.10.001.

[307] M.C. Kelley, IONOSPHERE, in: J.R. Holton (Ed.), Encycl. Atmospheric Sci., Academic Press, Oxford, 2003: pp. 1022–1030. https://doi.org/10.1016/B0-12-227090-8/00184-6.

[308] W. De-jin, C. Ling, Plasma Astrophysics and Modern Plasma Cosmology, Chin. Astron. Astrophys. 47 (2023) 490–535. https://doi.org/10.1016/j.chinastron.2023.09.003.

[309] A.I. Shumeiko, V.D. Telekh, V.I. Mayorova, Development of a novel wave plasma propulsion module with six-directional thrust vectoring capability, Acta Astronaut. 191 (2022) 431–437. https://doi.org/10.1016/j.actaastro.2021.11.028.

[310] Y. Xu, A general comparison between tokamak and stellarator plasmas, Matter Radiat. Extrem. 1 (2016) 192–200. https://doi.org/10.1016/j.mre.2016.07.001.

[311] Z.M. Liu, S. Cui, Z. Luo, C. Zhang, Z. Wang, Y. Zhang, Plasma arc welding: Process variants and its recent developments of sensing, controlling and modeling, J. Manuf. Process. 23 (2016) 315–327. https://doi.org/10.1016/j.jmapro.2016.04.004.

[312] E. Akdoğan, H.T. Şirin, Plasma surface modification strategies for the preparation of antibacterial biomaterials: A review of the recent literature, Mater. Sci. Eng. C 131 (2021) 112474. https://doi.org/10.1016/j.msec.2021.112474.

[313] A. Haji, M. Naebe, Cleaner dyeing of textiles using plasma treatment and natural dyes: A review, J. Clean. Prod. 265 (2020) 121866. https://doi.org/10.1016/j.jclepro.2020.121866.

[314] C. Karthik, S. Rajalakshmi, S. Thomas, V. Thomas, Intelligent polymeric biomaterials surface driven by plasma processing, Curr. Opin. Biomed. Eng. 26 (2023) 100440. https://doi.org/10.1016/j.cobme.2022.100440.

[315] J.A. Oke, T.-C. Jen, Atomic layer deposition and other thin film deposition techniques: from principles to film properties, J. Mater. Res. Technol. 21 (2022) 2481–2514. https://doi.org/10.1016/j.jmrt.2022.10.064.

[316] E. Santecchia, A.M.S. Hamouda, F. Musharavati, E. Zalnezhad, M. Cabibbo, S. Spigarelli, Wear resistance investigation of titanium nitride-based coatings, Ceram. Int. 41 (2015) 10349–10379. https://doi.org/10.1016/j.ceramint.2015.04.152.

[317] F. Liang, J. Yang, Y. Zhao, Y. Zhou, Z. Yan, J. He, Q. Yuan, J. Wu, P. Liu, Z. Zhong, M. Han, A review of thin film electrolytes fabricated by physical vapor deposition for solid oxide fuel cells, Int. J. Hydrog. Energy 47 (2022) 36926–36952. https://doi.org/10.1016/j.ijhydene.2022.08.237.

[318] F.G. Aras, A. Yilmaz, H.G. Tasdelen, A. Ozden, F. Ay, N.K. Perkgoz, A. Yeltik, A review on recent advances of chemical vapor deposition technique for monolayer transition metal dichalcogenides (MX2: Mo, W; S, Se, Te), Mater. Sci. Semicond. Process. 148 (2022) 106829. https://doi.org/10.1016/j.mssp.2022.106829.

[319] N. Schalk, M. Tkadletz, C. Mitterer, Hard coatings for cutting applications: Physical vs. chemical vapor deposition and future challenges for the coatings community, Surf. Coat. Technol. 429 (2022) 127949. https://doi.org/10.1016/j.surfcoat.2021.127949.

[320] V. Lotito, T. Zambelli, Playing with sizes and shapes of colloidal particles via dry etching methods, Adv. Colloid Interface Sci. 299 (2022) 102538. https://doi.org/10.1016/j.cis.2021.102538.

[321] B. He, Y. Yang, M.F. Yuen, X.F. Chen, C.S. Lee, W.J. Zhang, Vertical nanostructure arrays by plasma etching for applications in biology, energy, and electronics, Nano Today 8 (2013) 265–289. https://doi.org/10.1016/j.nantod.2013.04.008.

[322] H. Yasuda, Y. Iriyama, Plasma Polymerization, in: Compr. Polym. Sci. Suppl., Elsevier, 1989: pp. 357–375. https://doi.org/10.1016/B978-0-08-096701-1.00136-1.

[323] O. Kylián, A. Choukourov, H. Biederman, Nanostructured plasma polymers, Thin Solid Films 548 (2013) 1–17. https://doi.org/10.1016/j.tsf.2013.09.003.

[324] U. Lommatzsch, J. Ihde, Plasma Polymerization of HMDSO with an Atmospheric Pressure Plasma Jet for Corrosion Protection of Aluminum and Low-Adhesion Surfaces, Plasma Process. Polym. 6 (2009) 642–648. https://doi.org/10.1002/ppap.200900032.

[325] R. Morent, N. De Geyter, T. Jacobs, S. Van Vlierberghe, P. Dubruel, C. Leys, E. Schacht, Plasma-Polymerization of HMDSO Using an Atmospheric Pressure Dielectric Barrier Discharge, Plasma Process. Polym. 6 (2009) S537–S542. https://doi.org/10.1002/ppap.200931101.

[326] Y.-C. Lin, M.-J. Wang, Fabrication of hydrophobic/hydrophilic HMDSO films by atmospheric pressure plasma jet deposition, Jpn. J. Appl. Phys. 58 (2019) SAAC01. https://doi.org/10.7567/1347-4065/aaea6c.

[327] M. Saget, C.F. Almeida, V. Fierro, A. Celzard, G. Delaplace, V. Thomy, Y. Coffinier, M. Jimenez, A critical review on surface modifications mitigating dairy fouling, Compr. Rev. Food Sci. Food Saf. 20 (2021) 4324–4366. https://doi.org/10.1111/1541-4337.12794.

[328] C. Françolle de Almeida, M. Saget, G. Delaplace, M. Jimenez, V. Fierro, A. Celzard, Innovative fouling-resistant materials for industrial heat exchangers: a review, Rev. Chem. Eng. 0 (2021) 000010151520200094. https://doi.org/10.1515/revce-2020-0094.

[329] B. Bansal, X. Chen, Fouling of heat exchangers by dairy fluids - a review., Http://Services.Bepress.Com/Eci/Heatexchanger2005/23/. (2005).

[330] O. Fysun, H. Kern, B. Wilke, H. Langowski, Formation of dairy fouling deposits on food contact surfaces, Int. J. Dairy Technol. 72 (2019) 257–265. https://doi.org/10.1111/1471-0307.12580.

[331] A. Haug, A.T. Høstmark, O.M. Harstad, Bovine milk in human nutrition – a review, Lipids Health Dis. 6 (2007) 25. https://doi.org/10.1186/1476-511X-6-25.

[332] R. Lajnaf, S. Feki, S. Ben Ameur, H. Attia, T. Kammoun, M.A. Ayadi, H. Masmoudi, Recent advances in selective allergies to mammalian milk proteins not associated with Cow's Milk Proteins Allergy, Food Chem. Toxicol. 178 (2023) 113929. https://doi.org/10.1016/j.fct.2023.113929.

[333] R.W. Currier, J.A. Widness, A Brief History of Milk Hygiene and Its Impact on Infant Mortality from 1875 to 1925 and Implications for Today: A Review, J. Food Prot. 81 (2018) 1713–1722. https://doi.org/10.4315/0362-028X.JFP-18-186.

[334] M. Indumathy, S. Sobana, B. Panda, R.C. Panda, Modelling and control of plate heat exchanger with continuous high-temperature short time milk pasteurization process – A review, Chem. Eng. J. Adv. 11 (2022) 100305. https://doi.org/10.1016/j.ceja.2022.100305.

[335] A. Sharma, S. Macchietto, Fouling and cleaning of plate heat exchangers: Dairy application, Food Bioprod. Process. 126 (2021) 32–41. https://doi.org/10.1016/j.fbp.2020.12.005.

[336] E. Wallhäußer, M.A. Hussein, T. Becker, Detection methods of fouling in heat exchangers in the food industry, Food Control 27 (2012) 1–10. https://doi.org/10.1016/j.foodcont.2012.02.033.

[337] P. Blanpain-Avet, C. André, L. Azevedo-Scudeller, T. Croguennec, M. Jimenez, S. Bellayer, T. Six, G.A.S. Martins, G. Delaplace, Effect of the phosphate/calcium molar ratio on fouling deposits generated by the processing of a whey protein isolate in a plate heat exchanger, Food Bioprod. Process. 121 (2020) 154–165. https://doi.org/10.1016/j.fbp.2020.02.005.

[338] A. Goswami, S.C. Pillai, G. McGranaghan, Micro/Nanoscale surface modifications to combat heat exchanger fouling, Chem. Eng. J. Adv. 16 (2023) 100519. https://doi.org/10.1016/j.ceja.2023.100519.

[339] W. Yao, W. Liang, G. Huang, B. Jiang, A. Atrens, F. Pan, Superhydrophobic coatings for corrosion protection of magnesium alloys, J. Mater. Sci. Technol. 52 (2020) 100–118. https://doi.org/10.1016/j.jmst.2020.02.055.

[340] S. Yao, H. Yan, S. Tian, R. Luo, Y. Zhao, J. Wang, Anti-fouling coatings for blood-contacting devices, Smart Mater. Med. 5 (2024) 166–180. https://doi.org/10.1016/j.smaim.2023.10.001.

[341] Z. Yang, X. He, J. Chang, X. Bai, P. Cao, C. Yuan, Fabrication of biomimetic slippery liquid-infused porous surface on 5086 aluminum alloy with excellent antifouling performance, Surf. Interface Anal. 53 (2021) 147–155. https://doi.org/10.1002/sia.6894.

[342] C.G.J. Prakash, R. Prasanth, Recent trends in fabrication of nepenthes inspired SLIPs: Design strategies for self-healing efficient anti-icing surfaces, Surf. Interfaces 21 (2020) 100678. https://doi.org/10.1016/j.surfin.2020.100678.

[343] W. Samah, P. Clain, F. Rioual, L. Fournaison, A. Delahaye, Review on ice crystallization and adhesion to optimize ice slurry generators without moving components, Appl. Therm. Eng. 223 (2023) 119974. https://doi.org/10.1016/j.applthermaleng.2023.119974.

[344] L. Zhao, Y. Shen, W. Liu, J. Tao, S. Liu, Solid-liquid-ice interfaces for anti-icing materials, Surf. Interfaces 42 (2023) 103510. https://doi.org/10.1016/j.surfin.2023.103510.

[345] A. Azimi Yancheshme, G. Momen, R. Jafari Aminabadi, Mechanisms of ice formation and propagation on superhydrophobic surfaces: A review, Adv. Colloid Interface Sci. 279 (2020) 102155. https://doi.org/10.1016/j.cis.2020.102155.

[346] P. Eberle, M.K. Tiwari, T. Maitra, D. Poulikakos, Rational nanostructuring of surfaces for extraordinary icephobicity, Nanoscale 6 (2014) 4874–4881. https://doi.org/10.1039/C3NR06644D.

[347] H. Wen, H. Xu, Y. Ma, C. Zhang, D. Zhang, X. Wang, Diverse and high pollution of microplastics in seasonal snow across Northeastern China, Sci. Total Environ. 907 (2024) 167923. https://doi.org/10.1016/j.scitotenv.2023.167923.

[348] R. Rangel-Alvarado, H. Li, P.A. Ariya, Snow particles physiochemistry: feedback on air quality, climate change, and human health, Environ. Sci. Atmospheres 2 (2022) 891–920. https://doi.org/10.1039/D2EA00067A.

[349] H.U. Sajid, A. Jalal, R. Kiran, A. Al-Rahim, A survey on the effects of deicing materials on properties of Cement-based materials, Constr. Build. Mater. 319 (2022) 126062. https://doi.org/10.1016/j.conbuildmat.2021.126062.

[350] S. Jiang, Y. Diao, H. Yang, Recent advances of bio-inspired anti-icing surfaces, Adv. Colloid Interface Sci. 308 (2022) 102756. https://doi.org/10.1016/j.cis.2022.102756.

[351] S. Li, F. Zhao, Y. Bai, Z. Ye, Z. Feng, X. Liu, S. Gao, X. Pang, M. Sun, J. Zhang, A. Dong, W. Wang, P. Huang, Slippery liquid-infused microphase separation surface enables highly robust anti-fouling, anti-corrosion, anti-icing and anti-scaling coating on diverse substrates, Chem. Eng. J. 431 (2022) 133945. https://doi.org/10.1016/j.cej.2021.133945.

[352] W. Samah, P. Clain, F. Rioual, L. Fournaison, A. Delahaye, Experimental investigation on the wetting behavior of a superhydrophobic surface under controlled temperature and humidity, Colloids Surf. Physicochem. Eng. Asp. 656 (2023) 130451. https://doi.org/10.1016/j.colsurfa.2022.130451.

[353] L. Oberli, D. Caruso, C. Hall, M. Fabretto, P.J. Murphy, D. Evans, Condensation and freezing of droplets on superhydrophobic surfaces, Adv. Colloid Interface Sci. 210 (2014) 47–57. https://doi.org/10.1016/j.cis.2013.10.018.

[354] Y. Zhao, Q. Guo, T. Lin, P. Cheng, A review of recent literature on icing phenomena: Transport mechanisms, their modulations and controls, Int. J. Heat Mass Transf. 159 (2020) 120074. https://doi.org/10.1016/j.ijheatmasstransfer.2020.120074.

[355] R. Hu, C. Zhang, X. Zhang, L. Yang, Research status of supercooled water ice making: A review, J. Mol. Liq. 347 (2022) 118334. https://doi.org/10.1016/j.molliq.2021.118334.

[356] S. Milles, M. Soldera, B. Voisiat, A.F. Lasagni, Fabrication of superhydrophobic and ice-repellent surfaces on pure aluminium using single and multiscaled periodic textures, Sci. Rep. 9 (2019) 13944. https://doi.org/10.1038/s41598-019-49615-x.

[357] L.B. Boinovich, K.A. Emelyanenko, A.M. Emelyanenko, Superhydrophobic versus SLIPS: Temperature dependence and the stability of ice adhesion strength, J. Colloid Interface Sci. 606 (2022) 556–566. https://doi.org/10.1016/j.jcis.2021.08.030.

[358] L.B. Boinovich, A.M. Emelyanenko, Recent progress in understanding the anti-icing behavior of materials, Adv. Colloid Interface Sci. 323 (2024) 103057. https://doi.org/10.1016/j.cis.2023.103057.